Contents

1 Introduction **14**

1.1 Ternary molybdenum chalcogenides 16

1.2 Transition-metal dichalcogenides 20

1.3 Li and Mg Battery System 21

1.4 Theoretical and Experimental Studies 24

1.4.1 Cathode materials 28

1.5 Motivation for the Study 30

1.6 Outline of the Thesis 33

2 Theoretical Background **35**

2.1 Force Field Methods 36

2.2 Quantum Mechanical Methods 38

2.2.1 The Many-Body Schrödinger Equation 39

2.2.2 Hartree-Fock Methods 41

2.3 Density Functional Method 47

2.3.1 The Kohn-Sham Equation 48

2.3.2 Solution of the Kohn-Sham Equations 51

2.3.3 Implementation of the Kohn-Sham Equations 52

2.3.4 The Exchange-Correlation Energy 55

2.3.5 Periodic Boundary Conditions and Bloch's theorem 61

2.3.6 k-point Sampling and Plane-wave Basis Sets 62

2.3.7 The Pseudopotential Approximation 65
2.3.8 Energy Minimization 72

3 Method of calculations **77**
3.1 Planewave Methods 77
3.1.1 CASTEP Code 78
3.1.2 Finite Planewave Basis Sets Corrections and Convergence. 80
3.2 Calculations of Optical Properties 81
3.2.1 Evaluation of the Dielectric Constant. 85
3.3 Commissioning of Computer Codes and Graph Analysis. 88
3.4 Hardware and Analytical Software 88

4 Ternary Molybdenum Chalcogenides **91**
4.1 Structural Properties of the Ternary Molybdenum Chalcogenides 91
4.1.1 Structural description 91
4.1.2 Structural Modelling 95
4.1.3 Interatomic and intercluster distances and their variation with Mg position. 99
4.1.4 Equation of State and Pressure Dependence of Lattice Parameters (Mo_6S_8 and $Mg_xMo_6S_8$) 102
4.2 Calculation of Voltage Curves and Structural Stability 113
4.2.1 Mg Battery System 113
4.2.2 Energies and cell voltages for $Mg_xMo_6S_8$ ($0 \leq x \leq 2$) 115
4.3 Electronic Properties 117
4.3.1 Electronic Description 117
4.3.2 Density of States (DOS) of $M_x^{n+}Mo_6X_8$ 119
4.3.3 Charge density of $M_x^{n+}Mo_6X_8$ 131
4.4 Optical Properties 138
4.4.1 Reflectivity and conductivity with polarization. 138

4.5 Concluding Remarks 138

5 Transitional-Metal Dichalcogenides 142

5.1 Structural Properties of Transitional-Metal Dichalcogenides 142

5.1.1 Structural Description 142

5.1.2 Structural Predictions 146

5.1.3 Equation of State and Pressure Dependence of Lattice Parameters of TiS_2 and $LiTiS_2$. 152

5.1.4 Elastic constants of TiS_2 and $LiTiS_2$ 154

5.2 Calculation of Voltage Curves and Structural Stability 156

5.2.1 Li Battery System 156

5.2.2 Energies and cell voltages of Li_xTiS_2 $(0 < x < 1)$ 158

5.3 Electronic Properties 162

5.3.1 Density of States (DOS) and Bandstructure 163

5.3.2 Charge density of TiS_2 and $LiTiS_2$ 165

5.4 Optical Properties 169

5.4.1 Reflectivity and Electron-Energy-Loss Spectra (EELS) with Polarization. 169

5.5 Concluding Remarks 171

6 Principal Conclusions and Future Work 174

6.1 The Future 175

A Schrödinger's Equation. 197

B Materials Modelling 201

B.1 Meaning of Terms 201

C Generation of Pseudopotentials 205

D BFGS Minimization Method 207

E Steepest Descent Minimization Method **209**

F Conjugate Gradients Minimization Method **211**

G Bulk Modulus and Elastic constant Calculations **213**

G.1 Elastic Constant of Hexagonal Materials. 214

H Publications and Papers Presented at International Conferences **218**

H.1 Publications 218

H.2 Papers Presented 219

H.2.1 International Conferences 219

H.2.2 Local Conferences 220

List of Figures

1-1 Equivalent circuit of TiS_2/PEO-$LiClO_4$-PC-EC/Li cell. (The figure is obtained from Moon et al.[7]) 23

2-1 Scheme of typical electronic structure calculations. The outer circle represents the geometry optimization or other manipulation of the geometry such as energy minimization, simulated annealing, dynamics trajectories or Monte Carlo procedures. The inner circle is the self-consistency procedure to solve the Kohn-Sham equations. Diagram obtained from E. Wimmer[188] 53

2-2 Overview of electronic structure methods for solving the Hartree-Fock and Kohn-Sham equations. Diagram obtained from E. Wimmer [201]. 54

2-3 The introduction of a supercell to allow periodic boundary conditions to be applied to an aperiodic system. 62

2-4 Schematic representation of the all-electron (solid lines) and pseodoelectron (dashed lines) potentials and their corresponding wave functions. The radius at which all-electron and pseudoelectron values match is designated r_c 67

2-5 Minimization path following a steepest descents path. When complete line searches starting from point **a** are used, the minimum is reached in about 12 iterations. Here, where a rigorous line search is carried out, approximately 8 function evaluations are needed for each line search using a quadratic interpolation scheme. The steepest descents consistently overshoots the best path to the minimum, resulting in an inefficient, oscillating trajectory. 73

2-6 Conjugate gradients method - only two steps are required to find the minimum 74

3-1 Convergence of the total energy for $LiTiS_2$ unit cell for different cut-off energy E_{cut}^{castep} using "ultrasoft" pseudopotentials. The inset shows the variation of the elapsed time. 87

3-2 Convergence of the total energy for $MgMo_6S_8$ unit cell for different cut-off energy E_{cut}^{castep} using "ultrasoft" pseudopotentials. The inset shows the variation of the elapsed time. 89

4-1 Basic crystal structure of the $Mg_xMo_6S_8$ ($0 \leq x \leq 2$) cathodes. (a) Basic atomic arrangements in the rhombohedral Chevrel phase sulphide cluster with (b) two possible Mg positions with a dumbell shape per cavity 2 ($\bar{1}$) and (c) six positions giving a hexagonal or puckered ring per cavity 1 ($\bar{3}$). 93

4-2 Crystal structure of the Chevrel phase $Mg_OMo_6S_8$, showing four Mo_6S_8 rhombohedral units (each unit is turned by an angle of about 27° around the ternary axis), the strong (Mo-Mo) intercluster and Mo-S(1) intercluster bonding and two types of chalcogen atoms [axial S(2) and peripheral S(1)]. Inserted Mg cations are located at position (0,0,0). A hexagonal unit cell can also be defined with Mg_0 being the origin. The vector from Mg_0 to Mg_1 is the c lattice parameter and the vectors from Mg_0 to Mg_2 and Mg_0 to Mg_3 are the a lattice parameters. 94

4-3 Hexagonal lattice parameters a_H (in Å) and c_H (in Å) variation with pressure for Mo_6S_8 and $Mg_OMo_6S_8$. 101
4-4 Rhombhohedral lattice parameters a_R (in Å) and α_R (∘) variation with pressure for Mo_6S_8 and $Mg_OMo_6S_8$. 103
4-5 Relative rhombohedral volume variation with pressure for $Mg_OMo_6S_8$ and Mo_6S_8. 104
4-6 The relative compression of Mo_6S_8 and $Mg_OMo_6S_8$. 106
4-7 Calculated c_H/a_H ratio's variation with pressure for $Mg_OMo_6S_8$ and Mo_6S_8. 108
4-8 Triclinic lattice parameters (in Å) as a function of pressure for $Mg_AMo_6S_8$. 109
4-9 Relative triclinic volume (in $Å^3$) as a function of pressure for $Mg_AMo_6S_8$ 111
4-10 LDA calculations of pressure variation with the principal distances (in Å) for Mo_6S_8. 112
4-11 LDA calculations of pressure variation with the principal distances (in Å) for $Mg_OMo_6S_8$. 114
4-12 The total density of states (DOS) of the Mo and S *s, p, d* levels in Mo_6S_8. The Fermi level (E_F) is set at zero. 118
4-13 The total density of states for $Mg_AMo_6S_8$. The Fermi level (E_F) is set at zero. 119
4-14 The partial density of states of Mo_6S_8 showing the *s*, *p*, and *d* -states of molybdenum (Mo) atoms. The Fermi level is set at zero. 120
4-15 The partial density of states showing the *s* and *p* -states of sulfur (S1) in Mo_6S_8. 121
4-16 The partial density of states showing the *s* and *p* -states of sulfur (S2) in Mo_6S_8. 122
4-17 The partial density of states for the *s*- and *p*-states of Mg in $Mg_AMo_6S_8$. 123
4-18 The partial density of states showing the *s* and *p* -states of sulfur (S1) in $Mg_AMo_6S_8$. 124

4-19 The partial density of states of $Mg_AMo_6S_8$ showing the s, p and d -states of molybdenum (Mo). 125
4-20 The total density of states for $Mg_{1B}Mo_6S_8$. 127
4-21 The total density of states for $Mg_{2B}Mo_6S_8$. 128
4-22 A comparison of the total density of states of Mo_6S_8, $Mg_{1A}M_6S_8$, $Mg_{2A}M_6S_8$, $Mg_{1B}M_6S_8$ and $Mg_{2B}Mo_6S_8$. 130
4-23 Contour plot of (a) the total valence electron pseudocharge density of $Mg_OMo_6S_8$ and (b) the pseudocharge difference of the Mo_6 cluster and the S_8 and Mg in the plane that spans the $Mo(1)_\triangle$-$Mo(1)_\triangle$ and $[Mo(1) - Mo(1)]_\triangle$ distances. The color coding is dark blue to red/magenta for increasing density. The contour values range from 0.03 to 1.09 and -0.59 to 0.28 $e/Å^3$, respectively. The isodensity (insert) is plotted at -0.15 within a range of -0.33 to 0.13 $e/Å^3$. 132
4-24 The charge density plot showing a slice of (a) the pseudocharge density and (b) pseudocharge-density difference for $Mg_OMo_6S_8$ along the plane that includes the S(2) sulfur and Mg at the origin parallel to the $\overline{3}$ axis. The color coding is dark blue towards red/magenta for increasing density. The density varies between 0.03 to 1.12 and -0.03 to 0.14 $e/Å^3$ respectively. 133
4-25 The charge-density plot showing a isosurface of the total charge-density difference of $Mg_OMo_6S_8$ and Mo_6S_8 along the plane that includes the S(2) sulfur and Mg at the origin parallel to the $\overline{3}$ axis. The color coding for the isosurface is light blue, plotted at 0.06 within a range of -0.09 to 0.15 $e/Å^3$. 135
4-26 The charge density difference plot of the total charge density of $Mg_OMo_6S_8$ and Mo_6S_8 in a plane parallel to the $[Mo\text{-}S(1)]_{intercluster}$ and Mo-S(1) distances. 136
4-27 The real part of the optical conductivity of $MgMo_6S_8$ 139

4-28 The real part of the optical conductivity of $EuMo_6S_8$ (a), $PbMo_6S_8$ (b), $Eu_{0.75}Sn_{0.25}Mo_6S_{7.6}Se_{0.4}$ (c), and $Eu_{0.5}Pb_{0.5}Mo_6S_8$ (d) as derived from the reflectivity spectra at room temperature. This figure has been taken from Ref. [111]. 140

5-1 Strucure of 1T - Lithium intercalated TiS_2. The metal atoms (Ti) are represented by the magenta polyhedra, while S and Li are represented by the yellow and pink atoms respectively. 144

5-2 Projection of the Li_xTiS_2 supercell for $x = 0, \frac{1}{4}, \frac{3}{4}, 1$. Lithium atoms occupy the octahedral sites in a disordered fashion. 145

5-3 A comparison of the calculated relative lattice parameters a/a_0 and c/c_0 of TiS_2 as a function of pressure with the experimental data of Allan *et al.* [130] at pressures below 10 GPa.. 148

5-4 The relative lattice parameters a/a_0 and c/c_0 of TiS_2 as a function of pressure. 149

5-5 Variation of the Sulfur-Titanium bond length with pressure for TiS_2 and $LiTiS_2$. 150

5-6 Variation of the sulfur free parameter (fractional coordinate) with pressure (in GPa) in TiS_2 and $LiTiS_2$. 151

5-7 Concentration dependence of lattice parameter a and c of Li_xTiS_2 compared with the variation of the stage package thickness with x in Li_xTiS_2 $(0 < x < 1)$ [270]. 151

5-8 Theoretical lattice volume V/V_0 of TiS_2 and $LiTiS_2$ as a function of pressure. 153

5-9 A comparison of the predicted average intercalation voltage of Li_xTiS_2 over the theoretical cycle $(0 < x < 1)$ with the secondary performance of EBC microbattery [5] over 2500 cycles. 159

5-10 A plot of the bandstructure and density of states of TiS_2. 161

5-11 A comparison of the total density of states for TiS_2 and $LiTiS_2$. 162

5-12 Variation of band structure with pressure for TiS_2. At zero pressure the top two bands are unoccupied. The band structure for the calculation at 2 GPa is not shown but is intermediate between those for the 0 and 4 GPa simulations. 164
5-13 Pressure variation effect to the bandstructure of ZrS_2. Metallization is observed along the L-symmetry point of the BZ. 166
5-14 Brillouin zone for ZrS_2. The atoms colour is blue for Zr and yellow for S. 166
5-15 The charge-density plot showing a slice of the total pseudocharge-density of $LiTiS_2$ alongside the total pseudocharge-density difference of $LiTiS_2$ and TiS_2 along the (110) plane. The atoms identified belongs to the plane. The color coding is dark blue towards red/magenta for increasing density. The density varies between 0.03 to 1.13 and -0.06 to 0.13 $e/\text{Å}^3$ respectively. . 167
5-16 A comparison of our calculated and experimental [55] reflectivity spectra of TiS_2 170
5-17 Reflectivity spectra of TiS_2 and $LiTiS_2$ for E$\perp c$ polarization. 170
5-18 A comparison of our calculated and experimental [149] reflectivity spectra of ZrS_2. 172

C-1 Flow chart describing the construction of an ionic pseodopotential for an atom. 205

List of Tables

4.1 Calculated and experimental structural parameters for rhombohedral and hexagonal Mo_6S_8 and $Mg_xMo_6S_8$ ($x = 1$ and 2) 96

4.2 Predicted principal distances and angles of Mo_6S_8, and $Mg_OMo_6S_8$ calculated within both the LDA and GGA compared with experimental distances. 98

4.3 Calculated interatomic distances for rhombohedral $Mg_OMo_6S_8$ and triclinic $Mg_AMo_6S_8$ compared with $LiMo_6S_8$. 100

4.4 First- and second-order axial compression coefficients of Mo_6S_8 and $Mg_OMo_6S_8$. B^{-1} is the linear compressibility at zero pressure and B' is the pressure derivative of B. 105

4.5 Theoretical value of the bulk modulus B and its presure derivative of $Mg_AMo_6S_8$ in comparison with the experimental value for $Cu_2Mo_6S_8$ [44]. 110

4.6 Calculated E^{tot} for Mo_6S_8, Mg_{metal}, $MgMo_6S_8$, $Mg_AMo_6S_8$, $Mg_BMo_6S_8$, and $Mg_{AB}Mo_6S_8$ systems. 115

4.7 Total ground state energy E^{tot} for Li_{metal}, Mo_6S_8, and $Li_1Mo_6S_8$ unit-cell systems. 116

4.8 Mulliken population analysis with a spilling parameter of 0.40% for the bond overlap populations ($|e|$ units) in Mo_6S_8, and $Mg_OMo_6S_8$ systems (LDA, Ultrasoft-pseudopotentials). 137

5.1 Pseudopotential calculated lattice parameters compared with the crystallographic data and bond lenghts from McTaggart and Wadsley (1958) and Greenaway and Nitsche (1965) with experimental distnaces in Å for TiS_2, ZrS_2 and $LiTiS_2$ compounds. 147
5.2 Theoretical and experimental values of the bulk moduli of TiS_2, and Li_xTiS_2 $(0 < x < 1)$. 152
5.3 Elastic constants of TiS_2 and $LiTiS_2$ (in GPa) calculated from PP and also using a density of 3.249 g/cm^{-3}. 155
5.4 Total ground state energy E^{tot} for Li_{metal}, TiS_2 and Li_1TiS_2 unit-cell systems. 158
5.5 Total ground state energies E^{tot} and calculated potential for Li_{metal}, TiS_2, $Li_{1.00}TiS_2$, $Li_{0.75}TiS_2$, $Li_{0.5}TiS_2$ and $Li_{0.25}TiS_2$ super-cell systems. 159

Chapter 1

Introduction

"*Through material design we can expect improvements in energy density. And although designing new materials can be intuitive or based on chemical concepts, coupling these efforts with those of theorist who are able to perform band-structure calculations on envisioned compounds will prove to be highly beneficial.*" J.-M. Tarascon and M. Armand [1].

Rechargeable batteries are becoming increasingly important in the field of energy storage and conversion devices among battery manufacturers and world markets. This has attracted extensive research in materials, surface, and electrochemical science because of the high complexity of these systems and hence, their basic study is very challenging. The major trends in research and development have been devoted to the rechargeable lithium battery, in particular Li-ion cells and solid-state batteries containing polymeric electrolyte. The lithium battery is regarded as one of the most promising power sources for this next century due to its high specific capacity and excellent storage property. One of the most important advances in recent years in the field of energy storage and conversion relates to the development of lithium and magnesium-ion batteries based on metallic magnesium or lithium anode, ternary molybdenum chalcogenides-magnesium intercalation or transitional metal dichalcogenides-lithium intercalation cathodes, and electrolyte systems of either polar aprotic solvent or lithium/magnesium-ion conducting

polymers. This thesis is concerned with the application of computer simulation methods to the study of the magnesium intercalated compound $MgMo_6S_8$ and lithium intercalated compound $LiTiS_2$.

A new kind of rechargeable battery has been developed in Israel [2]. Made from magnesium, it is light, non-toxic and cheap. The technology might eventually replace lead-acid and nickel-cadmium packs for powering vehicles and electricity storage or uninterrupted power systems. Lithium makes batteries small but is costly and volatile. Lead and cadmium render batteries rechargeable but are heavy and potentially environmentally hazardous. Magnesium is safe with a low electrochemical equivalent (12.15 g eq^{-1}), less expensive and the seventh most abundant metal in the Earth's crust ; in many ways, it is the ideal metal for making a battery. Researchers have been trying to make batteries from magnesium since the 1980's. Aurbach *et al.* [2] are the first to make a practical prototype. It generates $0.9 - 1.2$ volts - about the same as a nickel-cadmium battery - and can be discharged and recharged many times without losing much power capacity. The researchers had previously discovered that magnesium ions can pass in and out of a type of molybdenum sulfide, called Mo_6S_8. They make this material from a copper-containing version, replacing the copper with magnesium. First they did the exchange electrochemically, but this in not the practical way to make commercial batteries. Currently, the most promising material is pure Chevrel framework, Mo_6S_8, free of any cation. Unfortunately, this compound is thermodynamically unstable and can be obtained only indirectly by chemical or electrochemical leaching of the more stable, cation-containing Chevrel phases, for example, $Cu_2Mo_6S_8$ [3, 4].

Development and commercialization of rechargeable batteries based on Li metal anodes and liquid electrolyte solutions has lessened in importance due to the possibility of safety and life-cycle problems. However, Li metal batteries have some unique advantages such as high densities and power densities, a flat discharge profile (stable operating voltages) and excellent low temperature performance. To fulfil the interesting need of the global battery market, in particular rechargeable Li batteries, renewed experimen-

tal and theoretical interest in the layered transition-metal dichalcogenides has brought about in the 90's much greater understanding of their unusual anisotropic optical and transport properties. Initially, materials such as layered TiS_2 or MoS_2 were developed as positive plates for practical secondary cells by Exxon, Moli energy and others. Commercial battery of this type has been available since 1996. A thin-film solid-state Li/TiS_2 microbattery has been developed by Eveready Battery Company (EBC) using sputtering for disposition contacts, TiS_2 cathode and glassy electrode [5].

Electrode materials such as TiS_2 has been used either as cathodic or anodic materials. Such systems have a lower voltage and therefore a lower energy density that the systems where carbons and metal oxides are mainly used as anodic and cathodic materials respectively. The higher stability of the latter system gives them a competitive edge but the introduction of polymeric electrolyte improves on the stability of the systems with TiS_2 as a cathode. Experimental Li-TiS_2 polymer cells where lithium superacid salts were used in polyethylene oxide (PEO) electrolytes have been tested for cycle life performance showing no significant loss in capacity [6]. Recently, TiS_2 composite cathode for lithium polymer battery has been developed, where the charge/discharge characteristics as a function of the temperature were investigated [7, 8].

A great amount of experimental data in Li-ion batteries is now available, while new data on Mg-rechargeable batteries is presently generated. Collection of these data and analyzing them with appropriate computational models is a way to obtain better insight into the physical and chemical process. $Mg_xMo_6S_8$ and Li_xTiS_2 models are used in this study to reduce the experimental effort and to design improved batteries.

1.1 Ternary molybdenum chalcogenides

The ternary molybdenum chalcogenides (TMC's) $M_xMo_6X_8$ (M = metal atom, X = S, Se, Te) have been intensively investigated [4, 9, 10, 11, 12, 13, 14, 15, 16, 17, 18] because of their high specific density, high electronic conductivity and high metal diffusion coef-

ficient. They have also attracted attention for their startling superconducting properties and for their possible thermoelectric [19, 20] and electrochemical [21, 22] applications. The Chevrel phase sulfides are unstable at high temperatures and can only be obtained in the presence of a metal element as cation which binds each Mo_6S_8 unit as big ion. The metal element plays an important role in stabilizing the whole structure and then the physical properties are strongly dependent of the metal species. Lattice instabilities were found to exist at low temperatures in compounds containing small cations such as Co, Cu and Li. In compounds containing large cations such as Pb and Sn, softening of the lattice was observed by Mössbauer and inelastic neutron scattering studies [23]. The crystallographic locations of large and small atoms has been found not to be identical because of the degree of delocalization of the M atoms from the $\overline{3}$-symmetry position which is small for the large atoms and large for the small atoms [23, 24, 25, 26, 27]. It has been reported that the lattice parameters of the different $RE_xMo_6S_8$ compounds do not differ very much from each other and that they are very close to the ones of $Sn_{1.2}Mo_{6.35}S_8$ and $PbMo_{6.35}S_8$, in particular $EuMo_{6.35}S_8$ [28]. In this study, we focus our attention on the ternary molybdenum sulfides of formula $M_xMo_6S_8$ ($0 < x \leq 4$, M = earth-alkaline or earth-alkali metal), which have been widely studied because of their unique physical and chemical properties. Mg intercalated Mo_6S_8 [2, 29] and $Cu_2Mo_6S_8$ [30] have been recently reported as possible candidate cathode materials in high-density rechargeable batteries. Electrochemical characteristics of intercalation compounds strongly depend on the morphology of the materials and on their structural perfection [31]. Insertion of magnesium is of particular theoretical and practical interest, because the ion sizes of the monovalent lithium (Li^+ = 0.76 Å) and divalent magnesium (Mg^{2+} = 0.72 Å) cations are similar.

Electronic structure investigations in Chevrel-phase systems has been conducted experimentally using photoemission spectroscopy [32]. Theoretical investigation enables one to understand bonding properties of these complex materials; in particular, the structural properties are related to electronic structure. A number of theoretical calculations have

been reported for the Chevrel phase compounds [19, 20, 32, 33, 34, 35, 36, 37, 38, 39]. Electronic structure calculation varied from semi-empirical molecular-orbital calculations for the Mo_6X_8 units to full bandstructure calculations. A clearer picture of the bonding properties, in particular, the structural properties were related to electronic structure. Andersen *et al.* [35] and Nohl *et al.* [37] have calculated level schemes and band structure using muffin-tin orbitals and atomic-sphere approximation to the Korringa-Kohn-Rostoker (KKR) method. Likewise, Jarlborg and Freeman [36] have obtained results for $EuMo_6S_8$, using muffin-tin orbitals with an *ab initio* method. Mattheis and Fong [33] have reported a tight-binding calculation for a cubic Mo_6S_8 cluster. Bullet [34] has deduced density of states (DOS) curves from computations with localized orbitals for the compounds $PbMo_6S_8$ and $PbMo_6Se_8$ together with the related binary compounds Mo_6S_8 and Mo_6Se_8. Burdett [38] has presented a tight-binding-E.H.T. calculation applied to the distortion of the idealized O_h geometry of the Mo_6S_8 unit. The twisting of the Mo_6X_8 units was related to relief of the interunit repulsion between negative X ions at the corners of neighbouring cubes [38]. Certain *et al.* [40] also used similar method to calculate bandstructure diagram and DOS curves for a cubic Mo_6S_8 unit and $PbMo_6S_8$. The superconducting properties of some of the $M_xMo_6X_8$ compounds may be related to a high Mo $4d$ DOS at the Fermi level [33].

The Chevrel phases are characterized by the valency electron concentration (VEC), i.e. the number of valence electrons on the metal-metal bonding of the Mo_6 cluster, which takes into account number of valence electrons that a metal ion can transfer to the Mo_6 cluster. There would be 20 electrons in the molecular orbitals of the metal-metal bonds of Mo octahedron [10], although theoretically the host Mo_6X_8 network can accommodate metal ions until a VEC value as high as 24 electrons per Mo_6 cluster. Addition of Mg atoms to the host results in electrons transfer, wherein electrons are accepted by the lowest lying vacant energy level of the host band (conduction band [41]), which acts as an electron sink. The number of the valence electrons increases due to easy redistribution of electronic charge on each element (Mo or S). This affects the stability of

Mo_6 which contracts and allows high mobility of the inserted metal ions. Charge transfer and the VEC is determined from the variation of the $Mo(1)_\triangle$-$Mo(1)_\triangle$ distances of the Mo_6 octahedron clusters and the model described by Yvon [10] for the Chevrel phases [42]. VEC is calculated by adding the number of valence electrons of the Mg atoms to the number of valence electrons of the Mo atoms and by subtracting the number of electrons required to fill the octet of the S atoms. This charge-transfer process is the basis of the cell reaction in which these materials are used as cathodes in solid-state batteries

An initial study [43] of pressure effects on the entire family of ternary molybdenum sulfides revealed remarkably large values of $\mathrm{d}T_c/\mathrm{d}p$; an order of magnitude greater than usually observed, which could be associated with the crystal structure in general as opposed to one specific compound. This work was followed by Webb *et al.* [44] who studied the room temperature compressibility of ten superconducting double molybdenum sulfides and selenides as well as the isostructural binary compound Mo_6Se_8. Materials formed from relatively small magnetic ion, such as divalent d transition elements destroys the superconductivity. Pressure induced superconductivity for the Chevrel phase $Eu_xMo_6S_8$ has been investigated both resistively and magnetically under hydrostatic pressure up to $\sim$18 kilobar and reported to be at pressure above $\sim$7 kilobar with $T_c = 11$ K [45]. This observation was also made in semiconducting $(Sn_xEu_{1-x})_yMo_6S_8$ [46] at superconducting temperature ($T_c \sim 10$ K), reached at pressures above $\sim$7 kilobar up to $\sim$12 kilobar. Several possible reasons for the absence of superconductivity at ambient pressure and the onset of superconductivity at a high pressure have been discussed [47, 48, 49] where a suppressed structural phase transition [47] or an impurity phase effect [48] had been cited. The pressure dependences of the structural and superconducting transition temperatures of $EuMo_6S_8$ have been measured under nearly hydrostatic pressure up to $\sim$15 kilobar [50]. The pressure dependencies of the superconducting transition temperature T_c has also been measured for divalent $SnMo_6S_8$, $PbMo_6S_8$ and $EuMo_6S_8$ [52] and recently for $Pb_{0.8}Sn_{0.2}Mo_6S_8$ [53] which included the dependency of hexagonal lattice parameters. T_c measurements on $Cu_2Mo_6S_8$ disordered by shock pressure has also been reported [54].

1.2 Transition-metal dichalcogenides

The transition-metal dichalcogenides (TMDC) layer compounds have been extensively studied in recent years. The experimental and theoretical studies on layered transition-metal dichalcogenides of type TX_2 has been studied since the late 1960s [55, 56, 57, 58] with the renewed interest from the early 1970s [59, 60, 61, 62, 63]. The research gained momentum into the 80s [64, 65, 66, 67], during which intercalation with various electron-donor species has been reported [67], and the 90s [68, 69, 70, 71, 72] with increasing theoretical analysis on the charge transfer phenomenon. TMDCs are of interest in fundamental research but are also promising materials in technological applications, such as solar energy conversion, battery systems and superconductivity. They exhibit a rich variety of interesting phenomena, e.g. periodic lattice distortions and charge-density waves [72]. There is considerable interest at both an applied and fundamental level in the structural, electronic and optical properties of the TMDCs and their intercalation compounds [65, 66, 67, 68, 70].

TiS_2 has been the subject of considerable experimental attention [73, 74, 75] with recognition that it holds a considerable potential for use in the construction of high energy density batteries [76]. The nature of the electronic properties of the stoichiometric TiS_2 has been discussed for the last two decades. ZrS_2 has memory and switching effects [58] leading to a perception of their utilization in solar energy conversion systems. Earlier Raman spectroscopy studies [77] of the disulfides and diselenides of Zr, Hf, and Ti found that the Raman frequencies were relatively insensitive to the identity of the metal ion.

New materials have been obtained by intercalating various atoms in the TMDCs. The type and concentration of the intercalated species have an effect on the physical properties of the host structure, resulting from charge transfer phenomena between the guest and the host [78]. Several of the alkali-intercalated transitional metal dichalcogenides have been extensively studied for use as a cathode materials in ambient temperature high density batteries [79, 80, 81]. Their two-dimensional (2D) ionic conductivity caused by the motion of intercalated metal ions, $1T$-type intercalation compounds, facilitated their

development as cathode materials in high energy density batteries. Of these compounds, Li_xTiS_2 is the most promising because of its nearly ideal electrochemical properties [82].

1.3 Li and Mg Battery System

In order to obtain a battery systems of high energy density, highly reactive components should be used, i.e. anode materials of the lowest redox potential possible, and cathode materials whose redox potential is sufficiently high compared with that of the anode, thus enabling the composition of battery systems of high working potentials [29]. High energy density rechargeable electrochemical cells with an alkali metal negative electrode, an aprotic electrolyte, and a positive electrode exploiting insertion electrochemistry have been under development. Lithium rechargeable battery has been commercialized with several kinds of cathode materials, mainly layered metal dichalcogenides and oxides such as TiS_2 and $LiCoO_2$, etc. Very little work has been published on alkaline earth metals, such as magnesium, for use in secondary batteries. Compounds capable of insertion of alkaline earth metal ions have seldom been investigated [83, 84, 85, 86, 87]. Magnesium cells are good candidates for high-energy density batteries having advantages over other available rechargeable battery systems, in terms of safety, low cost and environmental considerations [2, 88]. Mg compounds (mostly $MgCO_3$) are highly abundant in the earth and are environmental benign. Owing to these merits, investigations on electrochemistry of Mg-based rechargeable battery systems assume significant importance.

Mg batteries are designed to compete with the environmentally problematic lead-acid and nickel-cadmium batteries for heavy load applications. Insertion of magnesium is of particular theoretical and practical interest, because of the similar ion size of the monovalent lithium (Li^+) and divalent magnesium (Mg^{2+}) cations. Hence, Li^+ ions in insertion compounds can easily be replaced by Mg^{2+} ions. However, the electrochemistry of metallic magnesium at ambient temperatures is still far from being well understood, and the electrochemical insertion reaction of magnesium have been seldom investigated

[89]. In terms of battery applications, the redox potential of the Mg/Mg^{2+} couple is 1 V higher than that of the Li/Li^{+} couple [29].

Realization of fast Mg^{2+} transport in the host is a requirement for a practical cathode material in magnesium cells. Fast Mg^{2+} transport may be expected in Mo_6X_8 compounds because of their large interstitial networks. However, the electrochemistry of metallic magnesium at ambient temperatures is still far from being well understood, and the electrochemical insertion reactions of magnesium have seldom been investigated [89]. Use of magnesium has also been found to be attractive in electrolyte activated reserve batteries for immediate use [90]. Reserve batteries are produced to fill the need of extreme storage temperature range and lengthy storage duration. They are usually designed for short duration and high power. Typical applications are military torpedoes, missiles, and radiosondes [90]. To produce a reserve type battery, usually the electrolyte is withheld from the cell structure until time of deployment.

TiS_2 is known to be one of the cathode materials for use in rechargeable lithium (metal-based) batteries [74, 91, 92]. Intercalation and ion conduction of lithium in TiS_2 has been exploited in its use as a positive electrode in rechargeable lithium batteries [93, 94]. Lithium-ion batteries [95, 96, 97, 98, 99] are the current and widely used rechargeable power source for portable electronics devices because of their high energy density. Cells using Li_xTiS_2 have been extensively explored having limitations that prevent their use in large scale consumer devices, such as electric vehicles. The Li/TiS_2 couple has too low a voltage, $1.7 - 2.5$ V, for use with carbon containing anodes [100]. This is a single phase over the entire composition range, so no energy need be expended in nucleating a new phase. This single phase behavior is noted in the emf of a Li/Li_xTiS_2 cell from around 2.5 V to 1.87 V [100]. The soft nature of the TiS_2 lattice enhances the diffusion of lithium ions, so that very high rates of reaction can be obtained. The phase Li_xTiS_2 is the thermodynamically stable compound over the entire range of lithium composition, so that there is no tendency to disproportionate for example to Li_2S and Ti_2S_3. Nor does there appear to be any tendency for the lithium and titanium to disorder in the lattice,

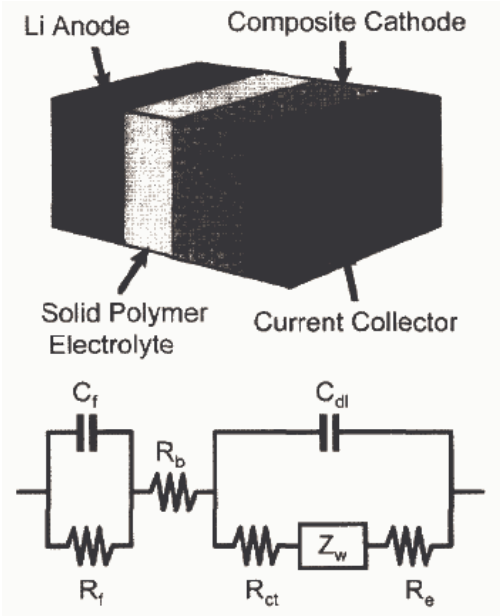

Figure 1-1: Equivalent circuit of TiS_2/PEO-$LiClO_4$-PC-EC/Li cell. (The figure is obtained from Moon et al.[7])

and only at high temperatures is there any tendency for the titanium atoms to migrate into the van der Waals layer.

$Li_xTi_{1-x}S_2$ intercalation results of TiS_2, performed well as a cathode material in lithium batteries at elevated temperatures. Composite cathode material TiS_2 for lithium polymer batteries requires solid polymer electrolyte (SPE) in order to improve lithium ionic conductivity in the cathode [7]. A good performance of charge/discharge cycling in the TiS_2/SPE/Li cells requires optimal composition of the composite cathode (TiS_2). The equivalent circuit representing the a.c. response of TiS_2/SPE/Li cell is given in Figure 1-1. In this type of battery, Li^+ ions are shuttled back and forth between an anode, where Li resides at high chemical potential, $\mu_{\mathbf{Li}}$, and a cathode where the Li chemical potential is low. In the latter instance, Li is stored in TiS_2 by ionic intercalation during the discharge cycle of the battery. The capacity of the battery depends directly on the amount of Li that can be intercalated and removed (charging/de-intercalation) reversibly from Li_xTiS_2.

1.4 Theoretical and Experimental Studies

Molybdenum sulfide Mo_6S_8 can only be prepared by de-intercalation of a small-sized cation (e.g. Cu or Ni) from an already synthesized ternary compound $M_xMo_6S_8$ [24]. Studies has been recently reported on the formation enthalpies of Mo_6S_{8-y} clusters [101] and the Chevrel-phase $Cu_xMo_6S_8$ [102, 103, 104]. X-ray absorption and photoemission studies were carried out on the manganese doped Chevrel-phase compounds $Mn_xSn_{1-x}Mo_6S_8$ for x = 0.1, where a maximum superconducting transition temperature T_c occurs [105]. Heat-capacity ($2 - 400$ K) and inelastic neutron scattering studies of the phonon spectra have been reported for superconducting, high critical field, Chevrel-phase, Pb and Sn molybdenum sulfides ($T_c \sim 11 - 15$ K) [106]. This work was later followed by the Born-von Kármán (BvK) lattice-dynamical calculations for the rhombohedral superconductors such as $PbMo_6S_8$ [107]. Jorgensen *et al.* [27] used the Mössbauer isomer-shift measurements to show that Yb is divalent in $YbMo_6S_8$. Friedt *et al.* [108] also conducted the Mössbauer-effect studies and susceptibility measurements to characterize the magnetic and structural properties of the Chevrel-phase compound $FeMo_6S_8$. The Mössbauer spectra indicated that a structural phase transition occurs at $T_0 \cong 100$ K from an ordered form at low temperature to a disordered form of the material at high temperature, accompanied by a hardening of Fe vibrational modes. The electronic structure of $Fe_xMo_6S_8$ has been studied by photoemission and Auger-electron spectroscopy [109]. Core-level shifts suggested a large charge transfer from the Fe atoms to the Mo_6S_8 clusters and a small Mo-to-S charge transfer within the cluster.

Fradin *et al.* [110] reported direct measurements of the conduction-electron spin polarization in $Sn_{0.5}Eu_{0.5}Mo_6S_8$, by means of the ^{95}Mo nuclear magnetic resonance (NMR), the ^{151}Eu Mössbauer effect, and bulk magnetization measurements. Fumagalli and Schoenes [111] investigated high-field superconductors $Eu_{1-x}Pb_xMo_6S_8$ and $Eu_{1-x}Sn_xMo_6S_{8-y}Se_y$ using Magneto-optical Kerr-effect. From the optical data they concluded that all these Chevrel-phase compounds are poor metals. Anderson *et al.* [35] used muffin-tin orbitals and the atomic sphere approximation to the KKR and LMTO methods to study the band

structures of $M_x Mo_6 X_{8-y}$ (M = Pb, Sn, Ag, Cu and X = S, Se, Te). Birrer *et al.* [112] presented a comprehensive analysis of results obtained by positive-muon spin-rotation (μ^+SR) spectroscopy in solid solutions of Chevrel-phase compounds of the composition $SnMo_6S_{8-x}Se_x$ ($x = 0, 4$) and $PbMo_6S_{8-x}Se_x$ ($x = 0, 1, 4, 7$). Band structure calculations of $SnMo_6Se_8$, $Cu_2Mo_6Se_8$ and $Zn_2Mo_6Se_8$,[113] and later of the $3d$ ions (Ti, Cr, Fe, Ni) intercalated/inserted Mo_6Se_8 [20] have been conducted to investigate their conductivity. Only $Zn_2Mo_6Se_8$ and $TiMo_6Se_8$ were found to be semiconducting, while the others are metallic.

Extensive experimental studies [114, 115, 116, 117] have been conducted on the effect of intercalation to the electronic band structure of TX_2 systems. The band structure of the TMDCs is fairly well understood [65, 118] and is simply described as consisting of a valence band predominantly based on the overlap of the chalcogen s and p orbitals (having its maximum at Γ point of the Brillouin zone), a conduction band constituted mainly from the transition-metal d orbitals (with a minimum at each L point of the Brilliouin zone). The four valence electrons of the transition metal fill up the valence band, leaving in principle, the conduction band empty. The separation between these bands increases from Ti through Zr to Hf, and decreases from the sulfides through the selenides to the tellurides [119]. Experimental and theoretical indirect p/d band gap has been reported as follows: Klipstein *et al.* [120] determined a 'p' - 'd' separation for TiS_2 and ZrS_2 of about 0.18 eV, while Greenway *et al.* [55] and Lee *et al.* [58] obtained a value of about 1.7 eV. Metallic behaviour in ZrS_2 has been observed [56, 120] to a lesser extent and only at temperatures greater than 150 K despite the presence of the p/d gap in the latter. Introduction of alkali-metal atoms into semiconductor ZrS_2 has been found to result in end products which are electrically metallic [121, 122]. Magnetic susceptibility measurements [123] over the temperature range $4.2-300$ K suggested the metallic nature of Li_xTiS_2 ($0 \leq x \leq 1$). Brown *et al.* [124] investigated the charge transfer in ZrS_2 during the intercalation/deintercalation process in order to compare the energy levels with TiS_2.

Detailed studies on the electronic structure of pure TiS_2 under ambient conditions

have produced conflicting conclusion [118, 125, 126, 127, 128, 129, 130]. Some band structure calculations [125, 127] indicate that an indirect p/d band overlap exists with an overlap ranging from 0.2 to 1.5 eV while others infer that TiS_2 is a narrow gap semiconductor. The p/d band overlap with TiS_2 exhibiting metallic behavior has been observed [62, 64, 126]. The linear combination of atomic orbitals (LCAO) [118] and the augmented planewave (APW) [128] band structure calculations produced an indirect band gap and an overlap between the S-based valence and the Ti-based conduction band respectively. The experimental evidence gathered in photoemission experiments has been interpreted as indicating either semimetallic [125] or semiconducting [127] behaviour. The angle-resolved photoemission experiments of Chen *et al.* on $TiSe_2$ and TiS_2 observed that the uppermost sulfur p bands of TiS_2 comes close to E_F at Γ but does not cross E_F. From this it was concluded that TiS_2 is a semiconductor. Resistivity measurements in highly stoichiometric titanium disulfide indicate a metallic behavior at all temperatures [131, 132], while Hall coefficient and thermoelectric power measurements support the semiconducting hypothesis [120].

X-ray Absorption Spectroscopy (XAS) and Electron-Energy-Loss Spectroscopy (EELS) measurements [129] combined with linear muffin-tin band structure calculations reported TiS_2 as a metal or semimetal at ambient pressure. X-ray diffraction studies [133] concluded that the electronic structure of stoichiometric TiS_2 has a band gap and two Ti-based conduction bands with a small energy difference. Recently a combination x-ray diffraction studies and *ab initio* pseudopotential calculations [130] of stoichiometric TiS_2 reported an isostructural semiconductor-semimetal phase transition between 4 and 6 GPa. X-ray Photoelectron Spectroscopy (XPS) valence band data [134] shows the valence bands to be strongly modified by the intercalant species in TiS_2.

During the intercalation process of either electron donors or acceptors, a charge transfer is always observed between the guest and the host. Such a transfer is at the origin of the use of lithium intercalation compounds in the present lithium batteries [135]. First-principle (semi-empirical TB) band structure calculations using simple charge-transfer

(rigid-band) model concluded that charge transfer from the alkali-metal atom appears to be more or less complete for $LiTiS_2$ [136]. A review by McKinnon [137] concluded that a charge transfer, based on a rigid band model, is well established for lithium intercalated transition metal compounds, lithium being largely ionized and its $2s$ electron being transferred to the transitional metal d orbitals. TiS_2 and $LiTiS_2$ were studied in thin film and bulk models using the self consistent linearized augmented plane-wave (LAPW) scheme [138]. Neutron Compton scattering has been used to study lithium-ion dynamics in the intercalation compounds $LiTiS_2$ [139]. In addition to being a good electronic conductor [140], Li_xTiS_2 is also a good ionic conductor [123] due to high mobility of the Li^+ ion in the van der Waal gap.

There are conflicting conclusions to the rigid-band model. Starnberg *et al.* [141] and Brauer *et al.* [142] tend to show that the later model is not adequate to study the intercalation process. X-ray Absorption Fine Structure (XAFS) and EELS studies [143] concluded from the band structure calculations in the Extended Hückel approach that there is a partial electronic transfer of lithium $2s$ electron to the host structure (TiS_2) and that it affects, in comparable amounts, both titanium and sulfur atoms. XAS and Tight Binding Linear Muffin Tin Orbitals method in the Atomic Spheres Approximation (TB-LMTO-ASA) results have shown that the electrons transferred from intercalated lithium are not only located on Ti $3d$ orbitals, as previously assumed, but also on the S $3p$ states [144]. A combination of XAS, Local Density Approximation (LDA) and TB-LMTO-ASA reported that sulfur is largely taking part in the intercalation process, in both lithium coordination and charge transfer [145]. The electronic structure of TiS_2 is of 3D character [72].

From the experimental point of view, the general optical properties of group-IV TMDCs have been known since 1965 from the pioneering work of Greenway *et al.* [55], who examined the room temperature reflectivity of several TMDCs. Bayliss *et al.* [146] performed an accurate study of the reflectivity R, between 1 and 4 eV, of most of the TMCs using polarized light parallel and perpendicular to the c-axis. Changes in the

optical spectra of a number of materials when intercalated with a variety of species has been interpreted on the basis of the rigid-band model [114, 115]. Optical properties of ZrS_2 have been investigated in the region between 1 and 12 eV [55, 59, 147, 148]. The study of both the absorption and λ-modulated absorption spectra for ZrS_2 have been investigated [149] in the region of the lowest band gap. Borghesi *et al.* [150] studied the optical structure due to interband transitions of group-IV TMDCs by means of thermoreflectance. The investigated photon energy ranges from 1 to 9 eV. Clark [151] conducted photoemission experiments on transition-metal intercalates. Boehm and Isomaki [152] calculated the optical-response spectra - Im $\epsilon^{-1}$of ZrS_2. The reflectance of TiS_2 in the infrared (ir) region has been studied by Lucovsky *et al.*[263]

Present theoretical and computational approaches, combined with the impressive advances in computer hardware and software, opens the possibility of accelerating the studies on systems from first principle. McCanny [136] studied the electrical characteristics of TiS_2 and $LiTiS_2$ using the semi-empirical tight-binding band structure calculations. The structural and electronic properties of Li_xTiS_2 has been recently studied by the *ab initio*, all-electron, periodic Hartree-Fock level [153].

1.4.1 Cathode materials

A large number of molybdenum cluster sulfides, $M_xMo_6S_{8-y}$, with a hexagonal or rhombohedral unit cell have been examined as cathode in organic electrolyte lithium secondary batteries at room temperature [18]. Electrochemical investigation of structural changes in $Li_xMo_6Se_8$ $(0 < x < 4)$ [154, 155], $Li_xMo_6Se_{8-y}I_y$ [156] and of the lithium site energy in $Li_xMo_6Se_yS_{8-y}$ $(0 \leq y \leq 8, 0 \leq x \leq 1)$ [157], and recently $Cr_xMo_6S_{8-y}$ [158] as the cathode in lithium rechargeable batteries have been reported. Chromium Chevrel phase sulfide was investigated as the cathode in lithium rechargeable batteries, where the compound was observed to have a triclinic unit cell in a wide range of chromium composition. Boulanger and Lecuire [159] studied the electrochemical behavior of Cd^{2+} cation insertion in the Chevrel Mo_6X_8 phases (X = S, Se, Te) and the condensed cluster phases

Mo_yX_z. Electrochemical measurement show that lithium and TiS_2 react continuously and reversibly over the composition range $0 \leq x \leq 1$ to yield the single phase product Li_xTiS_2. X-ray studies [160, 161] of $LiTiS_2$ also show that the original symmetry of the host is retained and that there is a continuous c-axis expansion for $0 \leq x \leq 1$.

Computer simulations may be used prior to the synthesis of new materials only requiring the crystal structure as input. Such calculations have the potential to point the way to interesting new classes of electrode materials for the next generation of advanced batteries. These calculations have reproduced electrochemical data well, hence they may be used to predict materials with enhanced energy storage abilities. The following are examples of theoretical studies of cathode materials: Reimers and Dahn [162] calculated the appropriate cell voltages for an Li/Li_yAl cell. Aydinol *et al.* [163] calculated the average voltages for $Li/LiMO_2$ and $Li/LiCoX_2$ (M = Ti, V, Mn, Co, Ni, Cu, Zn, Al; X= O, S, Se) cells. Courtney *et al.* [164] used the *ab initio* pseudopotential plane-wave method and the approximation by Aydinol *et al.* [163] to calculate the average voltage for the anode material tin oxide (in particular, lithium-tin, Li_xSn_y). Deiss *et al.* [165] calculated the energy density and cell voltage of $LiC_6/LiMoO_2$ (anode/cathode) and LiC_6/NiO_2 using the average voltage between the fully charged and the discharged states. Benco *et al.* [166] calculated the average voltages of $Li/LiTi_2S_4$ and $Li/LiTi_2O_4$ systems using the full-potential linearized augmented plane-wave method and Doyle *et al.* [167] recently developed a mathematical model to simulate impedance response of the lithium-polymer cell $Li|PEO_{18}LiCF_3SO_3|LiTiS_2$. Braithwaite *et al.* [168, 169, 170] used the *ab initio* pseudopotential plane-wave method and the finite difference approximation to calculate the variation of the cell potential of Li/LiV_2O_5, Li/LiV_6O_{13} and $Li/Li_xCo_yMn_{4-y}O_8$ systems with the degree of discharge. Recently, Koudriachova *et al.* [171, 172] also used the *ab initio* pseudopotential plane-wave method to calculate the open-cell voltage of $Li/LiTiO_2$. We have also successfully calculated and compared the energetics of anode system LiC_6 with that of metallic Li using the latter method [173]. These types of calculations have established the reliability of density-functional theory

(DFT) techniques in modelling the energetics of intercalation.

1.5 Motivation for the Study

The need for new, high performance battery systems with possible long cycle life and high energy density requiring highly reactive components, is huge. Natural candidates for anode materials of high energy density batteries are active metals such as lithium, magnesium, etc. Magnesium electrochemistry at or near ambient temperature is scarcely investigated and rather poorly understood, and a substantial research effort will be required in order to develop competitive secondary magnesium electrodes [21, 83]. In this work we focus our attention on the cathode materials Li_xTiS_2 and $Mg_xMo_6S_8$, where the latter is new and being recently investigated. From many points of view, the very complicated behavior of magnesium electrodes can be better understood by comparison with that of more established and understood world of lithium batteries [22]. Little relevant work has so far been published on rechargeable negative electrodes based on metallic magnesium, Mg alloys, or Mg^{2+} insertion materials. In our study *ab initio* planewave method and the finite difference approximation [168] will be used to calculate the variation of the cell potential with the degree of discharge for $LiTiS_2$. Energetics of the cathode system $MgMo_6S_8$ compared to metallic magnesium (anode-active) will also be calculated.

In this study, a self-consistent density-functional approach will be followed, using the norm-conserving pseudopotentials and the recently applied "ultra-soft" pseudopotentials within both the local density (LDA) and generalized gradient approximations (GGA) for exchange and correlation. These are accompanied by precautionary measures taken to attain convergence before electronic, structural and optical properties were calculated from the ground-state total-energy. There is considerably less theoretical prediction on structural properties and lattice parameter of Mo_6S_8 and $M_xMo_6S_8$ $(0 < x \leq 2)$. Theoretical investigation enables one to understand bonding properties of these complex

materials; in particular, the structural properties are related to electronic structure. In the present work we therefore aim to improve the understanding of the electronic structure of both Mo_6S_8 and $Mg_xMo_6S_8$. The DFT method will be used to probe structure and energetic properties of Mg inserted Chevrel phases with a view to providing insight into their use as cathode materials.

We aim to report, for the first time, *ab initio* pseudopotential results for $Mg_xMo_6S_8$ ($0 < x \leq 2$). Lattice parameters corresponding to minimum total-energies will be calculated and the results will be compared with experimental parameters. Atomic positions determination is important for electronic structure calculations. We aim to increase the knowledge of the symmetry of the Chevrel phase in relation to inserted Mg cations. The predicted structures will be subjected to high-pressure calculations, from which we report the first theoretical bulk and linear moduli of the new Chevrel phase structures.

There exists a number of measurements for structural properties transitional-metal dichalcogenides (TMDCs) in particular, Li_xTiS_2 ($0 < x \leq 4$) and calculated lattice parameters have been reported at ambient pressure (as discussed in section 1.2). However, not much work has been reported in regard to the pressure variation of the relative lattice parameters for Li_xTiS_2 ($0 < x \leq 1$). There is a considerable less theoretical work on compressed Li_1TiS_2 and almost no high-pressure work reported on $Mg_xMo_6S_8$ ($0 < x \leq 2$). Such calculation are of interest since the variation of the c-axis parameter with pressure in layered Li_1TiS_2 is an important observable. We also compare the effect of this variation in $Mg_xMo_6S_8$ ($0 < x \leq 2$) in this case the c-axis is along the $R3$. There is relatively no theoretical work, in particular *ab initio* pseudopotential calculations, reported in literature on structural stability, cations "site energy" calculations, and pressure work. These calculations are vital in contributing to the understanding of this new Chevrel phase.

Systematic studies have been performed on a change of lattice constants a and c vs. the concentration of the $3d$ transition metals for M_xTiS_2 (M = V, Cr, Mn, Fe, Co and Ni) [78], for Cu_xTiS_2 [174] and a few for Li_xTiS_2. TiS_2 and Li_xTiS_2 have relatively simple structures hence enabling us to study different stages or "phase". In particular, we look

at the different stages of Li_xTiS_2 ($x = 0, \frac{1}{4}, \frac{3}{4}, 1$) and aim to predict the effects of staging, if any, to the structure of TiS_2. We present static simulations of lithium diffusion in Li_1TiS_2 from the pseudopotential (PP) method.

The electrochemical intercalation and de-intercalation of lithium and magnesium involve charge and mass transfer at the interface between the active TiS_2 and Mo_6S_8 electrode respectively, and the electrolyte. From the density of energy states, we obtain (i) electron occupation, (ii) their variation with energy and (iii) occupation probability which can also be visualized accompanied by the energy band scheme. In this work we therefore aim to improve the understanding of the electronic structure of both $Mg_xMo_6S_8$ and Li_xTiS_2 systems, which will be achieved by calculating and comparing the density of states (DOS), the charge density and the band structure of both systems. Introduction of guest species (cations) in the Mo_6S_8 systems has effects on the size of both the Mo_6 and S_8 clusters and the charge transferred is said to stabilize the clusters. We aim to improve the understanding of these effects by calculation of electronic charge density, the optical spectra, density of states and accompanying bandstructure.

There are conflicting conclusions on the electronic structure of TiS_2. In our study, we also consider the electronic and optical properties of ZrS_2, in order to better understand the electronic structure of TiS_2 as a host material. The electronic structure of Mo_6S_8 and TiS_2 as hosts specimen is of fundamental interest for the study of energy conversion with insertion materials. Electronic properties will be calculated from the newly predicted $Mg_xMo_6S_8$ structure and compared with the reported trends in similar compounds. We aim to report the first *ab initio* pseudopotential partial density of states (PDOS) for $Mg_xMo_6S_8$ ($0 < x \leq 2$). The effect on the electronic structures of Mo_6S_8 and TiS_2 on intercalation with magnesium and lithium respectively is also investigated. These results are shown in the form of the electron charge density difference plots. We aim to report on our *ab initio* pseudopotential calculations of the complex dielectric tensor for $Mg_xMo_6S_8$ ($0 < x \leq 2$), compared with available experimental results for $M Mo_6S_8$ ($0 < x \leq 2$).

To summarize the above, alkali-metal intercalated transitional-metal dichalcogenides

(TiS_2 and ZrS_2) and molybdenum chalcogenides (Mo_6S_8), in particular $MgMo_6S_8$ and $LiTiS_2$ will be studied as possible anode materials in high density rechargeable batteries. Insertion of magnesium is of particular theoretical and practical interest, because of the similar ion size of the monovalent lithium (Li^+) and divalent magnesium (Mg^{2+}) cations. *Ab initio* pseudopotential calculations will be performed to predict the space lattice structures, bulk properties, energy of intercalation, ion diffusion, voltage profiles, electronic charge density distributions, density of states and optical spectra. These properties should enable us to better understand the process of recycling in battery systems and also in prediction of a new materials, e.g. $MgMo_6S_8$.

1.6 Outline of the Thesis

The thesis now continue in Chapter 2, by reviewing both force field and quantum mechanical simulation methods, in particular, the *ab initio* total-energy pseudopotential method. In Chapter 3 we discuss the computational hardware used and details involved in the methods (e.g. CASTEP) applied. These are accompanied by precautionary measures taken to attain convergence before electronic, structural and optical properties were calculated from the ground-state total-energy. In Chapter 4, we present and discuss results obtained for the ternary molybdenum chalcogenides. We investigate the structural and energetic properties of $Mg_xMo_6S_8$ ($0 < x \leq 2$) using the density-functional technique. We present our predicted structures of $Mg_1Mo_6S_8$ and $Mg_2Mo_6S_8$ from which the voltage profile, electronic and optical properties are calculated. Structural properties of $Mg_xMo_6S_8$, such as lattice constants, volume, and the bulk modulus are reported in Section 4.1. In Sections 4.3 and 4.4 we present and discuss the partial density of states (PDOS) for $Mg_xMo_6S_8$ ($0 < x \leq 2$), the effect on the electronic structure of Mo_6S_8 on intercalation with magnesium through charge density plots and the optical spectra. We end the chapter with the summary of our principal conclusion. Transitional-metal dichalcogenides are discussed in details in Chapter 5. Elastic constants of TiS_2 and

$LiTiS_2$ are presented in Section 5.1.4. The voltage profile of Li_xTiS_2 is discussed in detail in Section 5.2. In sections 5.3 and 5.4 we present and discuss the partial density of states (PDOS) for TiS_2 and $LiTiS_2$, the effect on the electronic structure of TiS_2 on intercalation with lithium through charge density plots and the optical spectra of both systems. We end the chapter with the summary of our principal conclusion in Section 5.5. The main conclusions are summarized in Chapter 6, where we also consider and propose future work.

Chapter 2

Theoretical Background

With the fundamental laws of quantum mechanics and statistical physics, the availability of high-performance computers, and with the growing range of sophisticated software systems accessible to an increasing number of scientists and engineers, the goal of designing novel materials from first principles seems to be closer than ever. Yet the complexity of real materials with their intriguing interplay between chemical composition, atomic arrangements, microstructures, and macroscopic behavior seems to elude any attempt of such first-principles materials design. Therefore, neither has first-principles materials design become a generally accepted practice nor unattainable, far from any reality. Chemists working with large and small molecules are accustomed to using computer codes and software modules that are based on quantum mechanical methods. But most properties of macroscopic materials depend on microscopic phenomena to one degree or another and also require for their correct description the application of quantum mechanics. In some cases, such as optical or magnetic properties, this is particularly obvious and direct. In other cases the link is less direct, but still very important. For example the density of a bulk solid is determined to a large extent by the forces that operate between neighboring atoms. As in a molecule, the equilibrium geometry, which ultimately determines the density, is a consequence of a balance of forces mediated by the electrons, which obey quantum mechanics. In a pure crystalline solid, the macroscopic density is

determined uniquely by the size of the unit cell and the mass of the atoms it contains. In a mixture, or polycrystal, the density is determined by a weighted average of the densities of the constituent crystalline phases. Thus even an obviously macroscopic materials quantity such as the density is a quantum property.

A wide variety of geometric and structural behavior, such as the location of impurities, the structure of defects, dislocations, grain boundaries, surfaces can be calculated from first principles. Once the geometry has been determined, a range of properties, electronic optical and magnetic can also be calculated with varying degrees of reliability. The advances that made this possible were largely incremental and are described in various contexts in terms of one-electron theory, band theory or self-consistent-field theory. Both Hartree-Fock (HF) and Density Functional Theory (DFT) methods have been applied successfully solve materials specific problems; the latter has been particularly successful on rear gear, and will be described in detail after we have discussed simpler approaches based on interatomic potential.

2.1 Force Field Methods

Early attempts to represent the interactions between atoms in organic molecules by quasi-classical force fields were quite successful in predicting molecular structures and relative energies. The first stage of this development was molecular mechanics, aimed at the prediction of static molecular structures. As long as no chemical bonds (other than hydrogen bonds) are broken and as long as there are no rearrangements of electronic charges, fairly simple analytical expressions of the total energy as a function of atomic positions can be formulated.

In the 1970s and 1980s, force field methods were increasingly used for the simulation of the dynamic behavior of liquids [175] macromolecules [176] and solids. Since the usefulness of force field methods hinges on the quality of the potential energy functions (force fields), considerate effort has been (and still is) devoted to the development and

improvements of potential energy functions and force field parameters (see, [177]). An important conceptual step was the systematic use of quantum chemical first-principles (*ab initio*) methods for the development and calibration of potential energy function [178]. In this way, force field parameters can be obtained by an unbiased procedure without prior experimental information about a system. If available, experimental data can then be used to fine-tune the parameters, thus achieving for the particular systems an accuracy which is superior to the quantum mechanical calculations.

The major advantage of force field methods is their computational simplicity and speed which allows energy minimization, molecular dynamics and Monte Carlo simulations on fairly large systems and significant statistical sampling. Using the methods of statistical mechanics one can evaluate thermodynamic properties such as entropy and free energy, which are at the heart of any chemical and physicochemical behavior.

For inorganic systems, the use of force field methods is not so straightforward and their successes depend strongly on the type of compound under investigation. Synthetic polymers have many physical and chemical characteristics in common with biopolymers. Hence, the experience gained in the development of force field methods for biomacromolecules has been transferred to synthetic polymers. However, the lack of any secondary and tertiary structure in most synthetic polymers makes it very hard to build realistic structural models for polymers. Furthermore, while the simulation of biopolymers is aimed at controlling their chemical functions, the industrially most important properties of synthetic polymers are their mechanical, thermoelastic, and diffusive characteristics. The link of these macroscopic properties to the atomistic behavior is not fully understood, it involves vastly different length and time-scales, and is thus much less amenable to quantitative predictions based solely on atomistic simulations.

The use of force field methods for inorganic systems such as metals, alloys, and semiconductors encounters difficulties and often fundamental limitations. Whereas the character of organic or biochemical molecules allows a natural separation into bonding and non-bonding interactions, this separation is usually not possible for inorganic systems

such as metal alloys. Furthermore, force fields usually assign static point charges to atoms to simplify the description of electrostatic interactions. This is a reasonable approach for organic molecules, but can be difficult to define for inorganic systems. However, for silicates, zeolites, and other oxides it is possible to create model potentials and meaningful structural results can be obtained, in particular if electronic polarizability is taken into account by approaches such as the shell model as reviewed by Catlow and Cormack [179]. If a clear separation between bonding and non-bonding interactions can be defined for a material, then force field approaches are very useful. This is the case, for example, in the description of the physi-sorption of molecules on surfaces (see, [180]) or the diffusion of molecules in the cage structure of zeolites [181]. Force field methods will have a continuing important role to play in modelling inorganic materials

2.2 Quantum Mechanical Methods

Quantum mechanics was developed independently in 1926 by Werner Heisenberg and Erwin Schrödinger. Heisenberg's approach is referred to as matrix mechanics and Schrödinger's approach is referred to as wave mechanics (see Appendix A). The richness of most physical and chemical properties of materials has its origin in the interplay between the position of the atomic nuclei and the electronic structure. Quantum mechanics as formulated at the beginning of the 20th century together with statistical mechanics offer a complete theoretical framework to describe the motions of the electrons and ensembles of atoms. Density functional theory is currently the principal quantum mechanical many-electron approach in solid state physics and is also being used increasingly to address chemical questions. Originally intended for calculating the electronic structure of metals and alloys, its range of applicability has proven to span all elements of the periodic table and all bonding types, thus making it the most widely used quantum mechanical method available today. Most practical density functional calculations are done with the local density approximation (LDA) together with so-called gradient corrections or generalized gradi-

ent approximation (GGA) to the exchange-correlation functional. Its spin-polarized form allows calculations for open-shell systems and magnetic systems. The major shortcoming of present density functional methods is the lack of systematic improvements towards the exact solution. Depending on the geometric aspects of the system under investigation, e.g. a bulk solid, a surface, or a molecular crystal, as well as on the type of desired properties, a range of different computational implementations have been developed.

Compared with density functional methods, Hartree-Fock [182, 183] based approaches are less widely used currently in electronic structure calculations of solids and surfaces, although the exact treatment of the exchange terms is conceptually very appealing. The inclusion of electronic correlation effects in the form of perturbation theory, coupled cluster methods, or configuration interaction expansion is very well developed for the calculation of molecular properties. However, in most cases these approaches are not suited for solid state systems. Quantum Monte Carlo (QMC) methods [184] represent a third type of theoretical approach for calculating the electronic structure of many-electron systems. Recent progress is promising, but further systematic developments and tests will be needed before this method can become a routine tool for the calculation of materials properties

2.2.1 The Many-Body Schrödinger Equation

The aim of an *ab initio* method is to find the solution to the many-body Schrödinger equation for the system being studied. The behavior of the N electrons in a system is described by the many body wavefunction Ψ, which is an anti-symmetric function of the electron coordinates $\{\mathrm{r}_i : i = 1...N\}$. For convenience, one can write such a wave function in the form of a so-called Slater determinant indicated by Eq. 2.1

$$\Psi(1, 2, ..., N) \approx \psi_1(1) \cdot \psi_2(2) \cdot ... \cdot \psi_N(N) + ... \tag{2.1}$$

The Hartree equations can be justified as minimizing the total energy over all wavefunctions of the form

$$\Psi = \psi_1(r_1)\psi_2(r_2)\ldots. \tag{2.2}$$

which is not properly asymmetric.

We can make a better approximation by taking the Slater determinant of some orbitals i as the many-body ground state. Note that the many-body state still can be thought of as N independent "orbitals", which is not true for a general state of N electrons, as we shall see. Minimizing over Slater determinants of independent orbitals gives the famous Hartree-Fock equation.

The wavefunction (Eq. 2.2) satisfies the many-body Schrödinger equation,

$$H\Psi = E\Psi \tag{2.3}$$

where

$$H = -\frac{\hbar^2}{2m}\sum_i \nabla^2_{r_i} + V_{ext}(\{r_i\}) + V_{e-e}(\{r_i\}) \tag{2.4}$$

and the eigenvalue E is the total energy of the system. The potential V_{ext} consists of the external potential imposed on the electrons by the nuclear configuration, $\{\mathbf{R}_I\}$ and V_{e-e} is the electron-electron interaction given by the Hatree term $\sum_{j>i}\frac{e^2}{|r_i-r_j|}$. i denotes the Cartesian coordinates and the spin coordinates of each electron.

In principle this equation can be solved to arbitrary accuracy by representing Ψ as a direct product wavefunction and diagonalizing the Hamiltonian. However, the cost of this calculation scales exponentially with the number of electrons in the system and is intractable for all but the smallest of systems. The variational principle shows that the ground state energy can then be found by minimizing the quantity

$$E[\Psi] = \frac{\langle \Psi \,|H|\, \Psi \rangle}{\langle \Psi \mid \Psi \rangle} \tag{2.5}$$

over all possible $\Psi(\{r_i\})$. The variational principle states that the expectation value of these total energy, using any approximate many-electron wave function, such as a Slater determinant, is an upper bound for the exact total energy. Therefore, by varying each one-electron wavefunction such that it minimizes the total energy

$$\frac{\delta E}{\delta \psi_i} = 0, \tag{2.6}$$

one obtains conditions for each wave function in the form of one-electron wave functions. These functions are known as Hartree-Fock (HF) equations

$$\left[-\frac{\hbar^2}{2m} \nabla^2 + V_{ext} + V_x^i \right] \psi_i = \varepsilon_i \psi_i \tag{2.7}$$

or Kohn-Sham equations (to be discussed later).

In the exact many-body formulation, the evaluation of $E[\Psi]$ involves the evaluation of $3N$-dimensional integrals, which are very computational intensive. Quantum Monte Carlo techniques may be used to evaluate $E[\Psi]$ for a given wavefunction and to perform the minimization over possible wavefunction configurations. However, the cost of such calculations is still high for complex systems.

2.2.2 Hartree-Fock Methods

The Hartree-Fock (HF) picture [182, 183] starts from the consideration of each electron and its interactions with all other electrons and nuclei. The "exact" quantum mechanical Hamiltonian operator is used to describe explicitly the motion of each electron and its Coulomb interactions with all other charged particles in the system under consideration. While the "exact" many-electron Hamiltonian operator can be written down, the corresponding exact many-electron wave function is not known. Hartree-Fock theory builds on the simplest possible approximation to such a many-body wave function,

namely a product of one-electron wave functions, where each one-electron wave function corresponds to an individual electron (Hartree approach). In Hartree-Fock theory, one additional aspect is included in the many-body wave function, namely the Pauli principle (electrons with the same spin cannot occupy the same orbital). To this end, the product of one-electron wave functions is generalized to a sum of such products with alternating sign (conveniently written in the form of a determinant). This accounts for the Pauli exclusion principle: electrons with the same spin avoid each other. One could say that each electron is surrounded by a region in space (called the "exchange hole") which is depleted of electrons with the same spin. Energetically, the exchange hole leads to a reduction in the Coulomb repulsion among electrons with the same spin and thus acts on the electrons as an effective attractive potential. This exchange hole is constructed by using all one-electron wave functions of the Slater determinant. The effective exchange operator of the HF equation can be written in the following form [185]:

$$\mu_x^i(r) = -\sum_j \delta(\sigma_i, \sigma_j) n_j \frac{\int \psi_i^*(r)\psi_j^*(r')\frac{1}{r-r'}\psi_j(r)\psi_i(r')dr'}{\psi_i^*(r)\psi_i(r)} \tag{2.8}$$

This operator is different for each eigenstate i. The negative sign in Eq. 2.8 indicates that the exchange operator acts as an effective attractive potential for the electrons, i.e. without this term the corresponding eigenvalue would be less negative.

Ab initio quantum chemistry methods based on Hartree-Fock theory thus use an exact Hamiltonian and approximate many-electron wave functions, the simplest of which is a single Slater determinant. More accurate many-electron wave functions such as a series of Slater determinants (Eq. 2.1) lead to so-called correlated methods. Quantum chemists often refer to computations using a single Slater determinant as "calculations on the SCF (self-consistent-field) level". In these calculations, the essential task consists in an iterative self consistency procedure required to solve the Hartree-Fock equations (Eq. 2.7). Because of the mathematical nature of the Hartree-Fock approach, Gaussian-type functions turn out to be the most efficient and perhaps the only practical way to expand the one-electron wave functions. Since their introduction [186] Gaussian-type

orbitals have dominated Hartree-Fock based approaches for almost half a century and enormous efforts have been devoted to the development of "optimal" Gaussian basis sets for quantum chemistry. The quality of basis sets is one possibility to control the trade-off between speed and accuracy. By the 1960s Hartree-Fock methods have been implemented in self-consistent computer programs using Gaussian basis functions and applied to simple molecules consisting of a few atoms. In essence, the computational procedure in such programs is as follows: one chooses a certain position of the atomic nuclei, then one selects a certain set of Gaussian basis functions, guesses an initial form of the one-electron wave functions by choosing the coefficients of the Gaussian basis functions representing each molecular orbital, and one solves the Hartree-Fock equations resulting in a new set of one-electron wave functions (i.e. coefficients for the basis functions). These are taken as new input and the procedure is repeated until the input and output wave functions are the same within a certain numerical tolerance, i.e. a self-consistent solution has been found. At that point, one can evaluate the total energy of the system originating from the kinetic energy of the electrons and the various electrostatic attractions and repulsions between electrons and nuclei while respecting the exchange holes around each electron. The self-consistent procedures can be repeated for different nuclear positions thus allowing a point-by-point mapping of the total energy of a molecule as a function of its internal geometry.

Hartree-Fock theory had been applied widely to small molecules. The prediction of energy differences is only possible if the equilibrium geometry of molecules can be determined efficiently. A point-by-point search of all possible nuclear positions is practical only for very simple molecules and more efficient geometry optimization techniques are called for to investigate larger molecules. This required the calculation of the forces acting on each atom, i.e. the gradient of the total energy with respect to the displacement of each nucleus. In the 1970s, analytic gradient methods were developed and successfully implemented in Hartree-Fock programs as described in the literature [187].

This computational capability, together with the availability of well-tested, docu-

mented, and user-friendly computer programs made *ab initio* molecular orbital theory a widely used tool for the organic chemist. The prediction of molecular geometries, the relative stabilities of various conformations and isomers, and the systematic estimation of thermochemical data from first principles had become possible. The calculation of vibrational frequencies as well as the search for minima and saddle points on the energy surface (e.g. transition states of chemical reactions) is greatly facilitated if the second derivatives of the total energy with respect to nuclear coordinates can be evaluated from analytical formulas. In Hartree-Fock methods, this capability became available in the 1980s (as reviewed by [187]). Electron correlation effects beyond the single-determinant approximation can be included in a systematic way by expanding the many-electron wave function in a series of Slater determinants representing different electronic configurations. Formally, such a "configuration interaction" (CI) expansion converges to the exact many-body solution, albeit at substantially increasing computational effort. Alternatively, many-body perturbation theory can be used to include the major correlation effects. In view of the six criteria stated above, the present status of Hartree-Fock based quantum chemical methods can by described as follows:

Capability: The major capability of Hartree-Fock methods is the prediction of the total energy as a function of atomic arrangements enabling geometry optimizations, searches of energetic transition states, and the calculation of vibrational spectra. Among the electronic, optical, and magnetic properties obtainable from Hartree-Fock (and post-Hartree-Fock) calculations, perhaps the most prominent are electronic charge distributions, infrared frequencies and intensities, polarizabilities, hyperpolarizabilities and NMR shifts. The one-electron energies of occupied levels can be used to interpret photoemission spectra, but only in a semi-quantitative way. The prediction of optical and UV spectra requires methods beyond a single determinate. While possible in principle, this capability is not practical with Hartree-Fock methods for most systems of industrial relevance.

Generality: Hartree-Fock based methods work best for stable organic molecules and small molecules or clusters of atoms from the main group of the periodic table. For certain

molecules such as F_2, ozone, and nitro-compounds a single determinant representation is inadequate and the Hartree-Fock SCF level leads to unsatisfactory results. Furthermore, the approach is not well suited for transition metals, rare earth metals, actinides, and their compounds [188]. In an admirable effort, the Hartree-Fock approach has also been implemented for periodic systems [189]. This approach is particularly suited for oxides and crystals of small organic molecules. The use of this approach for metallic systems is questionable.

Accuracy: For systems where the Hartree-Fock approach is applicable, bond lengths are typically predicted to within ± 0.03 Å and bond angles and dihedral angles to within a few degrees. Binding energies are typically underestimated by as much as 50%. Relative energies between isomers or different molecular conformations can be calculated to within about 5 kJ/mol provided that basis sets and other computational parameters are carefully controlled. Typically, vibrational frequencies calculated on the Hartree-Fock SCF level are too high by about 10% compared with the harmonic part of experimental data. Because of the completely analytical nature of the computational implementation, the numerical precision (but not the physical accuracy) of total energies, forces and vibrational frequencies can be close to machine precision (usually about 14 significant digits). In principle, the accuracy of the many-body wave function can be systematically improved through the successive inclusion of correlation terms.

System size: The practical limit for accurate geometry optimizations and determinations of relative energies with the above mentioned Hartree-Fock calculations is in the range of about 50 carbon-like atoms. Single SCF energies can be evaluated for molecules containing up to several hundred atoms. Inclusion of correlation reduces the accessible system size to perhaps $10-20$ atoms, depending on the level of theory. The most accurate correlated methods are restricted to molecules with just a few atoms.

Time scale: At present, Hartree-Fock calculations are too slow for performing dynamic simulations even for very small molecules and time scales in the picosecond range.

Computational requirements: Hartree-Fock calculations on molecules of the above

mentioned sizes can be carried out on present high-performance workstations in the range of $10 - 100$ hours and on vector supercomputers (MPP systems) approximately $10 - 100$ times faster. For molecules in the range of $10 - 50$ atoms the computational effort is dominated by the evaluation of four-center integrals of products of Gaussian functions. Formally, the computational effort increases with a fourth power in the number of basis functions. However, for larger and open molecular structures, many of these integrals vanish and can be eliminated in advance so that for large molecules the computational effort grows with the third power in the number of basis functions because of the matrix diagonalizations involved in the SCF scheme.

The inclusion of electron correlations in *ab initio* calculations dramatically increases the computational effort while the accuracy of the results is improved only gradually. In particular configurational interaction expansions, while leading to the possibility of formally exact solution, are impractical for all but very small systems consisting of a few atoms. Among practical correlation treatment based on Hartree-Fock theory, second-order Møller-Plesset perturbation theory (often referred to as MP2) is a reasonably efficient approach provided that a single Slater determinant is an appropriate description of the system. Coupled-cluster theory, (see [190]) can give quite accurate results even for "difficult" molecules like ozone. However, such calculations are very sensitive to the choice of basis sets and the computational effort scales approximately with a seventh power in the number of basis functions. Hence, the practical value of such an approach is limited. The Hartree-Fock picture is best suited for small organic molecules and compounds of main group elements which do not contain large number of electrons and where the electrons are fairly localized.

In other words, the Hartree-Fock picture seems to be adequate as long as the "individual character" of electrons is reasonably maintained. Hartree-Fock theory is less appropriate for systems with high electron density such as transition metals or systems with delocalized metallic like states. In fact, the theory breaks down qualitatively for the perfect metal, because it fails to account for collective Coulomb screening in a completely

delocalized electron system [191].

2.3 Density Functional Method

Density functional theory (DFT) is based on concepts by Thomas [192] and Fermi [193], who introduced the idea of expressing the total energy of a system as a functional of the electron density. In 1951 Slater [194] used ideas from the electron gas with the intention to simplify HF theory to a point where electronic structure calculations of solids became feasible. In the 1960s Hohenberg & Kohn [195] and Kohn & Sham [196] formulated a rather remarkable theorem that states that the total energy of a system such as a bulk solid or a surface depends only on the electron density of its ground state. Earlier, motivated by the search for practical electronic structure calculations, Slater [185] had developed an approach, later to become the Xα method, which was originally intended as an approximation to Hartree-Fock theory [182, 183]. Today, the Xα method is generally viewed as a simplified form or precursor of density functional theory [188].

The idea of using the electron density as the fundamental entity of a quantum mechanical theory of matter originated in the early days of quantum mechanics [197]. However, in subsequent decades, the Hartree-Fock approach developed and was applied to small molecular systems. From the Born-Oppenheimer [198] approximation, the motions of the electrons can be decoupled with those of the nuclei. Assuming fixed positions of the atomic nuclei, the Schrödinger's equation is solved only for the electrons. The nonrelativistic Hamiltonian can be written in atomic units as:

$$H = -\frac{1}{2}\sum_i \nabla_i^2 + \frac{1}{2}\sum_{i\neq j}\frac{1}{|r_i - r_j|} + \sum V_{ion}(r_i) + E_{ion}(\{R_I\}) \tag{2.9}$$

where i and j run over all the electrons in the system, R_I are the ionic positions, $V_{ion}(r)$ is the ionic potential, $E_{ion}(\{R_I\})$ is the ion-ion interaction energy. Many properties of practical interest, such as ground-state total energies, ionic forces, charge densities, and electrostatic potentials can be obtained by solving the ground-state wavefunction of the

Schrödinger's equation:

$$H\Psi(\{r_i\}) = E\Psi(\{r_i\}) \tag{2.10}$$

2.3.1 The Kohn-Sham Equation

Density functional theory starts with a consideration of the entire electron system. The total energy of a system is expressed as a function of the total electron density, which in turn depends on the position of the atoms.

$$E = E[\rho(r), R_\alpha] \tag{2.11}$$

where R_α denotes the position of atom α and

$$\rho(r) = \sum_i |\psi_i(r)|^2 \tag{2.12}$$

the charge density, which is the sum over all occupied molecular orbitals ψ_i.

Kohn and Sham showed that solving for the ground-state energy in Eq. 2.10 is formally equivalent to minimizing the functional $E_{KS}[\{\psi_i\}]$:

$$E_{KS}[\{\psi_i\}] = -\frac{1}{2}\sum_i n_i \int \psi_i \nabla^2 \psi_i dr + \int V_{ion}(r)\rho(r)dr$$

$$+\frac{1}{2}\int \frac{\rho(r)\rho(r')}{|r-r'|} dr dr' + E_{xc}[\rho(r)] + E_{ion}(\{R_I\}) \tag{2.13}$$

with respect to an orthonormal set of single-particle wavefunctions $\psi_i(r)$. In Eq. 2.13, E_{KS} is the Kohn-Sham functional, the index i runs over all single particle orbitals, n_i is the occupational number for state i, E_{xc} is the exchange-correlation functional..

Practical application of the formalism in the previous section usually rely on approximations related to the Thomas-Fermi approach; many of the drawbacks of this method

can be traced to the approximate treatment of the kinetic energy. The task of finding good approximations to the energy functional is greatly simplified by using a different separation introduced by Kohn and Sham:

T_0 is the kinetic energy that a system with density ρ would have if there were no electron-electron interactions, V is the classical Coulomb potential for electrons, and E_{xc} may be viewed as a definition of the exchange correlation energy. Although T_0 is different from the true kinetic energy T, it is of comparable magnitude and is treated exactly in this approach. The exact treatment of T_0 removes many deficiencies of the Thomas-Fermi approximations, such as the lack of shell structure of atoms or the absence of chemical bonding in molecules and solids.

The variational principle applied to Eq. 2.13 yields

$$\frac{\delta E[\rho]}{\delta \rho(r)} = \frac{\delta T_0}{\delta \rho(r)} + V_{ext}(r) + V(r) + \frac{\delta E_{xc}[\rho]}{\delta \rho(r)} = \mu \tag{2.14}$$

where μ is the Lagrange multiplier associated with the requirement of constant particle number. If we compare this with the corresponding equation for a system with a effective potential $V_{eff}(r)$ but without electron-electron interactions:

$$\frac{\delta E[\rho]}{\delta \rho(r)} = \frac{\delta T_0}{\delta \rho(r)} + V_{eff}(r) = \mu \tag{2.15}$$

we see that the mathematical problems are identical, provided that:

$$V_{eff}(r) = V_{ext}(r) + V(r) + \frac{\delta E_{xc}[\rho]}{\delta \rho(r)} \tag{2.16}$$

The solution of Eq. 2.16 can be found simply by solving the Schrödinger's equation for non-interacting particles:

$$\left[-\frac{1}{2}\nabla^2 + V_{eff}(r)\right] \psi_i(r) = \varepsilon_i \psi_i(r) \tag{2.17}$$

yielding

$$\rho(r) = \sum_i n_i \psi_i^*(r)\psi_i(r) = \sum_i n_i \left|\psi_i(r)\right|^2 \tag{2.18}$$

It is necessary to satisfy the condition Eq. 2.16, and this can be achieved in a self-consistent procedure. The solution of this system of equations leads then to the energy and density of the lowest state and to all quantities derivable from them.

The wavefunction that minimize the Kohn-Sham functional of Eq. 2.11 obey an eigenvalue equation of the form:

$$H_{KS}\psi_i = \varepsilon_i \psi_i \tag{2.19}$$

where H_{KS} is the Kohn-Sham Hamiltonian:

$$H_{KS} = -\frac{\hbar^2}{2m}\nabla^2 + V_{ion}(r) + V_H(r) + \mu_{xc}(r) \tag{2.20}$$

$V_H(r)$ is the Hartree potential:

$$V_H(r) = \int \frac{\rho(r')}{|r - r'|} dr' \tag{2.21}$$

and μ_{xc} is the exchange-correlation potential:

$$\mu_{xc}(r) = \frac{\delta E_{xc}[\rho]}{\delta \rho(r)} \tag{2.22}$$

ε_i and ψ_i are referred to as the Kohn-Sham eigenvalues and Kohn-Sham wavefunction, respectively.

For the purpose of practical calculation, the Kohn-Sham functional must be supplemented by an approximation for the exchange and correlation. As an approximation, the exchange-correlation energy is taken from known results of an interacting electron system of constant density ("homogeneous electron gas") and its is assumed that the exchange and correlation effects are not strongly dependent on inhomogeneities of the

electron density away from a reference point, r.

$$E_{xc}^{h}[\rho(r)] = \int \rho(r) \cdot \varepsilon_{xc}^{h}[\rho(r)]dr \tag{2.23}$$

where $\varepsilon_{xc}^{h}(\rho)$ is the exchange correlation energy of a homogeneous electron gas having density ρ. In this local density approximation (LDA) it is assumed that the electrons are "near sighted", i.e. the detailed inhomogeneous structure of the electron density near a reference point is not important. This quantity has been calculated in several ways by different groups. The calculations gives similar but not identical results.

2.3.2 Solution of the Kohn-Sham Equations

Consider the Kohn-Sham equations:

$$\left[-\frac{\hbar^2}{2m}\nabla^2 + V_{ion}(r) + V_H(r) + \mu_{xc}(r)\right]\psi_i(r) = \varepsilon_i\psi_i(r) \tag{2.24}$$

, following standard mathematical techniques for solving eigenvalue problems, one can expand the unknown solutions $\psi_i(r)$ in a set of known functions, $\psi_j(r)$, with unknown linear coefficients, c_{ij}:

$$\psi_i(r) = \sum_j c_{ij}\psi_j(r) \tag{2.25}$$

These coefficients are determined through a variational procedure which leads to the solution of the following matrix problem:

$$(\mathbf{H} - \varepsilon\mathbf{S})\mathbf{c} = 0 \tag{2.26}$$

H and **S** are the so-called Hamiltonian and overlap matrices with the following matrix elements:

$$H_{ij} = \int \psi_i^*(r)\left[-\frac{\hbar^2}{2m}\nabla^2 + V_C(r) + \mu_{xc}(r)\right]\psi_j(r)dr \tag{2.27}$$

$$S_{ij} = \int \psi_i^*(r)\psi_j(r)dr \tag{2.28}$$

ε represent an eigenvalue and c are the coefficients of a solution denoted as a column vector. In standard density functional calculations one diagonalizes the matrix $(\mathbf{H} - \varepsilon\mathbf{S})$ to find the eigenvalues and coefficients (eigenvectors). The dimension of the matrices is determined by the number of basis functions in the expansion Eq. 2.25. A direct diagonalization can be avoided if one uses a Car-Parrinello [199] or a conjugant gradient scheme (see Appendix F) as it is done for pseudopotential planewave methods.

Both the Coulomb potential and the exchange-correlation potential in the Kohn-Sham equations depend on the charge density, which is constructed from the one-particle wave functions. In other words, in order to set up the Kohn-Sham equations one needs to know their solutions. This problem is solved by an iterative, self-consistent procedure as shown in Figure 2-1.

The solution of these equations give access to the total energy as a functional of nuclear position as well as all properties that can be derived from this theory.

2.3.3 Implementation of the Kohn-Sham Equations

At present, there is not a single density functional implementations that would be equally applicable and efficient for all systems including molecular solids and magnetic transition metal heterostructures [188]. Therefore a number of different approaches have emerged as shown in Figure 2-2. The center of this figure shows the Kohn-Sham equations, which are the effective one-electron Schrödinger equations of density functional theory. The solutions of these equations give access to the total energy as a functional of nuclear position as well as all properties that can be derived from this theory. The three terms in the square bracket represent the kinetic energy of electrons, the Coulomb potential due to the all charges in the system, and the exchange-correlation potential. The definition of the system and the level of the theoretical approach are given by these three terms. The one-particle wave functions are labeled according to the number of electron level, i. In a

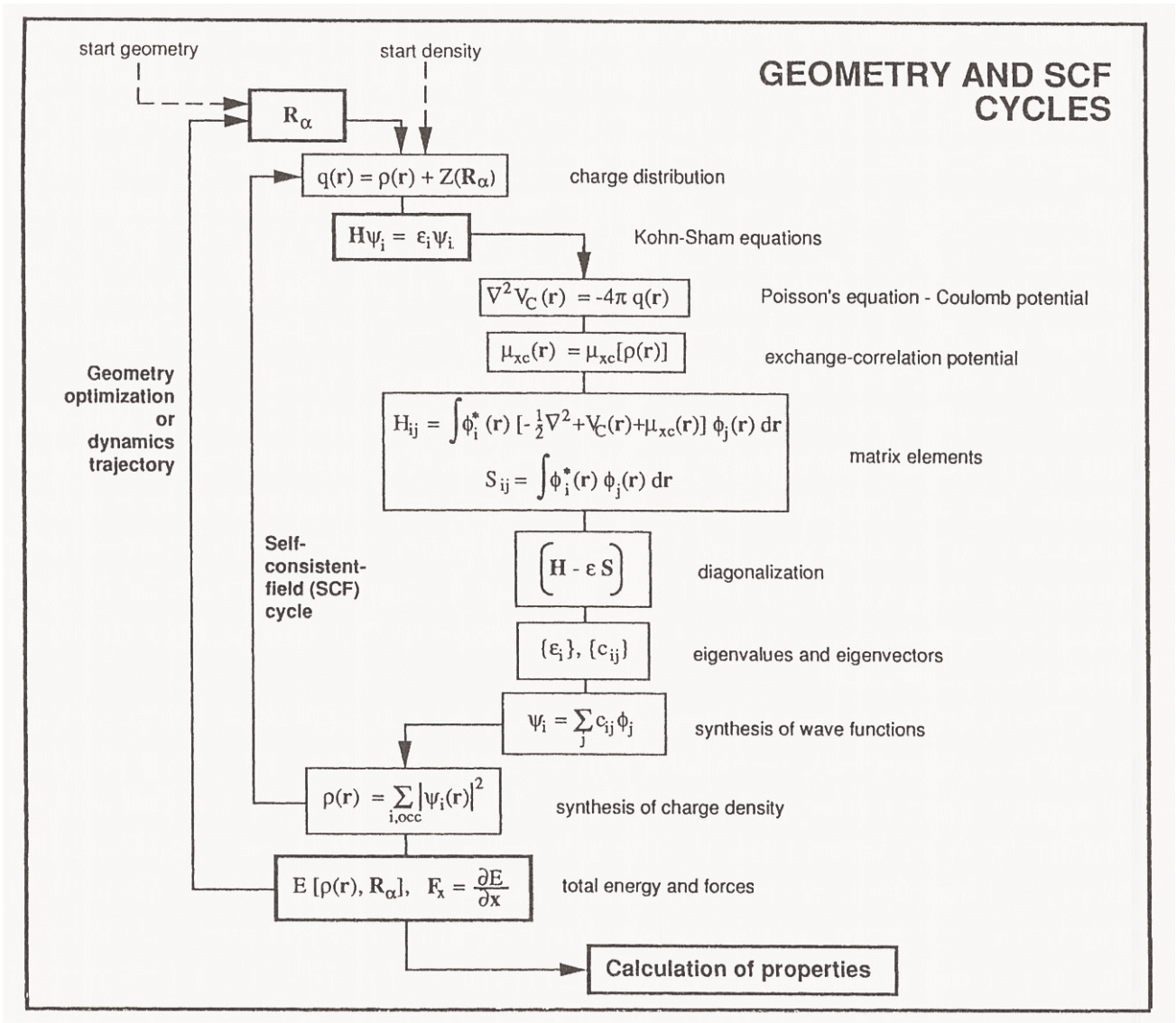

Figure 2-1: Scheme of typical electronic structure calculations. The outer circle represents the geometry optimization or other manipulation of the geometry such as energy minimization, simulated annealing, dynamics trajectories or Monte Carlo procedures. The inner circle is the self-consistency procedure to solve the Kohn-Sham equations. Diagram obtained from E. Wimmer[188]

periodic system, the wave functions are characterized by an additional quantum number, k, which corresponds to the momentum of the electron in the crystal. The one-electron eigenvalues carry the same labels. DFT calculations for systems with lighter elements (up to about Z = 54) are usually done non-relativistically. The systems investigated in our study are the $M\mathrm{Mo_6S_8}$, TX_2 and Li and Mg intercalated $\mathrm{Mo_6S_8}$ and $\mathrm{TiS_2}$ systems.

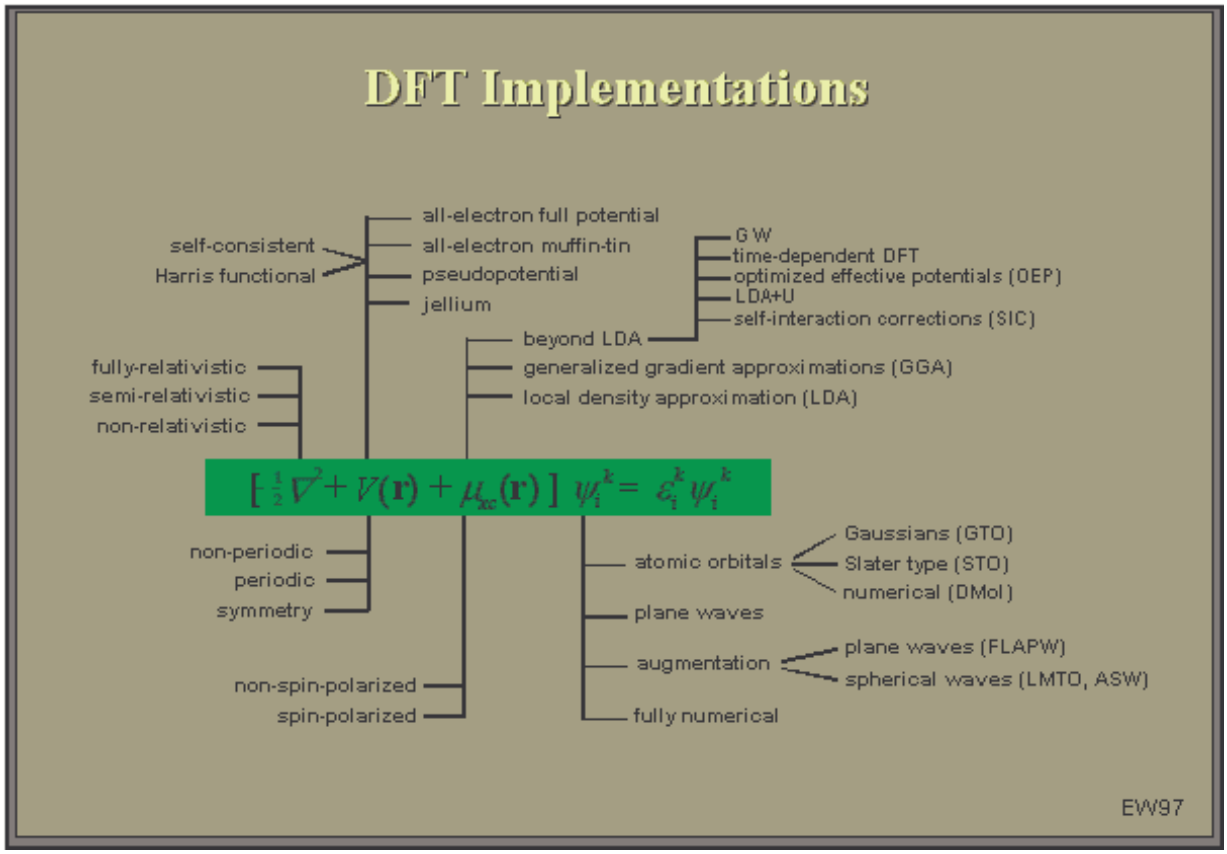

Figure 2-2: Overview of electronic structure methods for solving the Hartree-Fock and Kohn-Sham equations. Diagram obtained from E. Wimmer [201].

It is possible to include relativistic effects through a scalar-relativistic or a fully relativistic description. Scalar-relativistic treatment means that the important kinematic effects due to the high kinetic energy of electrons near heavy nuclei are taken into account, but that one averages over the spin-orbit splitting of the electronic levels [200]. The chemical and structural definition of a system is contained in the Coulomb poten-

tial term $V(r)$. DFT calculations are possible for non-periodic systems such as clusters and molecules and for systems with one-, two-, and three-dimensional periodicity. The use of point or space group symmetry can lead to significant reduction in computational cost as well as to a clearer interpretation of the resulting wave functions that reflect this symmetry.

In all-electron full-potential calculations, the Coulomb singularities arising from the nuclear charges and the full three-dimensional structure of the potential are being taken into account without any approximations. In densely packed systems such as metals and alloys, the effective potential is quite well represented by a muffin-tin shaped potential. Around each atom the potential is assumed to be completely spherical up to a certain radius, which is typically about 1 Å. Between these atomic spheres the potential is assumed to be constant. In this approximation, the Coulomb singularities at the atomic positions as well as the steep variation of the potential near the nuclei is still present. Another shape approximation to the potential has become widely used in the form of pseudopotentials [202, 203, 204, 205]. The objective of pseudopotentials is the elimination of the Coulomb singularities at the nuclear positions and the smoothening of the potential near these singularities. However, no other shape approximations such as constant potentials between the atoms are made in pseudopotential calculations.

2.3.4 The Exchange-Correlation Energy

The wave function of a many-electron system must be antisymmetric under exchange of any two electrons because the electrons are fermions. The antisymmetric of the wave function produces a spatial separation between electrons that have the same spin and thus reduces the Coulomb energy of the electronic system. The reduction in the energy of the electronic system due to the antisymmetry of the wave function is called the **exchange energy**. Inclusion of the exchange in a total-energy calculation is generally referred to as the Hartree-Fock approximation. The Coulomb energy of the electronic system can be reduced below its Hartree-Fock value if electrons that have opposite spins are also

spatially separated. In this case the Coulomb energy of the electronic system is reduced at the cost of increasing the kinetic energy of the electrons. The difference between the many-body energy of an electronic system and the energy of the system calculated in the Hartree-Fock approximation is called the **correlation energy**.

The **exchange-correlation** term captures the many-body interactions between electrons. Hartree-Fock theory and density functional theory provide the two major current approaches to describe these complex interactions. For magnetic systems or molecules with open shells one has to use a spin-polarized form of the exchange-correlation potential, as given, for example, by von Barth and Hedin [206]. The local density approximation tends to overestimate binding energies. Generalized gradient corrections (sometimes also called non-local corrections) are intended to remedy this situation. In fact, molecular dissociation energies and the geometry of weakly bound systems involving, for example hydrogen bonds or carbonyl bonds, seem to be significantly improved by using gradient corrected potentials as suggest, for example, by Perdew [207] and Becke [208].

Local-Density Approximation (LDA)

The Hartree-Fock (HF) exchange energy of an inhomogeneous many-electron system can be reasonably approximated by the so-called local-density approximation (LDA) which, in atomic units, is given by:

$$E_X^{\mathbf{LDA}} = -C_X \sum_\sigma \int \rho_\sigma^{4/3} d^3r \tag{2.29}$$

$$C_X = \frac{3}{2}\left(\frac{3}{4\pi}\right)^{1/3} \tag{2.30}$$

where σ denotes either "up" or "down" electron spin, and where the intergrand is essentially the volume exchange-energy density of a uniform spin-polarised electron gas of spin density ρ_σ. In this approximation an assumption is made that the exchange-correlation energy depends only on the local electron density around each volume element

dr.

$$E_{xc}^{LDA}[\rho(r)] = \int \rho(r)\varepsilon_{xc}[\rho(r)]dr \tag{2.31}$$

In any atomic arrangement such as a crystal, a surface, or a molecule, there is a certain electron density $\rho(r)$ at each r in space. The LDA rests on two basic assumptions: (i) the exchange and correlation effects come predominantly from the immediate vicinity of a point r and (ii) these exchange and correlation effects do not depend strongly on the variation of the electron density in the vicinity of r. If conditions (i) and (ii) are reasonably well fulfilled, then the contribution from volume dr would be the same as if this volume elements were surrounded by a constant electron density of the same value as within dr. This is an excellent approximation for metallic systems, but represents quite a severe simplification in systems with strongly varying electron density.

The LDA tends to overemphasize the metallic character and one needs to be careful in the interpretation of the density functional one-electron energies. Furthermore, weaker bonds such as hydrogen bonds are significantly overestimated in the LDA. The primary results of density functional calculations are the electron density, the spin density, the total energy, and the one-particle energies and wave functions. From these quantities, one can derive important electronic, optic and magnetic properties including dipole (and higher) moments, polarizabilities and hyper-polarizabilities, and magnetic moments. LDA calculations for systems in their electronic ground state can be used to estimate electronic excitation energies including work functions, optical and ultraviolet (UV) spectra, and core level spectra for solids, surfaces, and molecules. Quite consistently, for a great number of strong bonds in solids, molecules, and surfaces, interatomic equilibrium distances are predicted by precise density functional calculations to within about 0.02 Å of experiment; bond angles and dihedral angles are found within a few degrees of their experimental values. Within the local density approximation, binding

energies are typically overestimated, sometimes by as much as a factor of two. Gradient-corrected density functionals as suggested by Perdew in 1986 [207] and Becke in 1988 [208] seem to offer a remedy.

Generalized Gradient Approximation (GGA)

Development within the density-functional theory has been ongoing within both the LDA and the GGA and both models, especially LDA, have been accepted for calculating electronic and structural properties. Our work contributes on validation of both models as presented. The LDA typically underestimates the exchange energies of atomic and molecular systems by roughly 10%, and correlations for the obvious non-uniformity of atomic and molecular densities have a long history [208]. The major obstacle toward an accurate self-consistent-field (SCF) theory for atoms, molecules, and solids is the electron correlation problem, since everything may be treated more or less exactly. Ground-state density-functional approximations, starting from the limit of the electron gas of slowly varying density, have traditionally made serious errors in the correlation energy for realistically inhomogeneous systems. The basic idea in these schemes is the inclusion of terms in the exchange-correlation expressions that depend on the gradient of the electron density and not only its value at each point in space. Therefore, these corrections are also sometimes referred to as "non-local" potentials. The form suggested by Becke [208] for the exchange part is :

$$E_x = b \sum_{\sigma} \int \frac{\rho_\sigma x_\sigma^2}{1 + 6bx_\sigma \sinh^{-1} x_\sigma} dr \tag{2.32}$$

$$x_\sigma = \frac{|\nabla \rho|}{\rho_\sigma^{4/3}} \quad \sigma = \uparrow or \downarrow \tag{2.33}$$

The energies are given in Hartree atomic units; the units for the electron and spin densities are number of electrons/(Bohr radius)^3. The constant b in is a parameter fitted to the exchange energy of inert gas. The following correlation functional as proposed by

Perdew and Wang [207] predicts correlation energies of useful accuracy for the electron gas of slowly varying density, atoms, and ions:

$$E_c[\rho_\uparrow, \rho_\downarrow] = \int \rho\epsilon_c(\rho_\uparrow, \rho_\downarrow)d^3r + \int \frac{C(\rho)\left|\nabla\rho\right|^2}{\rho^{4/3}de^{\Phi}}d^3r \tag{2.34}$$

$$V = 1.745f\left[\frac{C(\infty)}{C(\rho)}\right]\frac{|\nabla\rho|}{\rho^{7/6}} \tag{2.35}$$

The correlation energy per particle of the uniform electron gas, $\epsilon_c(\rho_\uparrow, \rho_\downarrow)$, is taken from a parametrization by Perdew and Zunger [209] of the Ceperly-Adler [210] results. Inclusion of non-local gradient corrections improve the values of binding energies and bring them to within about 10 kJ/mol of experiment. The results obtained at this level of theory are comparable with sophisticated correlated quantum mechanical methods such as coupled cluster theory. Within GGA, the exchange-correlation energy for spin-unpolarised systems is written as

$$E_{xc}^{GGA}[\rho] = \int d^3r f(\rho(r), \nabla\rho(r)) \tag{2.36}$$

where the function f is not unique and many different forms have been suggested. When constructing a GGA one usually. When constructing a GGA one usually tries to incorporate a number of known properties of the exact functional into the restricted functional form of the approximation. The impact of GGAs has been quite dramatic, especially in quantum chemistry where DFT is now competitive in accuracy with more traditional methods while being computationally less expensive.

meta-GGA and Hybrid functional

Most recently, so called meta-GGA functionals were proposed, where besides the local density and its gradient also the laplacian (or the kinetic energy density) enters the equation. In recent years, still following the lines of GGA development, a new class of "meta-GGA" functionals has been suggested. In addition to the density and its first

gradient, meta-GGA functionals depend on the kinetic energy density of the Kohn-Sham orbitals,

$$\tau(r) = \frac{1}{2}\sum_i |\psi_i(r)|^2 \tag{2.37}$$

The meta-GGA functional then takes the form

$$E_{xc}^{MGGA}[\rho] = \int d^3r g(\rho(r), \nabla\rho(r), \tau(r)) \tag{2.38}$$

The additional flexibility in the functional form gained by the introduction of the new variable can be used to incorporate more of the exact properties into the approximation. In this way it has been possible to improve upon the accuracy of GGA for some physical properties without worsening the results for others. Unlike LDA or GGA, which are explicit functionals of the density, meta-GGAs also depend explicitly on the Kohn-Sham orbitals. It is important to note, however, that we are still in the domain of DFT since, through the Kohn-Sham equation (Eq. 2.17), the orbitals are functionals of the Kohn-Sham potential and therefore, by virtue of the Hohenberg-Kohn theorem, also functionals of the density.

The so-called hybrid functionals mixes a fraction of exact exchange with GGA exchange,

$$E_x^{HYB}[\rho] = aE_x^{EXX}[\rho] + (1-a)E_x^{GGA}[\rho], \tag{2.39}$$

where a is the (empirical) mixing parameter and E_x^{EXX} is the exact exchange energy function

$$E_x^{EXX}[\rho] = -\frac{1}{2}\sum_\sigma \int d^3r \int d^3r' \sum_{i,j} \frac{\psi_{i\sigma}(r)\psi_{i\sigma}^*(r)\psi_{j\sigma}(r)\psi_{j\sigma}^*(r)}{|r-r'|} \tag{2.40}$$

This exchange functional is then combined with some GGA for correlation. Hybrid functionals are tremendously popular and successful in quantum chemistry but much less

so in solid-state physics. This last fact highlights a problem pertinent to the construction of improved functionals: available approximations are already very accurate and hard to improve upon.

2.3.5 Periodic Boundary Conditions and Bloch's theorem

The supercell approximation allows one to deal with a periodic configurations of atoms within the framework of Bloch's theorem [211]. One simply constructs a large unit cell containing the configuration in question and repeats it periodically throughout space. By studying the properties of the system for larger and larger unit cells, one gauge the importance of the induced periodicity and systematically filter it out. This approach has been successfully tested against "exact" Koster-Slater Green's-function [212] methods, which are only tractable for very-high-symmetry configurations [213]. Calculation of wave functions for an infinite number of electrons must be expressed in terms of an infinite basis because of the infinite extent of the system. These problems are overcome by performing calculations on periodic systems (which may involve introducing some fictitious long-range periodicity into aperiodic systems, as is demonstrated for the case of a single impurity atom in a crystal in Figure 2-3 and applying Bloch's theorem.

Bloch's theorem states that in a periodic solid each electronic wave function can be written as the product of a cell-periodic part and a wavelike part [211],

$$\psi_i(r) = \exp[ik \cdot r] f_i(r) \tag{2.41}$$

The cell-periodic part of the wave function can be expanded using a basis set consisting of a discrete set of plane waves whose wave vectors are reciprocal lattice vectors of the crystal,

$$f_i(r) = \sum_G c_{i,G} \exp[iG \cdot r], \tag{2.42}$$

where the reciprocal lattice vectors G are defined by $G \cdot l = 2\pi m$ for all l where l is a

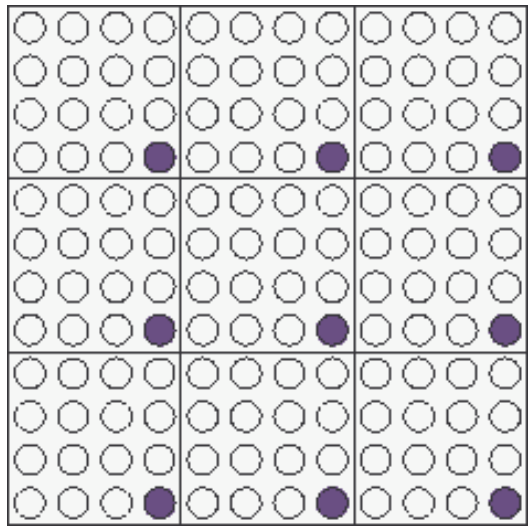

Figure 2-3: The introduction of a supercell to allow periodic boundary conditions to be applied to an aperiodic system.

lattice vector of the crystal and m is an integer. Therefore each electronic wave function can be written as a sum of plane waves,

$$\psi_i(r) = \sum_G c_{i,i+G} \exp[i(k+G) \cdot r] \tag{2.43}$$

Many calculations in crystals involve integrating periodic functions of a Bloch wave vector over either the entire Brillouin zone (BZ) or over specified portion. To optimize the calculations it is helpful only to compute these functions at a careful selected set of points in the BZ.

2.3.6 k-point Sampling and Plane-wave Basis Sets

Electronic states are allowed only at a set of k-points determined by the boundary conditions that apply to the bulk solid. The density of allowed k-points is proportional to the volume of the solid. The infinite number of electrons in the solid are accounted for by an infinite number of k-points, and only a finite number of electronic states are occu-

pied at each k-point. The Bloch theorem changes the problem of calculating an infinite number of electronic wave functions to one of calculating a finite number of electronic wave functions at an infinite number of k-points. The occupied states at each k-point contribute to the electronic potential in the bulk solid so that, in principle, an infinite number of calculations are needed to compute this potential. However, the electronic wave functions at k-points that are very close together will be almost identical. Hence it is possible to represent the electronic wave functions over a region of K space by the wave functions at a single k-point. In this case the electronic states at only a finite number of k-points are required to calculate the electronic potential and hence determine the total energy of the solid.

Methods have been devised for obtaining very accurate approximations to the electronic potential and the contribution to the total energy from a filled electronic band by calculating the electronic states at special sets of k-points in the Brillouin zone [214, 215, 216, 217]. Using these methods, one can obtain an accurate approximation for the electronic potential and the total energy of an insulator or a semi-conductor by calculating the electronic states at a very small number of k-points. The electronic potential and total energy are more difficult to calculate if the system is metallic because a dense set of k-points is required to define the Fermi surface precisely.

The magnitude of any error in the total energy due to inadequacy of the k-point sampling can always be reduced by using a denser set of k-points. The computed total energy will converge as the density of k-points increases, and the error due the k-point sampling then approaches zero. In principle, a converged electronic potential and total energy can always be obtained provided that the computational time is available to calculate the electronic wave functions at a sufficiently dense set of k-points. The computational costs of performing a very dense sampling of k-space can be significantly reduced by using the $k \cdot p$ total-energy method [218, 219]. In this technique solutions on the dense set of k-points are generated from the solutions on a much coarser grid of k-points using $k \cdot p$ perturbation theory.

Bloch's theorem states that the electronic wave functions at each k-point can be expanded in terms of a discrete planewave basis set. In principle, an infinite planewave basis set is required to expand the electronic wave functions. However, the coefficients $c_{i,k+G}$ for the plane waves with small kinetic energy $(\hbar^2/2m)|k+G|^2$ are typically more important than those with large kinetic energy. Thus the planewave basis set can be truncated to include only plane waves that have kinetic energies less than some particular cut off energy. If a continuum of planewave basis states were required to expand each electronic wave function, the basis set would be infinitely large no matter how small the cutoff energy. Application of the Bloch theorem allows the electronic wave functions to be expanded in terms of a discrete set of plane waves. Introduction of an energy cutoff to the discrete planewave basis set produces a finite basis set.

The truncation of the planewave basis set at a finite cutoff energy will lead to an error in the computed total energy. However, it is possible to reduce the magnitude of the error by increasing the value of the cutoff energy. In principle, the cutoff energy should be increased until the calculated total energy has converged, but it will be shown later that it is possible to perform calculations at lower cutoff energies.

One of the difficulties associated with the use of planewave basis sets is that the number of basis states changes discontinuously with cutoff energy. In general these discontinuances will occur at different cutoffs for different k-points in the k-point set. (In addition, at a fixed-energy cutoff, a change in the size or shape of the unit cell will cause discontinuation in the planewave basis set). This problem can be reduced by using denser k-point sets, so that the weight attached to any particular planewave basis state is reduced. However, the problem is still present even with quite dense k-point samplings. It can be handled by applying a correction factor which accounts approximately for the difference between the number of states in a basis set with infinitely large number of k-points and the number of basis states actually used in the calculation [220].

When planewaves are used as a basis set for the electronic wave functions, the Kohn-Sham equations assume a particularly simple form. Substitution of Eq. 2.43 into 2.24

and integration over r gives the secular equation

$$\sum_{G'} \left[\frac{\hbar}{2m} |k+G|^2 \delta_{GG'} + V_{ion}(G-G') + V_H(G-G') + V_{XC}(G-G') \right] c_{i,k+G'} = \varepsilon_i c_{i,k+G}. \tag{2.44}$$

In this form, the kinetic energy is diagonal and the various potentials are described in terms of their Fourier transforms. Solution of Eq. 2.44 proceeds by diagonalization of a Hamiltonian matrix whose elements $H_{k+G,k+G'}$ are given by the terms in the brackets above. The size of the matrix is determined by the choice of cutoff energy $(h^2/2m)|k+G_c|^2$, and will be intractably large for systems that contain both valence and core electrons. This is a severe problem, but it can be overcome by use of the pseudopotential approximation.

2.3.7 The Pseudopotential Approximation

Pseudopotential theory approximation [203, 205, 221] allows one to replace the strong electron-ion potential with a much weaker potential — a pseudopotential — that describes all the salient features of a valence electron moving through the solid, including relativistic effects. Thus the original solid is now replaced by pseudo valence electrons and pseudo-ion cores. These pseudoelectrons experience exactly the same potential outside the core region as the original electrons but have a much weaker potential inside the core region. The fact that the potential is weaker is crucial, however, because it makes the solution of the Schrödinger's equation much simpler by allowing expansion of the wave functions in a relatively small set of plane waves. Use of plane waves as basis functions makes the accurate and systematic study of complex, low-symmetry configurations of atoms much more tractable. An ionic potential, valence wave function and the corresponding pseudopotential and pseudo wavefunction are illustrated schematically in Figure 2-4. The most general form for a nonlocal pseudopotential V^{NL} is

$$V^{NL} = \sum_{lm} |lm\rangle V_l \langle lm| \tag{2.45}$$

where $|\ lm\rangle$ are spherical harmonics and V_l is the pseudopotential for angular momentum l. A pseudopotential that uses the same potential for all the angular momentum components of the wave function is called a local pseudopotential. The generation procedure for an ionic pseudopotential or is described in Appendix C.

Norm-Conserving (NC) Pseudopotentials

The main requirement of the pseudopotential approach is that it reproduces the valence charge density associated with chemical bonds. It has been shown [222] that for pseudo and all-electron wavefunctions to be identical beyond the core radius, r_c, it is necessary for the integrals of squared amplitudes of the two functions be the same. This is equivalent to requiring norm-conservation from pseudo wavefunctions, i.e. that each of them should carry exactly one electron. This condition ensures that the scattering properties of the pseudopotential are reproduced correctly.

The typical method for generating pseudopotentials is as follows. All-electron calculations are carried out for an isolated atom in a chosen electronic configuration (not necessarily in the ground state). This provides valence electron eigenvalues and valence electron wavefunctions for the atom (shown as Ψ_r in Fig. 2-4). A parameterized form for the ionic pseudopotential (or the pseudo wavefunction) is chosen. The parameters are then adjusted, so that a pseudoatom calculation with the same exchange-correlation potential as in the all-electron atom gives pseudo wavefunctions, Ψ_{pseudo}, that match the valence wavefunctions outside some cutoff radius, r_c , and pseudo eigenvalues that are equal to the valence eigenvalues. This procedure involves direct inversion of the radial Kohn-Sham equation in the case when the pseudo wavefunction and not the pseudopotential itself are parameterized. If each wavefunction, pseudo and all-electron, is normalized to one, then the norm-conservation constraint is automatically satisfied as a result of

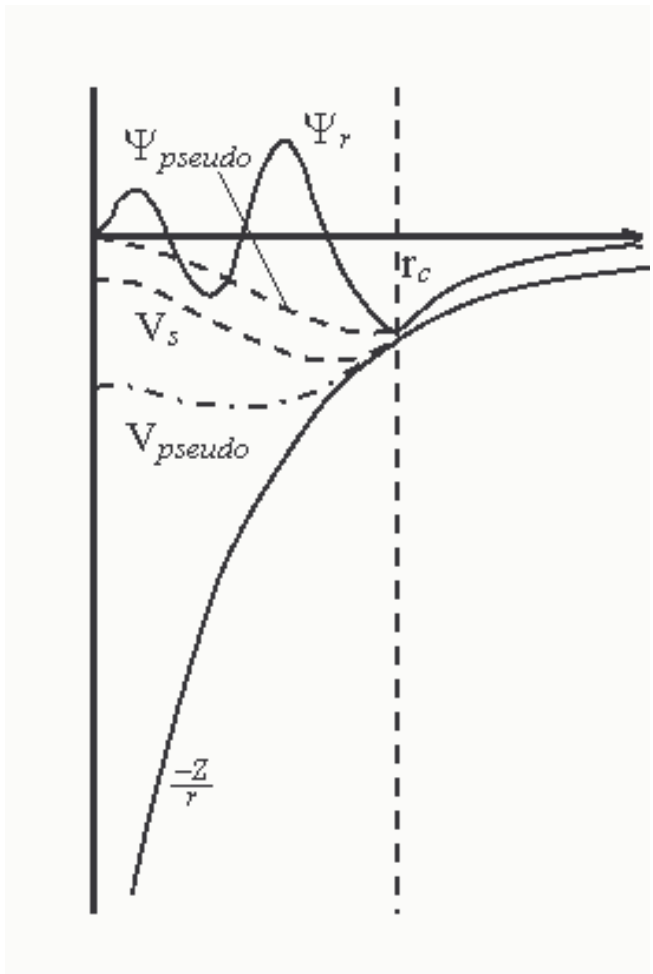

Figure 2-4: Schematic representation of the all-electron (solid lines) and pseodoelectron (dashed lines) potentials and their corresponding wave functions. The radius at which all-electron and pseudoelectron values match is designated r_c

matching the wavefunctions outside r_c.

The core electrons and the Coulomb singularity from the atomic nuclei are replaced by a smooth pseudopotential around each atom. At a certain cut-off radius away from each atomic position, the pseudopotentials becomes the actual effective potential. There are three major reasons for using pseudopotentials: (i) simple basis functions such as plane waves work well with pseudopotentials, (ii) there are fewer electrons thus simplifying the calculation, and (iii) relativistic effects which are mainly due to core electrons can be included in the pseudopotential. Together, these features lead to efficient and relatively simple computational implementations. The physically reasoning behind the pseudopotential approximation is as follows: since the core-electron wave function of an atom remain essentially unchanged when placed into different chemical environments and since that the core wave functions' only major contribution to chemical bonding is to enforce the valence wave functions orthogonality to core states, the true atomic potential can justifiably be replaced by a pseudopotential that effectively reproduces the effects of the core electrons. The objective is to determine what auxiliary conditions are needed to produce a pseudopotential that both adequately reproduces the all-electron behavior outside the core region when placed in different chemical environments, and is still computational efficient.

The majority of the pseudopotentials currently used in electronic-structure are generated from all-electron atomic calculations. Within the density-functional theory, this is done by assuming a spherical screening approximation and self-consistently solving the radial Kohn-Sham equation

$$\left[\frac{-1}{2}\frac{d^2}{dr^2} + \frac{l(l+1)}{2r^2} + V[\rho;r]\right] r\psi_{nl}(r) = \varepsilon_{nl} r\psi_{nl}(r) \tag{2.46}$$

where $V[\rho;r]$ is the self-consistent one electron potential

$$V[\rho;r] = \frac{-Z}{r} + V_H[\rho;r] + V_{xc}^{LDA}(\rho(r)) \tag{2.47}$$

$\rho(r)$ is the sum of the electron densities for the occupied wave functions $\psi_{nl}(r)$, $V_H[\rho; r]$ is the Hartree potential and $V_{xc}^{LDA}(\rho(r))$ is the local-density approximation for the exchange-correlation potential. Most pseudopotentials are then constructed such that they satisfy four general conditions. The first is that the valence (the principal quantum number n is further omitted for simplicity) pseudo-wave-functions generated from the pseudopotential should contain no nodes. Second, the normalized atomic radial pseudo-wave-function (PP) with angular momentum l is equal to the normalized radial all-electron wave function (AE) beyond a chosen cut-off radius r_c,

$$\psi_l^{PP}(r) = \psi_l^{AE}(r) \text{ for } r > r_c \tag{2.48}$$

or converges rapidly to that value. Third, the charge enclosed within r_{cl} for the two wave functions must be equal,

$$\int_0^R \left|\psi_l^{PP}(r)\right|^2 r^2 dr = \int_0^R \left|\psi_l^{AE}(r)\right|^2 r^2 dr \tag{2.49}$$

Last, almost redundantly, the valence all-electron and pseudopotential eigenvalues must be equal,

$$\varepsilon_l^{PP} = \varepsilon_l^{AE} \tag{2.50}$$

If a pseudopotential meets the condition outlined above, it is commonly referred to as a 'norm-conserving pseudopotential'.

The general rules for constructing a pseudopotential and their consequences for the description of the logarithmic derivatives results in the constraint that the pseudoization radius r_c should never exceed a maximum value $r_{c,max}$ of the order half nearest-neighbour distance d_{NN}, i.e.,

$$r_{c,max} \approx 0.5 d_{NN} \tag{2.51}$$

This is a compulsory criterion that holds for any kind of pseudopotential. However, a highly transferable pseudopotential is subject to a further restriction: any charge transfer process (e.g, promotion, polarization, ionization, change of the spin state) must be described correctly. The norm conserving (or more generally charge conservation) properties of a pseudopotential in conjuction with the rule Eq. 2.51 guarantees a correct description of the logarithmic derivatives of the wave functions for the fixed reference Hamiltonian. The ionic pseudopotentials are constructed with r_c ranging from one to two times the value of the physical core radius. The smaller the value of R_c, the harder and more transferable the potential. The conflicting effect of r_c creates an obvious trade-off between accuracy and efficiency.

Ultrasoft Pseudopotentials

The idea of ultrasoft pseudopotentials (USP) as put forward by Vanderbilt [223] is that the relaxation of the norm-conserving condition can be used to generate much softer potentials. One first constructs a non-norm-conserving ultrasoft (US) pseudowave function ψ_i^{US} for each angular momentum quantum number l and energy channel ε (the index i shall represent a compound index determining the channel $l\varepsilon$). The fully separable nonlocal pseudopotential V^{NL} is then given by:

$$V^{NL} = \sum_{i,j} D_{ij} \left|\beta_j\right\rangle\left\langle\beta_i\right| \tag{2.52}$$

where $\mid \beta_j\rangle$ the are localised projectors which are dual to $\mid \psi_i^{US}\rangle$,

$$\left\langle \beta_j \mid \psi_i^{US} \right\rangle = \delta_{ij} \tag{2.53}$$

The coefficients D_{ij} give the strength of each contribution. The localised projectors must form a complete basis within the pseudoization spheres.

Important ingredients of the US pseudopotentials are the augmentation charges restoring the correct norm of the pseudocharge. These augmentation charges are defined as

the difference between the charge density derived from norm-conserving wave functions ψ_i^{NC} and that derived from the ultrasoft wave functions ψ_i^{US},

$$Q_{ij}(r) = \psi_i^{NC}(r)\psi_j^{NC}(r)^* - \psi_i^{US}(r)\psi_j^{US}(r)^* \tag{2.54}$$

In contrast to ordinary norm-conserving wave functions ψ_i^{NC} the wave function introduced above may possess nodes. However, nodeless wave functions ψ_i^{NC} should be preferred since then one can control the quality of the augmentation charges very well by performing calculations with the corresponding normconserving pseudopotentials.

In this scheme the pseudo-wave-functions are allowed to be as soft as possible within the core region, so that the cutoff energy can be reduced dramatically. Technically, this is achieved by introducing a generalized orthonormality condition. The electron density given by the squared moduli of the wave functions has to be augmented in the core region in order to recover the full electronic charge. The electron density is thus subdivided into (i) a smooth part that extends throughout the unit cell, and (ii) a hard part localized in the core regions. The augmented part appears in the density only, not in the wavefunctions. This differs from "Atomic-sphere methods" like linear augmented plane wave (LAPW) or Linear-muffin tin orbitals (LMTO), where a similar approach is applied to wavefunctions.

Ultrasoft potentials have another advantage, besides being much softer than the norm-conserving potentials. The USP generation algorithm guarantees good scattering properties over a pre-specified energy range, which results in much better transferability and accuracy of pseudopotentials. USP usually also treats "shallow" core states as valence by including multiple sets of occupied states in each angular momentum channel. This also adds to high accuracy and transferability of the potentials, although at a price of computational efficiency.

2.3.8 Energy Minimization

In this section two general methods are described that can be used to locate the minimum of function $F(x)$, where x is a vector in the multidimensional space [a detailed description of the techniques outlined in this section can be found in the book by Gill, Murray, and Wright (1981, p.144)]. It will be assumed that the function $F(x)$ has a single minimum. If the function had several minima the methods described here would locate the position of the minimum "closest" to the initial sampling point (strictly speaking, it would locate the minimum in whose basin of attraction the initial sampling point lies).

The variation of the total energy with the nuclear coordinates is usually referred to as the potential energy surface. In molecular modelling, the interest is in minimum points on the energy surface. Minimum energy arrangements of the atoms correspond to stable states of the system; any movement from the minimum gives a configuration with a higher energy. There may be a very large number of minima on the energy surface. The minimum with the very lowest energy is known as the global energy minimum. Minimization algorithm is used to identify those geometries of the system that correspond to minimum points on the energy surface. The lowest point on the pathway between two minima is of special interest and is known as the saddle point with the arrangement of atoms being the transition structure.

Suppose we have an estimate of the minimum of $F(x)$. We can refine this by choosing some direction vector u and searching for the minimum along the line $x + \lambda u$. We can refine this by choosing some direction vector u and searching for the minimum along the line λ which minimizes the function $F(x + \lambda u)$. The simplest algorithm for locating the minima of $F(x)$ is to repeat this process, cycling through the $\mathbf{n}$ unit direction vectors which span the parameter space. However, this can prove to be very inefficient if we end up making many small steps, zigzagging along a valley, when it would be better to move in directions aligned with the valley. The method of steepest descent (SD) performs particularly poorly when the minimum of the function $F(x)$ lies in a long narrow valley such as the one illustrated in Figure 2-5, and a number of improved procedures are

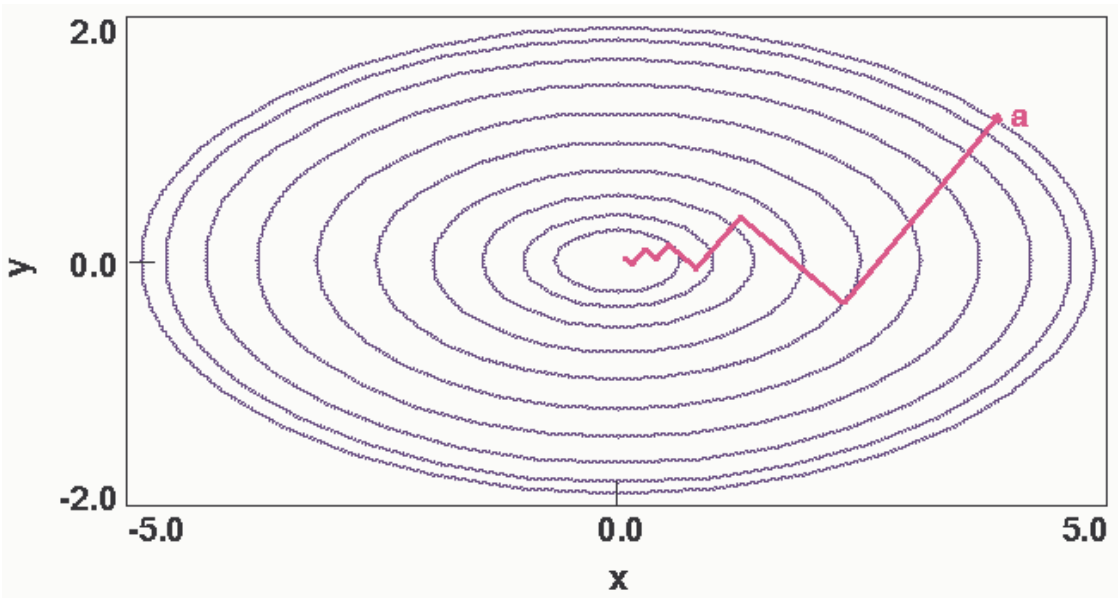

Figure 2-5: Minimization path following a steepest descents path. When complete line searches starting from point **a** are used, the minimum is reached in about 12 iterations. Here, where a rigorous line search is carried out, approximately 8 function evaluations are needed for each line search using a quadratic interpolation scheme. The steepest descents consistently overshoots the best path to the minimum, resulting in an inefficient, oscillating trajectory.

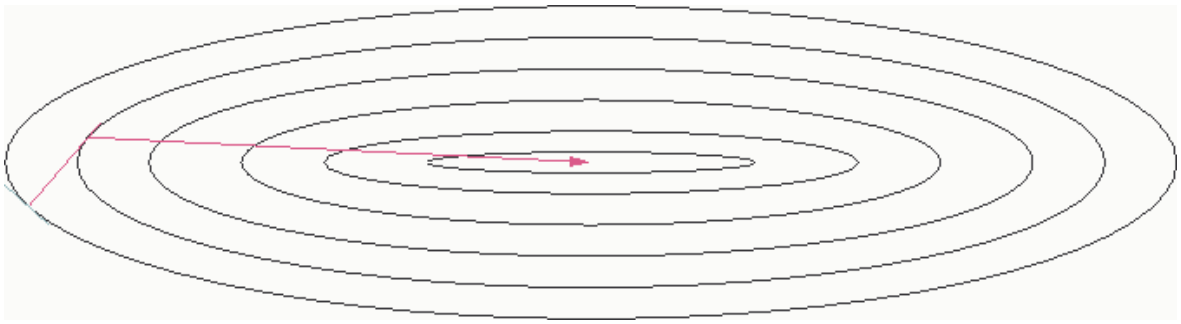

Figure 2-6: Conjugate gradients method - only two steps are required to find the minimum

available.

Conjugate-Gradients (CG) Technique: The rate of convergence of the steepest-descents method (see Appendix E) is limited to the fact that, after a minimization is performed along a given gradient direction, subsequent minimization along the new gradient reintroduces errors proportional to the previous gradient. The conjugate-gradient technique (see Appendix F) provides a simple and effective procedure for implementation of such a minimization procedure. The CG method was originally designed to minimize convex quadratic functions but, through several variations, has been extended to the general case [224, 225]. The first iteration in CG is the same as in SD, but successive directions are constructed so that they form a set of mutually conjugate vectors with respect to the (positive-definite) Hessian $\mathbf{A}$ of a general convex quadratic function $q_A(x)$. Whereas the rate of convergence for SD depends on the ratio of the extremal eigenvalues of $\mathbf{A}$, the convergence properties of CG depend on the entire matrix spectrum. Faster convergence is expected when the eigenvalues are clustered. In exact arithmetic, convergence is obtained in at most $\mathbf{n}$ steps. In particular, if $\mathbf{A}$ has $\mathbf{m}$ distinct eigenvalues, convergence to a solution requires $\mathbf{m}$ iterations. Conjugate-gradients method allows convergence in two steps (see Fig. 2-6).

Certain practical aspects of the conjugate gradient method should be pointed out. First, the conjugate gradient algorithm requires convergence along each line search before

continuing in the next direction. The gradient at step i+1 must be perpendicular to $\mathbf{h}_i$ or the derivation guaranteeing a conjugate set of directions breaks down. Second, to start conjugate gradients, an initial direction $\mathbf{h}_0$ must be chosen that is equal to the initial gradient. Finally, additional storage is required for an extra vector of N elements to hold the N components of the old gradient. For energy minimization in Cartesian space this would be the $3N$ derivatives of the energy with respect to the x, y, and z coordinates of each atom. This makes conjugate gradient the method of choice for systems that are too large for storing and manipulating a second-derivative matrix, as is required by the Newton-Raphson minimizers.

Newton-Raphson methods: As a rule, N^2 independent data points are required to solve a harmonic function with N variables numerically. Since a gradient is a vector N long, the best you can hope for in a gradient-based minimizer is to converge in N steps. However, if you can exploit second-derivative information, a minimization could converge in one step, because each second derivative is an $N \times N$ matrix. This is the principle behind the variable metric minimization algorithms, of which Newton-Raphson is perhaps the most commonly used.

Another way of looking at Newton-Raphson is that, in addition to using the gradient to identify a search direction, the curvature of the function (the second derivative) is also used to predict where the function passes through a minimum along that direction. Since the complete second-derivative matrix defines the curvature in each gradient direction, the inverse of the second-derivative matrix can be multiplied by the gradient to obtain a vector that translates directly to the nearest minimum. This is expressed mathematically as:

$$r_{\min} = r_0 - \mathbf{A}^{-1}(r_0) \cdot \Delta E(r_0) \tag{2.55}$$

where r_{min} is the predicted minimum, r_0 is an arbitrary starting point, $\mathbf{A}(r_0)$ is the matrix of second partial derivatives of the energy with respect to the coordinates at r_0 (also known as the Hessian matrix), and $\Delta E(r_0)$is the gradient of the potential energy

at r_0.

The energy surface is generally not harmonic, so that the minimum-energy structure cannot be determined with one Newton-Raphson step. Instead, the algorithm must be applied iteratively:

$$r_i = r_{i-1} - \mathbf{A}^{-1}(r_{i-1}) \cdot \Delta E(r_{i-1}) \tag{2.56}$$

Thus, the ith point is determined by taking a Newton-Raphson step from the previous point $(i-1)$. Similar to conjugate gradients, the efficiency of Newton-Raphson minimization increases as convergence is approached [226].

Chapter 3

Method of calculations

In this chapter we discuss methods applied and precautionary measures taken before calculations of the electronic, optical and structural properties. We also describe the main computer codes and facilities used in the study.

3.1 Planewave Methods

Our calculations were performed using the density functional technique (DFT) in both the local density approximation (LDA) and gradient-corrected LDA (GGA). LDA is known to underestimate bond lengths in molecules and cell parameters in crystals, while GGA typically remedies this shortcoming. However, there is much evidence that GGA is prone to overcorrect the LDA results in ionic system; it often overestimates cell parameters when LDA data is in good agreement with experiment. The work was carried out using Cambridge Sequential Total Energy Package (CASTEP) [202] and Planewave [227] codes. In the latter we used a preconditioned conjugate-gradient method to minimize the electronic degrees of freedom. The electronic wave functions were expanded in a planewave basis set with periodic boundary conditions. To test convergence with respect to the basis set size, calculations were performed at various kinetic energy cutoffs.

CASTEP employs special point integration over the Brillouin zone (BZ) and a planewave

basis for the expansion of the wavefunctions. Norm-conserving non-local pseudopotentials of the form suggested by Kleinmann and Bylander [228] were used. Cutoff energies of up to 500 eV and 600 eV were used for the expansion of the wavefunctions. Ceperly and Adler [210] using Monte Carlo techniques calculate the exchange-correlation energy function numerically for a large range of densities. An analytical fit to these results by Perdew and Zunger [209] is used in our calculation. A gradient-corrected form of the exchange-correction functional is used in the form suggested by White and Bird [229]. Fast Fourier transforms (FFT) sampling of special k-points was used to perform the integration in k-space over the first Brillouin zone.

3.1.1 CASTEP Code

As noted, all calculations use the total-energy (E^{tot}) code CASTEP [230], which employs pseudopotentials to describe electron-ion interactions and represents electronic wave functions using a plane-wave basis set [202]. Norm-conserving non-local pseudopotentials of the form suggested by Kleinmann and Bylander [228] were used. In order to describe the relatively hard potentials of both the Ti, S, Hf, Zr, and lithium atom, cutoff energies of up to 400 eV for TiS_2, ZrS_2 and $LiTiS_2$ (Fig. 3-1), were used for the expansion of the wavefunctions.

In a first-principle LDA calculation, the exchange-correlation energy is not an adjustable function; it is locally defined to be the exchange-correlation of a homogeneous electron gas. The function which is now widely accepted as the most accurate is the energy calculated numerically for a large range of densities by Ceperly and Adler using Monte Carlo Techniques. An analytical fit to these results by Perdew and Zunger [209] is used in our calculation. A gradient-corrected form of the exchange-correction functional (GGA) was used in the form suggested by White and Bird. Fast Fourier transforms (FFT) sampling of special k-points was used to perform the integration in k-space over the first Brillouin zone.

Geometry optimization was performed using a BFGS-based minimization technique

(see Appendix D). The optimization procedure incorporates symmetry constraints. The Hessian matrix in the mixed space of internal coordinates and cell variables was updated using *ab initio* calculated atomic forces and stress tensor. The total energies were corrected using the finite-basis set correction method developed by Francis and Payne [220]. Pullay stress corrections were evaluated numerically by performing total energy calculation at three different values of the kinetic energy cutoff.

Calculations were also conducted on metallic magnesium (Mg_{metal}), the low-symmetry $R\bar{3}$ structures of $Mg_xMo_6S_8$: Mo_6S_8 ($x = 0$) and $Mg_OMo_6S_8$ ($x = 1$, Mg at origin); the $P\bar{1}$ structures for ($x = 1$) of $Mg_AMo_6S_8$ (Mg in the inner ring) and $Mg_BMo_6S_8$ (Mg in the outer ring); and for ($x = 2$) of $Mg_{AB}Mo_6S_8$ (Mg in both site A and site B), $Mg_{2A}Mo_6S_8$ (two Mg's in site A), and $Mg_{2B}Mo_6S_8$ (two Mg's in site B), which involves up to 16 atoms in a unit cell per system. Energy cutoffs of up to 500 eV (see Fig. 3-2)were used for the expansion of the wave functions and a single point sampling of the Brillouin zone produced converged results.

The total energy is calculated both within the framework of the local-density approximation (LDA), the Perdew and Zunger [209] parametrization of the numerical results of Ceperley and Alder [210], for the exchange-correlation energy, and the nonlocal or gradient-corrected approximations (Perdew-Burke-Ernzerhof [231]) implemented according to the method described by White and Bird [229] (i.e. GGA_{PBE}). The interactions between the ionic cores and the electrons are described by the Troullier-Martins [232] pseudopotential, the pseudopotential in Kleinman-Bylander [228] form, and the associated Vanderbilt [223] pseudopotential. The earlier pseudopotentials were specifically used for the calculations of electronic properties rather than structural parameters, the latter being well predicted by the Vanderbilt pseudopotential which requires significantly less computational resources.

The pseudo-wave functions, the smooth part of the charge density and the potential are represented on a fast-Fourier- transform (FFT) grids of $18 \times 18 \times 30$, $40 \times 40 \times 40$, and $45 \times 45 \times 45$ for Mg_{metal}, Mo_6S_8, and $Mg_xMo_6S_8$ ($0 \leq x \leq 2$), respectively. These minimum

FFT grids applied to the exchange-correlation potential [$V_{xc}(G - G')$] are sufficient for the cutoff energies. The 36 and 6 k points were generated with the Monkhorst-Pack [217] scheme with parameters $(9 \times 9 \times 6)$ and $(3 \times 3 \times 3)$ for Mg_{metal} and $Mg_xMo_6S_8$ $(0 < x \leq 2)$ respectively. Each k point in the irreducible Brillouin zone was represented with an equivalent of 6500 to 9600 plane waves. All calculations involve full geometry optimizations of Mg_{metal}, Mo_6S_8, and $Mg_xMo_6S_8$. Geometry optimization at zero pressure was performed with the variable lattice parameter and full relaxation of the internal coordinates. Calculations were considered to be converged when the maximum force on an atom was below 0.01 eVÅ^{-1}.

3.1.2 Finite Planewave Basis Sets Corrections and Convergence.

One of the difficulties associated with the use of plane-wave basis sets is that the number of basis states changes discontinuously with cutoff energy. In general these discontinuities will occur at different cutoffs for different k-points in the k-point set. In addition, at a fixed cutoff energy, a change in the size or shape of the unit cell will cause discontinuities in the plane wave basis set. This problem can be reduced by using a denser k-point set, so that the weight attached to any particular plane wave basis state is reduced. However, the problem is still present even with quite dense k-point samplings. It can be handled approximately by applying a correction factor that accounts for the difference between the number of a states in a basis set with an infinitely large number of k-points and the number of basis states actually used in the calculation [220].

The finite basis set correction is of utmost importance when cell optimization is performed with a basis set that is not absolutely converged. For example, the ultrasoft Mo_6S_8 pseudopotential is sufficiently soft and provides fairly accurate results with a cutoff energy for plane waves of about 400 eV. However, if one calculates the equation of state (EOS) using this cutoff (i.e. the volume dependence of the total energy and pressure), the volume that corresponds to the minimum in the total energy does not coincide with the volume that gives zero pressure. As one repeats such EOS calculations at progressively

higher cutoff energies and with better k-point sampling, the difference between the two volume values becomes smaller and smaller. In addition, the E-V curve calculated at low cutoff energy is jagged but becomes more and more smooth as the cutoff energy is increased. The reason for the jagged appearance of the E-V curve is the discontinuous change in the number of plane waves used at the same cutoff energy but for different lattice constants. The finite basis set correction, when added to the total energy, allows one to perform calculations with a fixed number of basis states and to interpolate the results as if the more physical condition of a fixed energy cutoff were used.

The idea behind the finite basis set correction is to use the results obtained at relatively low cutoff energy and low k-point sampling and correct them analytically, thus eliminating the necessity of running calculations with prohibitively large basis sets. The only parameter that has to be known in order for this correction term to be evaluated can be expressed as dE_{tot} /dlnE_{cut}, where E_{tot} is the total energy of the system and E_{cut} is the cutoff energy. The value of the dE_{tot} /dlnE_{cut} derivative gives a good indication of the convergence of the calculation with respect to the energy cutoff and k-point sampling. When its value per atom is smaller than 0.01eV atom^{-1}, the calculation can be considered very well converged.

3.2 Calculations of Optical Properties

In general, the difference in the propagation of an electromagnetic wave through vacuum and some other material can be described by a complex refractive index.

$$n \equiv k(c/\omega) = n_1 + in_2 \tag{3.1}$$

Since n_1 is just the usual index of refraction in regions where the crystal is non-absorbing, the velocity of propagation in a crystal, c/n_1,is slower than in vacuum.

In vacuum n it is real, and equal to unity. For transparent materials it is purely real, the imaginary part being related to the absorption coefficient by,

$$\eta(\omega) = \frac{2k\omega}{c} \tag{3.2}$$

the fraction of energy lost by the wave on passing through a unit thickness of the material concerned. This is derived through considering the rate of production of Joule heat in the sample. The reflection coefficient can be obtained for the simple case of normal incidence on a plane surface by matching both the electric and magnetic fields at the surface,

$$R(\omega) = \left|\frac{1-n}{1+n}\right|^2 = \frac{(n_1-1)^2+n_2^2}{(n_1+1)^2+n_2^2} \tag{3.3}$$

However, when performing calculations of optical properties it is common to evaluate the complex dielectric constant, and then express other properties in terms of it. The dispersion relationship relating the spatial variation of $\mathbf{k}$ to the time variation ω is

$$\mathbf{k}\cdot\mathbf{k} = k^2 = \varepsilon(\omega/c)^2 \tag{3.4}$$

It can be written in the form

$$\varepsilon = (c/\omega)^2\mathbf{k}\cdot\mathbf{k} = (c/\omega)^2(k_1^2 - k_2^2 + 2i\mathbf{k}_1\cdot\mathbf{k}_2) \equiv (n_1 + in_2)^2 \tag{3.5}$$

The complex dielectric constant $\varepsilon(\omega)$ is given by,

$$\varepsilon(\omega) = \varepsilon_1(\omega) + i\varepsilon_2(\omega) = n^2 \tag{3.6}$$

and hence the relation between the real and imaginary parts of the refractive index and dielectric constant is

$$\begin{aligned} \varepsilon_1(\omega) &= n_1^2 - n_2^2 \\ \varepsilon_2(\omega) &= n_1^2 - n_2^2\varepsilon_2(\omega) = 2n_1n_2 = \frac{4\pi\sigma_1}{\omega} \end{aligned} \tag{3.7}$$

For a tetragonal or hexagonal structure we need to calculate two components of the dielectric function, corresponding to light polarized parallel and perpendicular to the c-axis. In that case the total $\varepsilon_2(\omega)$ is given by:

$$\varepsilon_2^{tot}(\omega) = \frac{\varepsilon_2^{\parallel}(\omega) + \varepsilon_2^{\perp}(\omega)}{3} \tag{3.8}$$

where $\varepsilon_2^{\parallel}$ and $\varepsilon_2^{\perp}$ are the imaginary parts of the frequency-dependent dielectric function for the light polarized parallel and perpendicular to the c-axis. The imaginary component $\varepsilon_2(\omega)$, can be calculated from a band structure.

Ohm's law in terms of conductivity, σ, is stated as,

$$\mathbf{J} = \sigma \mathbf{E} \tag{3.9}$$

where $\mathbf{J}$ is the current density and $\mathbf{E}$ is the electric field. Considering the macroscopic picture of the free electron, conductivity can be expressed as

$$\sigma = (N/V)e^2\tau/m \tag{3.10}$$

where N is the number of electrons of charge -e, with an average drift velocity , $\mathbf{v}_d = -e\mathbf{E}\tau/m$,across the area A in a time dt. Consider an oscillating electric field so that the time dependence can be taken as $\mathbf{E}(t) = Re\left[\mathbf{E}(\omega)\exp(-i\omega t)\right]$ where $\mathbf{E}(\omega)$ is complex. Drude contribution to conductivity is

$$\sigma(\omega) = \frac{\sigma_0}{1 - i\omega\tau} \tag{3.11}$$

where $\sigma_0 \equiv (N/V)e^2\tau/m$. By taking the real and imaginary parts of σ we find

$$\sigma(\omega) = \frac{\sigma_0}{1 + (\omega\tau)^2} + i\frac{\sigma_0\omega\tau}{1 + (\omega\tau)^2} \tag{3.12}$$

where τ is the relaxation time. From Maxwell's equation for free space, a complex dielectric constant is defined as

$$\begin{aligned} \nabla^2 \mathbf{E} &= \frac{\omega^2}{c^2}\varepsilon(\omega)\mathbf{E} \\ \varepsilon(\omega) &= 1 + \frac{4\pi i\sigma}{\omega} \end{aligned} \tag{3.13}$$

For frequencies such that $\omega\tau \gg 1$

$$\begin{aligned} \varepsilon(\omega) &= 1 - \frac{\omega_p^2}{\omega^2} \\ \omega_p &= \frac{4\pi(N/V)e^2}{m} \end{aligned} \tag{3.14}$$

where ω_p is called the plasma frequency.

A further frequent form for the expression of optical properties is the optical conductivity,

$$\sigma(\omega) = \sigma_1 + i\sigma_2 = -i\frac{\omega}{4\pi}(\varepsilon(\omega) - 1) \tag{3.15}$$

But, this is most useful for metals, which are not treated. In a metal the conduction electrons may half fill a band. Free carrier absorption takes place when photons promote electrons to a higher energy state within the same band. Free carrier electrons move over many interatomic distances. Therefore they respond to the external applied field rather than to any local field. Thus, there are non-local field corrections. Free carrier effects are closely related to plasma effects. A plasma is an ionized gas in which the free electrons typically have a high mobility compared to the ions. Since the optical effects of the free carriers are treated within the Drude free electron model (i.e. a free electron gas), these results are applicable also to true plasma. For good metals $\omega\tau \gg 1$; at the plasma frequency, or what is sometimes called the plasma edge, the damping is small compared to the frequency.

A further property calculated from the complex dielectric constant is the loss function.

It describes the energy lost by a point electron passing through a homogeneous dielectric material, and is given by,

$$\mathrm{Im}\left(\frac{-1}{\varepsilon(\omega)}\right) \tag{3.16}$$

Experimentally, the most accessible optical parameters are the absorption $\eta(\omega)$, and the reflection $R(\omega)$ coefficients.

In principle, given the knowledge of both these, real and imaginary parts of N can be determined. However, in practice, the experiments are more complicated than the case of normal incidence considered in our calculations. Polarisation effects must be counted for, and the geometry can become quite involved (for example, transmission through multilayered films or incidence at a general angle). Our calculations only consider normal incidence, but polarization effects are taken into account.

The interaction of a photon with the electrons in the system under study is described in terms of the time dependent pertubations of the ground state electronic states. Transition are caused between occupied and unoccupied states by the electric field of the photon (the magnetic field affect is weaker by a factor of v/c). When these excitations are collective they are known as plasmons (which are most easily observed by the passing of a fast electron through the system rather than a photon, in a technique known as Electron Energy Loss Spectroscopy (EELS), described by Eq. 3.16 - since transverse photons do not excite longitudinal plasmons. When the transitions are independent they are as single particle excitations. The spectra resulting from these excitations can be thought of as a joint density of states (JDOS) between the valence and conduction bands, weighted by appropriate matrix elements (introducing selection rules).

3.2.1 Evaluation of the Dielectric Constant.

We calculate the imaginary part of the dielectric constant, which is given by,

$$\varepsilon\left(\mathbf{q} \rightarrow \mathbf{O}_{\hat{\mathbf{u}}}, \hbar\boldsymbol{\omega}\right) = \frac{2e^2\pi}{\Omega\varepsilon_o} \sum_{\mathbf{k},v,c} \left|\left\langle \psi_k^c \left|\hat{\mathbf{u}} \cdot \mathbf{r}\right| \psi_k^v \right\rangle\right|^2 \delta\left(E_k^c - E_k^v - E\right) \tag{3.17}$$

where $\mathbf{u}$ is the vector defining the polarization of the incident electric field. This expression is similar to Fermi's Golden rule for time dependent perturbations, and $\varepsilon_2(\omega)$ can be thought of as detailing the real transitions between occupied and unoccupied electronic states. Since the dielectric constant describes a casual response, the real and imaginary parts are linked by a Kramers-Kroning transform. This is used to obtain the real part, $\varepsilon_1(\omega)$.

The current approach to integration over the Brillouin Zone involves taking a symmetrized Monkhorst-Pack grid, and smearing each energy level with a Gaussian spread function. The matrix elements that are required to describe the electronic transitions in the above equation are $\langle \psi_k^c \left|\mathbf{r}\right| \psi_k^v \rangle$, which may normally be written as $(1/i\omega m) \langle \psi_k^c \left|\mathbf{P}\right| \psi_k^v \rangle$ allowing straight forward calculation in reciprocal space. However, this depends on the use of local potentials, while in CASTEP non-local potentials are the norm. The corrected form of the matrix elements are,

$$\langle \psi_k^c \left|\mathbf{r}\right| \psi_k^v \rangle = \frac{1}{i\omega m} \langle \psi_k^c \left|\mathbf{P}\right| \psi_k^v \rangle + \frac{1}{\hbar\boldsymbol{\omega}} \langle \psi_k^c (\left|V_{nl}\right|, \mathbf{r}) \psi_k^v \rangle \tag{3.18}$$

For materials that do not display full cubic symmetry (e.g. hexagonal $Mg_xMo_6S_8$ and Li_xTiS_2 systems used in the present study), the optical properties will display some anisotropy. This can be include in the calculations by taking the polarization of the electromagnetic field into account.

The level of approximation used does not take any local field effects into account. These arise from the fact that the electric field experienced at a particular site in the system is screened by the polarizability of the system itself. So, the local field is different from the applied external field. (i.e., the photon electric field). This can have a significant effect on the spectra calculated. The non-local nature of the GGA is not taken into account on evaluating the matrix elements, but it is expected that this will have a small

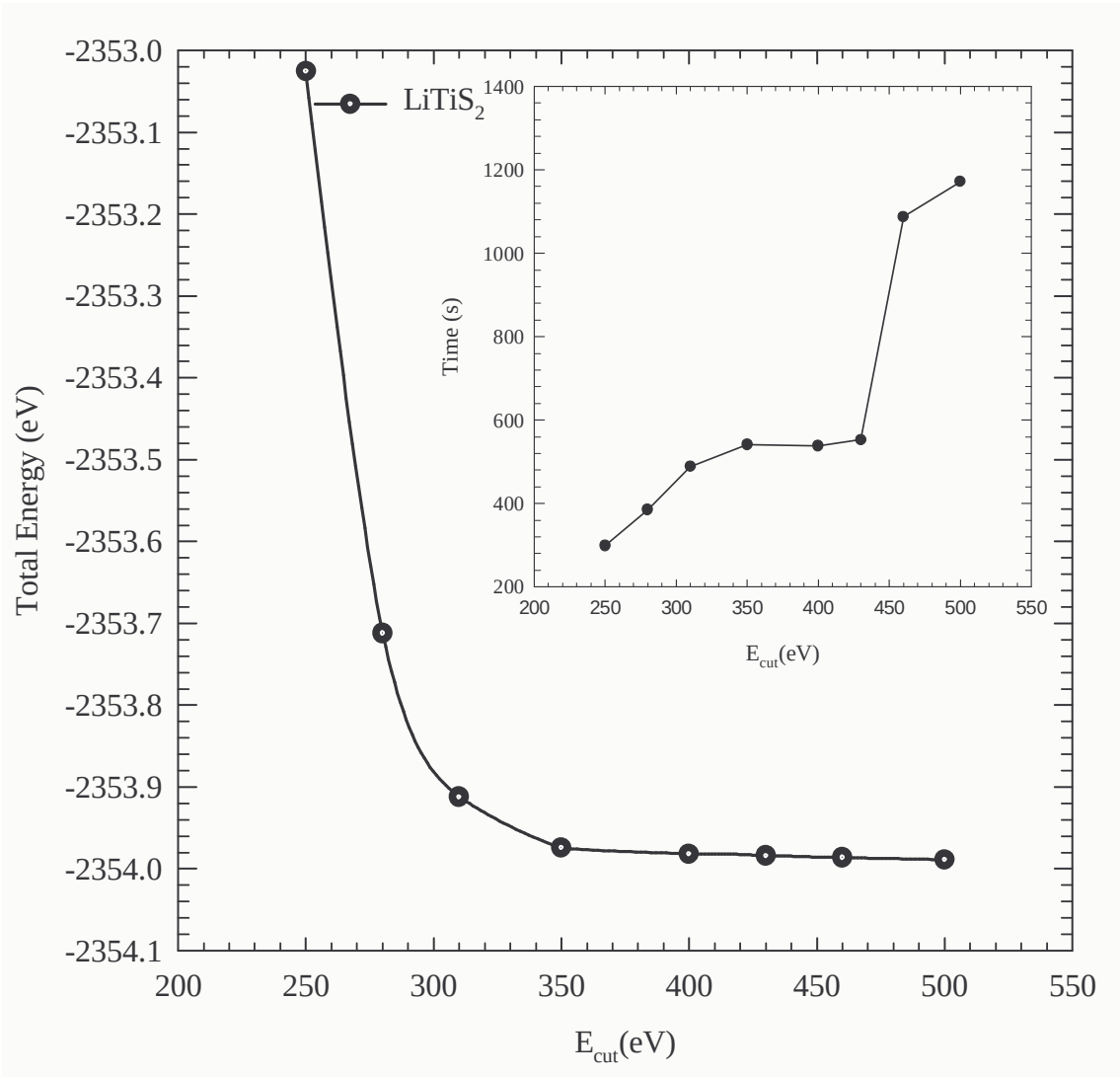

Figure 3-1: Convergence of the total energy for $LiTiS_2$ unit cell for different cut-off energy E_{cut}^{castep} using "ultrasoft" pseudopotentials. The inset shows the variation of the elapsed time.

effect on the calculated spectra. There is an intrinsic error in the matrix elements for optical transition due to the fact that pseudo-wavefunctions have been used (i.e., they deviate from the true wavefunctions in the core region), leading to small numerical errors.

3.3 Commissioning of Computer Codes and Graph Analysis.

Before any calculations, the main problems somewhat "technical" in their nature, associated with any new application of the total-energy method will be solved. The prime difficulty encountered when using plane waves is closely related to the problem of convergence in Fourier space. From a plot of total-energy vs. planewave cut-off E_{cut}, we are guided as to how large a value of E_{cut} is required, or in practice how small an E_{cut} will suffice. The same calculation to test for convergence using CASTEP were done and are shown in Figures 3-1 and 3-2. $MgMo_6S_8$ and $LiTiS_2$ converges at about $E_{cut} = 500$ eV and about 400 eV respectively. We have also shown how the time varies with the increase in the number of planewaves used. We observe that the time increases with the increase in the energy cutoff even after convergence.

3.4 Hardware and Analytical Software

The following equipment, available in the Materials Modelling Center are used:

1 Workstations: SGI Inc. - Challenge XL (12 CPUs), ORIGIN 2000 (16 CPUs), Octane, O2 and Indys (Operating System - IRIX 6.X (Unix System V))

1. Personal computer - Pentium based computers (Operating System - Microsoft Windows 98/2000/XP and Open Source Software - Linux)

2. Computational Software: Accelrys Inc. - Cerius2 and Materials studio interfaces, Castep codes [230].

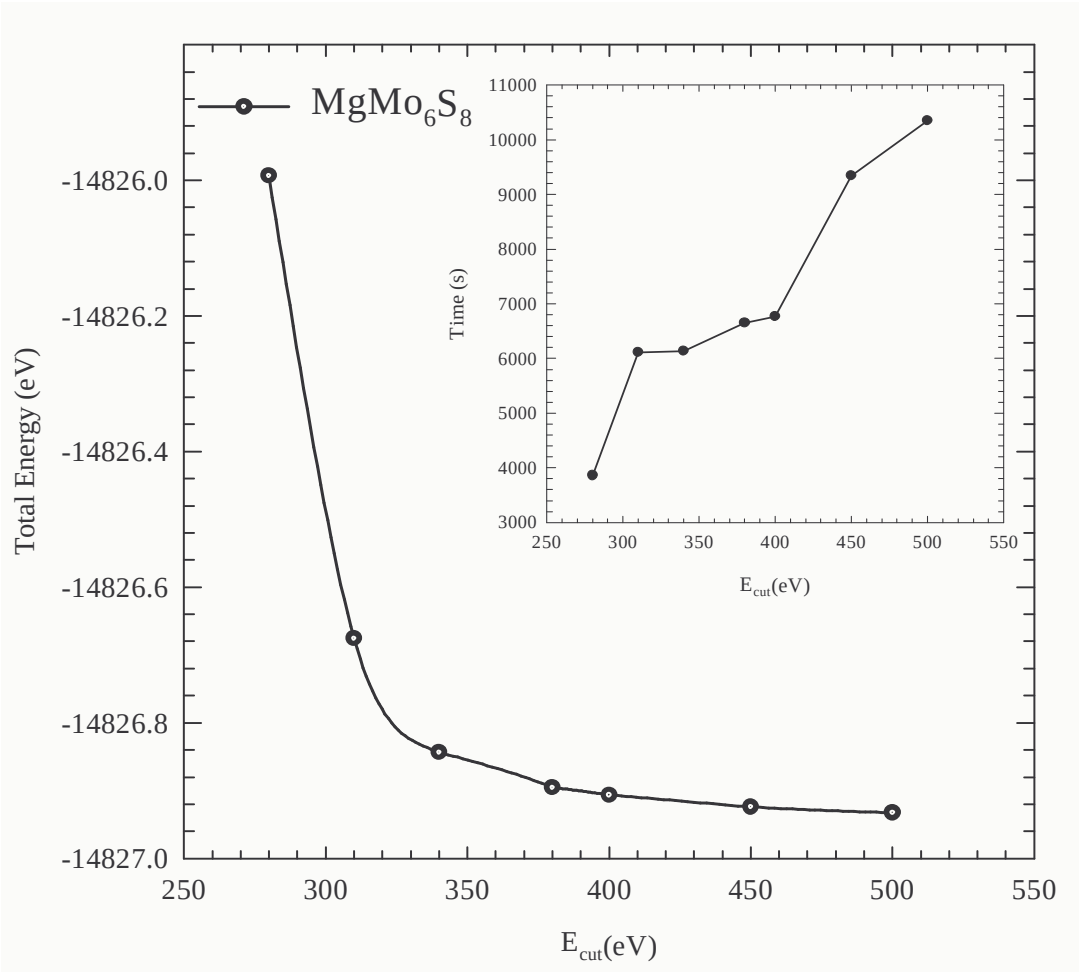

Figure 3-2: Convergence of the total energy for $MgMo_6S_8$ unit cell for different cut-off energy E_{cut}^{castep} using "ultrasoft" pseudopotentials. The inset shows the variation of the elapsed time.

3. Analytical Software: SYSTAT Inc. - Sigma Plot and MacKichan Software Inc. - Scientific Workplace.

Chapter 4

Ternary Molybdenum Chalcogenides

In this chapter we investigate the structural properties of $Mg_xMo_6S_8$ ($0 < x \leq 2$) based on the reported structure of Chevrel phase compounds $Ni_2Mo_6S_8$ [25, 26] and $Li_xMo_6S_8$ ($0 < x \leq 4$) [17] using the Density-Functional technique. We present our predicted structure of $Mg_1Mo_6S_8$ and $Mg_2Mo_6S_8$ from which the voltage profile, electronic and optical properties are calculated.

4.1 Structural Properties of the Ternary Molybdenum Chalcogenides

4.1.1 Structural description

As shown in Fig. 4-1, Chevrel phase structures are made up of blocks of slightly distorted cubes or clusters of Mo_6X_8 units, with eight X atoms at the cube corners and six Mo atoms slightly outside the middle of the cube faces. Most have rhombohedral structures at room temperature and many distort to triclinic structures at low temperatures [154]. Mo_6S_8 is rhombohedral with space group $R\overline{3}$ (C_{3i}^2), and lattice parameters $a_R = |\overrightarrow{a}| = \left|\overrightarrow{b}\right| = |\overrightarrow{c}| = 6.43$ Å and $\alpha_R = \alpha = \beta = \gamma = 91.34°$ [233]. Earlier work on $Li_xMo_6S_8$ [155], showed that there are two phases, a rhombohedral phase with an incommensurate

lattice distortion, and a triclinic phase for $0 < x < 1$.

A network of interconnecting channels, parallel to the rhombohedral axes, runs between the Mo_6S_8 clusters which contains the interstitial sites or cavities where the M atoms reside. Cavity 1, which is the largest, has a quasicubic shape and is formed by eight sulfur atoms belonging to eight different Mo_6S_8 units centered at the origin (the position of Mg_O in Fig. 4-2) of the rhombohedral unit cell with point symmetry $\overline{3}$. Cavity 2, situated at the middle of the rhombohedral axes ($\overline{1}$-point symmetry), has a more irregular cubic shape and is formed by eight sulfurs belonging to four Mo_6S_8 units sharing edges (see Fig. 4-2). This cavity shares opposite pseudosquared faces with two other cavities 1 along the rhombohedral axes. Cavity 3, formed by eight sulfur atoms belonging to two different Mo_6S_8 units, is always empty because of the Mo-S intercluster bond (Fig. 4-2). For smaller M atoms, α_R is larger and the M atoms are displaced from the $\overline{3}$ axis, and partially occupy one ring of six inner sites inside cavity 1 (site A) and one ring of six outer sites in cavity 2 (site B) per formula unit of Mo_6X_8. When α_R is small, the S($2c$) site is significantly closer to the interstitial site than the S($6f$) site (Fig. 4-1). The two chalcogens on the $\overline{3}$ axis ($2c$) have the greatest influence on the M-atom site energy because of their closer proximity than the other six chalcogens ($6f$) [157]. Two Mo-Mo distances describe the molybdenum cluster: the $[\mathrm{Mo}(1) - \mathrm{Mo}(1)]_{\triangle}$ intratriangle and $\left[\mathrm{Mo}(1)_{\triangle} - \mathrm{Mo}(1)_{\triangle}\right]$ intertriangle. The first distance concerns two molybdenum atoms belonging to the same triangular plane which is perpendicular to the ternary ($\overline{3}$) axis, while the second distance concerns two adjoining triangular planes in the same cluster [Fig. 4-1(a)].

The crystal structure of $Mg_xMo_6S_8$ may also be considered as a stacking of Mo_6X_8 clusters. There are 12 potential formal lattice sites for Mg atoms between each set of two blocks, around the unit-cell origin [Figs. 4-1 (b) and 4-1 (c)]. The first ring has sixfold positions (Mg_A) close to the unit-cell origin, forming the inner sites; a second ring with sixfold positions (Mg_B) which forms the outer sites is located around the inner positions. The intercalated metal plays an important role in stabilizing the whole structure. It

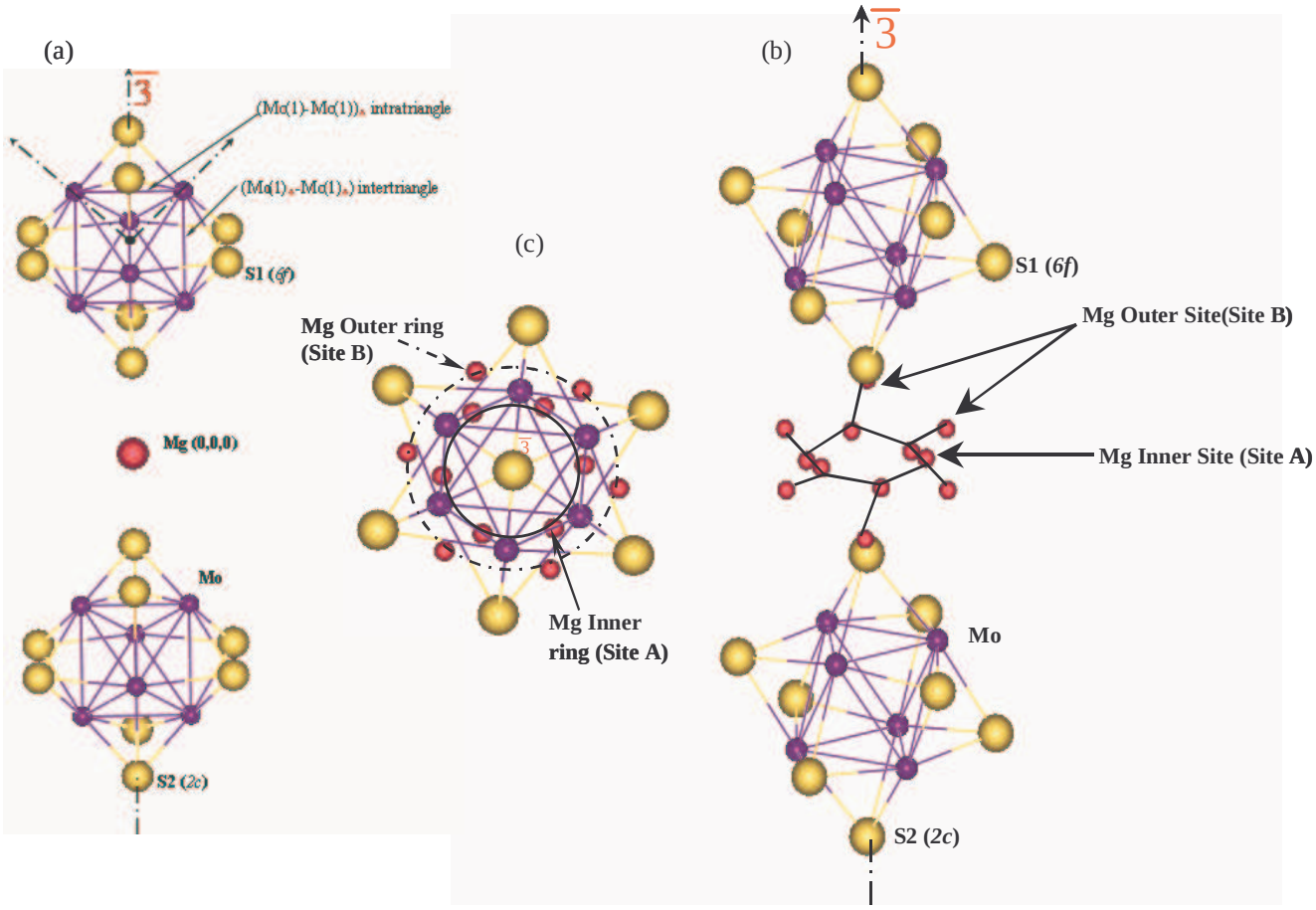

Figure 4-1: Basic crystal structure of the $Mg_xMo_6S_8$ ($0 \leq x \leq 2$) cathodes. (a) Basic atomic arrangements in the rhombohedral Chevrel phase sulphide cluster with (b) two possible Mg positions with a dumbell shape per cavity 2 ($\overline{1}$) and (c) six positions giving a hexagonal or puckered ring per cavity 1 ($\overline{3}$).

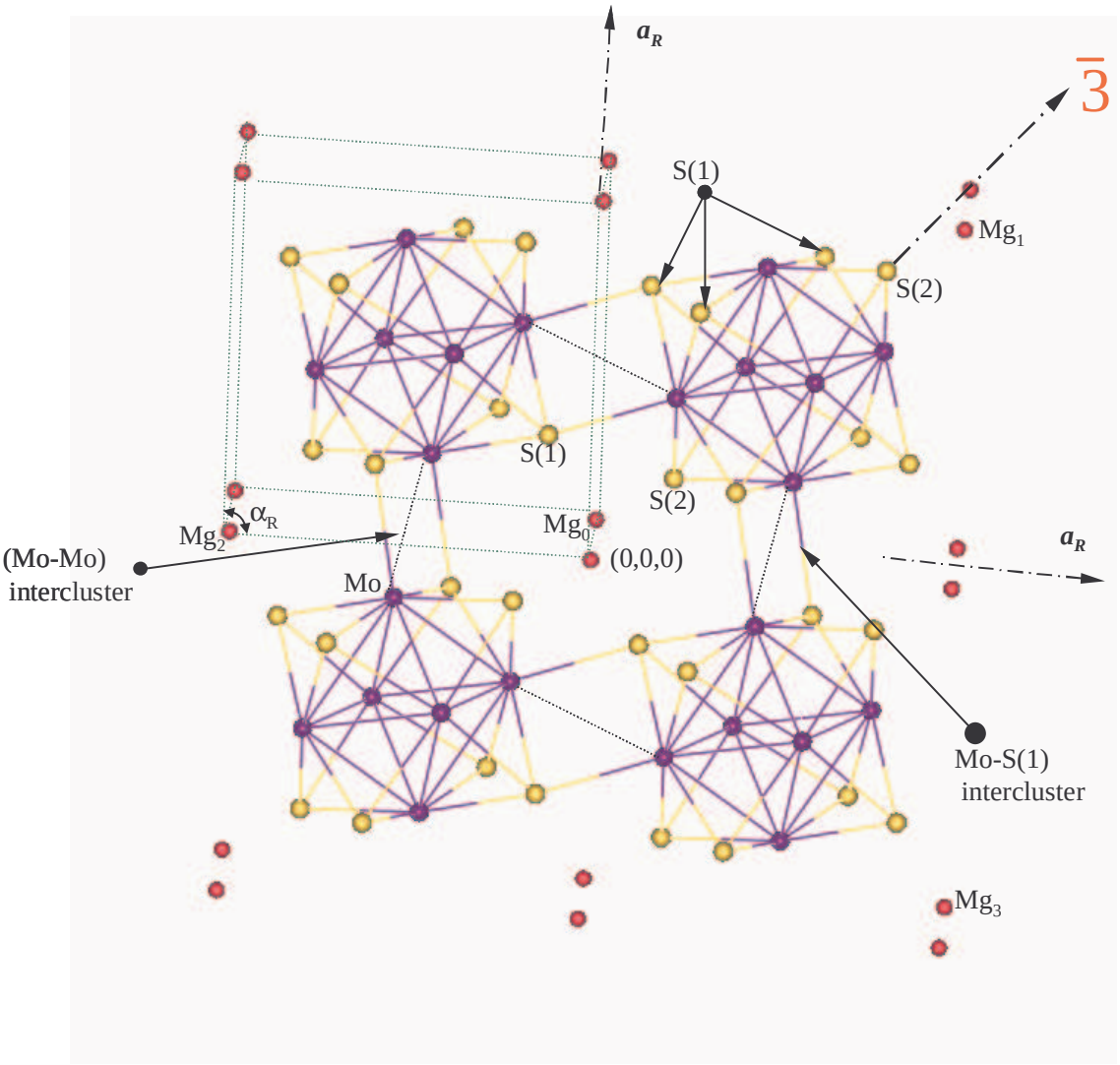

Figure 4-2: Crystal structure of the Chevrel phase $Mg_OMo_6S_8$, showing four Mo_6S_8 rhombohedral units (each unit is turned by an angle of about 27° around the ternary axis), the strong (Mo-Mo) intercluster and Mo-S(1) intercluster bonding and two types of chalcogen atoms [axial S(2) and peripheral S(1)]. Inserted Mg cations are located at position (0,0,0). A hexagonal unit cell can also be defined with Mg_0 being the origin. The vector from Mg_0 to Mg_1 is the c lattice parameter and the vectors from Mg_0 to Mg_2 and Mg_0 to Mg_3 are the a lattice parameters.

modifies the distances between the Mo atoms due to charge transfer from the metal atoms to the Mo or S atoms. The maximum charge transfer is predicted to be four electrons per Mo_6S_8 cluster, which results in the maximal insertion of four monovalent Li^+ cations or two bivalent Mg^{2+} cations. Magnesium insertion into $Mg_xMo_3S_4$ takes place in stages corresponding to the formation of new phases. A new intercalation phase differs from the previous one by occupation of different sites [site A or B, see Figs. 4-1 (b) and 4-1 (c)] in the host crystal with a different insertion energy. Mg can be inserted electrochemically up to a stoichiometry of $Mg_xMo_3S_4$ ($x = 1$) [2].

Mg insertion into Mo_3S_4 can be understood by reference to the crystal structure of $Li_xMo_3S_4$ ($0 < x \leq 2$) [17]. The ionic model description [10] suggests a maximum uptake formally of two Mg ions into the electron-deficient Mo_6 cluster, which leaves us with two possible vacant sites: the inner Li1 site (substituted by Mg_A) close to the unit-cell origin with the atom coordinates $(0.598, 0.359, 0.381 : \beta = 2.9)$, and the outer Li2 site (substituted by Mg_B) with the atom coordinates $(0.156, 0.272, 0.872 : \beta = 1.3)$. This configuration leads us to new structures $Mg_AMo_6S_8$ and $Mg_BMo_6S_8$ used in our calculations. A model of the structure of $NiMo_3S_4$ [25, 26] is also considered, using the structure of the stoichiometric compound as a reference and substituting the atomic positions of Ni $(0.0144, 0.3458, 0.9404 : \beta = 1.45)$ and $(0.0558, 0.797, 0.8192 : \beta = 1.89)$ by Mg leading to $Mg_{AB}Mo_6S_8$. We also consider Mg occupation of cavity 1 (Mg_O) with the following fractional coordinates $(0, 0, 0)$, the site normally occupied by large atoms (see Fig. 4-2).

4.1.2 Structural Modelling

We report our results in each of the crystal structures, i.e., $R\overline{3}$ structures of $Mg_xMo_6S_8$: metastable Mo_6S_8 ($x = 0$) and $Mg_OMo_6S_8$ ($x = 1$); the $P\overline{1}$ structures for ($x = 1$) of $Mg_AMo_6S_8$and $Mg_BMo_6S_8$; and for ($x = 2$) of $Mg_{AB}Mo_6S_8$, $Mg_{2A}Mo_6S_8$, and $Mg_{2B}Mo_6S_8$. The cell voltages are calculated from the optimized total energies E^{tot} of the latter structures and that of metallic magnesium (Mg_{metal}). Lastly, details of electronic charge

Table 4.1: Calculated and experimental structural parameters for rhombohedral and hexagonal Mo_6S_8 and $Mg_xMo_6S_8$ ($x = 1$ and 2)

Compounds	a_R (Å)	α_R (°)	V_R (Å^3)	a_H (Å)	c_H (Å)	V_H (Å^3)	c_H/a_H
Mo_6S_8 (LDA)	6.347	91.39	255.4	9.084	10.722	766.19	1.180
Mo_6S_8 (GGA-PBE)	6.465	91.50	269.9	9.261	10.899	809.78	1.177
Mo_6S_8[233]	6.432	91.34	265.8	9.201	10.879	797.50	1.182
Mo_6S_8[23]	6.432	91.34	265.8	9.202	10.877	797.60	1.182
Mo_6S_8[234]	6.425	91.25	265.0	9.185	10.881	795.10	1.185
Mo_6S_8[41]	6.424	91.26	264.9	9.184	10.880	794.63	1.185
Mo_6S_8[101]	6.430	91.31	265.6	9.197	10.879	796.90	1.183
Mo_6S_8[157]	6.428	91.26	265.4	9.189	10.886	796.21	1.185
$Mg_OMo_6S_8$ (LDA)	6.367	91.52	257.8	9.122	10.730	773.35	1.176
$Mg_OMo_6S_8$ (GGA-PBE)	6.489	92.12	272.7	9.346	10.815	818.23	1.153
Triclinic	a (Å)	b (Å)	c (Å)	α (°)	β (°)	γ (°)	V_T (Å^3)
$Mg_AMo_6S_8$	6.393	6.402	6.385	93.65	93.05	91.62	260.358
$Mg_BMo_6S_8$	6.409	6.386	6.396	93.95	91.03	93.63	260.564
$Mg_{2A}Mo_6S_8$	6.480	6.490	6.557	99.60	90.53	98.04	269.088
$Mg_{AB}Mo_6S_8$	6.505	6.521	6.535	97.27	93.58	92.99	273.936
$Mg_{2B}Mo_6S_8$	6.629	6.515	6.501	94.26	96.78	91.40	277.850

density, including analysis into the effects of intercalation on the electronic structure, are calculated self-consistently for the selected relaxed crystal structures.

Table 4.1 gives the calculated structural parameters for both the LDA and generalized-gradient-approximation -Perdew-Burke-Ernzerhof (GGA-PBE) calculations using an ultrasoft representation of the core. The LDA calculations for the rhombohedral structure Mo_6S_8 underestimate the reported experimental [157] parameters well within the expected error: the lattice parameter $a_R = 6.347$ Å is less than the experimental values [23, 41, 101, 157, 233, 234] which are within the range of 6.424 Å to 6.432 Å while the angle $\alpha_R = 91.39°$ is slightly above the experimental range of 91.25° to 91.34°. The same trends follow for the hexagonal Mo_6S_8 structure, with $a_H = 9.084$ Å and $c_H = 10.722$ Å underestimating the reported experimental parameters which are within the ranges of 9.184 Å to 9.200 Å and 10.877 Å to 10.880 Å, and $V_H = 766.190$ Å^3 is below the

experimental parameters which range from 794.63 Å^3 to 797.60 Å^3, again well within the expected LDA error.

In contrast, the GGA calculations overestimate lattice parameters in both rhombohedral and hexagonal Mo_6S_8. The lattice parameter $a_R = 6.465$ Å and the angle $a_R = 91.50°$ are more than the experimental values, and the volume $V_R = 269.928$ Å^3 exceeds experiment [157] by 1.7%. The same trends are noted for the hexagonal Mo_6S_8 structure with $a_H = 9.261$ Å and $c_H = 10.901$ Å, overestimating the reported experimental parameters. Although the GGA slightly overestimates the parameters, the predictions are close to experimental parameters and acceptable for a calculation using the GGA [235]. It has already been shown for a wide range of bulk solids that the GGA tends to overestimate the equilibrium volume V_0 with the least overestimation provided by PBE [236]. The predicted c/a ratio is 1.177 and 1.183 for the GGA and LDA, respectively, similar to the experimental values of 1.182 to 1.185 [23, 41, 101, 157, 233, 234].

Since no crystallographic data for $Mg_xMo_6S_8$ have been reported, we infer the position of Mg atoms by analogy with Chevrel compounds suggested by other authors [17, 25, 26]. The structure of Ritter *et al.* [17] is used, with Mg replacing Li in the $Li_1Mo_6S_8$ structure, where Li exclusively occupies the inner ring (site A), denoted $Mg_AMo_6S_8$. The LDA results suggest a phase transition from a rhombohedral phase to a triclinic phase, an illustration of the very complex structural behavior of the M atoms in the MMo$_6$S$_8$ compounds. The existence of triclinic MMo$_6X_8$ compounds, such as MMo$_3$S$_4$ (M = Mg, Fe, Zn, Mn, and Cd), and the low-temperature modification of $Cu_{0.9}Mo_3S_4$ have been reported earlier [9, 11]. Yvon *et al.* [10, 23] noted a phase transition in the $Cu_xMo_6S_8$ system, with both rings (site A and site B) occupied by Cu ions at high temperature leading to the rhombohedral structure. However, at lower temperatures, the Cu ions are found in positions which are very close to the inner ring (site A) with an empty outer ring leading to a triclinic modification of the structure.

The triclinic phase was also observed for $Cu_{1.8}Mo_6S_8$ ($2 \leq T_0 \leq 270$ K), [51] with two Cu atom positions per unit cell in the interstices, $Fe_2Mo_6S_8$ at $T_0 \cong 400$ K, [11] with Fe

atoms occupying equivalent inner rings sites, and $FeMo_6S_8$ at $T_0 \cong 100$ K, [108].

Table 4.2: Predicted principal distances and angles of Mo_6S_8, and $Mg_OMo_6S_8$ calculated within both the LDA and GGA compared with experimental distances.

Distances (Å)		Mo_6S_8		$Mg_OMo_6S_8$	
	Experiment.[3, 24]	LDA	GGA_{PBE}	LDA	GGA_{PBE}
$(Mo\text{-}Mo)_\triangle$	2.698	2.694	2.719	2.683	2.702
$Mo_\triangle\text{-}Mo_\triangle$	2.862	2.853	2.878	2.754	2.762
$(Mo\text{-}Mo)_{intercluster}$	3.084	3.006	3.104	3.067	3.190
Mo-S(2)	2.439	2.408	2.418	2.388	2.418
Mo-S(1)	2.426	2.391	2.424	2.393	2.424
S(1)	2.431	2.395	2.424	2.403	2.429
S(1)	2.460	2.417	2.436	2.463	2.486
$[Mo\text{-}S(1)]_{intercluster}$	2.425	2.378	2.422	2.439	2.496
$S(2)\text{-}S(2)_{diagonals}$ via Mo_6	6.155	6.067	6.090	5.912	5.973
$S(2)\text{-}S(2)_{diagonal}$ via origin	4.724	4.655	4.796	4.821	4.825
S(1)-S(2)-S(1) angle (°)	85.94	85.87	86.46	88.54	88.80
Mg-S(2)	-	-	-	2.410	2.413
Mg-Mo(1)	-	-	-	4.503	4.536
Mg-S(1)	-	-	-	5.261	5.286

We have also observed a similar phase transition in all the other structures (see Table. 4.1) where Mg occupies site A or B for $x = 1$, and both sites for $x = 2$. The volume increases as the concentration increases from $x = 0$ to 2. At $x = 2$, the volume is largest when each Mg atom occupies two site B positions ($Mg_{2B}Mo_6S_8$), decreases when the two Mg atoms occupy both site A and site B ($Mg_{AB}Mo_6S_8$) and is smallest for $Mg_{2A}Mo_6S_8$.

Although the origin cavity, along the $\overline{3}$-symmetry, appears to be too large for small atoms, we nevertheless considered a model with Mg inserted at the origin. The predicted LDA parameters for the rhombohedral $Mg_OMo_6S_8$ with Mg at the origin are $a_R = 6.367$ Å and $\alpha_R = 91.52°$, an increase by 0.3% and 0.1%, respectively, compared to the predicted lattice parameters for Mo_6S_8. The equilibrium volume is predicted to be $V_R = 257.784$ Å^3, an increase of 0.9%. The hexagonal $Mg_OMo_6S_8$ lattice parameters $a_H = 9.122$ Å and $c_H = 10.73$ Å predicted a small increase in the basal plane and almost no variation along the c-axis, probably confirming the relatively large size of cavity 1 for Mg. Increasing a_H caused the c/a ratio to decrease by 0.3%, a trend observed for $LiMo_6S_8$ [17], where

$c/a = 1.161$. The GGA results also predicted increments of 0.36%, 0.67%, and 1% for a_R, α_R, and V_R, respectively in comparison with the predicted lattice parameters for Mo_6S_8 with a notable decrease in the c_H lattice parameter.

4.1.3 Interatomic and intercluster distances and their variation with Mg position.

Table 4.2 shows the interatomic and intercluster distances of Mo_6S_8 and their variation with Mg position. We predicted, well within the LDA error margin, the reported experimental internal parameters for Mo_6S_8, a metastable compound only obtained by deintercalation using a ternary compound such as $Cu_2Mo_6S_8$ or $Ni_2Mo_6S_8$ [24]. Notably the GGA overestimated the internal parameters by a small margin with the exception of the Mo-S(1) and Mo-S(2) distances which are underestimated but are very close to the experimental values. Mg insertion introduces distortion of the Mo_6S_8 structure in the $Mg_OMo_6S_8$ compound. The LDA calculated distances generally increase upon inserting Mg in Mo_6S_8. The Mo-S(2) distance of 2.408 Å increases by 0.6% and the intercluster Mo-S(1) distance of 2.378 Å increases by 2.5%. The Mo-S(1) distances of 2.391 Å, 2.395 Å and 2.417 Å, where S(1) is one of the eight triply bridging sulfur atoms capping each Mo octahedron face (see Fig. 4-2), increase by $(1.4 - 1.7)\%$. The S(1)-S(2)-S(1) angle predicted by both the LDA and GGA show an increase from 85.87° to 88.54° and 86.46° to 89.1°, respectively.

It is known that intercalation of Cu in $Cu_xMo_6S_8$ leads, via parallel electron transfer, to reduced Mo-Mo distances [23]. LDA and GGA predictions in $Mg_OMo_6S_8$ show a decrease in both the $[\mathrm{Mo}(1) - \mathrm{Mo}(1)]_\triangle$ intratriangle and the $\mathrm{Mo}(1)_\triangle$-$\mathrm{Mo}(1)_\triangle$ intertriangle distances. A notable exception occurs with the first distance between two molybdenum atoms belonging to the same triangular plane, perpendicular to the ternary $(\overline{3})$ axis, which decreases by $\sim 0.5\%$, while the second distance between two adjoining triangular planes in the same cluster decreases by $\sim 3\%$. The distance between Mg and Mo of 4.503 Å is large enough to exclude direct bonding; hence the cluster Mo_6S_8 can be regarded as

a pseudoatom acting as an electron acceptor.

If one compares analogous distances between the binary Mo_6S_8 and $Mg_AMo_6S_8$ (see Table 4.3), the Mo-Mo distances decrease by $(0.5 - 1)\%$. This decrease corresponds to an anisotropic contraction of the Mo_6 octahedron. The Mo cluster of the rhombohedral compounds forms an elongated octahedron of symmetry $\overline{3}$, while the Mo octahedron of the present structure is triclinically distorted. The S(2)-S(2) diagonal distance via the Mo_6 cluster decreases by 1.6%. The bond and intercluster contact distances of the triclinic $Mg_AMo_6S_8$ modification have small, though varying, differences from those of the rhombohedral $Mg_OMo_6S_8$. The cell volume at the rhombohedral-to-triclinic phase transition increases by 2.6 Å^3.

Table 4.3: Calculated interatomic distances for rhombohedral $Mg_OMo_6S_8$ and triclinic $Mg_AMo_6S_8$ compared with $LiMo_6S_8$.

Distances (Å)	$Mg_OMo_6S_8$	$Mg_AMo_6S_8$	$LiMo_6S_8$ [17]
$(\text{Mo-Mo})_{\triangle}$	2.683	2.682	2.688
$\text{Mo}_{\triangle}\text{-Mo}_{\triangle}$	2.754	2.741	2.821
$(\text{Mo-Mo})_{intercluster}$	3.067	3.117	3.133
Mo-S(2)	2.388	2.417	2.429
Mo-S(1)	2.393	2.389	2.402
S(1)	2.403	2.413	2.448
S(1)	2.463	2.453	2.455
$[\text{Mo-S(1)}]_{intercluster}$	2.439	2.454	2.474
$\text{S(2)-S(2)}_{diagonals}$ via Mo_6	5.912	5.969	-
M-S(2)	2.401	4.702	2.005
S(2)	-	3.851	2.985
M-S(1)	5.261	2.543	2.407
S(1)	-	5.587	2.888
S(1)	-	-	2.295
M-Mo(1)	4.503	3.453	3.608

Table 4.3 shows the interatomic distances for rhombohedral $Mg_OMo_6S_8$ and triclinic $Mg_AMo_6S_8$ compared with $LiMo_6S_8$. Our results are in good correspondence with those of structural investigation reported on $Li_xMo_6S_8$ [17]. All interatomic distances have values that are typical for Mo sulphides: Mo-S, 2.35 Å (MoS_2) and $2.36 - 2.57$ Å (Mo_2S_3); S-S, $3.31 - 3.55$ Å (Mo_3S_4) [23]; and Mo-S, 2.46 Å [$LiMoS_2$ [235] and $M\text{Mo}_2\text{S}_4$, $M =$

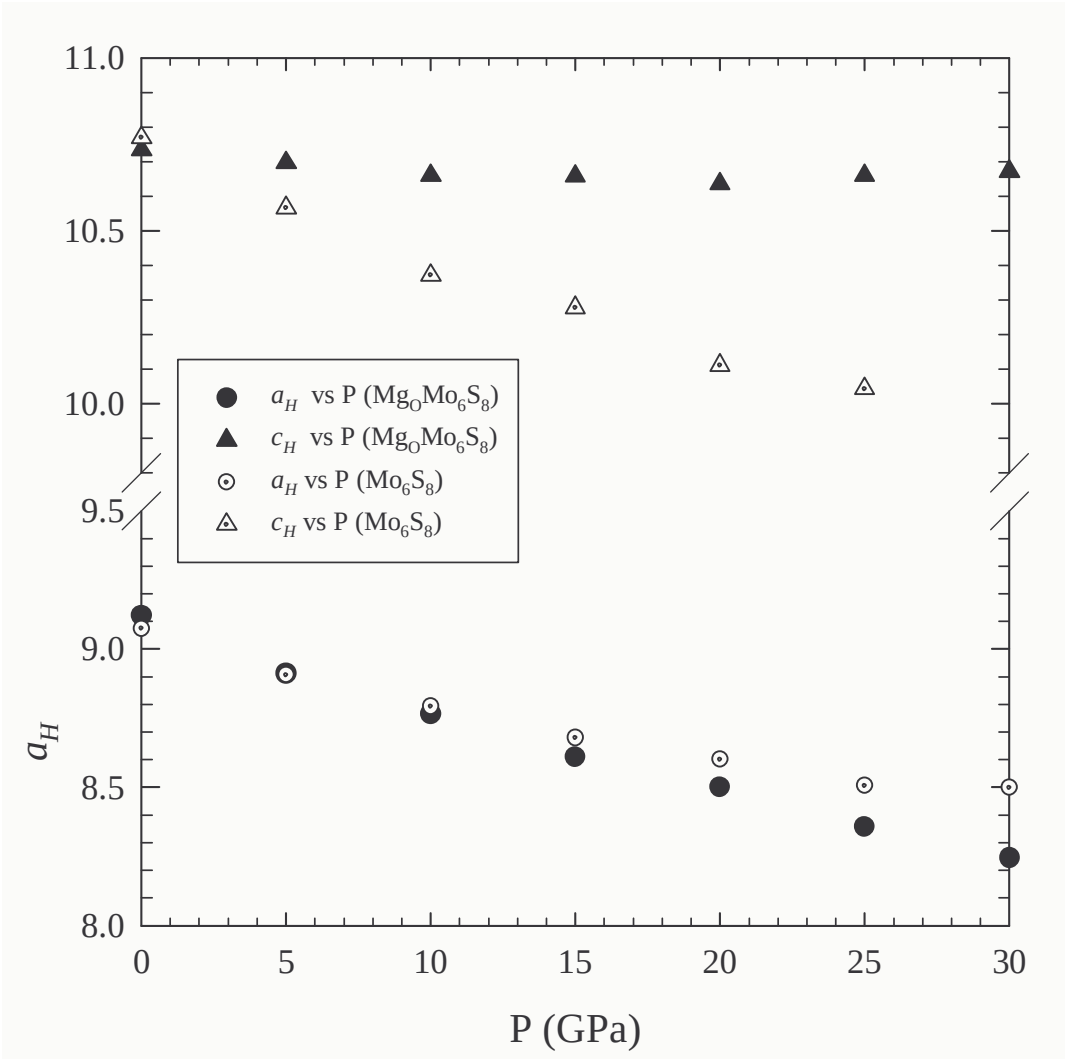

Figure 4-3: Hexagonal lattice parameters a_H (in Å) and c_H (in Å) variation with pressure for Mo_6S_8 and $Mg_OMo_6S_8$.

Fe or Co [237]]. The Mo-Mo distances in pure metal are 2.72 Å and 2.85 Å in Mo_2S_3, 2.91 Å in $LiMoS_2$, [235] and 2.89 Å and 2.90 Å in $M Mo_2S_4$: M = Fe, Co [237]. Mg in $Mg_A Mo_6S_8$ is coordinated by four S atoms with the Mg-S distance ranging from 2.5 to 5.5 Å. The Mg sulphide interatomic distances correspond well with Mg-S, 2.011 Å in $MgS_2O_3 \cdot 6H_2O$, [238] for Mg-S(2). The cell constant for the cubic (rocksalt) structure of MgS has been reported as 5.201 Å, 5.2036 Å, 5.1913 Å, and 5.2018 Å [239] and for the zincblende phase at about 5.66 Å, [240] such that the Mg-S bond distance is $\sim$ 2.6 Å and 4.6 Å, respectively, the latter comparing closely with the Mg-S(2) distance of 4.7 Å. The small Mg coordination number may be responsible for the weak Mg-S hybridization.

4.1.4 Equation of State and Pressure Dependence of Lattice Parameters (Mo_6S_8 and $Mg_x Mo_6S_8$)

We have calculated the volume of Mo_6S_8 and $Mg_x Mo_6S_8$ as a function of pressure. The internal energy of Mo_6S_8 and $Mg_O Mo_6S_8$ have been calculated at experimental (for Mo_6S_8) and predicted (for $Mg_O Mo_6S_8$) volumes corresponding to pressures from 0 to 30 GPa. At a given volume, the position of the atoms are determined by minimizing the forces on the ions, and the unit cell edges by equalizing the stress on the cell. It should be noted that our calculations are done at $\sim$ 0K, hence some caution is necessary when making a comparison with experimental data.

Figure 4-3 shows our calculated pressure variation of the hexagonal lattice parameters a_H and c_H of Mo_6S_8 and $Mg_O Mo_6S_8$. The lattice parameter a_H responds near linearly to increasing pressure for both Mo_6S_8 and $Mg_O Mo_6S_8$ and becomes nonlinear above $\sim$ 10 GPa. In addition the a_H value for $Mg_O Mo_6S_8$ reduces more rapidly than that of Mo_6S_8, which is more apparent above 10 GPa. The lattice parameter c_H for $Mg_O Mo_6S_8$ is linear up to 10 GPa, and becomes near constant up to 30 GPa. Similarly c_H for Mo_6S_8 is linear to 10 GPa, however it decreases substantially above 10 GPa. The plot of $Mg_O Mo_6S_8$ is relatively flat when compared to that of Mo_6S_8 hence the presence of Mg at the origin renders the structure almost incompressible in this direction.

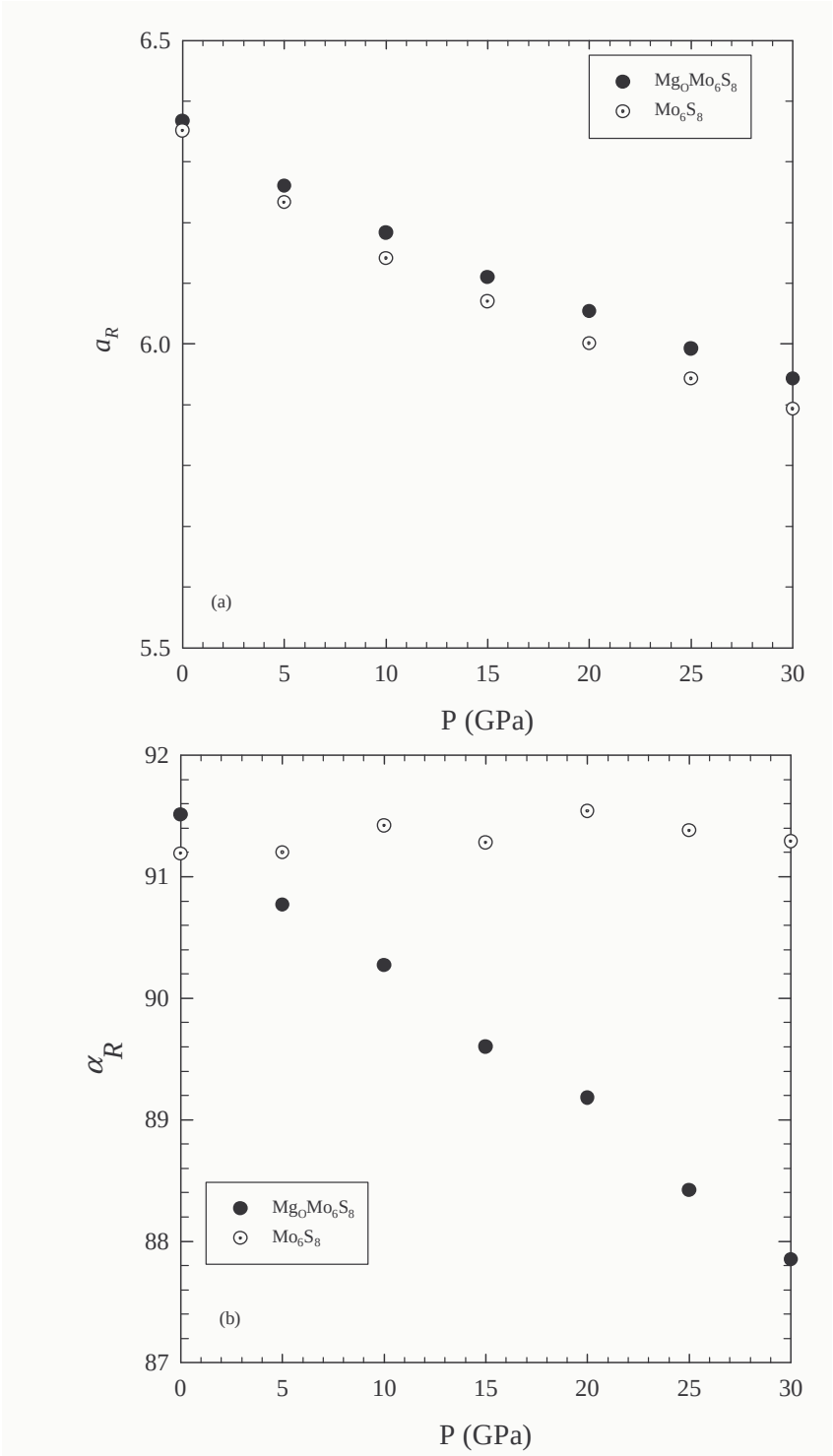

Figure 4-4: Rhombhohedral lattice parameters a_R (in Å) and α_R (○) variation with pressure for Mo_6S_8 and $Mg_OMo_6S_8$.

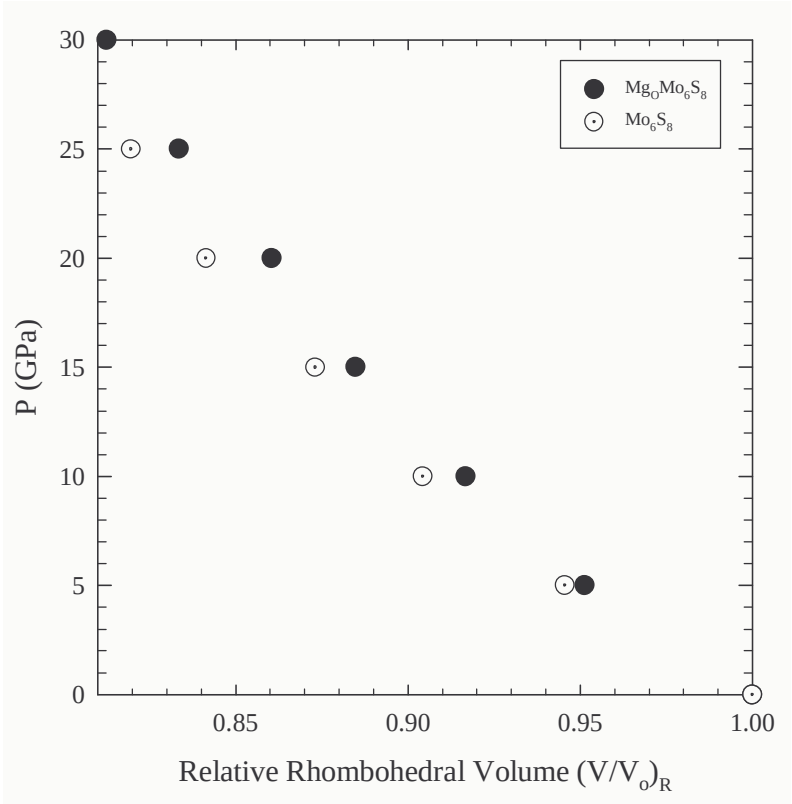

Figure 4-5: Relative rhombohedral volume variation with pressure for $Mg_OMo_6S_8$ and Mo_6S_8.

Figure 4-4 shows the rhombohedral lattice parameters α_R and a_R of Mo_6S_8 and $Mg_OMo_6S_8$ as a function of pressure. There is a decrease of $\sim 7\%$ and $\sim 4\%$ in the lattice parameter and the rhombohedral angle respectively. The lattice parameter a_R responds almost linearly to increasing pressure for both Mo_6S_8 and $Mg_OMo_6S_8$ up to 10 GPa and a curvature is shown above this pressure. The lattice parameter for Mo_6S_8 decreases faster than that for $Mg_OMo_6S_8$. The rhombohedral angle a_R for $Mg_OMo_6S_8$ changes linearly with pressure while remaining almost constant or flat for Mo_6S_8.

The variation of the pressure with relative volume change ($\Delta V/V_0$) (see Figures 4-5 and 4-6) is analysed in terms of the Murnaghan equation of state (see Appendix G) and the values derived for the bulk modulus and its first pressure derivative are considered.

The lattice constants and equilibrium unit cell volumes V_0 are found by minimizing the total energy E per cell as a function of the cell volume:

$$\left(\frac{\partial E}{\partial V}\right)_{V_0} = 0. \tag{4.1}$$

More generally,

$$P = -\left(\frac{\partial E}{\partial V}\right)_V \tag{4.2}$$

is the pressure at volume V. The pressure can be calculated from the slope of the $E(V)$ curve as:

$$P(V) = \frac{B}{B'}\left[\left(\frac{V_0}{V}\right)^{B'} - 1\right], \tag{4.3}$$

with the bulk modulus of elastic stiffness given by

$$B = -V\left(\frac{\partial P}{\partial V}\right)_V. \tag{4.4}$$

Table 4.4: First- and second-order axial compression coefficients of Mo_6S_8 and $Mg_OMo_6S_8$. B^{-1} is the linear compressibility at zero pressure and B' is the pressure derivative of B.

	B	B_c (GPa)	B_a (GPa)	B'_c	B'_a
Mo_6Se_8 [44]	35.46				
Mo_6S_8	81.368	280.992	224.412	3.680	17.873
$Mg_OMo_6S_8$	96.945	167.618	220.679	617.356	5.789
$Pb_{1.0}Mo_6S_8$ [44]	30.64				

We calculated the bulk modulus and its first pressure derivative from ~ 0 K compressibility measurement for Mo_6S_8 and $Mg_xMo_6S_8$. Parameters of EOS are collected in Tables 4.4 and 4.5. V_0 is the volume at 0 GPa, B, the bulk modulus at 0 GPa, and B', the first pressure derivative of B. Table 4.4 also shows the calculated linear moduli (B_a and B_c) for Mo_6S_8 and $Mg_OMo_6S_8$. Fitting was performed so that the deviations of the volume calculated through geometry optimization from the equation of state are

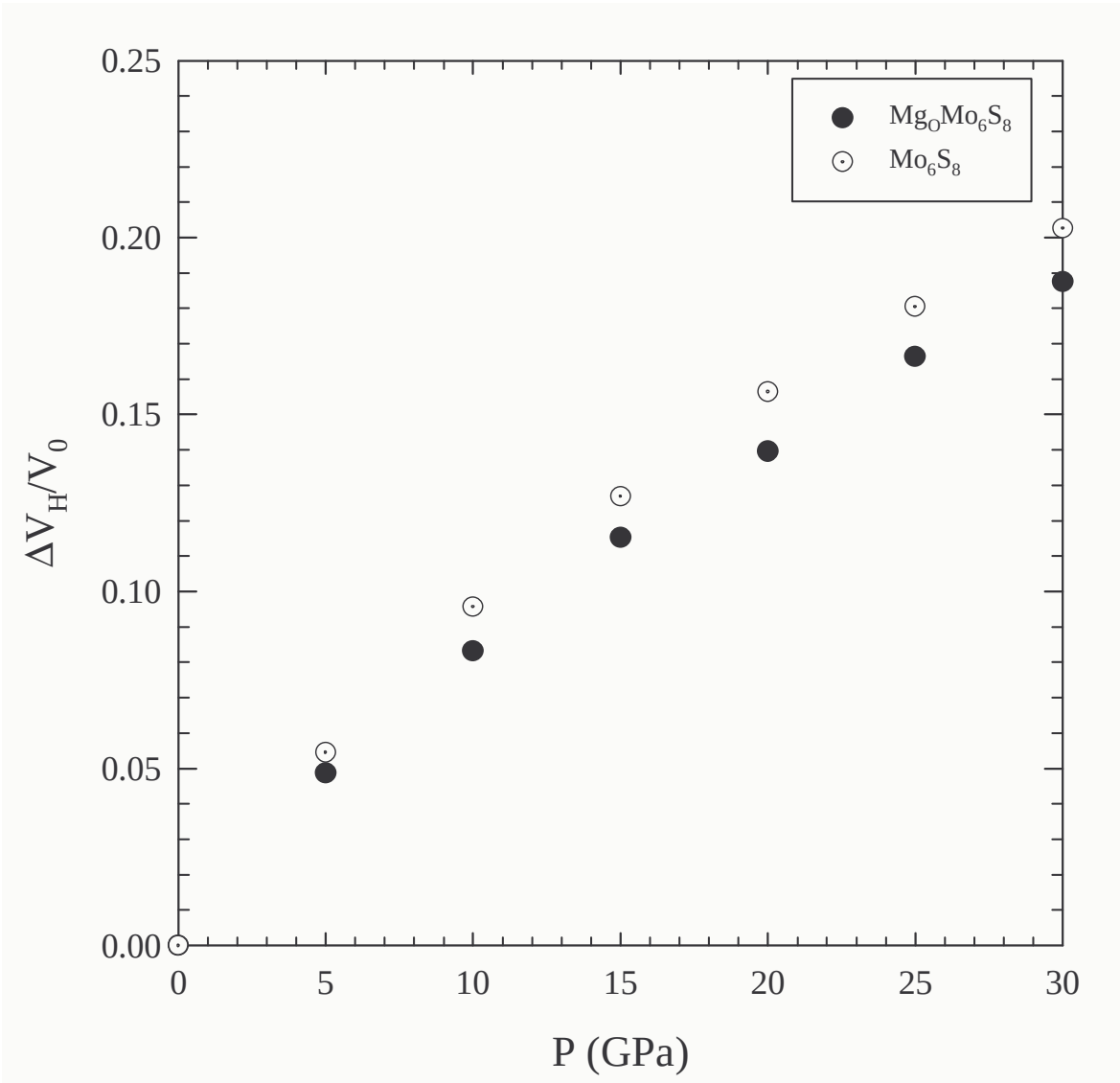

Figure 4-6: The relative compression of Mo_6S_8 and $Mg_OMo_6S_8$.

minimized. It should also be noted that B was evaluated at the theoretical volume V_0, which can be the main source of error in the theoretical bulk modulus.

In order to compare the bulk moduli along the c-axis and the a-axis, we only considered the rhombohedral or hexagonal structures, Mo_6S_8 and $Mg_OMo_6S_8$. The result of fitting done for the Mo_6S_8 and $Mg_OMo_6S_8$ curves (see Figures 4-5 and 4-6) with equation 4.3 showed that the bulk modulus along the c-axis, B_c, tends to decrease by approximately 40% on intercalation of magnesium into Mo_6S_8, while we observe a negligible decrease of 1.7% along the a-axis. Extremely high values of $B_c^{'} = 617.356$ for $Mg_OMo_6S_8$ and $B_c^{'} = 17.873$ for Mo_6S_8, seem to be unrealistic and does not represent a real compression. The bending around $15 - 20$ GPa observed in the compression curve of Mo_6S_8 reflects that the bulk modulus of this compound could change. Mo_6S_8 in more compressible than $Mg_OMo_6S_8$ and the compressibility increases markedly with increasing pressure. As the applied pressure increases, the bulk modulus rises very rapidly due to the exceptional values of $B^{'}$.

Due to a lack of experimental data, we also compare the moduli with the experimental values of Mo_6Se_8 and $Pb_{1.0}Mo_6S_8$ respectively. Rather low values of B were found, combined with exceptionally large values of $B^{'}$. These results all served to heighten the sense of anomaly found in this family of compounds. This anomaly has been earlier observed by Webb *et al.* [44] for a number of superconducting ternary molybdenum sulphides and selenides. The decrease in sensitivity to external pressure or a stiffening of the crystal lattice, was reported to be reflected in the predominant large depression of T_c with pressure. The $B^{'}$ values found for the Chevrel phase materials Mo_6Se_8 (2.35), $Pb_{1.0}Mo_6S_8$ (4.53), $Cu_{2.0}Mo_6S_8$ (5.73),$Yb_{1.0}Mo_6S_8$ (1.84), $Cu_{1.4}Mo_6Se_8$ (3.52) and $Yb_{1.0}Mo_6Se_8$ (1.68) are very large compared to the largest reported [44] values for the elements.

Figure 4-7 shows the calculated hexagonal c/a -ratio of Mo_6S_8 and $Mg_OMo_6S_8$ and its variance with pressure. The c/a values for $Mg_OMo_6S_8$ responds linearly to increasing pressure while there is evidently no response for Mo_6S_8 implying that its anisotropy ratio is unaffected by pressure. In an anisotropic crystal structure, one would expect

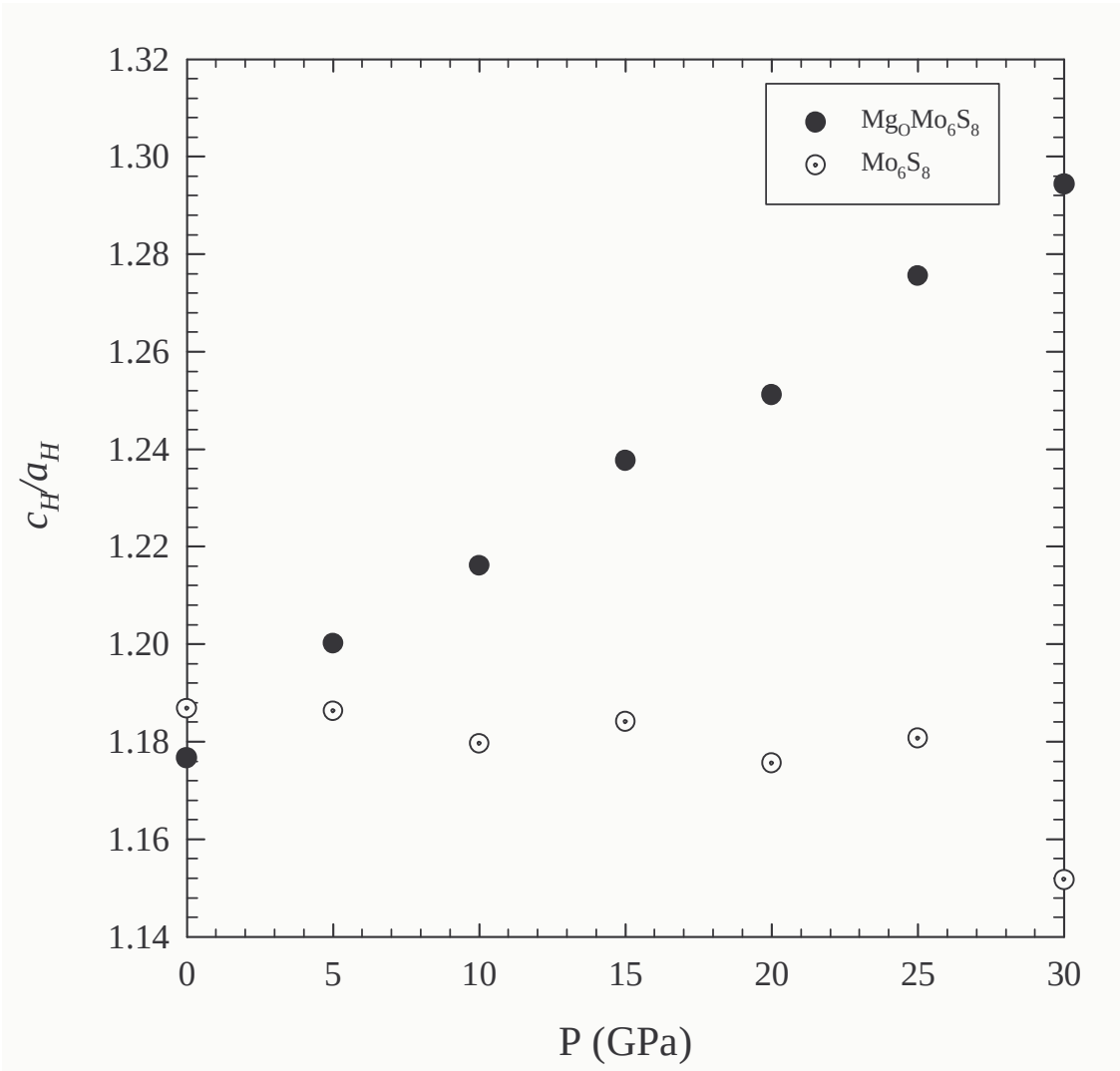

Figure 4-7: Calculated c_H/a_H ratio's variation with pressure for $Mg_OMo_6S_8$ and Mo_6S_8.

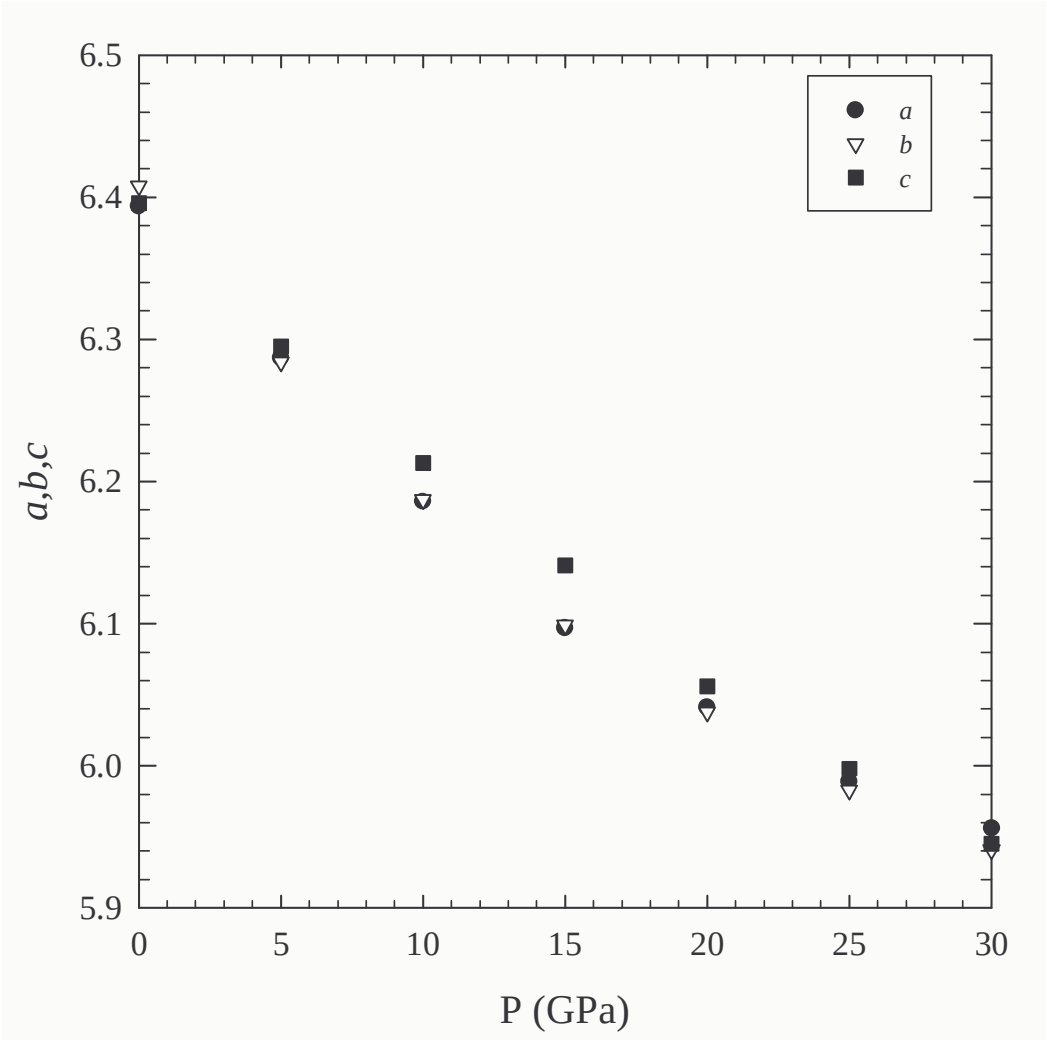

Figure 4-8: Triclinic lattice parameters (in Å) as a function of pressure for $Mg_AMo_6S_8$.

the compressibility parallel and perpendicular to a network of interconnecting channels running between the Mo_6S_8 clusters, to be very different. The linear plot for $Mg_OMo_6S_8$, wherein the channels containing the interstitial sites or cavities are occupied by Mg atom, signifies a uniform compression.

Figure 4-8 displays the comparison of the triclinic lattice parameters a, b and c as a function of pressure for $Mg_AMo_6S_8$. The lattice parameters c responds linearly to pressure while a and b responds almost similarly deviating at around $15 - 20$ GPa . Figure 4-9 shows the relative triclinic volume V/V_0 as a function of pressure for $Mg_AMo_6S_8$. The bulk modulus derived from Figure 4-9 and its first pressure derivative from ~ 0 K compressibility measurement for $Mg_AMo_6S_8$ are reported in Table 4.5 along with the values of $Cu_2Mo_6S_8$ [44]. The calculated value of the first pressure derivative B' (3.85) compares well with that of a lower concentrated $Cu_{1.4}Mo_6Se_8$ (3.52). Although $Mg_AMo_6S_8$ has a triclinic structure, we note an increase of $\sim 6\%$ in the total bulk moduli from that of hexagonal Mo_6S_8.

Table 4.5: Theoretical value of the bulk modulus B and its presure derivative of $Mg_AMo_6S_8$ in comparison with the experimental value for $Cu_2Mo_6S_8$ [44].

	B(GPa)	B'
$Mg_AMo_6S_8$	86.30	3.85
$Cu_2Mo_6S_8$ [44]	24.07	5.729

Interatomic and intercluster distances and their variation with pressure

Metastable Mo_6S_8 is said to be stabilized by the intercalated metal which through charge transfer modifies the distance between Mo atoms. Figure 4-10 shows LDA calculations of pressure variation of the principal distances in Mo_6S_8. We note that the Mo-Mo distances $[\mathrm{Mo}(1) - \mathrm{Mo}(1)]_\triangle$ intratriangle and the $\mathrm{Mo}(1)_\triangle$-$\mathrm{Mo}(1)_\triangle$ intertriangle decrease linearly and uniformly with increasing pressure. The decrease in this distances is also observed upon intercalation of Mg in Mo_6S_8, corresponding to an anisotropic contraction of the Mo_6 octahedron. Hence, we can expect Mo_6S_8 to stabilize at higher pressures. The molyb-

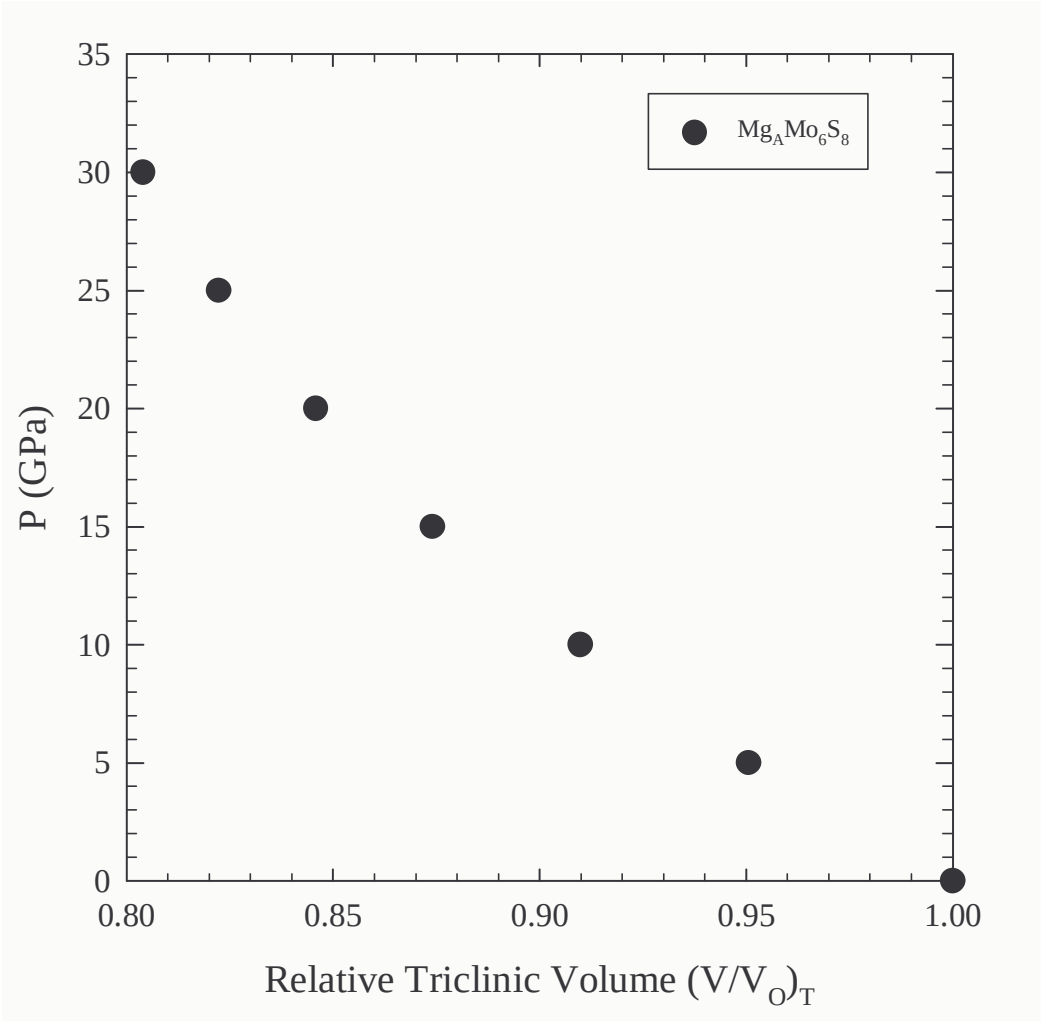

Figure 4-9: Relative triclinic volume (in Å^3) as a function of pressure for $Mg_AMo_6S_8$

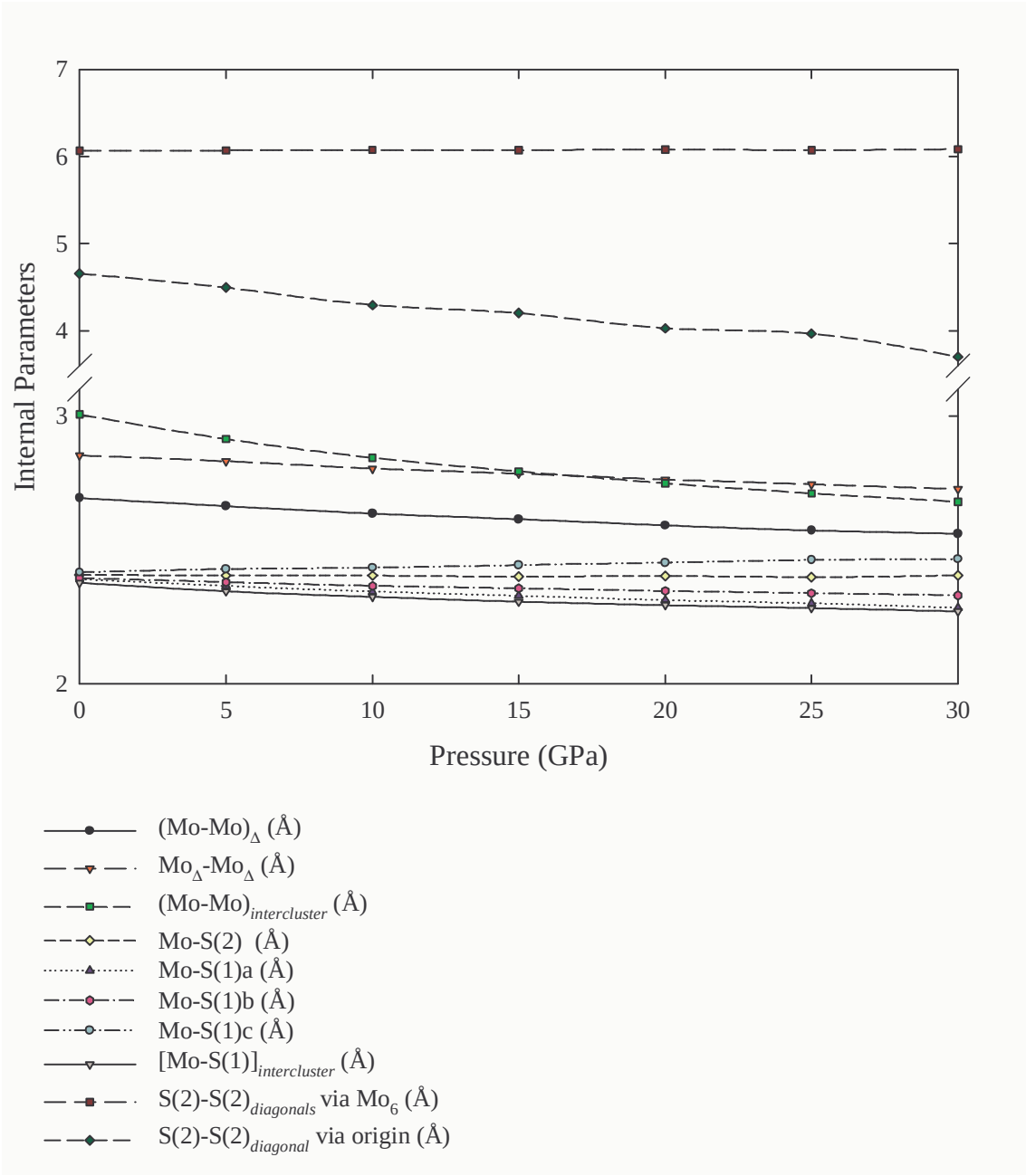

Figure 4-10: LDA calculations of pressure variation with the principal distances (in Å) for Mo_6S_8.

denum intercluster distances $(\mathrm{Mo}-\mathrm{Mo})_{intercluster}$, $[\mathrm{Mo}-\mathrm{S}(1)]_{intercluster}$ distances and the S(2)-S(2) diagonal distance via the origin decreases rapidly with increasing pressure.

Figure 4-11 shows LDA calculations of pressure variation of the principal distances in $\mathrm{Mg}_O\mathrm{Mo}_6\mathrm{S}_8$. We again notice a similar behavior in the $[\mathrm{Mo}(1)-\mathrm{Mo}(1)]_\triangle$ intratriangle and the $\mathrm{Mo}(1)_\triangle$-$\mathrm{Mo}(1)_\triangle$ intertriangle distances as the pressure increases. The is an upward swing at the applied pressure of 20 GPa, which appears in all plots for Mo interatomic distances within the cluster including the $[\mathrm{Mo}-\mathrm{S}(1)]_{intercluster}$ distance. This behavior was earlier observed for the bulk modulus at $15-20$ GPa suggesting a possible change in the bulk modulus. The Mo-S and S-S distances almost show no responses to increasing pressure.

4.2 Calculation of Voltage Curves and Structural Stability

4.2.1 Mg Battery System

The newly proposed rechargeable Mg-ion battery cells employ magnesium intercalation materials as their anode and cathode active materials. Special complex electrolyte solutions are used in which Mg electrodes behave reversibly. A solution comprising of tetrahydrofuran (THF) as the solvent and the $\mathrm{Mg}(\mathrm{AlCl}_2\mathrm{R}_2)_2$ (R=$\mathrm{CH}_3\mathrm{CH}_2^-$, $\mathrm{C}_4\mathrm{H}_9^-$) salt [241] is mostly used, although it was found that the initial insertion and final deinsertion of Mg-ion to/from the $\mathrm{Mo}_6\mathrm{S}_8$ compound is severely limited due to low Mg-ion conductivity caused by both low Mg-ion concentration and mobility. Novel polymeric gel electrolytes consisting of poly(ethylene oxide) - modified poly(methacrylate) (PEO-PMA) with magnesium imide $(\mathrm{Mg}[(\mathrm{CF}_3\mathrm{SO}_2)_2\mathrm{N}]_2$ has been recently investigated in rechargeable battery systems [242].The key issues in the development of rechargeable Mg batteries is obtaining a reversible Mg negative electrode and an appropriate nonaqueous media that effectively conduct Mg^{2+} species. Our present focus is on the prediction of the "site energy" of Mg

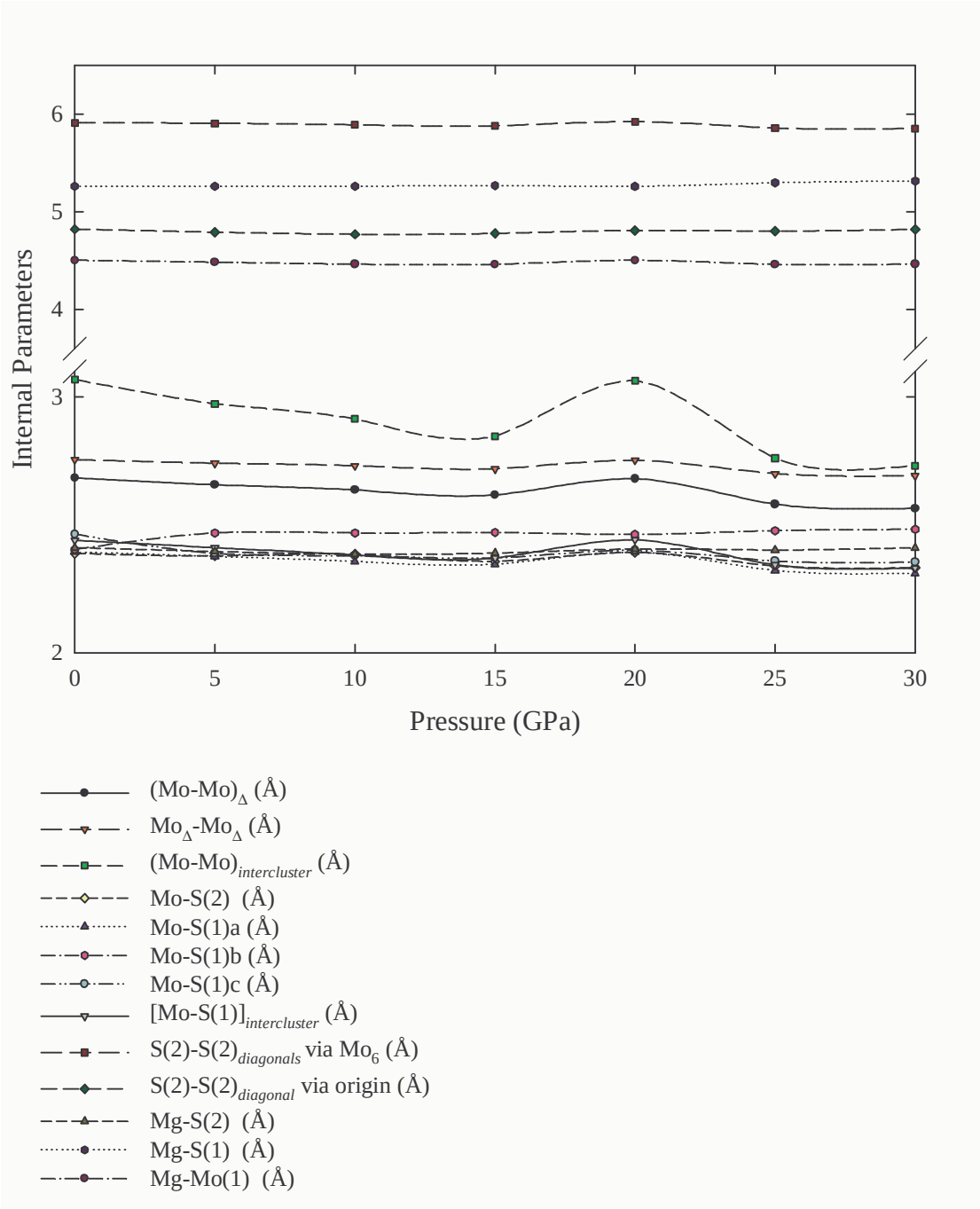

Figure 4-11: LDA calculations of pressure variation with the principal distances (in Å) for $Mg_OMo_6S_8$.

in Mo_6S_8.

4.2.2 Energies and cell voltages for $Mg_xMo_6S_8$ $(0 \leq x \leq 2)$

Table 4.6: Calculated E^{tot} for Mo_6S_8, Mg_{metal}, $MgMo_6S_8$, $Mg_AMo_6S_8$, $Mg_BMo_6S_8$, and $Mg_{AB}Mo_6S_8$ systems.

	Total energy, E^{tot} (eV)	$\triangle E$ (eV)
Mg_{metal}	-1947.012	-
Mo_6S_8	-13851.641	-
$Mg_OMo_6S_8$	-14827.188	-2.03
$Mg_AMo_6S_8$	-14827.366	-2.22
$Mg_BMo_6S_8$	-14827.374	-2.23
$Mg_{2A}Mo_6S_8$	-15802.625	-1.99
$Mg_{AB}Mo_6S_8$	-15802.458	-1.91
$Mg_{2B}Mo_6S_8$	-15802.450	-1. 90

The electrochemical topotactic redox reactions can be summarized as follows:

$$x\mathrm{Mg}^{n+} + nxe^- + \mathrm{Mo_6S_8} \iff (\mathrm{Mg}^{n+})_x \left[\mathrm{Mo_6S_8}\right]^{nx-}.$$

The negative excess charge in $[Mo_6S_8]^{2x-}$ is compensated by the simultaneous uptake of the mobile Mg^{2+} cation, which occupies empty sites in the lattice channels. Table 4.6 reports the calculated total energies E^{tot} for the host Chevrel phase Mo_6S_8; metallic magnesium Mg_{metal}; and the intercalate compounds $Mg_OMo_6S_8$, $Mg_AMo_6S_8$, $Mg_BMo_6S_8$, and $Mg_{AB}Mo_6S_8$. From these we calculate the value of $\triangle E$ for the intercalation reaction, which is given by:

$$\triangle E = E^{tot}_{\mathbf{Mg_xMo_6S_8}} - (E^{tot}_{\mathbf{Mo_6S_8}} + E^{tot}_{\mathbf{Mg}_{metal}}). \tag{4.5}$$

Comparison of the energies from Table 4.6 clearly shows that Mg preferential positions are the two sixfold crystallographic positions (sites A and B), away from the origin position such as in $Mg_OMo_6S_8$. These positions are indeed expected distributions for small ions in the Chevrel phases. When comparing the geometrical arrangement of inner

and outer Mg sites from the $Mg_1Mo_6S_8$ transition to $Mg_2Mo_6S_8$, noticeable changes in the site energy are observed. The occupation of the inner Mg_A site, for $x = 2$, close to the unit-cell origin seems preferable while for $x = 1$, site A or B will be equally occupied. Using the values given in Table 4.6, we obtain an average value of about -2.00 eV for $\triangle E_{LDA}$ for $x = 1$. This result can be compared with experimental data of Aurbach *et al.* [2], who report a value of ~ 2 V. The agreement between theory and experiment is gratifying. This result can be compared with experimental data per Mg for intercalation of Mg from the liquid phase into Mo_6S_8; the heat of fusion of magnesium (0.0928 eV), which is the heat required to convert a solid phase metallic magnesium into a liquid phase with no temperature change, is added to the value to give corrected value of 2.09 eV.

Table 4.7: Total ground state energy E^{tot} for Li_{metal}, Mo_6S_8, and $Li_1Mo_6S_8$ unit-cell systems.

	Total energy, E^{tot} (eV)	$\triangle E$ (eV)
Li_{metal}	-187.98	
Mo_6S_8	-13851.28	
$LiMo_6S_8$	-14041.47	-2.20

Lithium insertion compound $Li_xMo_6S_8$ $(0 < x < 1)$ with lithium occupying sites on the $\overline{3}$ axis (cavity 1, see Fig. 4-2) has a site energy (the energy to remove a lithium atom from lithium metal and place it into these sites) of 2.41 eV [13]. To obtain ΔE for the intercalation reaction using the values given in the Table 4.7, we write:

$$E^{tot}_{\mathbf{Li}_x\mathbf{Mo}_6\mathbf{S}_8} - (E^{tot}_{\mathbf{Mo}_6\mathbf{S}_8} + E^{tot}_{\mathbf{Li}_{metal}}) = \triangle E. \tag{4.6}$$

Our calculated value of 2.20 eV for ΔE can be compared with the experimental data of McKinnon *et al.* [13], who report a value of 2.41 eV per lithium for the intercalation of Li from the liquid phase into Mo_6S_8; when corrected for the heat of fusion of lithium, we obtain -2.23 eV which compares well with our calculated value. This result supports the accuracy of our earlier calculation in $MgMo_6S_8$ and the reliability of such calculations to be used in determining the contribution of the anode and cathode processes to the cell

voltage. Hence they may be used to predict new materials with enhanced energy storage capability.

4.3 Electronic Properties

4.3.1 Electronic Description

Bonding in the Chevrel-phase compounds has been described as both ionic and covalent in character. Strong covalent bonding occurs between the six Mo atoms in the Mo_6S_8 cluster, whereas predominantly ionic interaction exists between the metal cations M_x and the highly electronegative Mo_6S_8 clusters. Molybdenum in Mo_6S_8 is reduced to the oxidation state III (d^3) forming Mo_3 triangles in the Mo_6 octahedron. As a result of the D_{4h} point-group symmetry at the Mo sites, the Mo $4d$ bands can be subdivided into four sub-bands, each of which possesses a distinct orbital energy: $E_d(x,\ y)$, $E_d(yz,\ zx)$, $E_d(x^2$-$y^2)$, and $E_d(3z^2$- $r^2)$. The S atom point symmetry is O_h hence the single orbital energy can be described as the S $3s$ or $3p$ manifold. In the case of $X =$ Se, Te the charge density of states of these ions seems to be less than -2 (i.e., more positive), leading therefore to an increased number of conduction d electrons per Mo_6X_8 cluster and shifting the Fermi level to a higher value [112].

Metastable Mo_6S_8 is an electron deficient compound containing four holes in the conduction band. The metal element plays an important role to stabilize the whole structure. It modifies the distances between the Mo atoms due to charge transfer from the metal atoms to Mo or S atoms. The maximum charge transfer is predicted to be four (4) electrons per Mo_6S_8 cluster, which results in the maximal insertion of four monovalent cations Li^+ or two divalent cations Mg^{2+}. Mg can be inserted electrochemically into Mo_3S_4 up to a stoichiometry of $Mg_xMo_3S_4$ ($x = 1$) [2]. Compounds containing divalent metal cation such as Mg^{2+} carry a formal charge of 22 electrons which corresponds to two holes in the conduction band. No calculations have been published for magnesium ions, as far as we know.

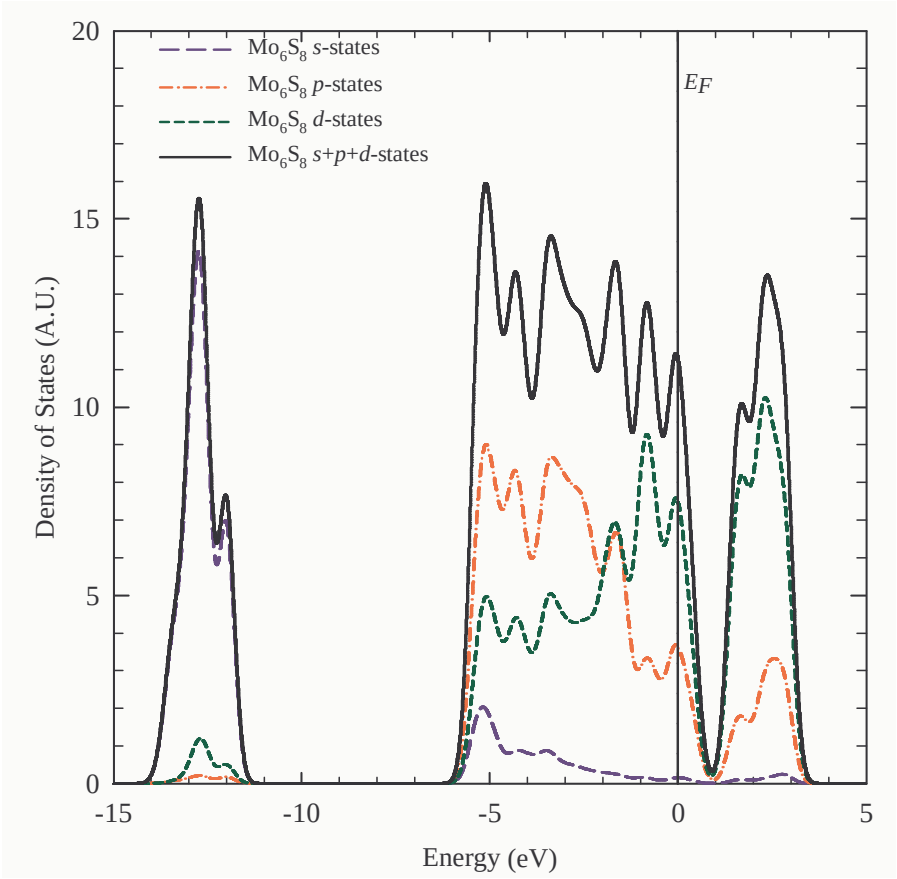

Figure 4-12: The total density of states (DOS) of the Mo and S *s, p, d* levels in Mo_6S_8. The Fermi level (E_F) is set at zero.

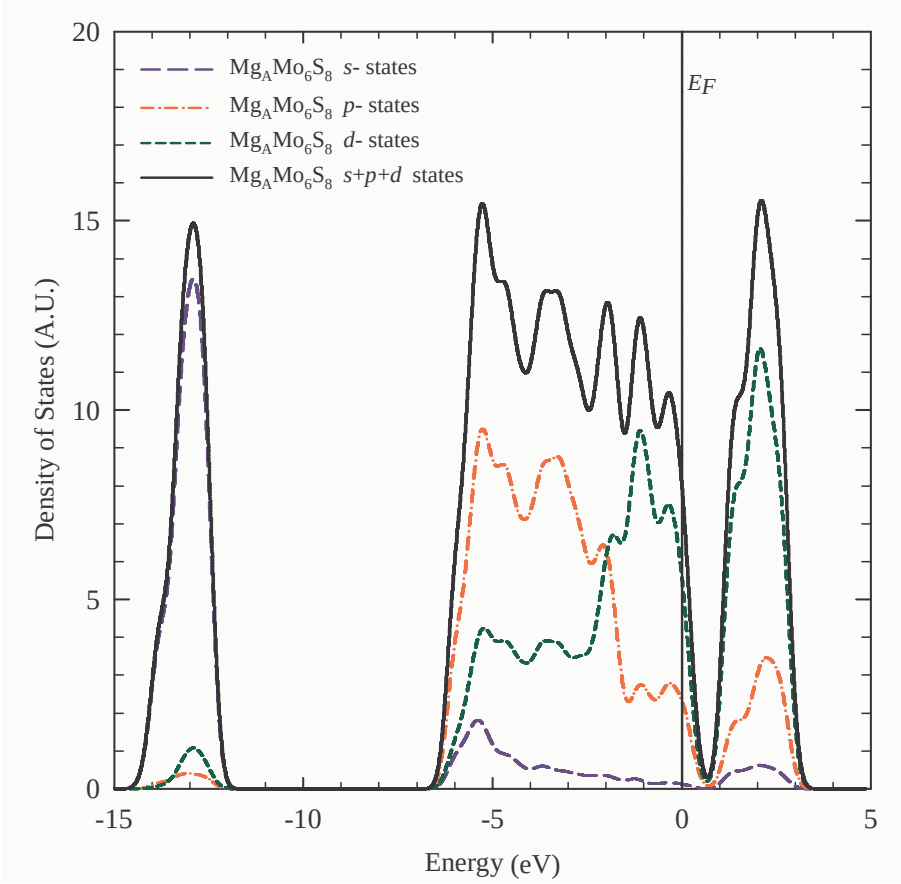

Figure 4-13: The total density of states for $Mg_AMo_6S_8$. The Fermi level (E_F) is set at zero.

4.3.2 Density of States (DOS) of $M_x^{n+}Mo_6X_8$

The calculated densities of states are shown in Figures 4-12 and 4-13 for Mo_6S_8 and $MgMo_6S_8$ respectively, and they are consistent with previous reports on other Chevrel-phase compounds [32, 33, 34, 35, 36, 37]. The total DOS for Mo_6S_8 is shown in Figure 4-12 where the main electronic contribution at the Fermi level is due to the t_{1u} and e_g molecular orbitals, of (x^2 - y^2) and z^2 local character. The latter orbital points toward the apical S atoms of a nearby cluster, while the former is of δ-symmetry and presents almost no overlap with neighboring units. The Mo (x^2 - y^2) molecular orbitals situated at the Fermi level (E_F) are confined within the cluster and do not hybridize with the

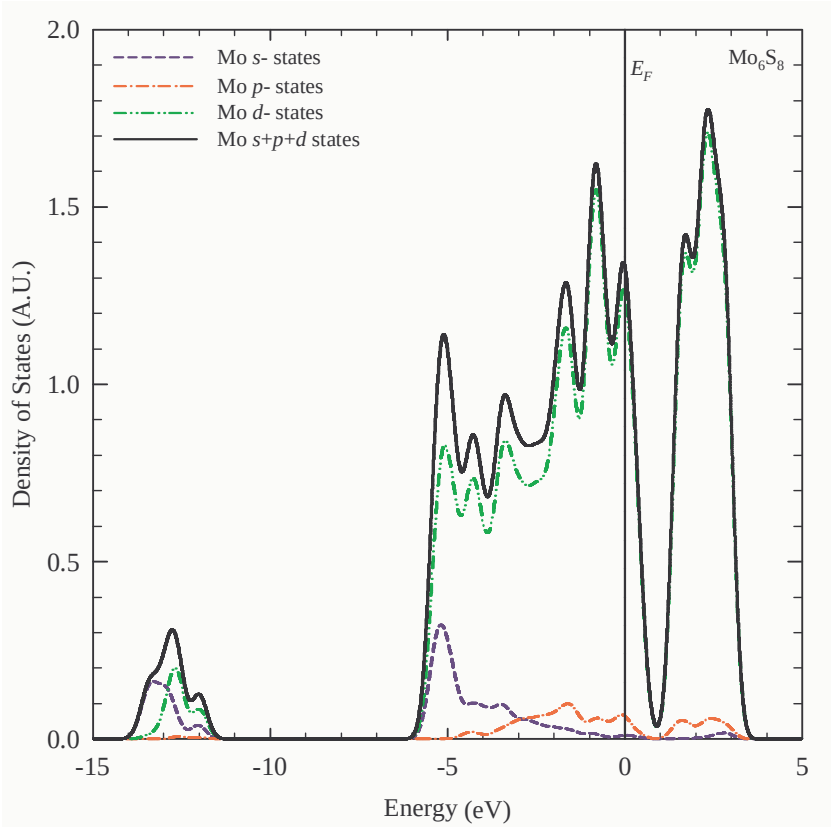

Figure 4-14: The partial density of states of Mo_6S_8 showing the s, p, and d -states of molybdenum (Mo) atoms. The Fermi level is set at zero.

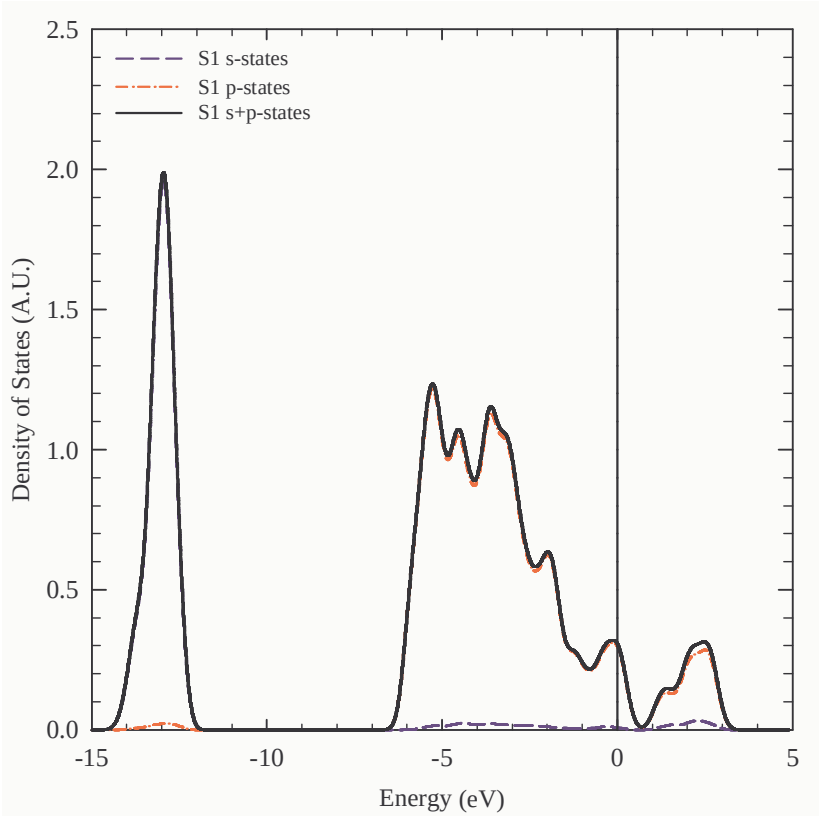

Figure 4-15: The partial density of states showing the s and p -states of sulfur (S1) in Mo_6S_8.

chalcogen p-orbitals. There is a high density of states (DOS) near the Fermi level mainly due to flatbands of Mo $4d$ character. This is clearly illustrated in Figure 4-14.

The density in the valence band, just below the Fermi level, is predominantly made up of the overlap (covalent mixing) between the Mo $4d$ and S $3p$-states (see Figs. 4-15 and 4-16). The S $3p$-states contributes less as the energy increases. The S s-states contributes minimally within this region but are dominant at the lower part of the valence band. The destabilization of the Mo $4d$ level in the conduction band is responsible for the non vanishing DOS in the "gap" area above the Fermi level (see Fig. 4-14). Two out of five d orbitals for each Mo atom are affected by the $pd\delta$ bonding (for the xy face they are xy and $3z^2 - r^2$). The total number of electrons in the pd states in Mo_6S_8 is

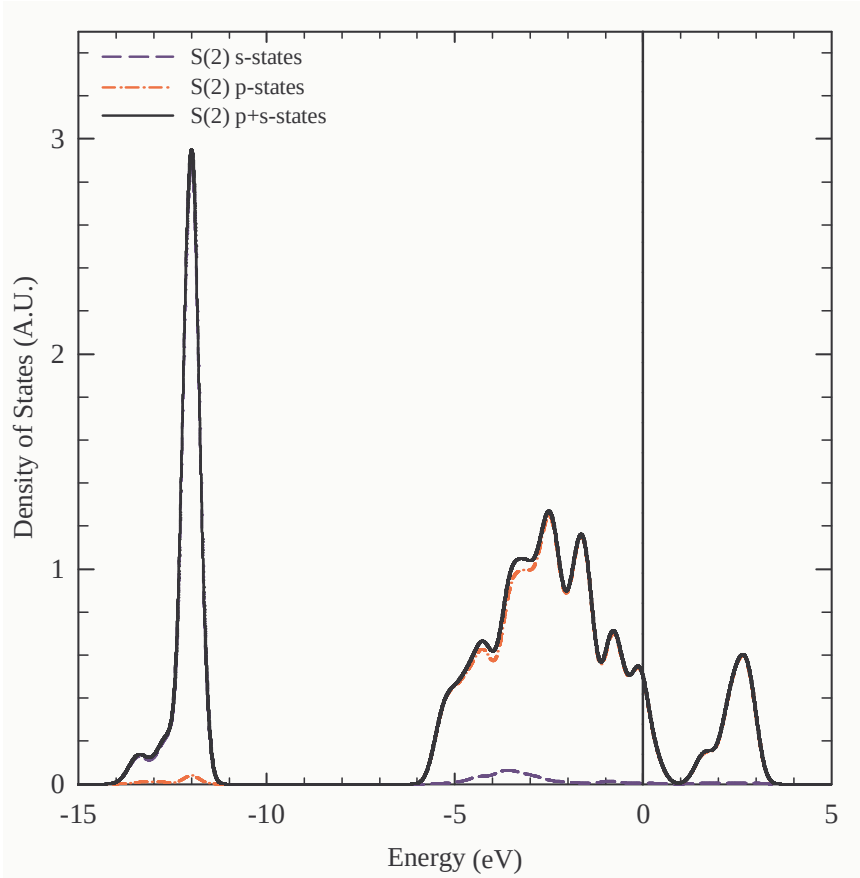

Figure 4-16: The partial density of states showing the s and p -states of sulfur (S2) in Mo_6S_8.

$8 \times 4 \times 6 \times 6 = 68$, 4 electrons short of reaching the gap. Thus, introducing two electrons in the system should make it metallic, and then the states of the bottom of the gap should be mostly of Mo d character.

The partial density of states (PDOS) of Mo in Mo_6S_8 is shown in Figure 4-14. The d-states of Mo in Mo_6S_8 are dormant with the s-states contribution to the valence-band spectra also negligible because of the small number of electrons. There is an energy gap like structure about 1 eV above the electron energy Fermi level set at $E_F = 0$ eV, arising from the splitting between the bonding and antibonding Mo $4d$ states. Its position relative to E_F depends on the number of electrons in the cluster. In case of 24 valence

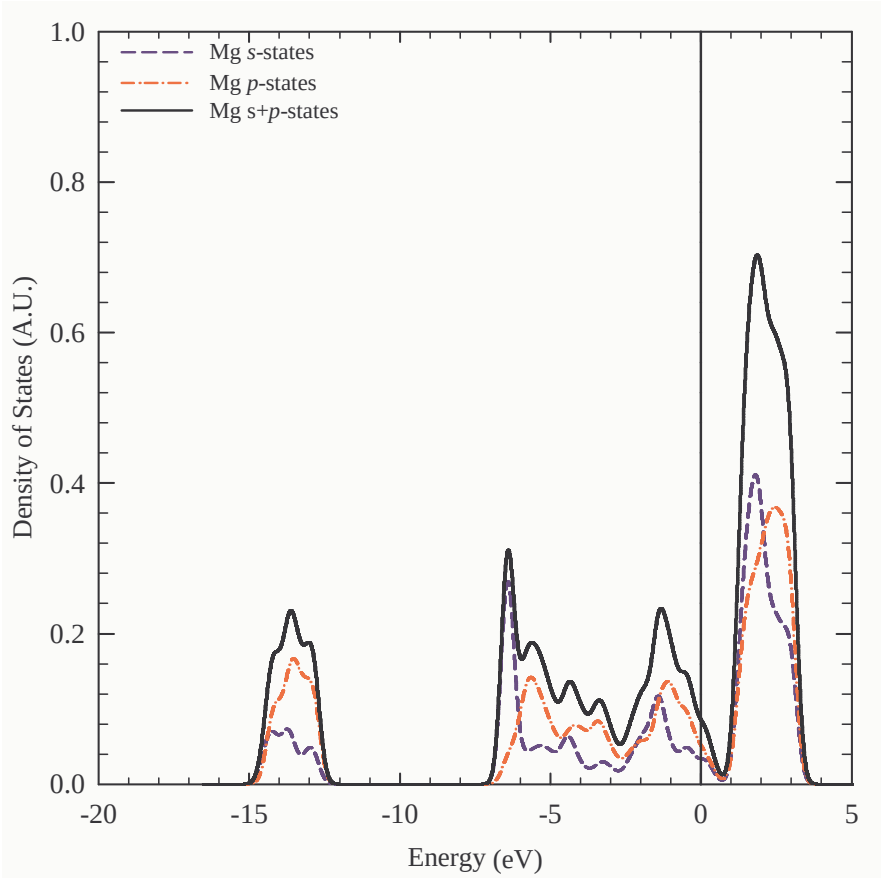

Figure 4-17: The partial density of states for the s- and p-states of Mg in $Mg_AMo_6S_8$.

electrons, E_F should be situated in the gap between the bonding and antibonding states. There are 20 and 22 electrons in Mo_6S_8 and $MgMo_6S_8$ respectively, since the Mg s and p-states (see Fig. 4-17) lies predominantly above, and the S s-states (see Fig. 4-15 and 4-18) lies entirely below the Fermi level. Mg and S act as a divalent cation and anion respectively. The electrons near E_F have predominantly $d_{x^2-y^2}$ symmetry in these Chevrel-phase compounds.

Figure 4-15 shows the partial density of states of the s and p-states of sulfur (S1) in Mo_6S_8. It can be seen that the valence band consists mainly of the sulfur p-states ranging from -5.5 to 0 eV and the sulfur s-states at about -13 eV, with some minimal contribution by the S p-states in the conduction band. Figure 4-16 shows the partial

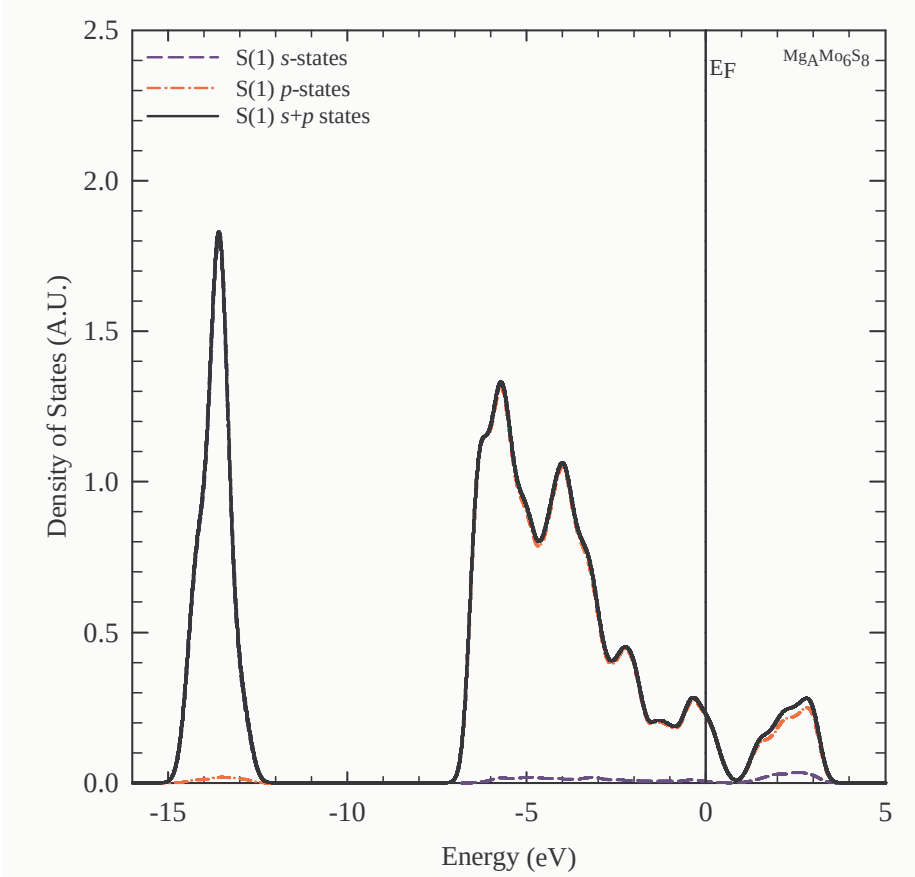

Figure 4-18: The partial density of states showing the s and p -states of sulfur (S1) in $Mg_AMo_6S_8$.

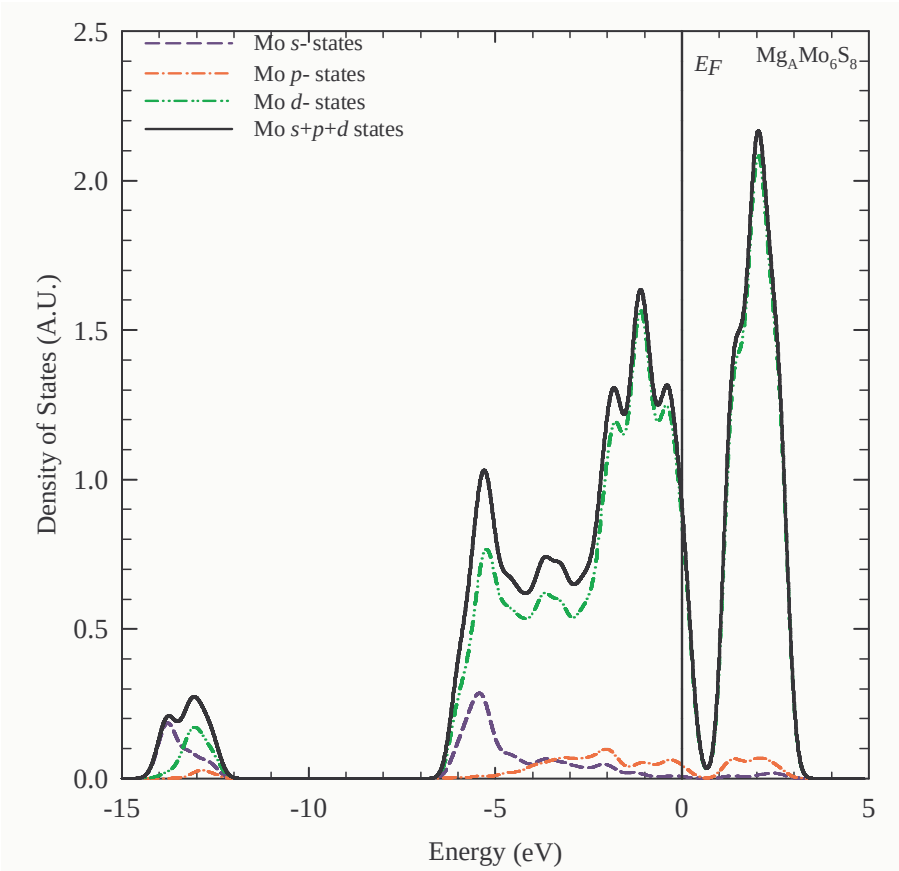

Figure 4-19: The partial density of states of $Mg_AMo_6S_8$ showing the s, p and d -states of molybdenum (Mo).

density of states depicting the s and p-states of sulfur (S2) in Mo_6S_8. The s and p-states of the sulfur along the $\overline{3}$ symmetry are at about -2.5 eV and -12 eV respectively. There is generally a larger $N(E_F)$ at the S sites. This is clearly illustrated in Figures 4-15 and 4-16 where the S(1) and S(2) $3p$ states in Mo_6S_8 are dominant just below the Fermi level and the s-states at the lower part of the valence band. There is negligibly small contribution from the S s-states in the conduction band particularly from S(1). In both instances, the energy gap is located at ~ 1 eV above the Fermi level.

Bulky metal atoms such as Pb provoke larger distortions of the Mo_6X_8 structure, which may be important in determining $N(E_F)$. Figure 4-13 shows the total DOS of

Mg intercalated Mo_6S_8 which adopted a triclinic structure: $Mg_AMo_6S_8$. The Fermi level E_F has shifted from the peak (observed for Mo in Mo_6S_8, see Fig. 4-12) by ~ 0.5 eV towards the "gap" and results in a reduced $N(E_F)$. This is attributed to the electron contribution from Mg to the Mo_6S_8 cluster. Usually for Mo compounds, the d bands are occupied up to the gap region where the DOS is low, but in Chevrel compounds, a large charge transfer from Mo to S (about one electron per Mo atom) was found to occur and E_F falls in a high-DOS region below the gap. We obtain below the main $p-d$ band (between d-orbitals of Mo and p-orbitals of S) and S s-band a narrow Mg s-band (see Fig. 4-17). This is filled by two electrons, so that the Mg intercalated compound is metallic and might be superconducting (with two holes in the $p-d$ band).

Introduction of the Mg atoms in Mo_6S_8 separates the Mo_6 units which results in a narrow Mo $4d$ band (see Fig. 4-19). The conduction-band levels around the Fermi level are derived from predominantly nonbonding Mo $4d$ states, and Mo $4d$ - S p bonding levels are formed about $3-8$ eV below E_F. The Mo $4d$ conduction bands near E_F have very small dispersion giving rise to a high DOS. The Mo $4d$ - S p anti-bonding levels are formed above E_F. The Mo d-states may hybridize strongly only with the S p and Mo s-states. It was found that the conduction-band structure is quite sensitive to the noncubic distortion mostly through the intercluster Mo $4d$ - S $3p$ hybridization [109].

Figure 4-18 shows the partial density of states illustrating the contributions the s and p-states of sulfur (S1) in $Mg_AMo_6S_8$. The S(1) $3p$-states are dominant just below the Fermi level with a band ranging from -5 to 0 eV and the s-states at the lower part of the valence band with a peak around -14 eV. The conduction band consists mainly of the p-states located around 3 eV. The contribution from the Mo $4d$ electrons clearly dominates that from S $3p$ at E_F.

The contribution of magnesium ion charges to the Mo_6S_8, where Mg occupies the inner and outer ring positions is shown in Figures 4-17, 4-20 and 4-21. We firstly note that on comparing the total density of states for $Mg_AMo_6S_8$ and $Mg_{1B}Mo_6S_8$ (see Figs. 4-13, 4-20 and 4-22), the similarity between the two plots is evident. These suggests that

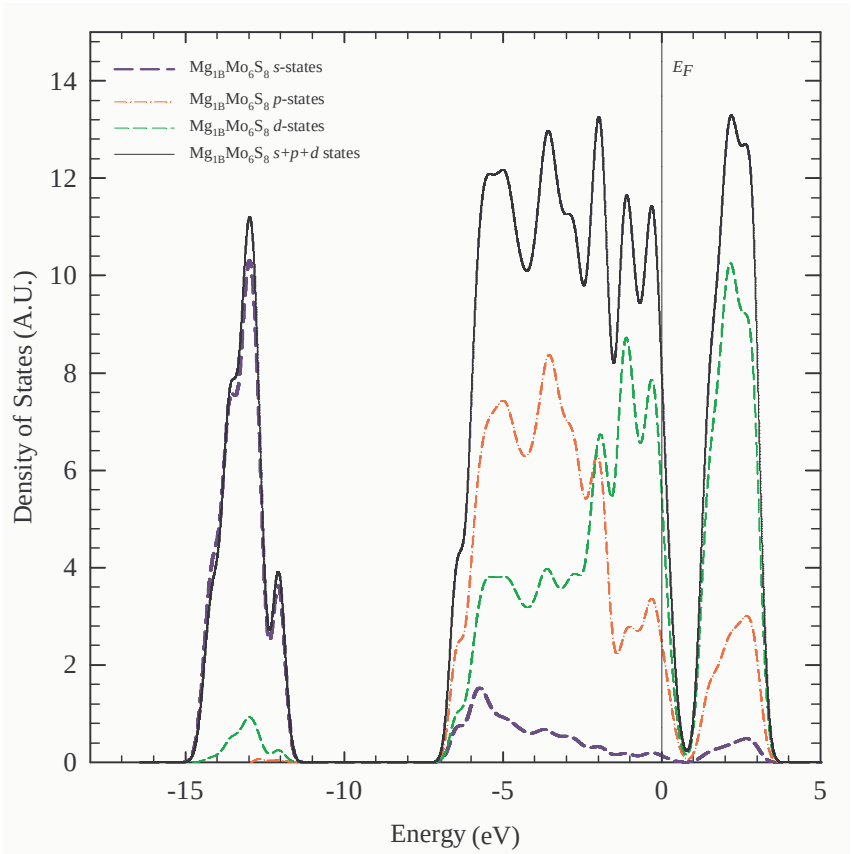

Figure 4-20: The total density of states for $Mg_{1B}Mo_6S_8$.

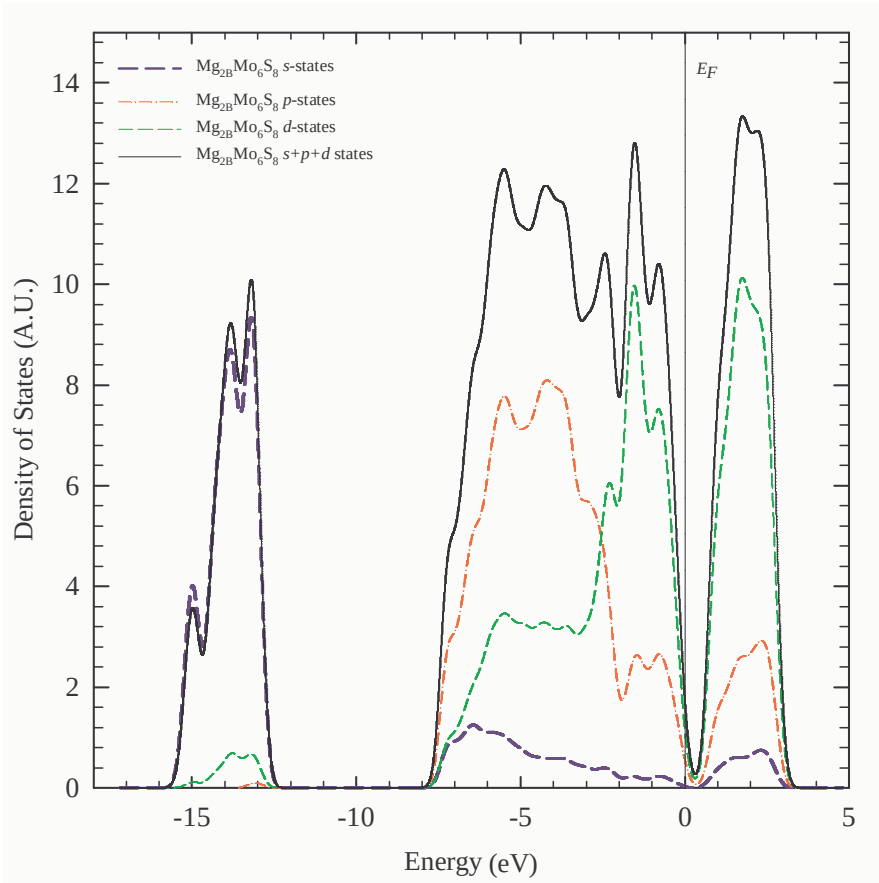

Figure 4-21: The total density of states for $Mg_{2B}Mo_6S_8$.

the energy differences between the two positions may be rather small as already reported in Table 4.6. The energy pseudo-gap is at 0.5 eV above the E_F. Mg s-states are located in the bottom of the conduction band (also of p-states of S and d-states of Mo origin). Mg has occupied conduction bands from the s and p-orbitals but their sum contribution to the total DOS in $Mg_AMo_6S_8$ (see Fig. 4-13) is minimal, signifying charge transfer from Mg to Mo_6S_8. The total DOS is obviously dominated by the average contribution of the Mo $4d$ states. It is believed that the Mo d electrons are responsible for superconductivity and that they do not have appreciable overlap onto the M sites [28].

Figure 4-22 shows a comparison of the total density of states in $Mg_xMo_6S_8$ for $Mo_6S_8(x = 0)$, $Mg_{1A}M_6S_8(x = 1)$, $Mg_{2A}Mo_6S_8(x = 2)$, $Mg_{1B}M_6S_8(x = 1)$ and $Mg_{2B}Mo_6S_8(x = 2)$. The energy-gap-like structure is evident in all Chevrel phase structures just above the E_F. The band gap position corresponds to 36 completed bands, which may accommodate 72 electrons, if the lower lying and well separated s-states of S are not taken into account. The band gap position relative to E_F depends on the number of electrons in the cluster. So, the physical properties of the $Mg_xMo_6S_8$ phases should mainly depend on the number of valence electrons in the cluster. Small variations in the number of valence electrons or in the covalent character of the chemical bonding moves the Fermi level toward a minimum in the density of states. In Mo_6S_8, the p-d block of bands is filled up to 34 bands due to $6\text{Mo} \times 6 + 8\text{S} \times 4 = 68$ valence electrons and the system has four holes below the gap. A similar analysis in $MgMo_6Se_8$, namely $6\text{Mo} \times 6 + 8\text{S} \times 4 + 1\text{Mg} \times 2 = 70$, allows describing this compound as a two hole system, taking into account the s band of Mg which appears just above the p-d Mo_6S_8 valence band (Mg is then in the Mg2+ state). This is confirmed by a notable shift of the band gap towards the E_F. Consequently, in the stoichiometric $Mg_2Mo_6S_8$ (e.g. $Mg_{2B}Mo_6S_8$, see Fig. 4-21), the 36 bands are completed since $6\text{Mo} \times 6 + 8\text{S} \times 4 + 2\text{Mg} \times 2 = 72$. The increase in the number of electrons is noted in the Fermi level that tends to move more closer towards the pseudogap (note that E_F is generally expected to fall into the gap).

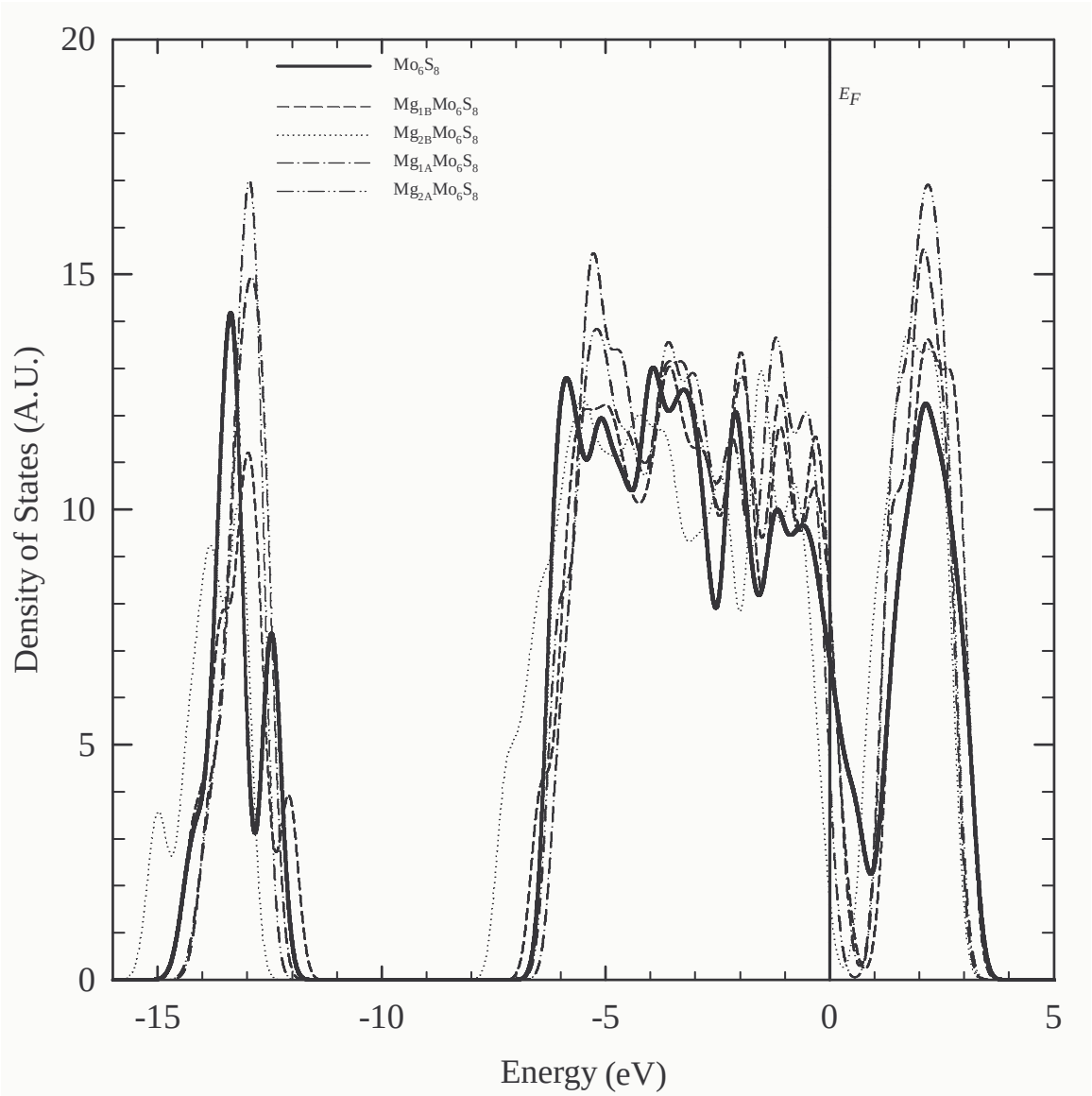

Figure 4-22: A comparison of the total density of states of Mo_6S_8, $Mg_{1A}M_6S_8$, $Mg_{2A}M_6S_8$, $Mg_{1B}M_6S_8$ and $Mg_{2B}Mo_6S_8$.

4.3.3 Charge density of $\mathbf{M_x^{n+}Mo_6X_8}$

In the $M_x^{n+}\mathrm{Mo}_6X_8$ Chevrel phases, a charge transfer of $(nx)e^-/\mathrm{Mo}_6$ is thought to occur at the Mo_6 cluster [10]. The most important electronic parameter of a Chevrel-phase compound is the number of valence electrons per Mo atom available for formation of covalent Mo-Mo bonds. For the sulfides this number primarily depends upon the oxidation state and concentration of the M atoms. A so-called valence electron concentration is calculated by adding the oxidation number of M to the number of valence electrons of the six Mo atoms (36), subtracting the number of the electrons necessary to form the eight sulfur ions (16) and dividing by the number of the Mo cluster atoms (6). Hence for $\mathrm{Mg_2Mo_6S_8}$, the maximum charge transfer predicted is equivalent to $4e^-/\mathrm{Mo_6S_8}$. The calculated total and difference (between crystal and atomic superpositions) of the valence electron pseudo-ion charge density of $\mathrm{Mg}_O\mathrm{Mo_6S_8}$ ($x = 1$), in the plane that spans the $\mathrm{Mo(1)}_\triangle$-$\mathrm{Mo(1)}_\triangle$ and $[\mathrm{Mo(1)} - \mathrm{Mo(1)}]_\triangle$ distances parallel to the ternary ($\overline{3}$) axis, are shown in Figs 4-23(a) and 4-23(b). The Mo atom deformation from a spherical shape is evident in the charge difference density. There is a four-lobe shape of the charge distribution around each Mo atom visible in the plane and an extra two lobes perpendicular to the plane in the isodensity plot (insert), resembling d-type orbitals. A notable gain of electrons between both the Mo atoms and Mo-S atoms is evident, showing covalent bonding, with the charges around the S atoms resembling the p-type orbitals.

In order to study the more interesting effects of charge transfer and polarization, we compared the charge density of $\mathrm{Mg}_O\mathrm{Mo_6S_8}$ and $\mathrm{Mo_6S_8}$. The total electron difference ($\mathrm{Mg}_O\mathrm{Mo_6S_8}$ - $\mathrm{Mo_6S_8}$) is shown in Fig 4-23(b) also in the plane that spans the $\mathrm{Mo(1)}_\triangle$-$\mathrm{Mo(1)}_\triangle$ and $[\mathrm{Mo(1)}_\triangle$-$\mathrm{Mo(1)}]_\triangle$ distances. The density varies between -0.03 and 0.07 $e/\text{Å}^3$. The charge concentration along $\mathrm{Mo(1)}_\triangle$-$\mathrm{Mo(1)}_\triangle$ is evidently higher than that along $[\mathrm{Mo(1)}$-$\mathrm{Mo(1)}]_\triangle$. This explains the earlier observation (see 4.1.3) that $[\mathrm{Mo(1)} - \mathrm{Mo(1)}]_\triangle$ intratriangle and the $\mathrm{Mo(1)}_\triangle$-$\mathrm{Mo(1)}_\triangle$ intertriangle distances decreases by $\sim$ 0.5%, and $\sim$ 3% respectively on intercalation. Figure 4-24(a) shows the total-valence-charge electron density of $\mathrm{Mg}_O\mathrm{Mo_6S_8}$ along the plane that includes the S(2) and

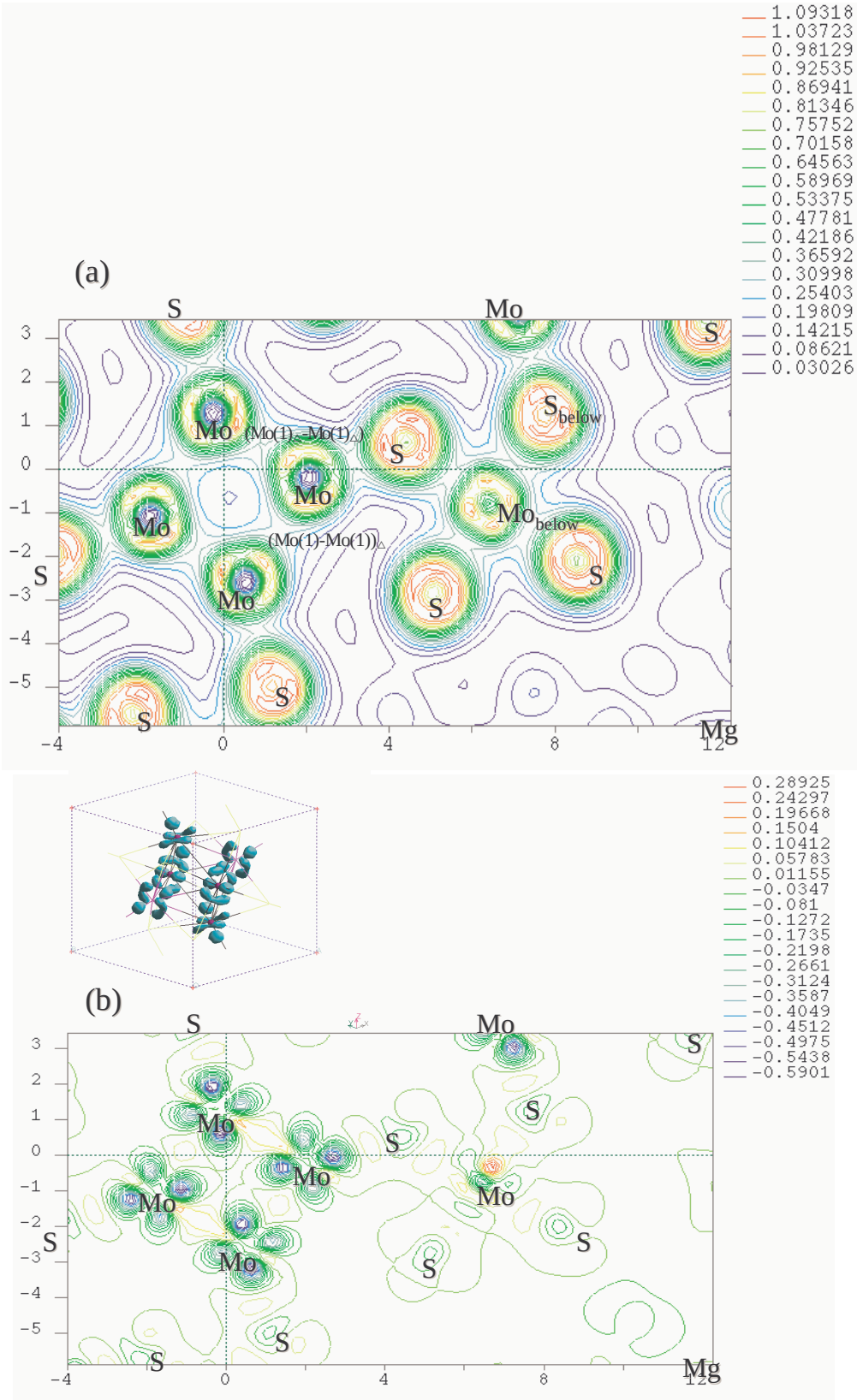

Figure 4-23: Contour plot of (a) the total valence electron pseudocharge density of $Mg_O Mo_6 S_8$ and (b) the pseudocharge difference of the Mo_6 cluster and the S_8 and Mg in the plane that spans the $Mo(1)_\triangle$-$Mo(1)_\triangle$ and $[Mo(1) - Mo(1)]_\triangle$ distances. The color coding is dark blue to red/magenta for increasing density. The contour values range from

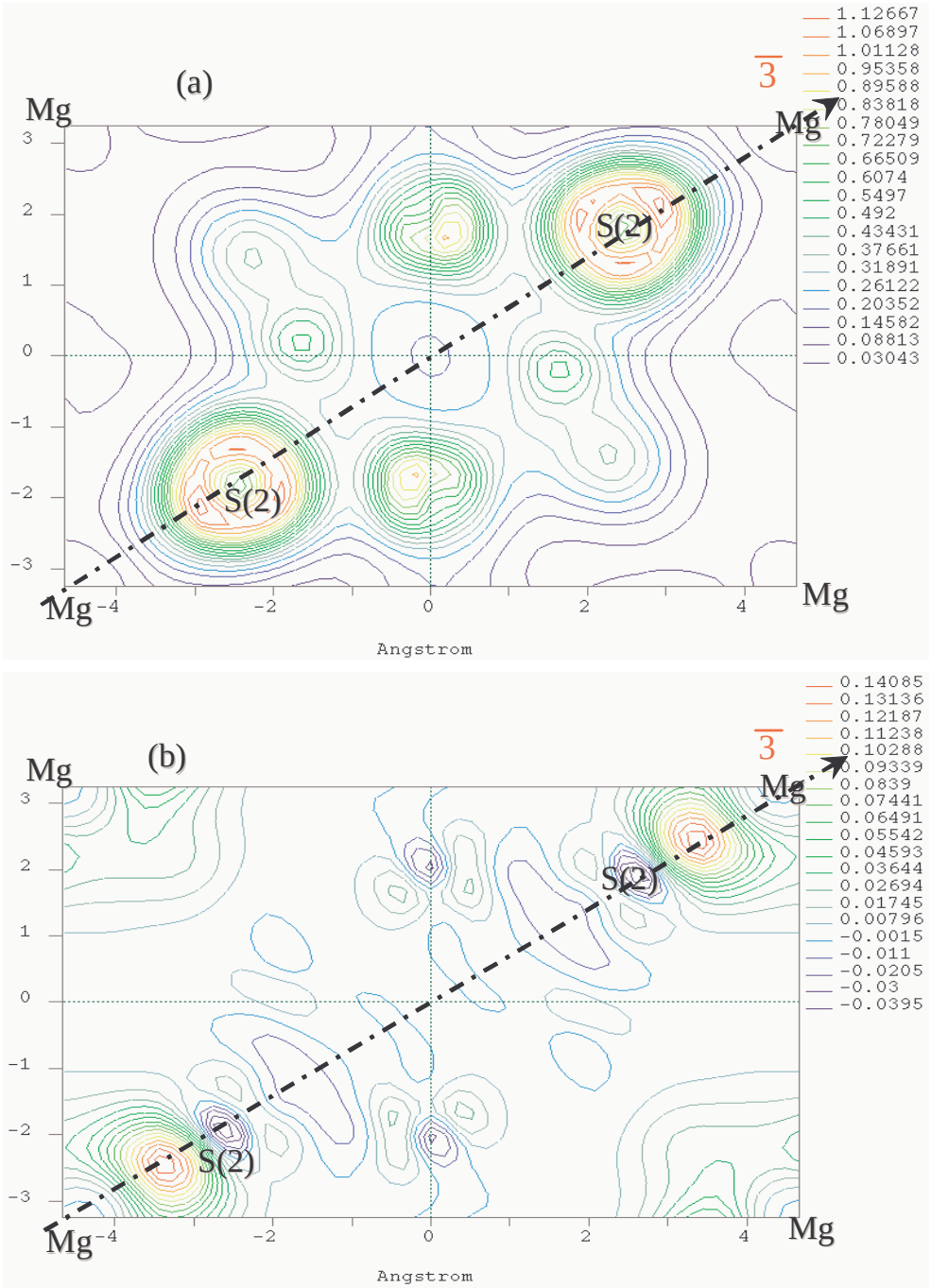

Figure 4-24: The charge density plot showing a slice of (a) the pseudocharge density and (b) pseudocharge-density difference for $Mg_OMo_6S_8$ along the plane that includes the S(2) sulfur and Mg at the origin parallel to the $\bar{3}$ axis. The color coding is dark blue towards red/magenta for increasing density. The density varies between 0.03 to 1.12 and -0.03 to 0.14 $e/\text{Å}^3$ respectively.

Mg at the origin parallel to the $\overline{3}$ axis. The density varies between 0.03 and 1.13 $e/\text{Å}^3$. There is a clear high charge concentration around the S(2) atoms with almost no charge around the Mg, hence signifying a loss of charge from Mg. The total electron difference ($Mg_O Mo_6S_8$ - Mo_6S_8) is shown in Fig. 4-24(b). A peak of 0.14 $e/\text{Å}^3$ is found at the midpoint between S(2) and Mg atoms. Although the charge transfer is consistent with the formula $Mg_2^{2+}[Mo_6^{2+}S_8^{2-}]^{4-}$, there is a substantial measure of charge transfer to the S(2) sulfur atom.

The isosurface in Fig 4-25 is plotted at 0.06 within a range of -0.09 to 0.15 $e/\text{Å}^3$. There is a quantitative charge transfer evident from the Mg site to the host lattice, confirming the idea that Mg is characterized by ionic bonding in this compound. The number of the valence electrons should increase due to easy redistribution of electronic charge on each element (Mo or S). Figure 4-26 shows the contour plot of the pseudocharge difference of the Mo_6 cluster and S_8 and Mg in a plane parallel to the $[\text{Mo-S(1)}]_{intercluster}$ and Mo-S(1) distances. The four-lobes around the Mo atoms resembling the d-type orbitals are visible. The formation of the intercluster bond is by $3p$ [S(1)] and $4d$ (Mo) orbitals. A smeared minimum is observed behind the S(1) atoms and extends towards the Mo atom.

Mulliken population

Population analysis is performed using a projection of the planewave states onto a localized basis [249]. Population analysis of the resulting projected states is then performed using the Mulliken formalism [250]. The Mulliken population analyses are used as an approximation overview of intercalation induced charge arrangements. It is widely accepted that the absolute magnitude of the atomic charges yielded by population analysis have little physical meaning, since they display a high degree of sensitivity to the atomic basis set with which they were calculated [251]. However, consideration of their relative values can yield useful information.

Mulliken population calculation for Mo_6S_8 gives a charge of -0.13 and -0.14 on each

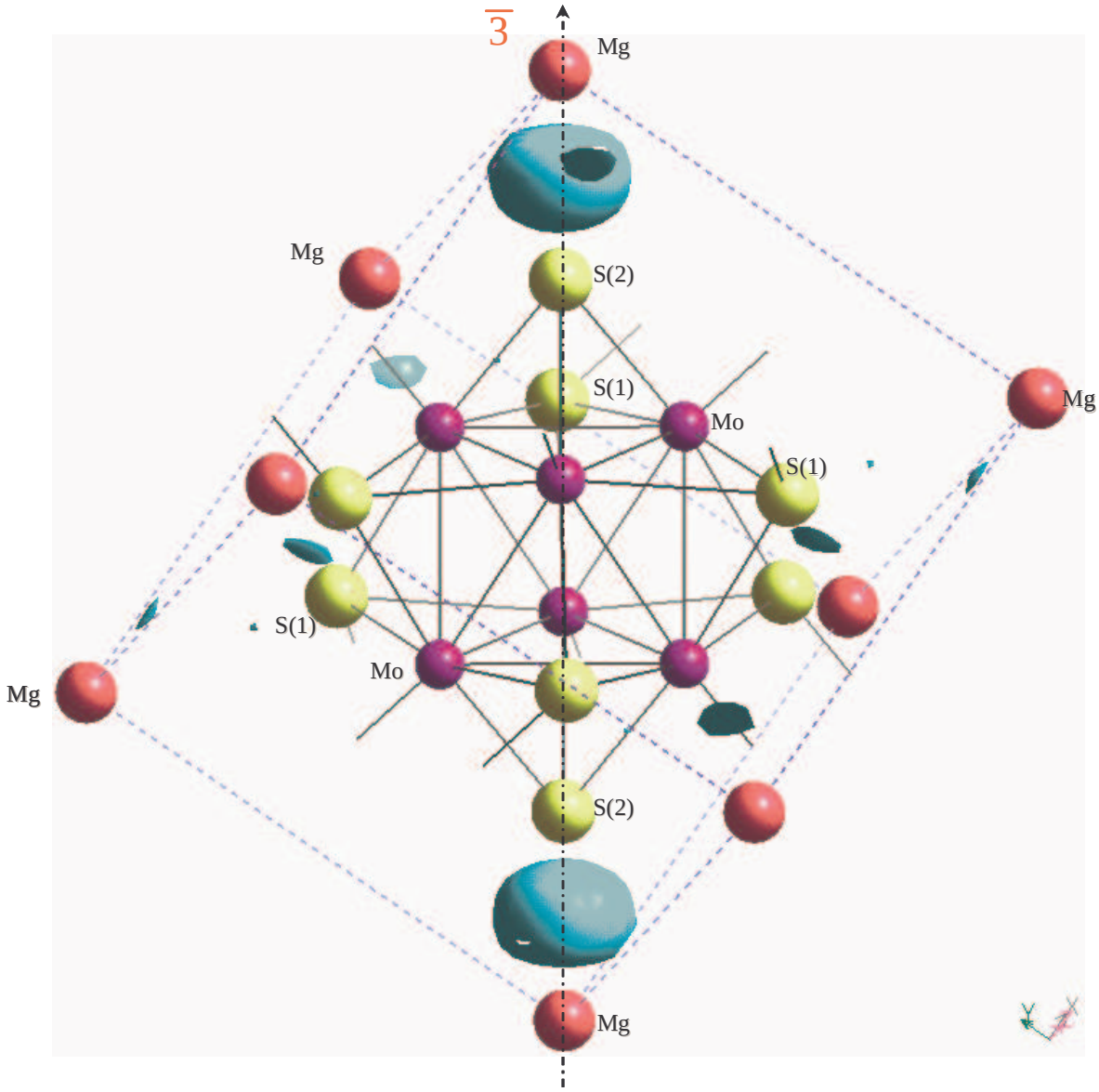

Figure 4-25: The charge-density plot showing a isosurface of the total charge-density difference of $Mg_O Mo_6S_8$ and Mo_6S_8 along the plane that includes the S(2) sulfur and Mg at the origin parallel to the $\bar{3}$ axis. The color coding for the isosurface is light blue, plotted at 0.06 within a range of -0.09 to 0.15 $e/\text{Å}^3$.

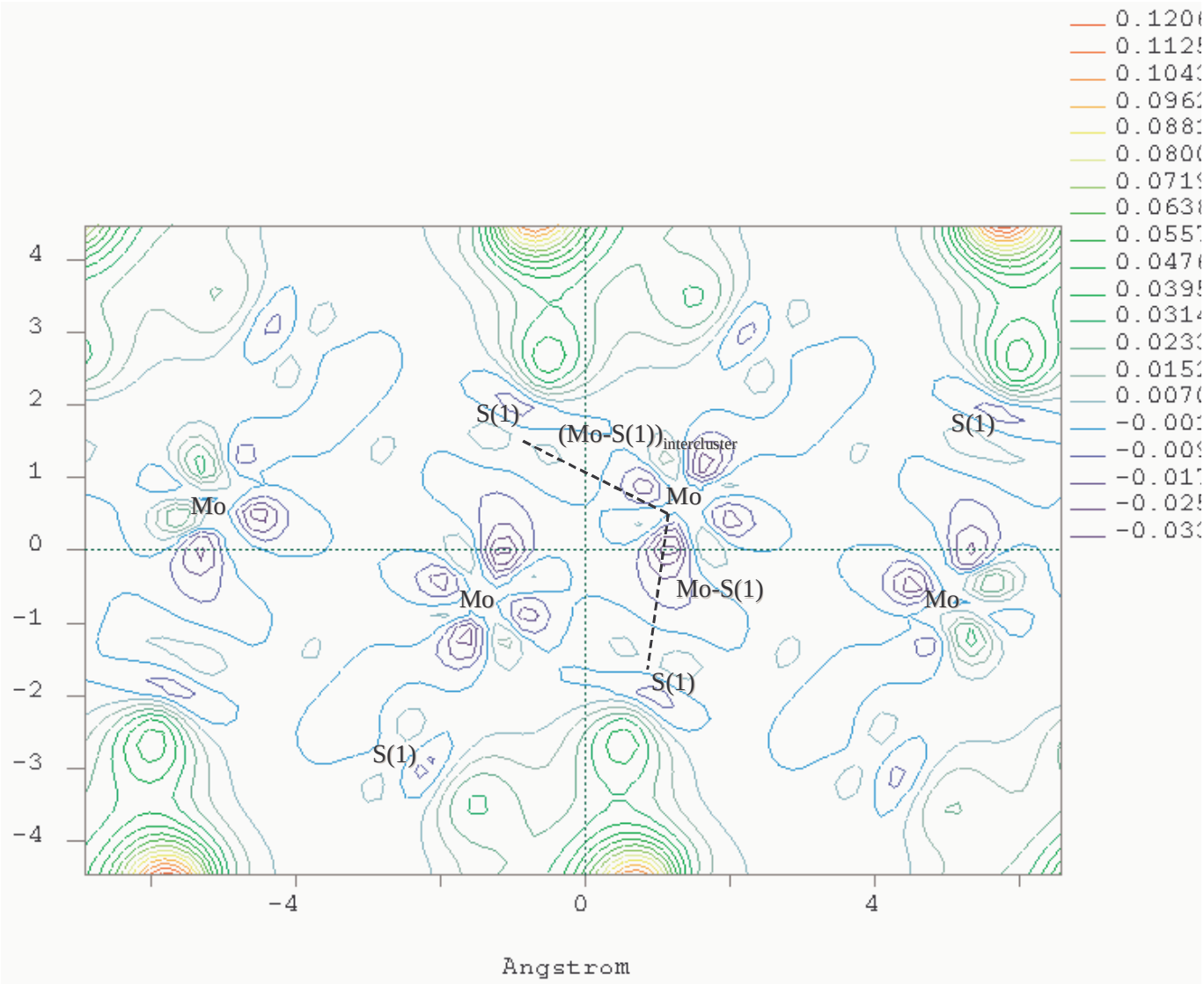

Figure 4-26: The charge density difference plot of the total charge density of $Mg_O Mo_6S_8$ and Mo_6S_8 in a plane parallel to the $[\text{Mo-S(1)}]_{intercluster}$ and Mo-S(1) distances.

of the six S(1) and two S(2) sulfur atoms respectively, counterbalanced by a charge of +0.18 on each of the six molybdenum atoms. These values are in agreement with the highly covalent character of this compound. The same calculations for $Mg_O Mo_6 S_8$ show that +0.66 electrons per magnesium are given to the host structure. This charge is shared almost equally between the sulfur and molybdenum atoms, whose charges becomes −0.22 and −0.29 per S(1) and per S(2) atom respectively and +0.21 per Mo atom. These results suggest a charge transfer of 0.03 electrons to the molybdenum, 0.09 electrons to S(1) and 0.15 electrons to S(2). The oxidation state for Mg is +2, such that theoretically the VEC for Mo is 3.67. This corresponds to the two holes in the conduction band.

Table 4.8: Mulliken population analysis with a spilling parameter of 0.40% for the bond overlap populations ($|e|$ units) in Mo_6S_8, and $Mg_O Mo_6 S_8$ systems (LDA, Ultrasoft-pseudopotentials).

Distances (Å)	Mo_6S_8	$Mg_O Mo_6 S_8$	
	LDA ($\|e\|$)	LDA ($\|e\|$)	$\nabla \|e\|$
$(Mo\text{-}Mo)_\triangle$	-0.80	-0.71	+0.09
$Mo_\triangle$-$Mo_\triangle$	-0.75	-0.85	-0.1
Mo-S(2)	+0.45	+0.35	-0.1
Mo-S(1)	+0.18	+0.15	-0.03
S(1)	+0.32	+0.33	+0.01
S(1)	+0.43	+0.45	+0.02
$(Mo\text{-}S(1))_{intercluster}$	+0.36	+0.36	0
Mg-S(2)	-	-0.28	-
Mg-Mo(1)	-	-	-
Mg-S(1)	-	-	-

Table 4.8 shows the Mulliken population analysis with a spilling parameter of 0.40% for the bond overlap populations in Mo_6S_8 and $Mg_O Mo_6 S_8$ systems. The overlap population provides an objective criterion for bonding between atoms. On comparison of the bond population for the intracluster distance $Mo(1)_\triangle$-$Mo(1)_\triangle$ for Mo_6S_8 and $Mg_O Mo_6 S_8$, we observe an increase in the charge in the latter system with the Mo-Mo bond overlap population difference of $-0.1\,|e|$. The observation was ealier noted from the total electron difference ($Mg_O Mo_6 S_8$ - Mo_6S_8, see Fig 4-23(b)) showing the plane that spans the $Mo(1)_\triangle$-$Mo(1)_\triangle$ distance. The results confirms the metallic bonds between the Mo

atoms and covalent bonds between Mo and S atoms.

4.4 Optical Properties

4.4.1 Reflectivity and conductivity with polarization.

Figure 4-27 show the calculated real part of the optical conductivity of $MgMo_6S_8$. Figure 4-28 which is taken from Ref. [111] shows the real part of the optical conductivity of $EuMo_6S_8$ (a), $PbMo_6S_8$ (b), $Eu_{0.75}Sn_{0.25}Mo_6S_{7.6}Se_{0.4}$ (c), and $Eu_{0.5}Pb_{0.5}Mo_6S_8$ (d) as derived from the reflectivity spectra at room temperature. Our calculated real part of the optical spectra at ~ 0 K resembles very closely that of $Eu_{0.75}Sn_{0.25}Mo_6S_{7.6}Se_{0.4}$ derived from the reflectivity spectra at room temperature. The peak at G in Figure 4-28(c) appears at ~ 6 eV while in our calculations it appears at ~ 4.5 eV. At energies higher than 8 eV we also observe an increase in δ due to the majority of valence electrons which must be excited upto ~ 20 eV . The dominant part of δ is due to S(1) $p \rightarrow$ Mo(1) d transitions [252].

4.5 Concluding Remarks

Both LDA and GGA calculation predicted the rhombohedral and hexagonal lattice parameters of both Mo_6S_8 and $MgMo_6S_8$ well within their expected error margins .We have also observed a phase transition in all the other structures (see Table. 4.1) where Mg occupies site A or B for $x = 1$, and both sites for $x = 2$. The volume increases as the concentration increases from $x = 0$ to 2. LDA and GGA predictions show a decrease in both the $[\mathrm{Mo}(1) - \mathrm{Mo}(1)]_{\triangle}$ intratriangle and the $\mathrm{Mo}(1)_{\triangle}$-$\mathrm{Mo}(1)_{\triangle}$ intertriangle distance. We have reported for the first time the total and partial DOS of $Mg_xMo_6S_8$ Chevrel phase compounds. The total DOS in all the systems in notably dominated by the average contribution of the Mo $4d$ states with the Fermi level at ~ 1 eV below the energy-gap-like structure. The increase in the number of electrons from Mg-ions is noted in the Fermi

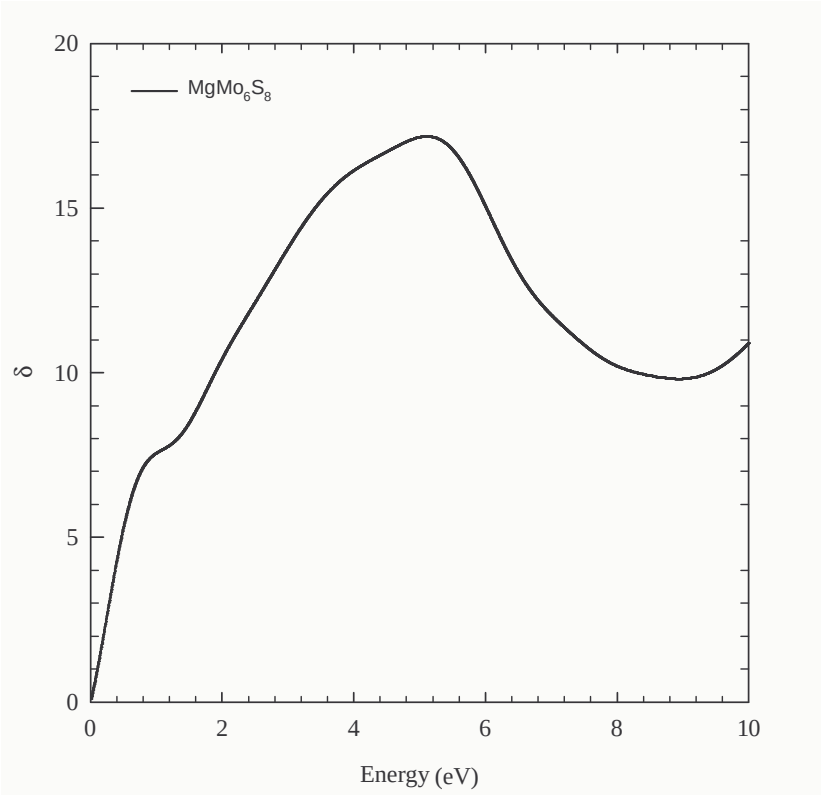

Figure 4-27: The real part of the optical conductivity of $MgMo_6S_8$

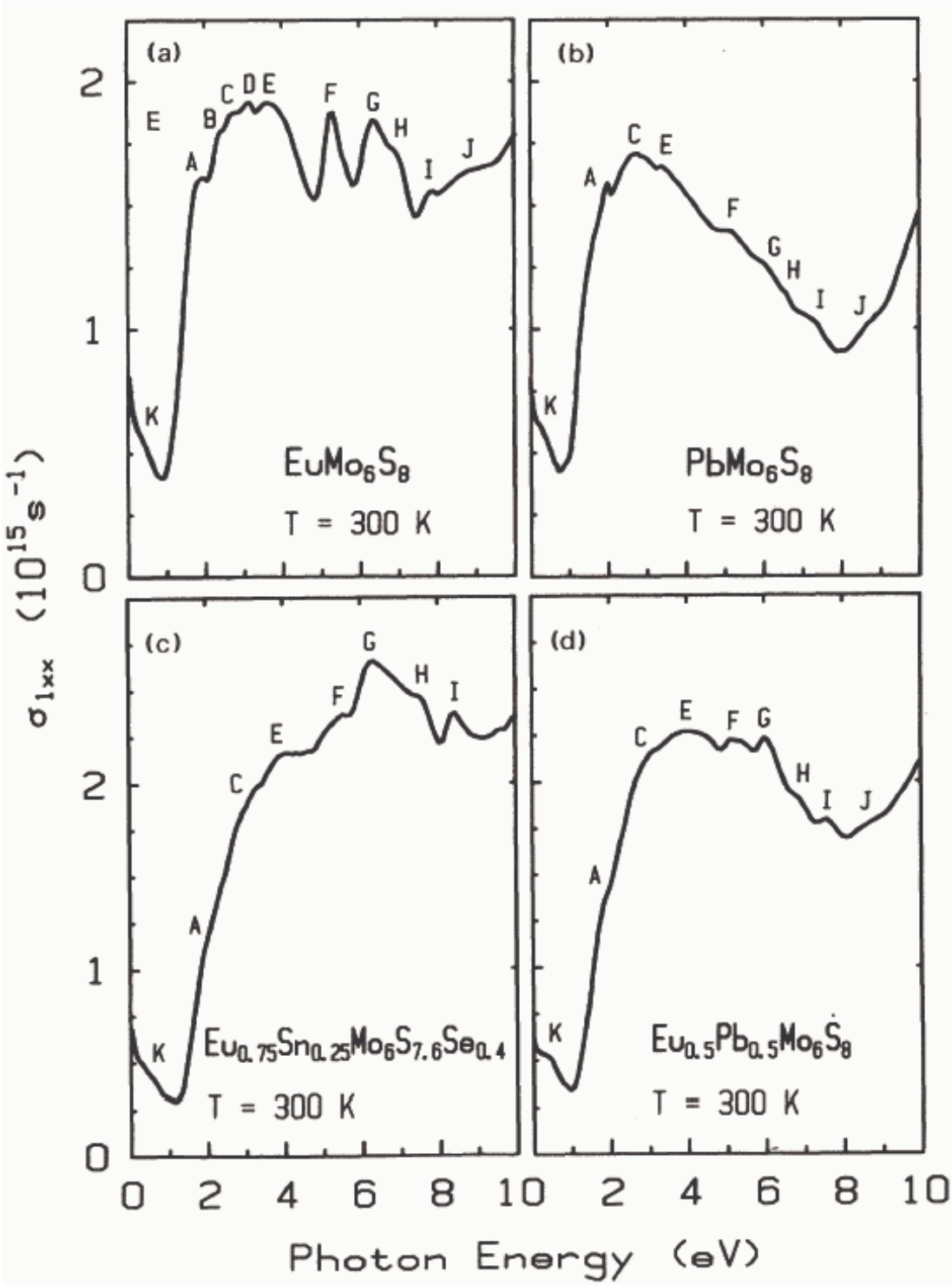

Figure 4-28: The real part of the optical conductivity of $EuMo_6S_8$ (a), $PbMo_6S_8$ (b), $Eu_{0.75}Sn_{0.25}Mo_6S_{7.6}Se_{0.4}$ (c), and $Eu_{0.5}Pb_{0.5}Mo_6S_8$ (d) as derived from the reflectivity spectra at room temperature. This figure has been taken from Ref. [111].

level that tends to move more closer towards the pesudogap. We have used the charge density plots to illustrate charge transfer from the Mg to the Mo_6S_8 host and this was also confirmed using the Mulliken population analysis method. Charge transfer from the cation towards the Mo_6 unit stabilizes the crystal structure because an increasing filling of the metal–metal bonding levels. This work has been published (see H.1).

No high pressure measurements of $Mg_xMo_6S_8$ have been reported. Mo_6S_8 in more compressible than $Mg_OMo_6S_8$ and the compressibility increases markedly with increasing pressure. The compression curve for Mo_6S_8 have a bending point around $15-20$ GPa pressure range, implying that the bulk modulus is not constant but changes discontinuously under pressure. We have shown that the PP methods calculates the voltage profile of $MgMo_6S_8$ very well compared to the experiment. The calculated value of $\Delta E = 2.20$ eV for $LiMo_6S_8$ compared very well with the experimental data of McKinnon *et al.* [13], who reported a value of 2.41 eV. This result affirms the accuracy of our earlier calculation in $MgMo_6S_8$. There is no reported optical spectra data for $MgMo_6S_8$, but our initial calculation show similar trends with other intercalated Mo_6X_8 Chevrel compounds. Optical conductivity is mainly due to transitions within the Mo_6X_8 cluster.

Chapter 5

Transitional-Metal Dichalcogenides

In this chapter we investigate the structural, electronic and optical properties of the TMDCs and the intercalation compound, Li_xTiS_2. We report the effect on the physical properties of the host structure, TiS_2, resulting from charge transfer phenomena. Intercalation and ion conduction of lithium in TiS_2 is exploited in the form of occupational energetics and voltage curve predictions.

5.1 Structural Properties of Transitional-Metal Dichalcogenides

5.1.1 Structural Description

The family of layered transitional-metal dichalcogenides (TMDCs) of the type TX_2 or MX_2 (M = group -IV B, -V B, or -VI B metal atoms and X = chalcogen atom S, Se or Te) have been studied extensively. Lucovsky *et al.* [263] conducted x-ray diffraction studies (Cu$K\alpha$) on some TMDCs obtaining extremely sharp lines for group -IV B chalcogenides corresponding to the hexagonal $1T$ or CdI_2 structure (space group $P\overline{3}m$). The observed [263] lattice parameters are : ZrS2 (a = 3.661 Å, c = 5.829 Å and c/a = 1.592) and TiS_2 (a = 3.404 Å, c = 5.699 Å and c/a = 1.674). The c/a ratio

is ideally equal to 1.633. ZrS_2 and TiS_2 crystallizes in a lattice of CdI_2 type with the space group $D_{3d}^3 - P\overline{3}m1$. The primitive Bravais cell contains one formula unit ($z_s = 1$). The anion (Sulfur) take $2d \sim \pm\ (1/3, 2/3, z)$ Wyckoff positions in the lattice and the cations (Zirconium and Titanium) take the common $1a \sim (0, 0, 0)$ positions. Taking into consideration the D_{3d}^3 symmetry, the transition-metals take the D_{3d}^3 symmetry and the chalcogens take the D_{3v} symmetry.

The transition-metals (e.g. Ti) lie in planes that are individually sandwiched between the two parallel planes of hexagonally packed chalcogens (S) and the layers are stacked in the c direction giving rise to the observed hexagonal structure analogous to that of graphite (see Figure 5-1). The thickness of the layer is $2cz$, and the distance between adjacent layers is $(1 - 2z)c$. The bonding within these X-T-X "layers" is of strong (ionic/covalent) type, whereas the coupling layer in relatively weak. The layers are held together by weak dispersion forces and the empty space between them is referred to as "the van der Waals gap". Several polytypes of a given compound can be formed, according to stacking and the number of the X-T-X sandwiches perpendicular to the c-axis, in the unit cell (in the notation $1T$, $2H$, and $3R$, the integers represent the number of slabs in the unit cell and T, H, and R denote trigonal, hexagonal, and rhombohedral symmetries respectively). The group-IV (Ti, Zr) dichalcogenides occur in the $1T$ stacking polytype in which the metal-ion configuration is octahedral.

The affinity of TX_2 for intercalation is due to this characteristic bonding anisotropy. They are highly anisotropic and sometimes referred to as two-dimensional (2D) solids. A variety of electron donor, such as alkali metals and organic molecules, can be easily intercalated between the layers. Depending on the intercalant, unusual and dramatic changes in the electronic, optical and physical properties of the host can occur, stimulating much research interest.

The hexagonal close-packing of the sulfur atoms in TiS_2 gives rise to two type of interlayer sites for lithium occupation. Two tetrahedral sites are at $(1/3, 2/3, 5/8)$ and $(2/3, 1/3, 3/8)$; one octahedral site is at $(0, 0, 1/2)$.

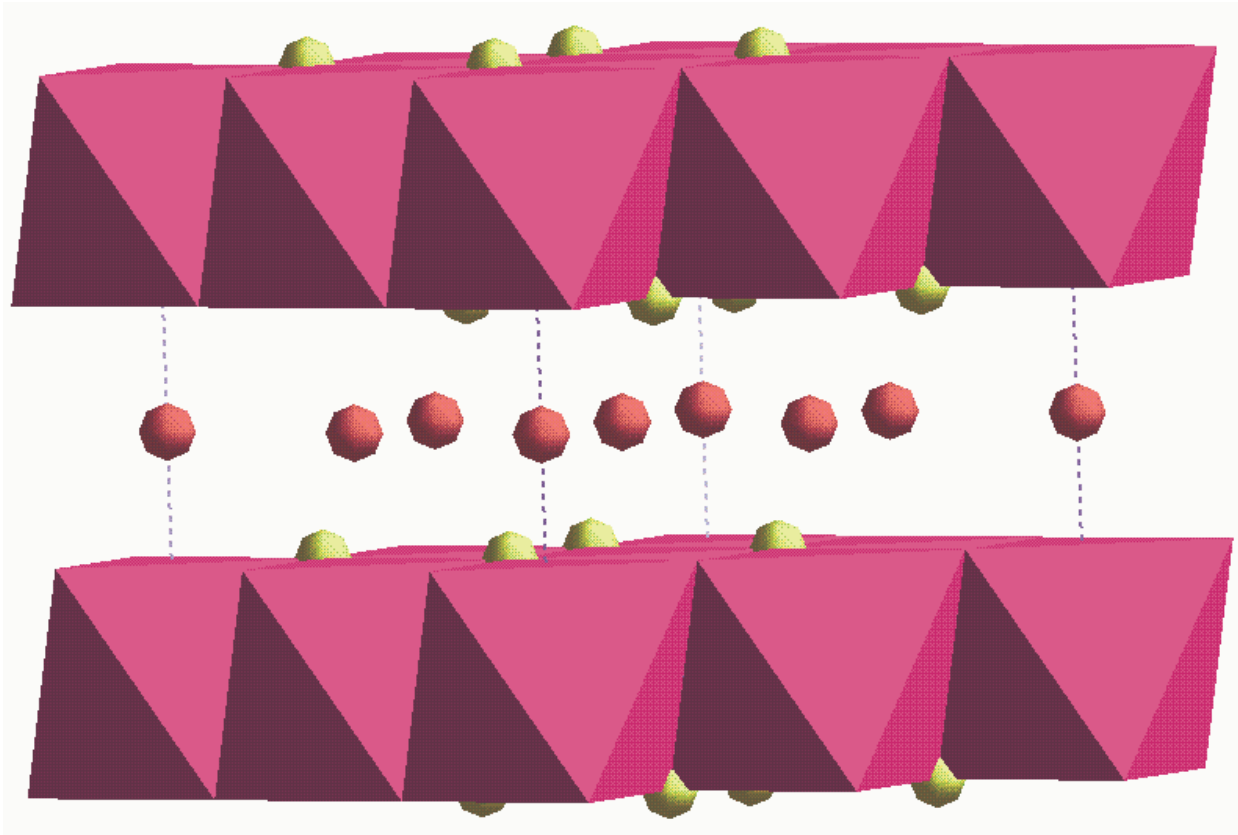

Figure 5-1: Strucure of 1T - Lithium intercalated TiS_2. The metal atoms (Ti) are represented by the magenta polyhedra, while S and Li are represented by the yellow and pink atoms respectively.

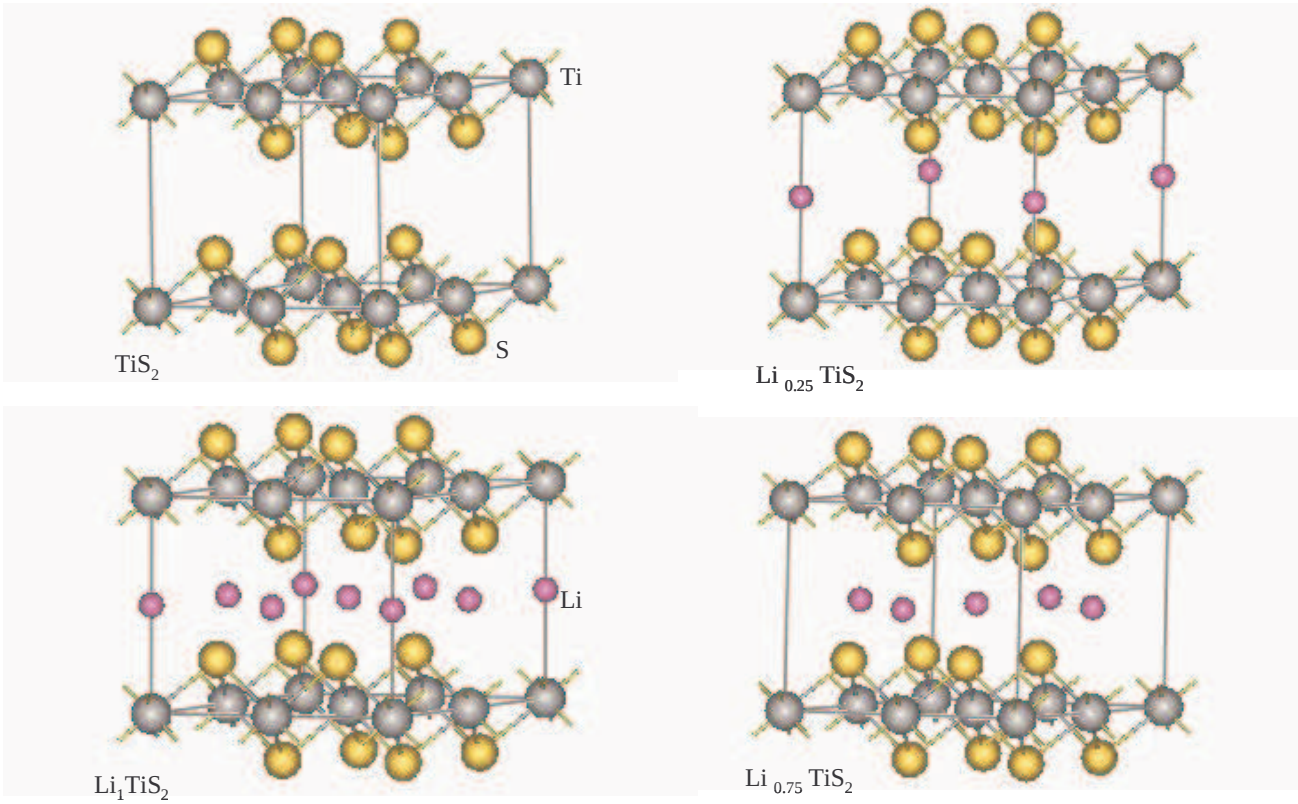

Figure 5-2: Projection of the Li_xTiS_2 supercell for $x = 0, \frac{1}{4}, \frac{3}{4}, 1$. Lithium atoms occupy the octahedral sites in a disordered fashion.

$LiTiS_2$ (see Figure 5-1) belongs to the family of the alkali intercalated transition metal dichalcogenides A_xTX_2 (A = Alkali metal). The lattices of TiS_2 and $LiTiS_2$ are both defined by vectors $\overrightarrow{a}$, $\overrightarrow{b}$ and $\overrightarrow{c}$, where $|\overrightarrow{a}| = \left|\overrightarrow{b}\right|$, $\overrightarrow{a} \perp \overrightarrow{b}$, $\overrightarrow{b} \perp \overrightarrow{c}$, and $\angle(\overrightarrow{b}, \overrightarrow{b}) = 120°$. In $LiTiS_2$, the lithium atom is positioned directly above the titanium atom as indicated by the following fractional coordinates [153]: Ti $(0, 0, 0)$, S $(1/3, 2/3, z_s)$, $(2/3, 1/3, -z_s)$, and Li $(0, 0, 1/2)$. Lithium atoms in Li_xTiS_2 occupy the octahedral sites in a disordered fashion. The projection of four primitive $LiTiS_2$ unit cells onto the titanium plane ($z = 0$) is shown in Figure 5-2.

An intercalation process is generally defined as a reversible topotactic reaction in which a guest species (e.g. Li-ion) occupies empty sites (tetrahedral or octahedral sites)

in a solid structure. Lithium-ions may be intercalated into graphite and many transition-metal dichalcogenides because of their 2D character. Elastic interactions play an important role in the structural chemistry of intercalation compounds. These can be modelled either as a collection of rigid planes held together by Hooke's law springs [268] or by local dipole strain fields arising from the deformation of host layers flanking an intercalate or "island" of intercalates [269]. The latter viewpoint has the advantage that it accounts in principle for contributions to both the interlayer and intralayer energetics. Li_xC_6 exhibits high stages at 300 K for various x while Li_xTiS_2 is restricted to stage 1 [270].

With lattice distortion neglected, the basic crystal structures on intercalation compounds belong to the hexagonal system [272]. In the literature, the "ordered structure" refers to that of intercalated alkali-metal ions in the fictitious plane of intercalated ions of the hexagonal lattice. The "stage structure" refers to that of lithium ion sub-lattices (the fictitious 1D plane of intercalated ions) along the c-axis [59, 65, 67, 68, 78]. An x-ray diffraction study [66] has shown a considerable variation of the c parameter (along the c-axis) that depends on the type and concentration of the intercalated species. EXAFS [273] studies on metal intercalated TiS_2 compounds have shown that the metal-sulfur distance (d_{T-X}) varies as a function of the concentration of the guest species.

5.1.2 Structural Predictions

Table 5.1 shows the calculated crystallographic data of TiS_2, ZrS_2 and $LiTiS_2$ compared with experimental data. The calculated lattice parameter a and c for TiS_2 underestimate the experimental [55, 79, 160, 263, 264, 265, 266, 267] parameters by 3% and 2.7% respectively. This is the expected trends from the LDA calculations, which overestimate the electron binding leading to an underestimate of the lattice parameter. The calculated c/a ratio of 1.678 is slightly higher than the ideal ratio of 1.633 for the $1T$ octahedral packing but compares well with the value of 1.674 reported by Lucovsky *et al.* [263]. On intercalation, the new structure $LiTiS_2$'s calculated c/a ratio is 1.812, while a and c deviates from experiment by 3% and 1. 9% respectively. The sulfur free parameter (z_s)

Table 5.1: Pseudopotential calculated lattice parameters compared with the crystallographic data and bond lenghts from McTaggart and Wadsley (1958) and Greenaway and Nitsche (1965) with experimental distnaces in Å for TiS_2, ZrS_2 and $LiTiS_2$ compounds.

	a	c	d_{T-X}	z_s
TiS_2	3.299	5.535	2.383	0.258
TiS_2 [55]	3.400	5.690	2.420	-
TiS_2 [265]	3.4076	5.6992	-	-
TiS_2 [266, 267]	3.405	5.689	-	-
TiS_2 [263]	3.404	5.699	-	-
TiS_2 [160, 264]	3.41	5.69	-	-
TiS_2 [79]	3.406	5.694	-	-
$LiTiS_2$	3.346	6.063	2.419	0.240
$LiTiS_2$ [55]	3.459	6.187	-	-
$LiTiS_2$[160, 264]	3.430	6.180	-	-
$LiTiS_2$[253]	3.459	6.188	-	-
ZrS_2	3.648	5.751	2.534	0.244
ZrS_2 [55]	3.66	5.82	-	-
ZrS_2 [263]	3.661	5.829	-	-
ZrS_2 [149]	3.662	5.813	-	-

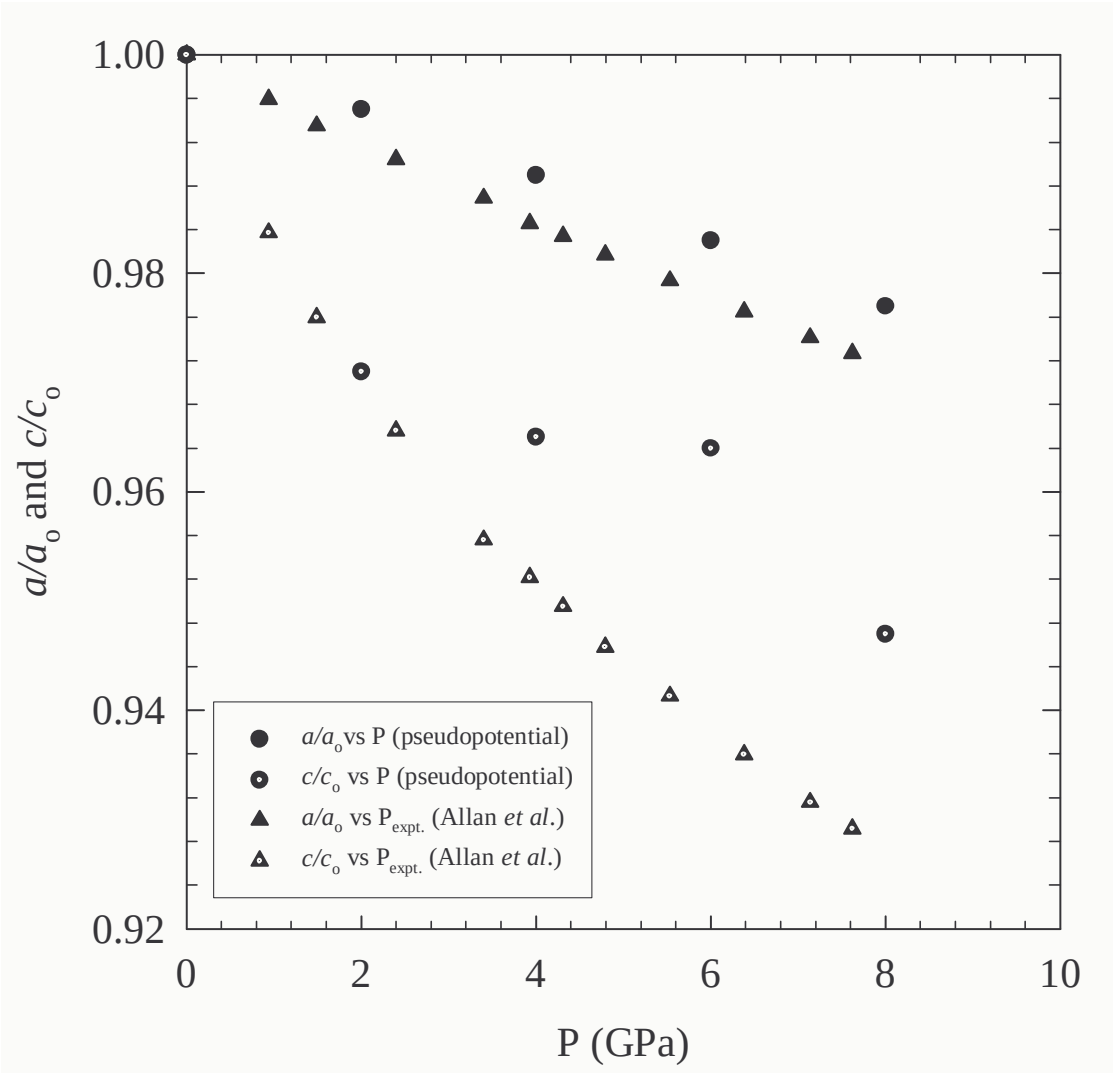

Figure 5-3: A comparison of the calculated relative lattice parameters a/a_0 and c/c_0 of TiS_2 as a function of pressure with the experimental data of Allan *et al.* [130] at pressures below 10 GPa..

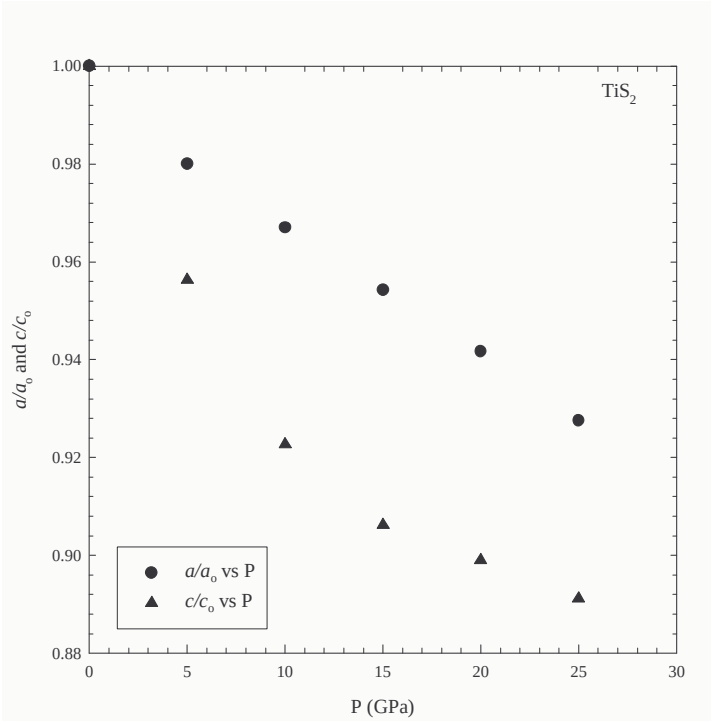

Figure 5-4: The relative lattice parameters a/a_0 and c/c_0 of TiS_2 as a function of pressure.

decreases by 0.018 Å and the titanium-sulfur bond length (d_{T-X}) increases by a small amount of 0.04 Å, affirming that both structures are highly anisotropic having strongly (ionic/covalent) bound layers. The change in the calculated lattice parameters after intercalation $\Delta a_{calc} = a_{L_iTiS_2} - a_{TiS_2} = 0.047$ Å compares well with the experimental $\Delta a_{expt} = 0.059$ Å. Similarly the difference between the calculated $\Delta c_{calc} = c_{L_iTiS_2} - c_{TiS_2} = 0.528$ Å and experimental $\Delta c_{expt} = 0.497$ Å is small enough showing that our predictions follow similar trends with experiment [55, 160, 253, 264]. The calculated lattice parameter a and c for ZrS_2 also underestimate the experimental [55, 149, 263] parameters by 0.5% and 1.2% respectively, while the calculated c/a ratio is 1.577.

The calculated results for the variation of the a/a_0 and c/c_0 lattice parameter with pressure for TiS_2 can be seen in Figures 5-3 and 5-4. On comparison with the experimental work [130] at pressures below 10 GPa (see Fig. 5-3), we note that the variation

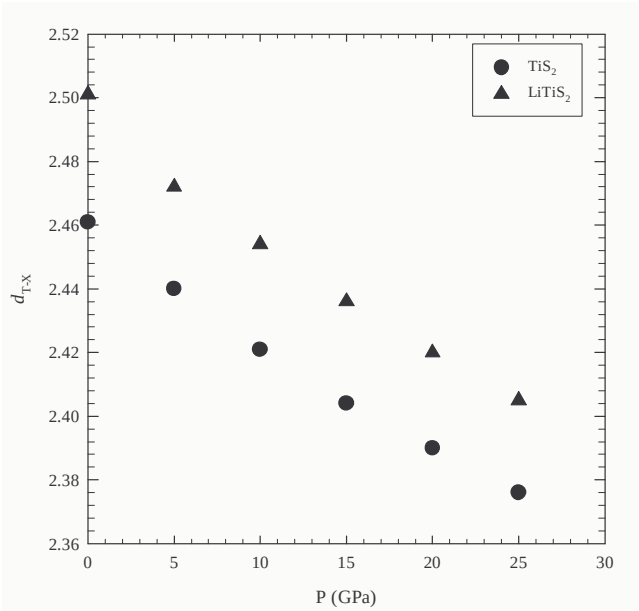

Figure 5-5: Variation of the Sulfur-Titanium bond length with pressure for TiS_2 and $LiTiS_2$.

of a/a_0 of our results compares well experiment. For pressures ranging from $0 - 30$ GPa (see Fig. 5-4), there is a notable deviation (for c/c_0) at pressures around 4 GPa, but this seems to be corrected at higher pressure ($\sim$ 10 GPa). It is clear that the compression is highly anisotropic with the c-axis decreasing rapidly over the pressure range studied. This can be attributed to the ease with which the volume between the octahedra can be reduced compared to distorting the octahedra which would require considerably more energy.

Figure 5-5 shows the variation of the Titanium-Sulfur bond length with pressure for TiS_2 and $LiTiS_2$. The Ti-S bond length decreases uniformly with increasing pressure for both systems. Figure 5-6 shows the variation of the sulfur free parameter (fractional co-ordinate) with pressure (in GPa) in TiS_2 and $LiTiS_2$. The sulfur free parameter increases rapidly with increasing pressure in TiS_2. On intercalation with lithium we note a rather uniform increase with pressure.

Figure 5-7 shows the concentration dependence of the lattice parameters a and c of

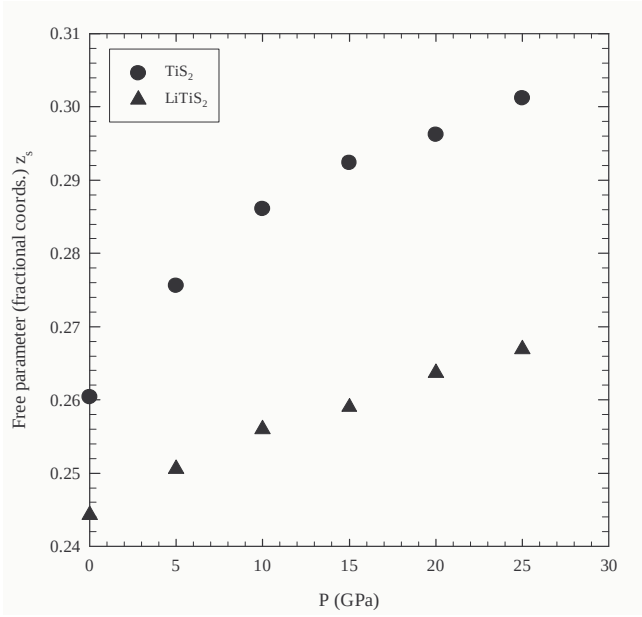

Figure 5-6: Variation of the sulfur free parameter (fractional coordinate) with pressure (in GPa) in TiS_2 and $LiTiS_2$.

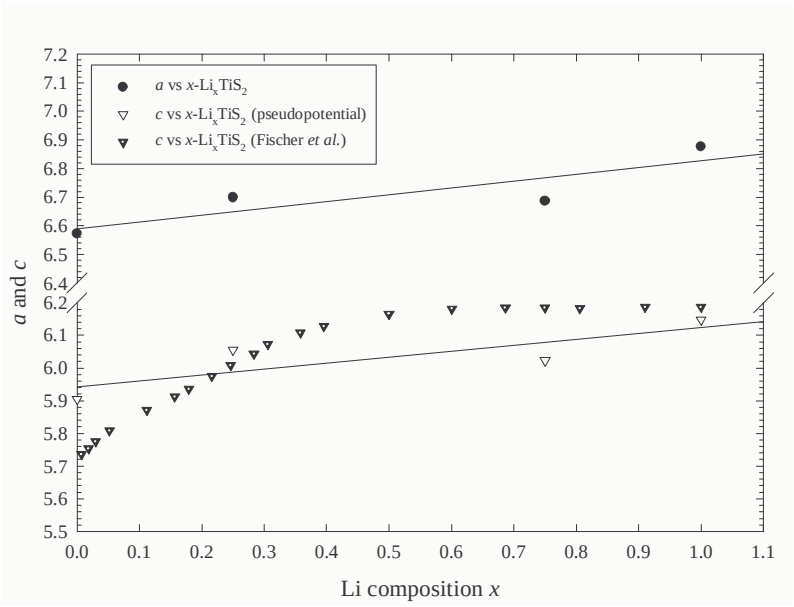

Figure 5-7: Concentration dependence of lattice parameter a and c of Li_xTiS_2 compared with the variation of the stage package thickness with x in Li_xTiS_2 $(0 < x < 1)$ [270].

Li_xTiS_2 compared with the variation of the stage package thickness with x in Li_xTiS_2 ($0 < x < 1$) [270]. Our calculations follow similar trends with the experimental prediction of the variation of the lattice parameter c with increase in Li concentration. The a and c-axis lattice constants increase gradually with x. The TiS_2 layers are stiffer due to the nonplanar Ti-S bonds within these layers. It is expected that the van der Waals gaps are enlarged by intercalated Li atoms and that the Li atoms have little influence on the intralayer spacing of TiS_2. There is no structural change in TiS_2 after intercalating Li atoms, i.e. only stage 1 structure exists, which may reflect the highly anisotropic environment of the Li ions in the intercalation compound where the lithium ion sublattices are effectively two-dimensional. The intercalation compounds of $3d$ transition metals (V, Cr, Mn, Fe, Co, and Ni) into TiS_2 layers also have no staging, as predicted by Inoue *et al.* [78]. Extra conduction electrons in the Cu atoms upon intercalation into TiS_2 have also been reported to have no influence on the staging for the compound Cu_xTiS_2 [174].

5.1.3 Equation of State and Pressure Dependence of Lattice Parameters of TiS_2 and $LiTiS_2$.

Table 5.2: Theoretical and experimental values of the bulk moduli of TiS_2, and Li_xTiS_2 ($0 < x < 1$).

	$B(GPa)$	$B_a(GPa)$	$B_c(GPa)$	$K_a 10^{-3}(GPa)^{-1}$	$K_c 10^{-3}(GPa)^{-1}$
TiS_2 (EOS, This work)	47.29	266.35	62.37	0.38	1.604
TiS_2 (Exp.)[254]	41.00	260.00	61.00	-	-
TiS_2 (Exp.)[69]	-	179.00	59.00	0.56	1.71
TiS_2 (Exp.)[255]	-	-	54.60	-	1.83
TiS_2 (Calc.)[153]	42.00	311.00	58.00	-	-
$LiTiS_2$ (EOS, This work)	74.93	267.57	170.46	0.37	0.59
$LiTiS_2$ (Exp.)[153]	116.00	384.00	295.00	-	-

Table 5.2 shows the theoretical and experimental values of the bulk moduli of TiS_2, and Li_xTiS_2 ($0 < x < 1$). Our calculated bulk modulus B for TiS_2 is in good agreement

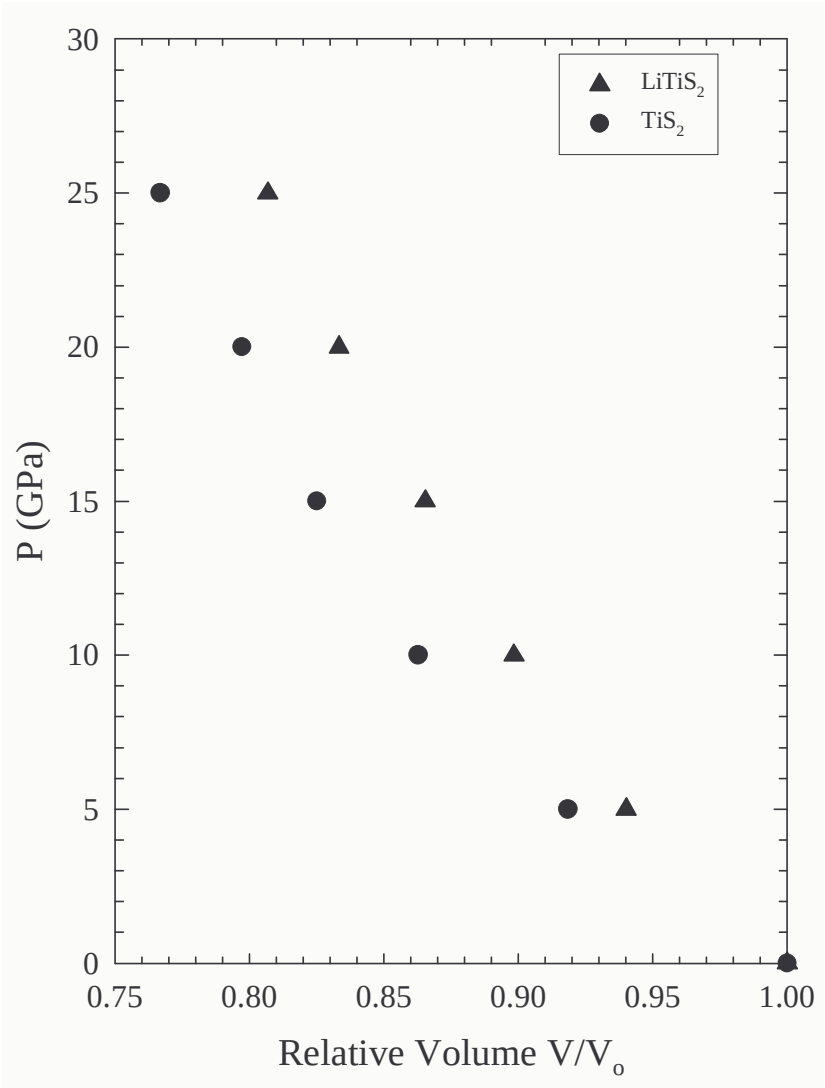

Figure 5-8: Theoretical lattice volume V/V_0 of TiS_2 and $LiTiS_2$ as a function of pressure.

with the experimental results [254] overestimating it by 13%. TiS_2 lattice is said to be soft nature hence enhancing the diffusion of lithium ions, so that very high rates of reaction can be obtained [100]. Similarly, the calculated linear moduli (B_a and B_c) are in good agreement with experimental results [69, 254, 255]. Our predicted B_a agrees within 2% with the results of Negishi *et al.* [254] and a notable 48% overestimation of the results of Zhou *et al.* [69]. This discrepancy is not observed for B_c where our predicted results are within 2% and 6% of the results of Negishi *et al.* [254] and Zhou *et al.* [69] respectively and are 14% values of Scharli *et al.* [255].

Figure 5-8 shows the calculated relative lattice volume V/V_o of TiS_2 and $LiTiS_2$ as a function of pressure. The TiS_2 and $LiTiS_2$ unit cells volume as a function of hydrostatic pressure are calculated from the negative slope of the $E(V)$ curve of equation 4.3. The curve shows a sharp rate of decrease (high compressibility) at lower pressure, which diminishes at higher pressures. The deduced bulk moduli of TiS_2 and $LiTiS_2$ show that intercalation enhances it by 36%. The linear moduli along the c-axis, B_c, tend to increase by approximately 63% on intercalation of lithium into TiS_2, while we observe almost no increase in B_a along the a-axis and $B_c(LiTiS_2)/B_c(TiS_2) \simeq 3$. Differences in intralayer stiffness are relatively small since $B_a(LiTiS_2)/B_a(TiS_2) \simeq 1.00$.

5.1.4 Elastic constants of TiS_2 and $LiTiS_2$

The crystal symmetry of TiS_2 and $LiTiS_2$ is hexagonal, hence there are five independent elastic constants (see G.1). The elastic properties are used to quantify the crystalline bonding strength or stiffness in a specific direction. C_{11} and C_{33} are the longitudinal moduli, where C_{33} is the interlayer stiffness in the c-direction, while the C_{44} and C_{66} are the shear moduli. An investigation of the elastic constants gives considerably more information about the interatomic interactions.

For completeness we have determined the five independent elastic constants. Table 5.3 shows the calculated and experimental elastic constants for TiS_2 and $LiTiS_2$. The DFT derived C_{33} and C_{44} for TiS_2 compares reasonably well with the experimental data

Table 5.3: Elastic constants of TiS_2 and $LiTiS_2$ (in GPa) calculated from PP and also using a density of 3.249 g/cm^{-3}.

	TiS_2		$LiTiS_2$
	This work	Expt. [255]	This work
C_{11}	124.06±0.36	-	140.29±0.24
C_{12}	21.86±0.78	-	30.94±0.40
C_{13}	10.90±0.81	-	22.67±0.30
C_{33}	35.09±0.92	54.6±5.3	113.21±1.41
C_{44}	15.90±4.19	17.9±3.8	40.87±3.72
C_{66}	51.10	-	54.67
$C_{11}+C_{12}$	145.92	-	171.23

[255] underestimating the constants by 35% and 11% respectively. The elastic constants C_{33} and C_{44} are distinctively higher in $LiTiS_2$ than in TiS_2 as one may qualitatively expect from the slightly higher degree of ionicity of the former compound. The interlayer stiffening follows from $C_{33}(LiTiS_2)/C_{33}(TiS_2) \simeq 3$ which also suggests that some degree of weak vd Waal type bonding exists in the interlayer space of TiS_2 which is replaced by the stronger ionic bonding in $LiTiS_2$. $C_{11}+C_{12}$, which is the stiffness in the directions parallel to **ab** plane, increases on intercalation but from $C_{11}+C_{12}(LiTiS_2)/C_{11}+C_{12}(TiS_2) \simeq 1.17$ we note that these intralayer stiffness change is very small. C_{13} which is the stiffness in linear combination of the direction along the c-axis and the direction parallel to the **ab** plane is almost double in $LiTiS_2$ compared to TiS_2. In addition we note that the anisotropy factor C_{11}/C_{33} is rather high (3. 53) for TiS_2 and (1. 24) for $LiTiS_2$ suggesting a shift to nearly isotropic system with intercation.

Further inspection of Table 5.3 indicates that for $LiTiS_2$, a marked stiffening in the **cb** direction occurs with a dramatic reduction of bonding anisotropy relative to results for TiS_2. The reduction of bonding anisotropy for $LiTiS_2$ is evidenced by $C_{11}+C_{12}\ /C_{33} \simeq 1.51$, whereas for TiS_2 we have $C_{11}+C_{12}/C_{33} \simeq 4.16$. C_{13} is less than C_{33} as observed for both TiS_2 and $LiTiS_2$. This is an expected trend for hexagonal systems. The phase Li_1TiS_2 has been observed to be thermodynamically stable compound over the entire range of lithium composition, so that there is no tendency to disproportionate for example

to Li_2S and Ti_2S_3 [100]. Cauchy derived relations for hexagonal materials which holds for atoms interacting with the central forces. The following relations are $C_{13} = C_{55}$ and $C_{66} = \frac{1}{2}(C_{11} - C_{12})$, hence the Cauchy ratios C_{12}/C_{66} and C_{13}/C_{55} must be close to one. From our calculations, the Cauchy ratios for $LiTiS_2$ are $C_{12}/C_{66} \simeq 0.57$ and $C_{13}/C_{55} \simeq 0.55$, and for TiS_2 are $C_{12}/C_{66} \simeq 0.43$ and $C_{13}/C_{55} \simeq 0.69$. These relations are fairly well fulfilled although for TiS_2, $C_{12} \ll C_{11}$ hence the deviation. To investigate this in more details we divide a specific elastic constant with the bulk modulus i.e. $C'_{ij} = C_{ij}/B$, hence normalizing the interatomic forces with an average restoring force of the system. The normalised elastic constants calculated for TiS_2 are $C'_{11} = 4.38$, $C'_{13} = 0.39$ and for $LiTiS_2$ are $C'_{11} = 2.35$, $C'_{13} = 1.89$. Hence the strong component of covalent bonding, is maintained on lithium intercalation thus minimizing the electrostatic repulsion between the lithium and titanium ions.

5.2 Calculation of Voltage Curves and Structural Stability

In this section we discuss the results of average intercalation voltage calculations and structural stability of different concentrations of lithium intercalated TiS_2 structures. We also discuss cohesive energies of both TiS_2 and $LiTiS_2$ and finally discuss the path of lithium along the c-axis. TiS_2 is suitable as a cathode material as it is a semi-metal, has a high energy of formation for the lithium intercalate and can perform more than 1000 intercalation/deintercalation cycles before the charging capacity of the battery is seriously affected [271].

5.2.1 Li Battery System

The cell voltage E, depends on the free energy of the intercalation reaction, which, for the TiS_2 system, can be written as:

$$x\text{Li (anode)} + \text{TiS}_2 \text{ (cathode)} \Longrightarrow \text{Li}_x\text{TiS}_2 \text{ (cathode)} \tag{5.1}$$

where Li is the metallic lithium.

In a metallic Li anode the chemical potential is constant and equal to the Gibbs free energy of Li metal. The potential of an electrochemical cell is obtained from the partial molar free energy, ΔG, of reaction 5.1 using the Nerst relationship. The standard-state free energy of reaction and the standard state cell potential for an electrochemical cell is given by

$$\Delta G = -zFE \tag{5.2}$$

where F is the Faraday constant and z is the charge (in electrons) transported by lithium in the electrolyte. In most nonelectronically conducting electrolytes, $z = 1$ for Li intercalation. The equilibrium voltage between negative and positive electrode is defined as the difference of the lithium chemical potential between the two electrodes:

$$E(x) = -\frac{\Delta G}{zF} = -\frac{\mu_{\mathbf{Li}}^{\text{positive}}(x) - \mu_{\mathbf{Li}}^{\text{negative}}}{zF} \tag{5.3}$$

The open-cell voltage (OCV) of a Li battery is also directly proportional to the chemical potential difference for Li in the anode (negative electrode) and in the cathode (positive electrode). The Gibbs free energy for any process is the maximum amount of work (other than pressure and volume change) that can be done by carrying out that process.

$$\Delta G = \Delta E + p \cdot \Delta V - T \cdot \Delta S \tag{5.4}$$

It was demonstrated by Ceder *et al.*[243] that acceptable average intercalation voltage (AIV) values are obtained when both the volume ($p \cdot \Delta V$) and the entropy ($T \cdot \Delta S$) components of ΔG are neglected. In this study we approximate ΔG by the internal

energy term ΔE, since the contribution on the vibrational and configurational entropy terms to the cell voltage at room temperature are expected to be small ($0 < 0.1$V).

5.2.2 Energies and cell voltages of $\mathbf{Li}_x\mathbf{TiS}_2$ $(0 < x < 1)$

The reversible ion-electron transfer reaction is classically represented by the scheme

$$x\mathbf{Li}^+ + xe^- + \mathbf{TiS}^2 \iff \mathbf{Li}^+\mathbf{TiS}_2^{x-}$$

Table 5.4: Total ground state energy E^{tot} for Li_{metal}, TiS_2 and Li_1TiS_2 unit-cell systems.

	Total energy, E^{tot} (eV)	$\triangle E$ (eV)
Li_{metal}	-187.975	
TiS_2	-2163.981	
$LiTiS_2$	-2354.103	-2.14

in the usual case, where x is the molar intercalation fraction. To calculate the reaction energies, we first consider the unit-cell models of Li_{metal}, TiS_2 and $LiTiS_2$ systems. Table 5.4 report the calculated total ground state energy, E^{tot}, for Li_{metal}, TiS_2 and $LiTiS_2$ systems. From these we calculate the value of $\triangle E$ for the intercalation reaction which is given by:

$$E^{tot}_{\mathbf{Li}_x\mathbf{TiS}_2} - (E^{tot}_{\mathbf{TiS}_2} + E^{tot}_{\mathbf{Li}_{metal}}) = \triangle E \tag{5.5}$$

We obtain a value of 2.14 eV for $\triangle E$. This result can also be compared with the reported experimental data [5, 8, 98, 99] in the range $2.2 - 2.8$ eV per Li for the intercalation of Li from the liquid phase into TiS_2; when corrected for the heat of fusion of lithium, we obtain $2.23 - 2.83$ eV which compares well with our calculated value.

In order to predict the average intercalation voltage for Li_xTiS_2 $(0 \leq x \leq 1)$ we estimate the internal energy by calculating the energy $E(x)$, of a number of Li_xTiS_2 compositions and of lithium metal from the total ground state energy (see Table 5.5).

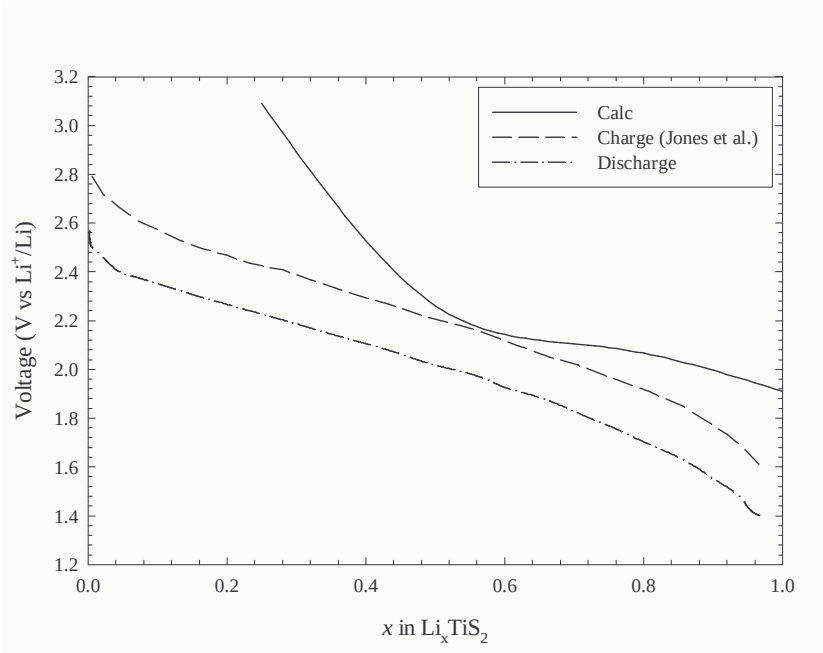

Figure 5-9: A comparison of the predicted average intercalation voltage of Li_xTiS_2 over the theoretical cycle ($0 < x < 1$) with the secondary performance of EBC microbattery [5] over 2500 cycles.

Table 5.5: Total ground state energies E^{tot} and calculated potential for Li_{metal}, TiS_2, $Li_{1.00}TiS_2$, $Li_{0.75}TiS_2$, $Li_{0.5}TiS_2$ and $Li_{0.25}TiS_2$ super-cell systems.

	Total energy, E^{tot} (eV)	E(V)
Li_{metal}	-187.975	
$Li_{0.00}TiS_2$	-8655.131	
$Li_{0.25}TiS_2$	-8846.194	-3.09
$Li_{0.5}TiS_2$	-9036.424	-2.26
$Li_{0.75}TiS_2$	-9226.487	-2.09
$Li_{1.00}TiS_2$	-9416.376	-1.91

Since we have already shown that there is no structural change in TiS_2 after intercalating Li atoms (i.e. x_1 and x_2 concentrations have the same phase), we use the following equation to determine the potential value:

$$E(x_1, x_2) = E^{tot}(\mathbf{Li}_{x_2}\mathbf{TiS}_2) - E^{tot}(\mathbf{Li}_{x_1}\mathbf{TiS}_2) - E^{tot}(\mathbf{Li}_{metal}) \tag{5.6}$$

where $x_1 > x_2$.

The number of configurations (see Fig. 5-2), and therefore, the resolution of the calculated voltage curve, is limited by the size of the simulation cell that is possible to use. We have shown in sub-section 5.1.2 that there is no structural change of the mother phase TiS_2 for Li_xTiS_2 ($0 \leq x \leq 1$) and only stage 1 exist. We therefore set the intercalation limits in this study to $x = 0$ and 1. We employ an ordered structure so that calculations are tractable. Specifically, we define a Li_xTiS_2 supercell by $2\overrightarrow{a}$, $2\overrightarrow{b}$, and $\overrightarrow{c}$. Lithium atoms are then inserted into the octahedral sites to satisfy the conditions $x = 0$, 1/4, 3/4, or 1. The supercell model used is explained in detail on how it is approximated in sub-section 2.3.5.

Figure 5-9 shows a comparison of our calculated average intercalation voltage with the experimental [5] charge and discharge voltage curves of $LiTiS_2$ microbattery. The voltage is highest at the beginning of the battery discharge (when there is no Li present in the cathode) and decreases as discharge brings more Li into the cathode. However, we note that for $x = 0.25$, our predicted curve tends to deviated from experiment. This can be ascribed to the failure in the supercell model at lower concentrations. In general, a relatively flat intercalation curve is desirable for application. Since the open-circuit potential function for Li_xTiS_2 ($0 < x < 1$), is symmetric about $x = 0.5$, the changes in the low-frequency impedance spectra with state of charge are also nearly symmetric about this point.

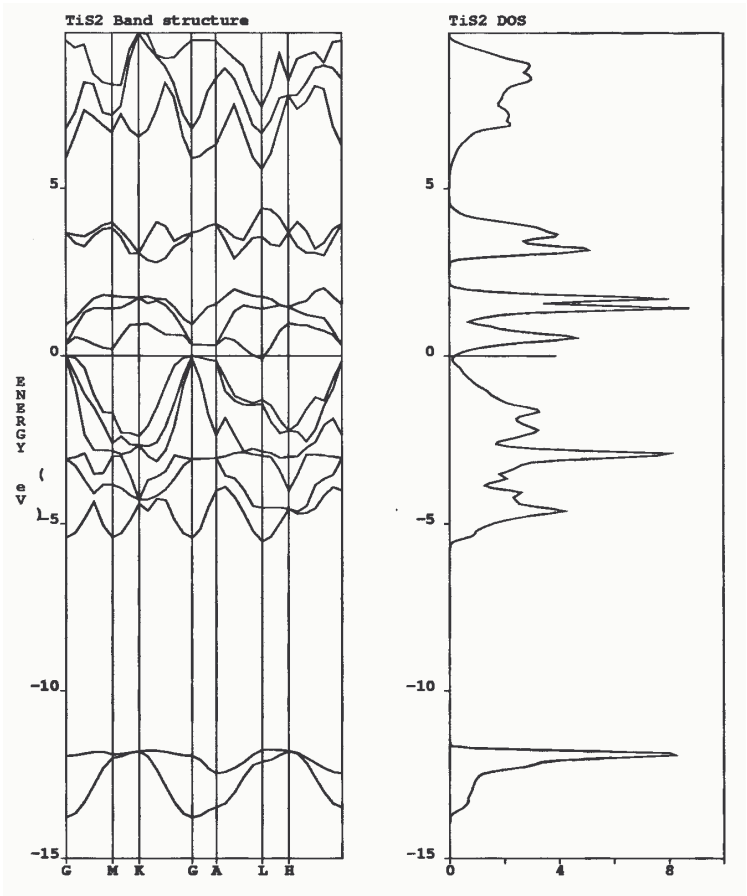

Figure 5-10: A plot of the bandstructure and density of states of TiS_2.

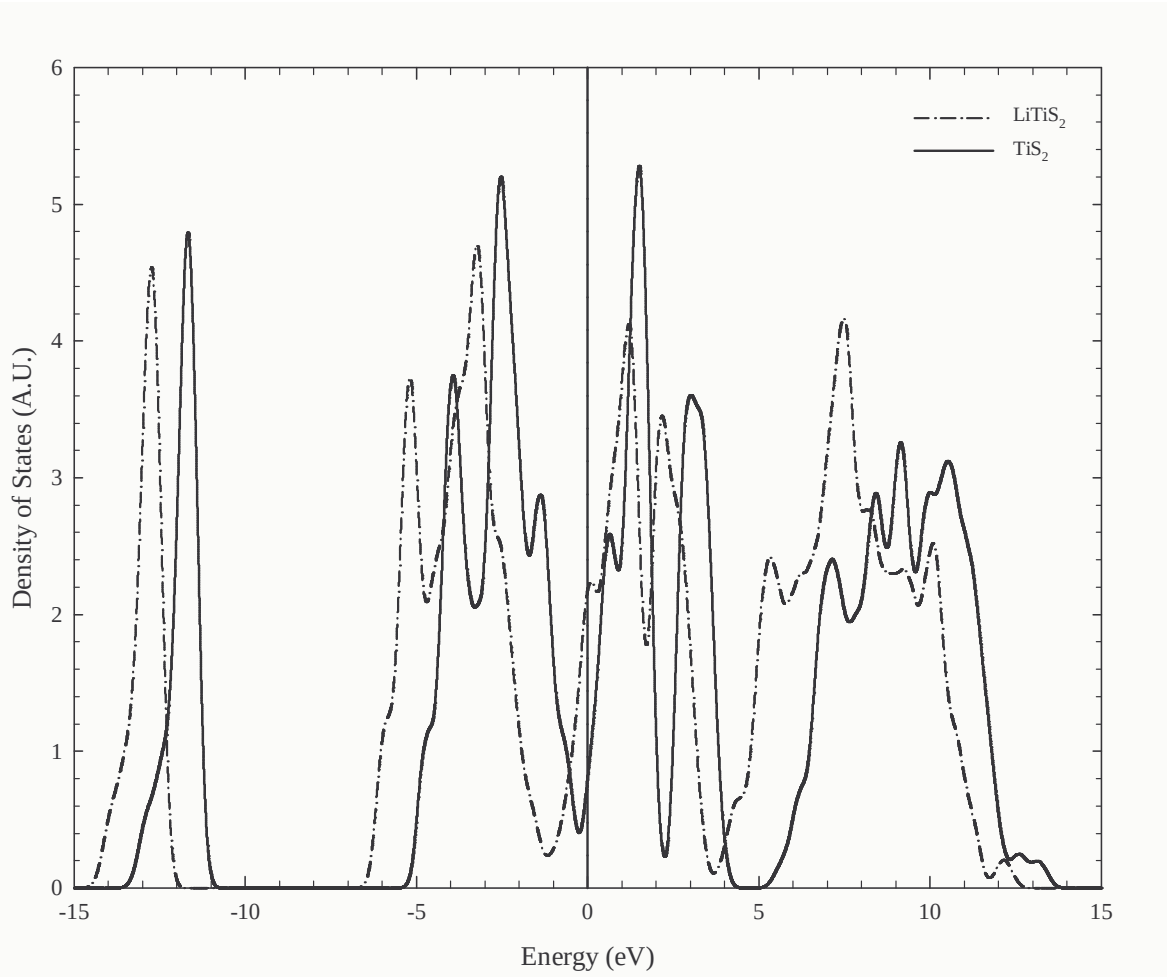

Figure 5-11: A comparison of the total density of states for TiS_2 and $LiTiS_2$.

5.3 Electronic Properties

In this section, the electronic properties of ZrS_2, TiS_2 and $LiTiS_2$ are studied using computed band structures, total densities of states (DOS) and charge density plots. Metallization is further explored by investigating this properties under pressure.

5.3.1 Density of States (DOS) and Bandstructure

There is an abundance of bands from theoretical calculations. We focus our attention to the bandstructure of TiS_2 and ZrS_2, and in particular on how they responds to pressure. Figure 5-10 shows the bandstructure and the density of states of TiS_2. The energy bands are grouped into distinct sets including six valence bands (VB1) directly below the Fermi level, E_F, two valence bands (VB2) below VB1, and five conduction bands (CB1) above VB1. VB1 is derived mainly from S ($3p$) orbitals and Ti ($3d$) contributions while VB2 derives from S($3s$) orbitals, and the lower energy states in CB1 is assigned to Ti ($3d$). The DOS between -5 and 0 eV is derived from S $3p$ orbitals with non-negligible admixture of Ti $3d$ orbitals. The characteristic triplet structure in the valence band spectrum is a result of these S $3p$–Ti $3d$ interactions.

The conduction bands are mostly formed by the $d_{z^2} d_{x^2-y^2}$ and d_{yx} orbitals of T_{2g} symmetry. The first few conduction bands are primarily metal d-like, of which there should be five bands unless an overlap with the antibonding bands occurs. There are enough electrons to fill the predominantly sulfur s-like and p-like valence band. A third band of E_g symmetry is also formed by d_{yz} and d_{xz} orbitals. The d-bands lying in the bonding - antibonding gap are unoccupied unless a p/d overlap occurs. E_F is found in the gap and $N(E_F)$ is almost zero.

Figure 5-11 shows a comparison of our calculated total density of states for TiS_2 and $LiTiS_2$. The simplest approximation to the band structure of an intercalation compound is just that of the parent host compound with the Fermi level moved up to accommodate the extra electrons. We also noted that upon intercalation of lithium into TiS_2, the valence band shift to lower energies and the Fermi level, E_F, also shift in the opposite direction due to the displacement of the first accepting levels and their partial filling. The lower empty levels, which mainly consist of Ti T_{2g} orbitals, have also shifted to a lower energy. In the simple picture, during intercalation, the donating-electrons will occupy one of the empty d-bands. The pseudo-gap increases on intercalation while the density of states are reduced. The E_F can be related the open circuit voltage (OCV) of a lithium

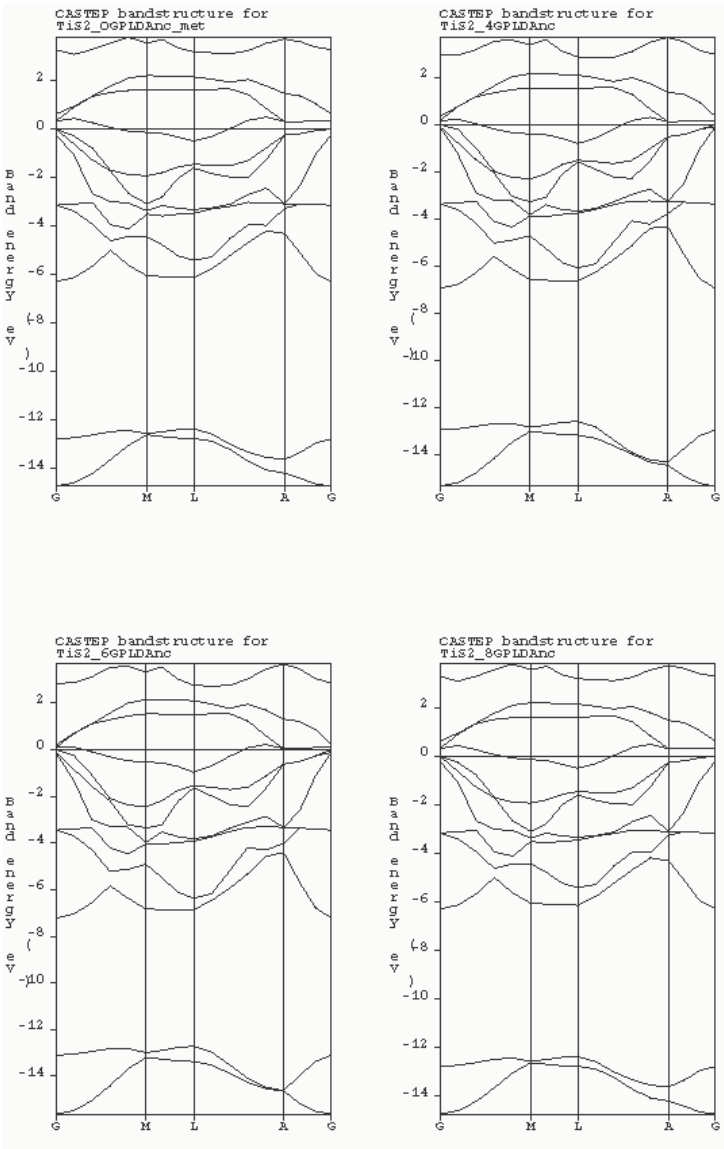

Figure 5-12: Variation of band structure with pressure for TiS_2. At zero pressure the top two bands are unoccupied. The band structure for the calculation at 2 GPa is not shown but is intermediate between those for the 0 and 4 GPa simulations.

battery, which to a first approximation, measures the potential of the first accepting levels of a positive material (E_F) versus the constant value for the electrochemical couple Li/Li^+ [143]. Therefore the E_F displacement must be close to the variation of the OCV.

Our calculated band structures of TiS_2 as they vary with pressure are shown in Figure 5-12. At zero pressure the top two bands are unoccupied. The band structure for the calculation at 2 GPa is not shown but is intermediate between those for the 0 and 4 GPa simulations. While there is no structural phase transition or discontinuity in the compression of the TiS_2 structure to 8 GPa, our calculations reveal a clear band-gap closure from 0 GPa which only occurred at 8 GPa as reported by Allan *et al.* [130]. Our results suggest that TiS_2 is semimetallic at zero pressure. Figure 5-13 shows the calculated pressure variation effect to the bandstructure of ZrS_2. There are two low-lying occupied bands that correspond to the $3s$ and $3p$ orbitals of the S atoms and high-lying empty bands that correspond to the s and p valence orbitals of the Zr atoms. There is a presence of the $4d$ bands above the Fermi level. An overlap into the valence band is observed along the L-symmetry point of the BZ as shown in Fig. 5-14. Hence ZrS_2 metallizes on application of pressure within the range $6 - 8$ GPa.

5.3.2 Charge density of TiS_2 and $LiTiS_2$

Figure 5-15 shows the charge-density plot showing a slice of the total pseudocharge-density of $LiTiS_2$ alongside the total pseudocharge-density difference of $LiTiS_2$ and TiS_2 along the (110) plane that includes the Li atom. To do it, we have performed single-point calculations on a unit-cell whose cell parameters are those of $LiTiS_2$, but without lithium in the van der Waals gap. This hypothetical compound takes into account the structural parameters but neither the change in the coordination number nor the charge transfer from lithium to host. The density varies between 0.03 to 1.13 $e/Å^3$ for the totat pseudocharge density and -0.06 to 0.13 $e/Å^3$ for the pseudocharge-density difference. Due to different plane representation of lithium (Li), sulfur (S) and titanium (Ti) atoms, S and Ti tends to dominate charge distribution plots. We observe a clear high concentration

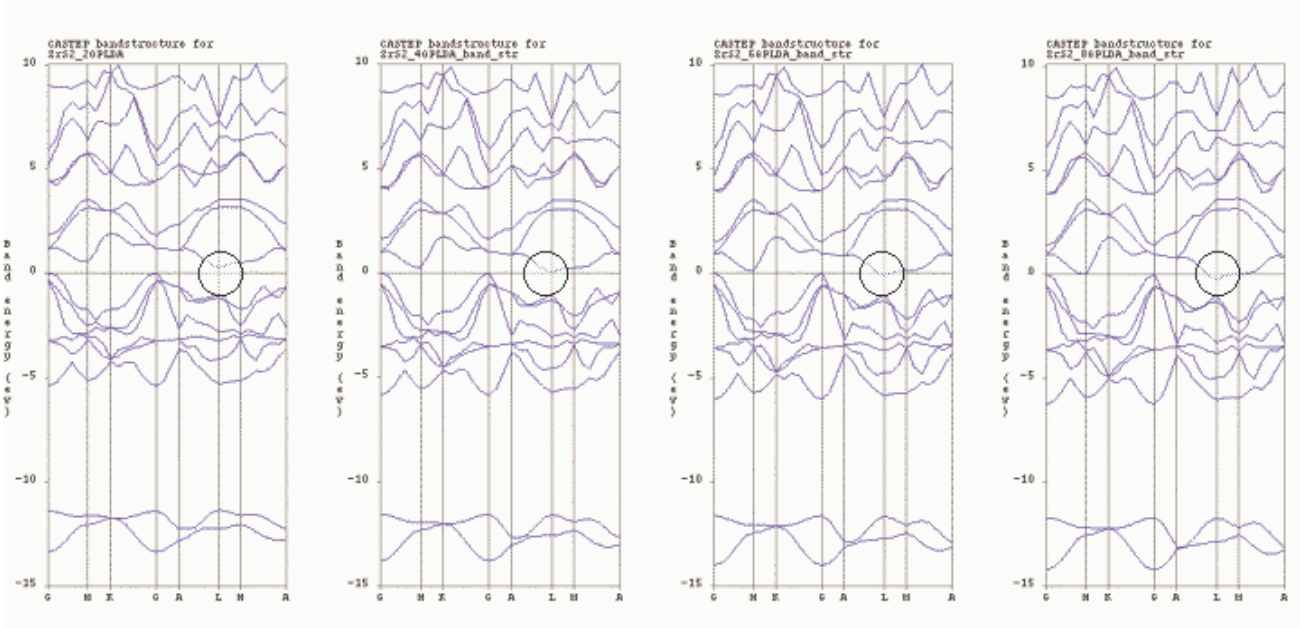

Figure 5-13: Pressure variation effect to the bandstructure of ZrS_2. Metallization is observed along the L-symmetry point of the BZ.

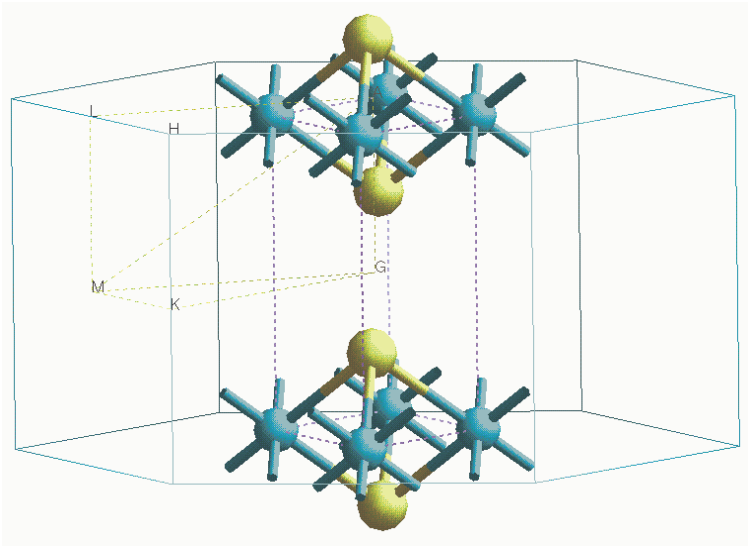

Figure 5-14: Brillouin zone for ZrS_2. The atoms colour is blue for Zr and yellow for S.

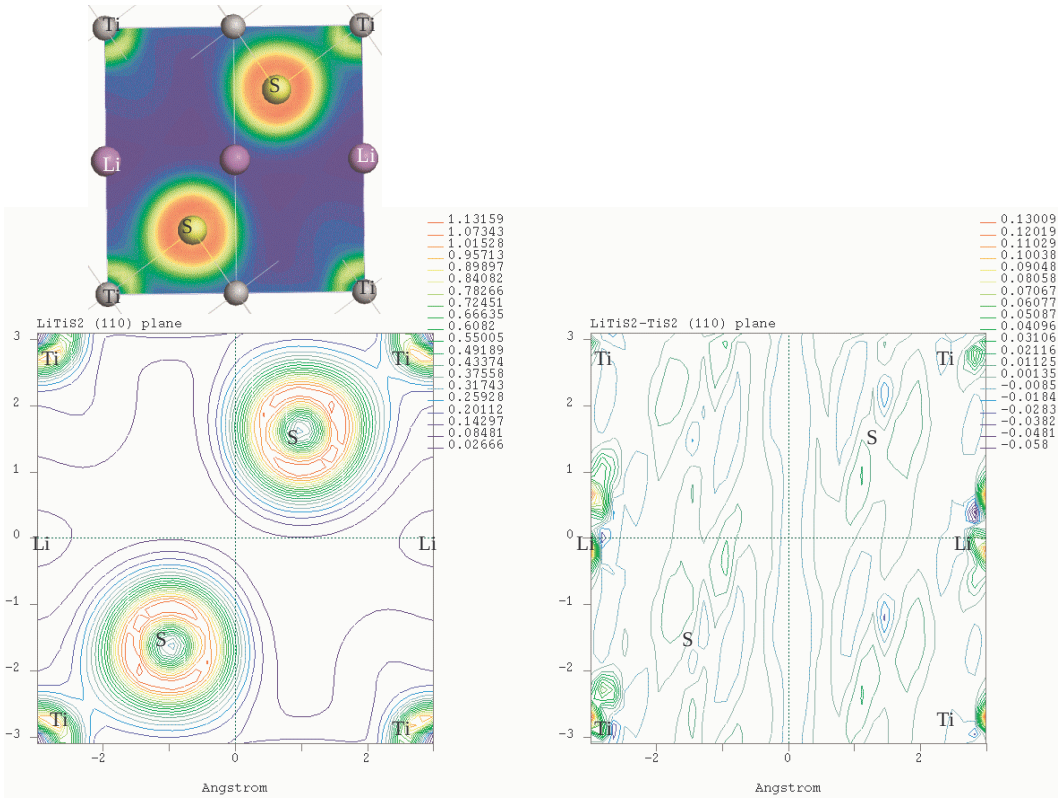

Figure 5-15: The charge-density plot showing a slice of the total pseudocharge-density of $LiTiS_2$ alongside the total pseudocharge-density difference of $LiTiS_2$ and TiS_2 along the (110) plane. The atoms identified belongs to the plane. The color coding is dark blue towards red/magenta for increasing density. The density varies between 0.03 to 1.13 and -0.06 to 0.13 $e/\text{Å}^3$ respectively.

of charges around the S atoms from the Ti (at the corners) towards sulfur atoms for the total pseudocharge-density of $LiTiS_2$. The charge density difference contour plots is relatively structureless. The is a notable high concentration of charges around Li and Ti atoms with the charge around Li moving away towards the Ti atoms.

On intercalation, the sulfur coordination increases from 3 in TiS_2 to 6 in Li_1TiS_2 (with the same bond lengths of S-Li), which increases hybridization. At the same time the Ti-S bond length increase from 2.383 to 2.419 (see Table. 5.1) and this will reduce the hybridization. Finally the hybridization in the ground states S $3p$ and Ti $3d$ will

decrease by the charge transfer from donor Li which increases the Ti electron density transferred in the T_{2g} level. A slight expansion of the lattice in the basal plane, as earlier observed, can be linked to the electron density increasing on the sulfur ions (see Figure. 5-15). This is also evident from the charge density difference plot (see Figure. 5-15) which shows that intercalated Li atoms tends to donate electrons. The spherical shape of the Li region proves the ionic character of the Li atoms. This confirms the fact that intercalated alkali metals has a strong tendency to donate their valence electron, which limits the hybridization between the alkali metal and the host valence band. It has been reported that in Li_xTiS_2, the magnitude of the Hall coefficient (R_H), decreases with increasing lithium content, confirming the occurrence of electron transfer from the intercalate to the host [120, 140, 286].

On intercalation of Li into TiS_2, the electronic chemical potential (i.e. the negative of the electronegativity) increases rapidly as the lattice gains negative charge, and correspondingly diminishes its tendency to acquire more. Experimental observation obtained from NMR studies also shows that as the intercalation proceeds, the electron donation becomes progressively less complete [75]. Mulliken population calculations for TiS_2 gives a charge of $+0.35$ on titanium, counterbalanced by a charge of -0.18 on each sulfur atom. These values are in agreement with the highly covalent character of this compound. The same calculations for $LiTiS_2$ show that $+0.45$ electrons per lithium are given to the host structure. This charge is shared almost equally between the titanium and sulfur atoms, whose charges become $+0.17$ (-0.18) and -0.31 (-0.13) per atom respectively. These results suggest a charge transfer of 0.18 electrons to the titanium d orbital which raises the energy level of the occupied electronic states. ^{7}Li NMR [261] and cell-emf [262] measurements suggest that electron transfer from Li to TiS_2 is not complete above $x = 0.80$, with $10\% - 20\%$ of the valence electron density remaining in the vicinity of the lithium atoms in $LiTiS_2$. Moreau *et al.* [143] also reported a charge transfer of 0.24 electrons from lithium atoms to the TiS_2 host structure for the composition Li_1TiS_2. This transfer is almost equivalent on titanium (0.09 electrons) and sulfur (0.075 electrons) per atom.

5.4 Optical Properties

In order to examine the optical and energy-loss properties of transitional metal dichalcogenides we have first calculated the imaginary parts of the elements of the second-rank dielectric tensor.

5.4.1 Reflectivity and Electron-Energy-Loss Spectra (EELS) with Polarization.

The absorption and reflectance of visible light by a solid is one of the most striking properties of a solid. The wavelength of the visible light falls between approximately 400 nm and 800 nm which corresponds to a photon energy of about 3 eV to 1.5 eV. The UV region is above 3 eV and IR part of the spectrum is below 1.4 eV. These ranges correspond to the energy scale of the levels in the valence region of a solid. Detailed knowledge of the possible electronic excitations in a solid thus enables the prediction of its optical absorption and reflectance properties and also its color. (The perceived color depends on a number of factors such as particle size and surface properties. The calculated optical spectrum of a bulk phase thus represents only the basic ingredient to predict the color of a solid.) In a periodic solid, the most important optical transitions do not change the momentum or the spin of the electrons involved in the transition.

In terms of an energy band structure this means that one has to consider excitations from an occupied to an unoccupied state of the same spin for each k-vector of the Brillouin zone. The intensity of each transition is determined by the dipole matrix elements between the wave functions of the ground state and the excited state. The major difficulty resides in the accurate calculation of transition energies. As was discussed earlier, the one-particle eigenvalues obtained from Hartree-Fock theory are about twice as large as actual excitation energies. On the other hand, DFT-LDA eigenvalues give energy gaps for insulators and semiconductors which are too small, usually by about $30 - 50\%$, but sometimes even lead to qualitative failures. This difficulty does not arise in metals where

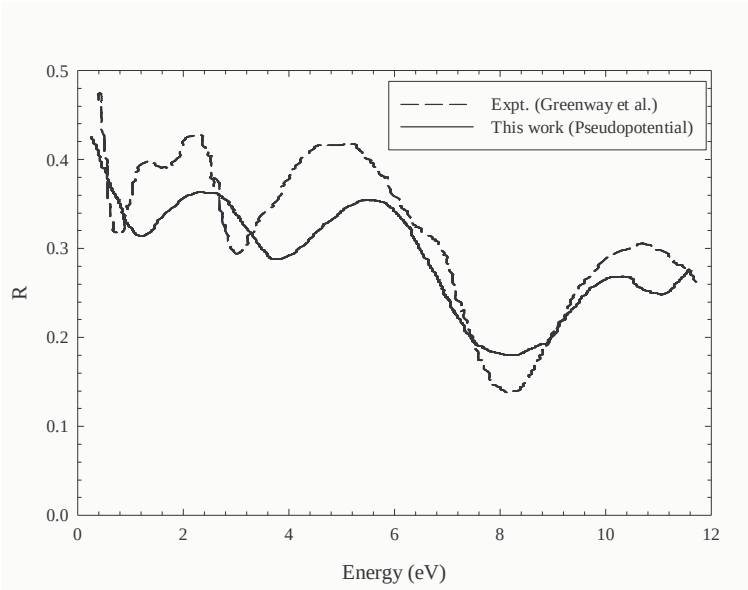

Figure 5-16: A comparison of our calculated and experimental [55] reflectivity spectra of TiS_2

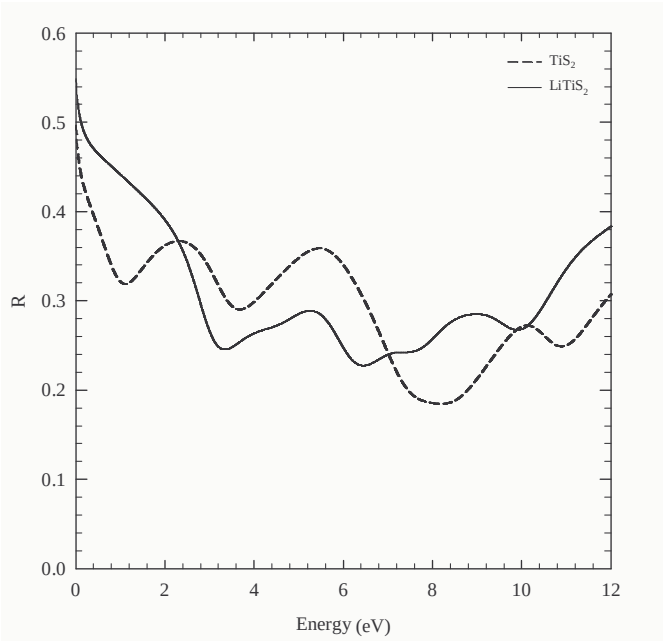

Figure 5-17: Reflectivity spectra of TiS_2 and $LiTiS_2$ for E$\perp c$ polarization.

the screening of the hole left by the excited electron as well as the effective potential experienced by the electron in the excited state are such that the DFT-LDA eigenvalues give a fairly accurate picture of the excitation energies.

TiS_2 Since TiS_2 has an easy cleavage plane parallel to the layer direction, optical calculation were done for the electric vector $\overrightarrow{E}$ perpendicular to the c-axis. Figure 5-16 shows a comparison of our calculated and experimental [55] reflectivity spectra of TiS_2. The agreement between theory and experiment is much better in the energy range $0-12$ eV, where the measurement of reflectivity is direct and the band structure underlying the calculation is more accurate. The calculated R has two pronounced peaks at $\sim$ 2.6 eV,and $\sim$ 6 eV and two minima at around $\sim$ 1.2 eV and $\sim$ 4 eV. For a completeness of the results we compare the calculated reflectivity spectra of TiS_2 with the spectra of $LiTiS_2$. Figure 5-17 shows a comparison of our calculated reflectivity spectra of TiS_2 and $LiTiS_2$. The spectra for $LiTiS_2$ shows a pronounced minima at $\sim$ 3.4 eV and a peak at $\sim$ 5.5 eV. Our calculated spectra resembles that of TiS_2 (see Fig. 5-16) and ZrS_2 (see Fig. 5-18) hence we can conclude that in the absence experimental data, the calculated spectra of $LiTiS_2$ is accurate enough.

ZrS_2 Figure 5-18 shows a comparison of our calculated and experimental [149] reflectivity spectra of ZrS_2. Again we observe a good resemblance of the experimental spectra although our results shows an upward shift towards the left. The calculated R is pronounced at 2 eV and 7 eV with a minimum at around 3.8 eV.

5.5 Concluding Remarks

The calculated crystallographic data of TiS_2, ZrS_2 and $LiTiS_2$ compared with experimental data. Our calculations follow similar trends as the experimental prediction of the variation of the lattice parameter c with increase in Li concentration. The c/a ratios are consistent with the experimental observations for the corresponding layered sulfides.

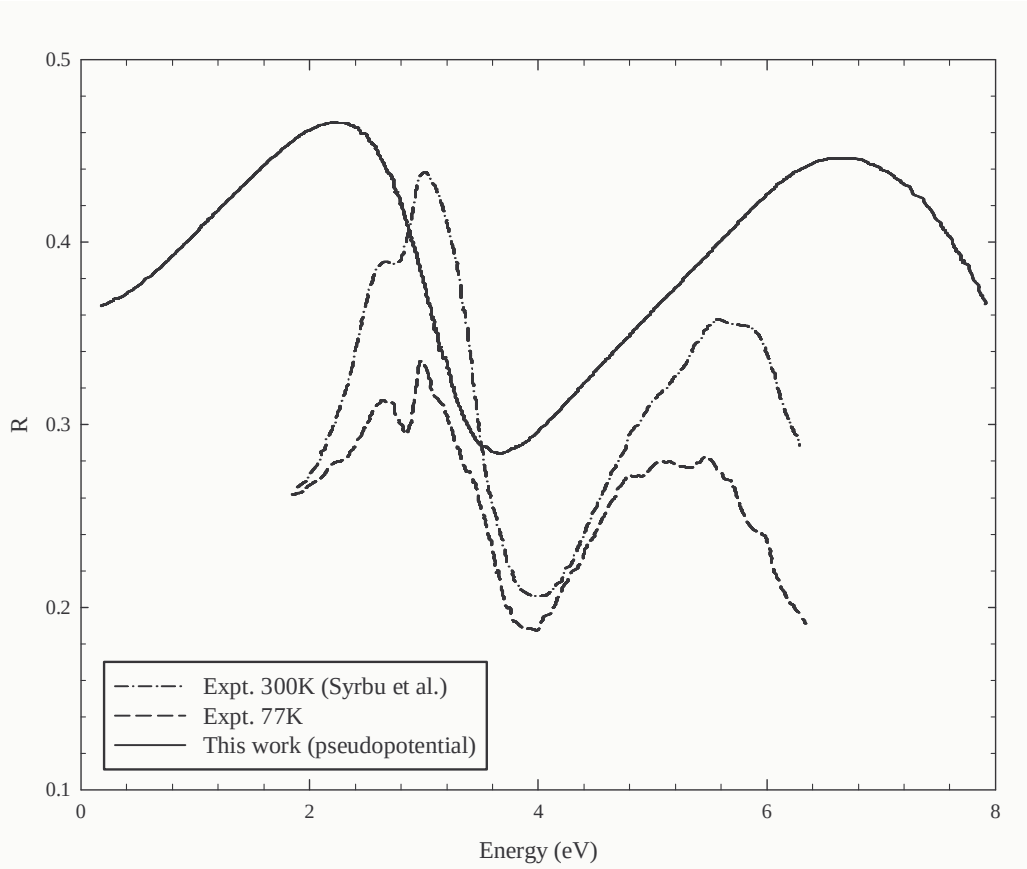

Figure 5-18: A comparison of our calculated and experimental [149] reflectivity spectra of ZrS_2.

The deduced bulk moduli of TiS_2 and $LiTiS_2$ show that intercalation enhances it by 36%. The DFT derived C_{33} and C_{44} for TiS_2 compares reasonably well with the experimental results. The elastic constants C_{33} and C_{44} are distinctively higher in $LiTiS_2$ than in TiS_2 as one may qualitatively expect from the slightly higher degree of ionicity of the former compound.

From the supercell calculations, we have shown that no staging for the compound Li_xTiS_2 ($0 \leq x \leq 1$) is observed. Energetics of the cathode systems $LiTiS_2$ and $LiMo_6S_8$ compares well with experiments. Preliminary results on the calculation of electrochemical properties of cathode materials resembles typical discharge curves for Li/$LiTiS_2$ batteries. The voltage is highest at the beginning of the battery discharge (when there is no Li present in the cathode) and decreases as discharge brings more Li into the cathode. However, we note that for $x = 0.25$, our predicted curve tends to deviated from experiment. This can be ascribed to the failure of the supercell model at lower Li concentrations.

It is evident from the charge density difference plot that intercalated Li atoms are strongly depleted of electron density. Li(*2s*) charge is donated to the Ti(*3d*) and S(*3p*) orbitals, with more distributed on the sulfur atoms. A slight expansion of the lattice in the basal plane is due to the electron density increasing on the sulfur ions. The evidence for the semi-metallic description for TiS_2 is overwhelming. The density of states calculations predicts that E_F for TiS_2 is found in the "gap" and $N(E_F)$ is almost zero while upon intercalation, $N(E_F)$ for $LiTiS_2$ is calculated at ~ 1.5 eV. We observed a filling of the conduction band through charge transfer and the opening of a $p-d$ gap between titanium and sulfur derived states. ZrS_2 metallizes on application of pressure within the range $6-8$ GPa. The net charges obtained for TiS_2 and $LiTiS_2$ via a Mulliken population analysis confirms the highly covalent character of these compounds and a charge transfer upon intercalation.

The calculated optical transition energies for TX_2 ($T =$ Ti, Zr and $X =$ S) systems in the $0 - 12$ eV range compare very favourably with optical reflectance spectra.

Chapter 6

Principal Conclusions and Future Work

We have performed high precision total energy calculations of the Chevrel phase TMC and TMDCs and their intercalation compounds. Lattice parameters of Mo_6S_8 have been calculated within the LDA and GGA with a good reproduction of experimental results. We have studied the insertion of Mg into different positions in Mo_6S_8. The Mg ions prefer to occupy the sixfold crystallographic sites (site A or B) to the origin site, and the final structure adopts a triclinic phase. We reported the first theoretical bulk and linear moduli of the new Chevrel phase structures. Calculated cell voltages are in good agreement with experiment.

We reported the first *ab initio* pseudopotential DOS and partial density of states (PDOS) for $Mg_xMo_6S_8$ ($0 < x \leq 2$). An indication of the energy gap located ~ 1 eV above the Fermi level, characteristic of the Chevrel system was obtained. Our results imply that the insertion of various atoms between the clusters influences the electronic structure around E_F through a change in the intercluster interaction. The increase in the number of electrons after intercalating Mg ions results in the Fermi level moving more closer towards the pseudogap. We have shown that from this type of calculation, an accurate determination of the charge transfer upon intercalation can be made. Charge

transfer from the Mg atom to the cluster is evident, with the transferred density being distributed on both Mo and S atoms.

Our first principles electronic structure calculations reveal that the CdI_2-type structures TiS_2, ZrS_2 and $LiTiS_2$are almost equally stable. The c/a ratios are consistent with the experimental observations for the corresponding layered sulfides. There is no structural change in TiS_2 after intercalating Li atoms, i.e. only stage 1 structure exists. Our calculated energies compared well with the average experimental voltages. A slight expansion of the lattice in the basal plane (**ab** - plane) is due to the electron density increasing on the sulfur ions. The predicted voltage curve resembles the typical charge and discharge curves for Li-ion batteries. The calculated dielectric function for TX_2 (T = Ti, Zr and X = S) systems is in good agreement with experiment for the reflectivity part of the dielectric functions.This results permitted us to present for the first time the calculated reflectivity spectra of $LiTiS_2$.

This work shows the necessary complement between both experimental and theoretical approaches to understand very accurately the electronic structures of intercalated compounds.

6.1 The Future

Niels Bohr, the Nobel Laureate, once cautioned that prediction is always dangerous, especially when it is about the future. With this disclaimer, then, we speculate on what is in store for rechargeable batteries.

The pioneering work of Gregory *et al.* [83] and Aurbach *et al.* [2] demonstrated that a secondary battery of the type Mg/organic electrolyte/insertion cathode is technically feasible. Magnesium-metal electrode was scarcely investigated and a few insertion materials (amongst them $MgMo_6S_8$) have been shown to reversibly accommodate Mg^{2+} ions. We have presented the structures of $Mg_xMo_6S_8$ for a concentration of Mg upto two (2). This should allow further studies on both electronic and structural properties,

hence facilitating considerable improvement needed before a competitive rechargeable magnesium-based battery can be realized.

We have also discussed the voltage profile for $x = 1$ in $Li_xMo_6S_8$ with Li at the origin. The system is said to be undergoing transitions leading to two rhombohedral phase, a rhombohedral phase with an incommensurate lattice distortions, and a triclinic phase [155]. The nature of this change should be studied by using several instrumental techniques to be performed under the high pressure conditions. The density of states and the phonon spectrum are also susceptible to pressure. Further discussions of the range of x from 1 to 4 in $Li_xMo_6S_8$ will be left for future discussion. Chevrel phases have superconducting and thermoelectric properties which can be thoroughly studied using the present theoretical methods. Systematic theoretical and experimental studies are needed to clarify the relationship between the inserted atoms and the electronic structures around E_F. Such information would be useful to finely tune the electronic properties of the Chevrel phase compounds.

Bibliography

[1] J.-M. Tarascon and M. Armand, Nature (London) 414, 359 (2001).

[2] D. Aurbach, Z. Lu, A. Schechter, Y. Gofer, H. Gizbar, R. Turgeman, Y. Cohen, M. Moshkovich, and E. Levi, Nature (London) **407**, 724 (2000).

[3] R. Chevrel, M. Sergent, and J. Prigent, Mater. Res. Bull. **9**, 1487 (1974).

[4] R. Schöllhorn, M. Kümpers, and J. O. Besenhard, Mater. Res. Bull., **12**, 781 (1977).

[5] S. D. Jones, and J. R. Akridge, Solid State Ionics **86**, 1291 (1996).

[6] G. Nagasubramanian, D. H. Shen, S. Surampudi, Q. Wang, and G. K. Surya, Electrochimica Acta. **40**, 2277 (1995).

[7] S. Moon, J. Kim, B. Jin, Y. Hyung, M. Yun, H. Gu, and Y. Ko, J. Power Source **68**, 660 (1997).

[8] K. Onishi, M. Matsumoto, and K. Shigehara, J. Power Source **92**, 120 (2001).

[9] R. Chevrel, M. Sergent, and J. Prigent, J. Solid State Chem. **3**, 515 (1971).

[10] K. Yvon, in *Current Topics in Materials Science*, edited by E. Kaldis (North-Holland, Amsterdam, 1979), Vol. **3**, p. 53.

[11] K. Yvon, R. Chevrel, and M. Sergent, Acta Crystallogr., Sect. B: Struct. Crystallogr. Cryst. Chem. **36**, 685 (1980) and references therein.

[12] J. M. Tarascon, F. J. Disalvo, D. Murphy, G. W. Hull, E. A. Rietman, and J. V. Waszczak, J. Solid State Chem. **54**, 204 (1984).

[13] W. R. McKinnon and J. R. Dahn, Solid State Commun. **52**, 245 (1984).

[14] P. J. Mulhern and R. R. Haering, Can. J. Phys. **62**, 527 (1984).

[15] Y. Takeda, R. Kanno, M. Noda, and O. Yamamoto, Mater. Res. Bull. **20**, 71 (1985).

[16] T. Uchida, K. Watanabe, M. Wakihara, and M. Taniguchi, Chem. Lett. **8**, 1095 (1985).

[17] C. Ritter, E. Gocke, C. Fischer, and R. Schöllhorn, Mater. Res. Bull. **27**, 1217 (1992).

[18] L. Guohua, H. Ikuta, T. Uchida, and M. Wakihara, J. Power Sources **54**, 519 (1995).

[19] R. W. Nunes, I. I. Mazin, and D. J. Singh, Phys. Rev B **59**, 7969 (1999).

[20] C. Roche, R. Chevrel, A. Jenny, P. Pecheur, H. Scherrer, and S. Scherrer, Phys. Rev. B **60**, 16 442 (1999).

[21] P. Novak, R. Imhof, O. Haas, Electrochimica Acta **45**, 351 (1999).

[22] D. Aurbach, R. Turgeman, O. Chusid and Y. Gofer, Electrochim. Comm. **3**, 252 (2001).

[23] K. Yvon, A. Paoli, R. Flükiger, and R. Chevrel, Acta Crystallogr., Sect. B: Struct. Crystallogr. Cryst. Chem. **33**, 3066 (1977).

[24] R. Chevrel and M. Sergent, in *Topics in Current Physics*, edited by Ø. Fischer and M. B. Maple (Springer-Verlag, Berlin, 1982), Vol. **32**, p. 25.

[25] J. Guillevic, O. Bar, and D. Grandjean, J. Solid State Chem. **7**, 158 (1973).

[26] J. Guillevic, O. Bars, and D. Grandjean, Acta Crystallogr., Sect. B: Struct. Crystallogr. Cryst. Chem. **32**, 1338 (1976).

[27] J. D. Jorgensen, D. G. Hinks, D. R. Noakes, P. J. Viccaro, and G. K. Shenoy, Phys. Rev. **B 27**, 1465 (1983).

[28] Ø. Fischer, in *Proceedings 14th International Conference on Low Temperature Physics*, edited by M. Krusius and H. Vuorio (North-Holland, Amsterdam, 1975), Vol. **5**, p. 172.

[29] D. Aurbach, Y. Gofer, Z. Lu, A. Schechter, O. Chusid, H. Gizbar, Y. Cohen, V. Ashkenazi, M. Moshkovich, R. Turgeman, and E. Levi, J. Power Sources **97**, 28 (2001).

[30] E. Levi, Y. Gofer, Y. Vestfreed, E. Lancry, and D. Aurbach, Chem. Mater. **14**, 2767 (2002).

[31] M. Winter, J. O. Besenhard, M. E. Spahr, and P. Novak, Adv. Mater. **10**, 725 (1998).

[32] K. Kobayashi, A. Fujimori, T. Ohtani, I. Dasgupta, O. Jepsen, and O. K. Andersen, Phys. Rev. B **63**, 195109 (2001).

[33] L. F. Mattheiss and C. Y. Fong, Phys. Rev. B **15**, 1760 (1977).

[34] D. W. Bullett, Phys. Rev. Lett. **39**, 664 (1977).

[35] O. K. Andersen, W. Klose, and H. Nohl, Phys. Rev. B **17**, 1209 (1978).

[36] T. Jarlborg and A. J. Freeman, Phys. Rev. Lett. **44**, 178 (1980).

[37] H. Nohl, W. Klose, and O. K. Andersen, in *Superconductivity in Ternary Compounds I*, edited by Ø. Fischer and M. B. Maple, Vol. **32** *of Topics in Current Physics* (Springer, Berlin, 1982), p. 165.

[38] J. K. Burdett and J.-H. Lin, Inorg. Chem. **21**, 5 (1982).

[39] T. Hughbanks and R. Hoffmann, J. Am. Chem. Soc. **105**, 1150 (1983).

[40] D. Certain, A. Le Beuze and R. Lissillour, Solid State Comm. **46**, 7 (1983).

[41] C. Fischer, E. Gocke, U. Stege, and R. Schöllhorn, J. Solid State Chem. **102**, 54 (1993).

[42] S. Belin, R. Chevrel, and M. Sergent, J. Solid State Chem. **155**, 250 (2000).

[43] R. N. Shelton, *Superconductivity in d and f Band Metals*, ed D.H. Douglass (New York: Plenum) p. 137.

[44] A. W. Webb and R. N. Shelton, J. Phys F: Metal Phys., **8**, 261 (1978) .

[45] C. W. Chu, S. Z. Huang, C. H. Lin, R. L. Meng, M. K. Wu, and P. H. Schmidt, Phys. Rev. Lett. **46**, 276 (1981).

[46] D. W. Harrison, K. C. Lim, J. D. Thompson, C.Y. Huang, P. D. Hambourger, and H. L. Luo, Phys. Rev. Lett. **46**, 280 (1981).

[47] R. Baillif, A. Dunand, J. Muller, and K. Yvon, Phys. Rev. Lett. **47**, (1981) 672.

[48] R. N. Shelton and A. R. Moodenbaugh, Phys. Rev. B **24**, 2863 (1981).

[49] M. M. Abd-Elmeguid and H. Micklitz, J. Phys. C: Solid State Phys. **15**, L479 (1982).

[50] M. Decroux, M. S. Torikachvili, M. B. Maple, R. Baillif, Ø. Fischer, and J. Muller, Phys. Rev B **28**, 6270 (1983).

[51] R. Baillif, K. Yvon, R. Flükiger, and J. Muller, J. Low Temp. Phys. **37**, 231 (1979).

[52] D. W. Capone II, R. P. Guertin, S. Foner, D. G. Hinks, and H.C. Li, Phys. Rev. B **29**, 6375 (1984).

[53] N. J. C. Ingle, T.C. Willis, D. C. Larbalestier and C. Meingast, Physica C **308**, 191 (1998).

[54] P. Chadda, I. K. Gopalakrishnan, J. V. Yakhmi, and B. K. Godwai, Phys. Rev. B **36**, 3941 (1987).

[55] D. L. Greenaway and R. Nitsche, J. Phys. Chem. Solids **26**, 1445 (1965).

[56] L. E. Conroy, K. C. Park, Inorg. Chem. **7**, 459 (1968).

[57] J. A. Wilson and A. D. Yoffe, Adv. Phys. **18**, 193 (1969).

[58] P. A. Lee, G. Said, and R. Davis, Solid State Commun. **7**, 1359 (1969).

[59] A. R. Beal, J. C. Knights, and W. Y. Liang, J. Phys. C: Solid State Phys. **5**, 3531 (1972).

[60] H. W. Myron, and A. J. Freeman, Phys. Lett. A **44**, 167 (1973).

[61] R. V. Kasowski, Phys. Rev. Lett. **30,** 1175 (1973).

[62] J. A. Benda, Phys. Rev. B **10**, 1409 (1974).

[63] C. Mankai, G. Martinez, and O. Gorochov, Phys. Rev. B **16,** 4666 (1977).

[64] R. H. Friend, D. Jérome, and A. D. Yoffe, J. Phys. C: Solid State Phys. **15**, 2183 (1982).

[65] W. Y. Liang, in *Intercalation in Layered Materials*, eds by M.S. Dresselhaus (Plenum, New York, 1986), p. 31

[66] M. Inoue, M. Koyano, H. Negishi, and Y. Veda. J. Phys. Soc. Jpn., **55**, 1400 (1986).

[67] R. H. Friend, and A.D. Yoffe, Adv. Phys. **36**, 1 (1987).

[68] A. D. Yoffe, Solid State Ionics **39**, 1 (1990).

[69] O. Zhou, J. E. Fischer, and K. S. Liang, Phys. Rev. **B 44**, 7243 (1991).

[70] W. Muller-Warmuth, and R. Schollhorn, Eds. *Progress of Intercalation Research*, (Kluwer Academic, Dordrecht, 1994).

[71] M. G. Faba, D. Gonbeau, and G. Pfister-Guillouzo, J. Electron Spectrosc. **73**, 65 (1995).

[72] H. E. Brauer, H. I. Starnberg, L. J. Hollenboom, H. P. Hughes, and V .N. Strocov, J. Phys. Condens. Matter **11**, 8957 (1999).

[73] B. G. Silbernagel, Solid State Comm. **17**, 361 (1975).

[74] M. S. Whittingham, and F. R. Gamble, Mater. Res. Bull. **10**, 363 (1975).

[75] B. G. Silbernagel, and M. S. Whittingham, J. Chem. Phys. **64**, 3670 (1976).

[76] M. S. Whittingham, Science, **192**, 1126 (1976).

[77] M. I. Nathan, M. W. Shafer, and J. E. Smith, Jr., Bull. Am. Phys. Soc. **17**, 336 (1972).

[78] M. Inoue, H. P. Hughes, and A.D. Yoffe, Adv. Phys. **38**, 565 (1989).

[79] M. J. Mckelvy, and W. S. Glaunsinger, J. Solid State Chem. **67**, 142 (1987).

[80] C. Julien, T. Sekine, and M. Balakanski, Solid State Ionics. **48**, 225 (1991).

[81] N. Imanishi, M. Toyoda, Y. Tadeka, and O. Yamamoto, Solid State Ionics. **58**, 333, (1992).

[82] B. Scrosati, A. Magistris, C. M. Mari, and G. Mariotto, Eds. *Fast Transport in Solids* NATO ASI Series, Series E: Applied Sciences; Vol. **250**, (1993).

[83] T. D. Gregory, R. J. Hoffman, and R. C. Winterton, J. Electrochem. Soc. **137**, 775 (1990).

[84] J. P. Pereira-Ramos, R. Messina, and J. Perichon, J. Electroanal. Chem. **218**, 241 (1987).

[85] P. G. Bruce, F. Krok, J. Nowinski, V. C. Gibson, and K. Tavakkoli, J. Mater. Chem. **1**, 705 (1991).

[86] P. Novak and J. Disilvestro, J. Electrochem. Soc. **140**, 140 (1993).

[87] J. L. Acosta and E. Morales, Electrochimica Acta. **43**, 791 (1998).

[88] K. Makino, Y. Katayama, T. Miura, and T. Kishi, J. Power Sources. **99**, 66 (2001).

[89] P. Novák, W. Scheifele, and O. Haas, J. Power Sources. **54**, 479 (1995).

[90] G. Kumar, A. Sivashanmugam, N. Muniyandi, S. K. Dhawan, and D. C. Trivedi, Synth. Met. **80**, 279 (1996).

[91] M. S. Whittingham, Prog. Solid State Chem. **12**, 41 (1978).

[92] T. Uchida, K. Kohiro, H. Hinode, M. Wakihara, and M. Taniguchi, Mater. Res. Bull. **22**, 935 (1978).

[93] B. Scrosati, Nature (London) **373**, 557 (1995).

[94] A. R. Armstrong, and P. G. Bruce, Nature (London) **381**, 499 (1996).

[95] T. Naguara and K. Takazawa, Prog. Batteries sol. Cells. **9**, 20 (1990).

[96] K. Brandt, Solid State Ionics **69**, 173 (1994).

[97] Y. Nishi, in: M. Wakihara, O. Yamamoto (Eds), *Lithium Ion Batteries*, Kodansha and Wiley-VCH, Tokyo (Japan), 1998, Chap 8.

[98] S. Hatake, J. Kuwano, M. Miyamori, Y. Saito, S. Koyama, J. Power Source, **68**, 416 (1997).

[99] Y. Chen, J. W. Evans, and G. Scharrer, J. Power Source **70**, 240 (1998).

[100] M. S. Whittingham, R. Chen, T. Chirayil, and P. Zavalij, Solid State Ionics **94**, (1997).

[101] H. Hinode, Y. Ohira, and M. Wakihara, Thermochim. Acta. **282**, 331 (1996).

[102] N. Lemée, M. Guilloux-Viry, J. Padiou, A. Perrin, M. Sergent, J. Lesueur, and F. Lalu, Solid State Commun. **101**, 909 (1997).

[103] N. Lemée, M. Guilloux-Viry, V. Ferré, A. Perrin, M. Sergent, J. Lesueur, and F. Lalu, J. Alloys and Compounds **262-263**, 54 (1997).

[104] N. Lemée, M. Guilloux-Viry, A. Perrin, M. Kugler, Ø. Fischer, Z. Z. Li, and H. Raffy, Thin Solid Films **353**, 62 (1999).

[105] F. C. Brown, B. A. Bunker, D. M. Ginsberg, T. J. Miller, W. M. Miller, and E. A. Stern, Phys. Rev. **B 34**, 7698 (1986).

[106] S. D. Bader, G. S. Knapp, S. K. Sinha, P. Schweiss, and B. Renker Phys. Rev. Lett. **37**, 344 (1976).

[107] S. D. Bader and S. K. Sinha, Phys. Rev **B 18**, 3082 (1978).

[108] J. M. Friedt, C. W. Kimball, A. T. Aldred, B. D. Dunlap, F. Y. Fradin, and G. K. Shenoy, Phys. Rev. **B 29**, 3863 (1984).

[109] A. Fujimori, M. Sekita, and H. Wada, Phys. Rev. **B 33**, 6652 (1986).

[110] F. Y. Fradin, G. K. Shenoy, B. D. Dunlap, A. T. Aldred, and C. W. Kimball, Phys. Rev. Lett. **38**, 719 (1977).

[111] P. Fumagalli and J. Schoenes, Phys. Rev. **B 44**, 2246 (1991).

[112] P. Birrer, F. N. Gygax, B. Hitti, E. Lippelt, A. Schenck, M. Webber, D. Cattani, J. Cors, M. Decroux, and Ø. Fischer, Phys. Rev. **B 48**, 16589 (1993).

[113] C. Roche, P. Pecheur, G. Toussaint, A. Jenny, H. Scherrer, S. Scherrer, J. Phys.: Condens. Matter **10**, L333 (1998).

[114] A. R. Beal, and W. Y. Liang, Phil. Mag. **27**, 1397 (1973).

[115] A. R. Beal, and W. Y. Liang, Phil. Mag. **33**, 121 (1976).

[116] J. V. Acrivos, W. Y. Liang, J. A. Wilson, and A. D. Woffe, J. Phys. C: Solid State Phys. L **3**, 18 (1971).

[117] R. H. Friend, A. R. Beal, and A. D. Yoffe, Phil. Mag. **35**, 1269 (1977).

[118] A. Zunger, and A. J. Freeman, Phys. Rev. B **16**, 906 (1977).

[119] A.M. Ghorayeb, R. H. Friend, J. Phys. C: Solid State Phys. **20**, 4181 (1987).

[120] P. C. Klipstein, and R. H. Friend, J. Phys. C **17**, 2713 (1984).

[121] H. E. Barz, A. S. Cooper, P. H. E. Coren, M. Marezio, B. T. Matthias, and P. H. Schmidt, Science **175**, 884 (1972).

[122] R. B. Somono, V. Hadek, A. Rembaum, J. Chem. Phys. **58**, 687 (1973).

[123] L. Bernard, W. Glaunsinger, and P. Colombet, Solid State Ionics **17**, 81 (1985).

[124] L. A. Brown, W. S. Glausinger, and M. J. McKelvy, J. Solid State Chem. **147**, 38 (1999).

[125] F. R. Sheperd, and P. M. Williams, J. Phys. C **7**, 4416 (1974).

[126] A. H. Thompson, Phys. Rev. Lett. **35**, 1786 (1975).

[127] C. H. Chen, W. Fabian, F. C. Brown, K. C. Woo, B. Davies, B. DeLong, and A. H. Thompson, Phys. Rev. B **21**, 615 (1980).

[128] N. Suziki, Y. Yamasaki, K. Motizuki, J. Phys. C **8**, 201 (1988).

[129] Z. Y. Wu, F. Lemoigno, P. Gressier, G. Ouvrard, P. Moreau, J. Rouxel, C. R. Natoli, Phys. Rev. B **54**, 11 009 (1996).

[130] D. R. Allan, A. A. Kelsey, S. J. Clark, R. J. Angel, and G. J. Ackland, Phys. Rev. B **57**, 5106 (1998).

[131] E. M. Logothetis, W. J. Kaiser, C. A. Kukkonen, S. Faile, R. Colella, and J. Gambold, Physica B **99**, 193 (1980).

[132] C. A. Kukkonen, W. J. Kaiser, E. M. Logothetis, B. Blumenstock, P. A. Schroeder, S. P. Faile, R. Colella, and J. Gambold, Phys. Rev. B **24**, 1691 (1981).

[133] H. Kobayashi, K. Sakashita, M. Sato, T. Nozue, T. Susuki, and T. Kamimura, Physics B **237-238**, 169 (1997).

[134] H. Martinez, S. F. Matar, C. Auriel, M. Loudet, and G. Psister-Guillouzo, J. Alloys and Compounds, **254**, 30 (1996).

[135] G. Ouvrard, and D. Guyomard, Current Opin. Sol. State Mater. Sci. **1**, 260 (1996).

[136] J. V. McCanny, J. Phys. C: Solid State Phys., **12**, 3263 (1979)

[137] W. R. McKinnon, in : A. P. Legrand, S. Flandrois (eds), *Chemical Physics of Intercalation*, Plenum Press, New York, (1987), p. 181.

[138] C. Umrigar, D. E. Ellis, D. Wang, H. Krakauer, and M. Posternak, Phys. Rev. **B 26**, 4935 (1982).

[139] L. Kosidowski, A. V. Powell, and J. Mayers, Physica B **241-243**, 335 (1998).

[140] C. Julien, I. Samaras, O. Gorochov,and A. M. Ghorayeb, Phys. Rev. B **45**, 13390 (1992).

[141] H. I. Starnberg, H. E. Brauer, P. O. Nilsson, L. J. Hollenboom, and H. P. Hughes, Mol. Cryst. **244**, 391, (1994).

[142] H. E. Brauer, H. I. Starnberg, L. J. Hollenboom, and H. P. Hughes, J. Phys. Condens. Matter **6**, 7741, (1995)

[143] P. Moreau, G. Ouvrard, P. Gressier, P. Ganal, and J. Rouxel, J. Phys. Chem. Sol. **57**, 1117 (1996)

[144] Z. Y. Wu, G. Ouvrard, S. Lemaux, P. Moreau, P. Gressier, F. Lemoigno, and J. Rouxel, Phys. Rev. Lett. **77**, 2101 (1996).

[145] G. Ouvrard, and Z. Wu, Nuclear Instruments and Methods in Physics Research B **133**, 120 (1987)

[146] S. C. Bayliss, and W. Y. Liang. J. Phys. C **15**, 1283 (1982).

[147] S. C. Bayliss, and W. Y. Liang, J. Phys. C: Solid State Phys. **12**, 3239 (1972).

[148] G. Peloguin, R. Provencher, S. Jandl, and M. Aubin, J. Phys. C: Solid State Phys. **19**, 3141 (1986).

[149] N. N. Syrbu, V. Z. Cebotari, N.P. Moldoveanu, J. Appl. Phys. **35**, 6126 (1996).

[150] A. Borghesi, Chen Chen-jia, G. Guizzetti, L. Nosenzo, E. Reguzzoni, and A. Stella, Phys. Rev. **B 33** 2422 (1986).

[151] W. B. Clark, J. Phys. C: Solid State Phys. L **9**, 693 (1976).

[152] J. von Boehm and H. M. Isomäki, Phys. Rev. B **26**, 5798 (1982).

[153] D. G. Clerc, R. D. Poshusta, and A. C. Hess, J. Phys. Chem. A **101**, 8926 (1997).

[154] J. R. Dahn, W. R. McKinnon, and S. T. Coleman, Phys. Rev. B **31**, 484 (1985).

[155] W. R. McKinnon and J. R. Dahn, Phys. Rev B **31**, 3084 (1985).

[156] L. W. ter Haar and F. J. Di Salvo, Solid State Commun **60**, 305 (1986).

[157] L. S. Selwyn, W. R. McKinnon, J. R. Dahn, and Y. Le Page, Phys. Rev. B **33**, 6405 (1986).

[158] K. Suzuki, T. Iijima and M. Wakihara, Solid State Ionics 109, 311 (1998).

[159] C. Boulanger and J. M. Lecuire, Electrochemica Acta. **33**, 1573 (1988).

[160] M. S. Whittingham, Electrochem. Soc. **122**, 70C (1975).

[161] M. S. Whittingham, Electrochem. Soc. **123**, 315 (1976).

[162] J. N. Reimers and J. R. Dahn, Phys. Rev. B **47**, 2995 (1993).

[163] M. K. Aydinol, A.F. Kohan, G. Ceder, K. Cho, and J. Joannopoulos, Phys. Rev. B **56**, 1354 (1997).

[164] I. A. Courtney, J. S. Tse, Ou Mao, J. Hafner, and J. R. Dahn, Phys. Rev. B **58**, 15 583 (1998).

[165] E. Deiss, A. Wokaun, J. L. Barass, C. Daul, and P. Dufek, J. Electrochem. Soc. **144**, 3877 (1997).

[166] L. Benco, J-L. Barras, M. Atanasov, and C. Daul, J. Solid State Chem. **145**, 503 (1999).

[167] M. Doyle, J. P. Meyers, and J. Newman, J. Electrochem. Soc. **147**, 99 (2000).

[168] J. S. Braithwaite, C. R. A. Catlow, J. H. Harding, and J. D. Gale, Phys. Chem. Chem. Phys. **2**, 3841 (2000).

[169] J. S. Braithwaite, C. R. A. Catlow, J. D. Gale, J. H. Harding, and P. E. Ngoepe, J. Mater. Chem.**10**, 239 (2000).

[170] J. S. Braithwaite, C. R. A. Catlow, J. H. Harding, and J. D. Gale, Phys. Chem. Chem. Phys. 3, 3841 (2001).

[171] M. V. Koudriachova, N. M. Harrison, and S.W. de Leeuw, Phys. Rev. Lett. **86**, 1275 (2001).

[172] M. V. Koudriachova, N. M. Harrison, and S.W. de Leeuw, Phys. Rev. B **65**, 235423 (2002).

[173] K. R. Kganyago, P. E. Ngoepe, and C. R. A. Catlow, Solid State Ionics 159, 21 (2003).

[174] T. Kusawake, Y. Takahashi, and K. Ohshima, Materials Research Bulletin. **33**, 1009 (1998).

[175] M. P. Allen, M. P.and D. J. Tildesley, Computer Simulation of Liquids, Clarendon Press, Oxford Science Publications (1987).

[176] W. F. van Gunsteren, and P. K. Weiner, Computer Simulation of Biomolecular Systems, ESCOM, Leiden (1989).

[177] G. V. Lewis and C. R. A. Catlow, J. Phys. C - Solid State Physics **18**, 1149 (1985).

[178] J. Maple, J. U. Dinur, and A. T. Hagler, Proc. Nat. Acad. Sci. USA **85**, 5350 (1988).

[179] C. R. A. Catlow and A. N. Cormack, Int. Rev. Phys. Chem. **6**, 227 (1987).

[180] K. S. Kim, M. A. Moller, D. J. Tildesley, and N, Quirke, Molecular Simulation **13**, 77 (1994).

[181] C. R. A. Catlow and J. M. Thomas, Phil. Trans. R. Soc. Lond. A **341,** (1992).

[182] D. R. Hartree, Proc. Camb.Phil. Soc. **24**, 89 (1928).

[183] V. Fock, Z. Phys. **61**, 126 (1930) and ibid. **62**, 795 (1930).

[184] N. Metropolis, A. W. Rosenbluth, M. N. Rosenbluth, A. H. Teller, and E. Teller, J.Chem. Phys. **21**, 1087 (1953); W. R. Magro, D. M. Ceperley, C. Pierleoni, and B. Bernu, Phys. Rev. Lett. **76**, 1240, (1996); C. Pierleoni, D. M. Ceperley, B. Bernu, and W. R. Magro, Phys. Rev. Lett. **73**, 2145 (1994).

[185] J. C. Slater, Quantum Theory of Molecules and Solids Vol. **4**, McGraw-Hill, New York (1974).

[186] S. F. Boys, Proc. R. Soc. **A 200** (1950).

[187] W. J. Hehre, L. Radom, P. Schleyer, and J. A. Pople, *Ab initio* molecular orbital theory, John Wiley & Sons, New York (1986).

[188] E. Wimmer, NATO Series: Electronic Structure Methods, (1996).

[189] R. Dovesi , V. R. Saunders, and C. Roetti, CRYSTAL 92 User Manual, University of Turin, Italy, and SERC Daresbury Laboratory, UK; August 17 (1992).

[190] A. Balková and R. J. Bartlett, J. Chem. Phys. **96**, 3739 (1992).

[191] D. Pines, Solid State Physics **1**, 367 (1951).

[192] L. H. Thomas, Proc. Camb. Phil. Soc. **23**, 542 (1926).

[193] E. Fermi, Z. Phys. **48**, 73 (1928).

[194] J. C. Slater, Phys. Rev. **81**, 385 (1951).

[195] P. Hohenberg and W. Kohn, Phys. Rev. **B 136**, 864 (1964).

[196] W. Kohn, and L. J. Sham, Phys. Rev. **A 140**, 1133 (1965).

[197] E. Wimmer, A. J. Freeman, M. Weinert, H. Krakauer, J. R. Hiskes, and A. M. Karo, Phys. Rev. Lett. **48**, 1128 (1982).

[198] M. Born and R. Oppenheimer, Ann. Physik **84**, 457 (1927).

[199] R. Car and M. Parrinello, Phys. Rev. Lett. **55**, 2471 (1985).

[200] D. D. Koelling and B. N. Harmon, J. Phys. **C 10**, 3107 (1977).

[201] E. Wimmer, Molecular Simulations Inc. documentation (1997).

[202] M. C. Payne, M. P. Teter, D. C. Allan, and J. D. Joannopoulos, Rev. Mod. Phys. **64**, 1045 (1992), and references therein.

[203] M. L. Cohen and V. Heine, Solid State Physics **24**, 37 (1970).

[204] G. B. Bachelet, D. R. Hamann, and M. Schlüter, Phys. Rev. **B 26**, 4199 (1982).

[205] J.C. Phillips, Phys. Rev. **112**, 685 (1958).

[206] U. von Barth and L. J. Hedin, Phys. C **5**, 1629 (1972).

[207] J. P. Perdew and Wang Yue, Phys. Rev. B **33**, 8800 (1986).

[208] A. D. Becke, Phys. Rev. B **33**, 8822 (1986).

[209] J. P. Perdew and A. Zunger, Phys. Rev. B **23**, 5048 (1981).

[210] D. M. Ceperley and B. J. Alder, Phys. Rev. Lett. **45**, 566 (1980).

[211] N. W. Ashcroft and N. D. Merming, Solid State Physics (Holt Saunders, Philadelphia), p. 113.

[212] J. C. Slater and G. F. Koster, Phys. Rev. **94**, 1498 (1954).

[213] G. A. Baraff and M. Lannoo, Rev. Phys. Appl. **23**, 863 (1988).

[214] D. J. Chadi and M. L. Cohen, Phys. Rev. **B 8**, 5757(1973).

[215] J. D. Joannopoulos and M. L. Cohen, J. Phys. **C 6**, 1572 (1973).

[216] R. A. Evarestov and V. P. Smirnov, Phys. Status. Solidi, **119**, 9 (1983).

[217] H. J. Monkhorst and J. D. Pack, Phys. Rev. B **13**, 5188 (1976).

[218] I. J. Roberstson and M. C. Payne, J. Phys.: Condens. Matter, **2**, 9837 (1990).

[219] I. J. Roberstson and M. C. Payne, J. Phys.: Condens. Matter, **3**, 8841 (1991).

[220] G. P. Francis and M. C. Payne, J. Phys.: Condens. Matter. **2**, 4395 (1990).

[221] M. T. Yin and M. L. Cohen, Phys. Rev. B **25**, 7403 (1982).

[222] D. R. Hamann, M. Schluter, and C. Chiang, Phys. Rev. Lett. **43**, 1494 (1979).

[223] D. Vanderbilt, Phys. Rev. B **41**, 7892 (1990).

[224] R. Fletcher, and C. M. Reeves., Comp. J **7**, 149 (1964).

[225] M. J. D. Powell, "*Nonconvex Minimization Calculations and the Conjugate Gradient Method*", Lecture Notes in Mathematics, Vol. **1066**, pp. 122, (1984).

[226] O. Ermer, "*Calculation of molecular properties using force fields. Applications in organic chemistry*", Structure and Bonding **27**, 161-211 (1976).

[227] M. P. Teter, M. C. Payne and D. M. Allan, Phys. Rev. B **40**, 12255 (1989).

[228] L. Kleinmann and D. M. Bylander, Phys. Rev. Lett. **48**, 1425 (1982).

[229] J. A. White and D. M. Bird, Phys. Rev. B **50**, 4954 (1994).

[230] V. Milman, B. Winkler, J. A. White, C. J. Pickard, M. C. Payne, E. V. Akhmatskaya, and R. H. Nobes, Int. J. Quant. Chem. **77**, 895 (2000).

[231] J. P. Perdew, K. Burke, and M. Ernzerhof, Phys. Rev. Lett. **77**, 3865 (1996).

[232] N. Troullier and J. L. Martins, Phys. Rev. B **43**, 1993 (1991).

[233] M. Sergent and R. Chevrel, J. Solid State Chem. **6**, 433 (1973).

[234] J. M. Tarascon, F. J. Di Salvo, J. V. Waszczak, and G. W. Hull, Jr., Phys. Rev B **31**, 1012 (1985); *ibid.* **31**, 8280 (E) (1985).

[235] X. Rocquefelte, F. Boucher, P. Gressier, G. Ouvrard, P. Blaha, and K. Schwarz, Phys. Rev. B **62**, 2397 (2000).

[236] S. Kurth, J. P. Perdew, and P. Blaha, Int. J. Quant. Chem. **75**, 889 (1999).

[237] J. Guillevic, J. Y. Le Marouille, and D. Grandjean, Acta Crystallogr., Sect. B: Struct. Crystallogr. Cryst. Chem. **30**, 111 (1974).

[238] Y. Elerman, H. Fuess, and W. Joswig, Acta Crystallogr., Sect. B: Struct. Crystallogr. Cryst. Chem. **38**, 1799 (1982).

[239] Y. Takeuchi, S. Sasaki, K.A. Bente, and K. Tsukimura, Acta Crystallogr., Sect. B: Struct. Crystallogr. Cryst. Chem. **49**, 780 (1993), and references therein.

[240] L. Konczewicz, P. Bigenwald, T. Cloitre, M. Chibane, R. Ricou, P. Testud, A. Briot, and R. L. Aulombard, J. Cryst. Growth **159**, 117 (1996).

[241] O. Chusid, Y. Gofer, H. Gizbar, Y. Vestfrid, E. Levi, D. Aurbach, and I. Reich, Adv. Mater. **15**, 627 (2003).

[242] N. Yoshimoto, S. Yakushiji, M. Ishikawa, and M. Morira, Electrochim. Acta. 48, 2317 (2003).

[243] G. Ceder and M. K. Aydinol, Solid State Ionics. **109**, 151 (1998).

[244] J. M. Tarascon, T. P. Orland and M. J. Neal, J. Electrochem. Soc., **135(4)** 804 (1988).

[245] D. Vanderbilt, Phys. Rev. B **32**, 8412 (1985).

[246] J. Furthmüller, P. Käckell, and F. Beschstedt, Phys. Rev. **B 61**, 4576 (2000).

[247] P. E. Bloechl, Phys. Rev. B **41**, 5414 (1990).

[248] D. R. Hamann, Phys. Rev. B **41**, 2980 (1989).

[249] M. D. Segall, R. Shah, C. J. Pickard, and M. C. Payne, Phys. Rev. B **54**, 16317 (1996).

[250] R. S. J. Mulliken, Chem. Phys. **23**, 1833 (1955).

[251] E. R. Davidson and S. Chakravorty, Theor. Chim. Acta **83**, 319 (1992).

[252] A. J. Freeman and T. Jarlborg, in *Superconductivity in Ternary Compounds*, edited by M. B. Maple and Ø. Fischer, (Springer, Berlin) 1982 Vol. **2**, p. 167.

[253] J. R. Dahn, W. R. McKinnon, R. R. Haering, W. J. L. Buyers, and B. M Powell., Can. J. Phys., **58**, 207(1980).

[254] H. Negishi, S. Ohara, and M. Inoue, Phys. Status Solidi (b), **151**, 441 (1989).

[255] M. Schärli, and F. Lévy, Phys. Rev. B **33**, 4317 (1986).

[256] D. Straub, M. Skibowski, F. J. Himpsel, and W. Drube, Phys. Rev. B **31**, 8254 (1985).

[257] M. Wakihara, T. Uchida, K. Suzuki and M. Taniguchi, Electrochim. Acta., **34** (1989) 867.

[258] T. Uchida, Y. Tanjo, M. Wakihara and M. Taniguchi, J. Electrochem. Soc., 137 (1990) 7.

[259] S. Yamaguchi, T. Uchida and M. Wakihara, J. Electrochem. Soc. **138,** 687 (1991).

[260] J. S. Lin, A. Qteish, M. C. Payne, and V. Heine, Phys. Rev B **47**, 4174 (1993).

[261] R. L. Kleinberg, and B. G. Silbernagel, Solid State Commun. **36**, 345 (1980).

[262] M. S. Whittingham, J. Solid State Chem. **29**, 303 (1979).

[263] G. Lucovsky, R. M. White, J. A. Benda, J. F. Revelli, Phys. Rev. B **7**, 3859 (1073).; G. Lucovsky, W. Y. Liang and R. M. White, Solid State Commun., **19**, 303 (1976).

[264] J. Bichon, M. Danot, and J. Rouxel, C. R. Acad. Sci. C **276**, 1283 (1973).

[265] T. Butz, R. -H. Flagmeyer, St. Jankuhn, T. Reinert, M. F. da Silva, J. C. Soares, and W. Tröger, Nucl. Instr. and Meth. in Phys. Res. B **136**, 253 (1998).

[266] J. B. Goodenough, in H. Reiss (Ed.), Progress in Solid State Chemistry, Pergamon, Oxford,Vol. **5**., (1971).

[267] D. Adler, in F. Sertz, D. Turnbull and H. Ehrenreich (Eds.), Solid State Physics, Academie, New York, 1968, Vol. 21, Rev. Mod. Phys. **40**, 714 (1968).

[268] J. R. Dahn, D. C. Dahn, and R. R. Haering, Solid State Commun, **42**, 179 (1982).

[269] S. A. Safran, Phys. Rev. Lett. **44**, 937 (1980).

[270] J. E. Fischer, H. J. Kim, Phys. Rev. B **35**, 3295 (1987).

[271] M. S. Whittingham, J. A. Panella, Mater. Res. Bull. **16,** 37 (1984).

[272] B. Gu, Q. Song, J. Ni, J. Appl. Phys. **85**, 819, (1999).

[273] H. Negishi, S. Ohara, Y. Takara, T. Yokoyama, M. Tarriguchi, M. Inoue, Mater. Sci. Forum, **91-93**, 603 (1992).

[274] M. Doyle, T. F. Fuller, and J. Newman, J. Electrochem. Soc., **140**, 1526 (1993).

[275] T. F. Fuller, M. Doyle, and J. Newman, J. Electrochem. Soc., **141**, 1 (1994)

[276] T. F. Fuller, M. Doyle, and J. Newman, J. Electrochem. Soc., **141**, 982 (1994)

[277] M. Doyle, J. Newman, A. S. Gozdz, C. N. Schmutz, and J. M. Tarascon, J. Electrochem. Soc., **143**, 1890 (1996)

[278] J. D. Jorgensen, D. G. Hinks, and F. J. Rotella, in *Ternary Superconductors*, edited by G. K. Shenoy, B. D. Dunlap, and F. Y. Fradin (Elsevier, Amsterdam, 1981), p. 6, 9.

[279] M. Potel, P. Gougeon, R. Chevrel, and M. Sergent, Rev. Chim. Miner. **21**, 509 (1984).

[280] A. Patrick, M. Glasse, R. Latham, R. Linford, Solid State Ionics **18 &** **19**, 1063 (1986).

[281] D. Aurbach, ITE Letters on Batteries, New Technologies & Medicinel **2**, 62 (2001).

[282] D. Aurbach, R. Turgeman, O. Chusid, and Y. Gofer, Electrochim. Comm. **3**, 252 (2001).

[283] S. T. Coleman, W. R. McKinnon, and J. R. Dahn, Phys. Rev. B **29**, 4147 (1984).

[284] R. B. McLellan, Acta Metall. **30**, 317 (1982).

[285] J. Yamaki, M. Egashira, and S. Okada, J. Power Sources. **90**, 116 (2000).

[286] P.C. Klipstein, and R.H. Friend, J. Phys. C **20**, 4169 (1987).

[287] F.D. Murnaghan, Proc. Natl. Acad. Sci. USA **30,** 244 (1944).

Appendix A

Schrödinger's Equation.

The wave function $\Psi(r,t)$ can be calculated from a partial differential equation called the *Schrödinger wave equation*. Consider the one-dimensional, non-relativistic motion of a free particle of mass m, having well defined momentum $p = p_x\hat{x}$ of magnitude $p = |p_x|$ and an energy E. Assuming that the particle is travelling in the positive x direction (so that $p_x = p$), it can be described by a monochromatic plane wave of the wave number $k = p_x/\hbar$ and angular frequency $\omega = E/\hbar$, namely

$$\Psi(x,t) = A\exp\{i[kx - \omega t]\} = A\exp\{i[p_x x - Et]/\hbar\} \tag{A.1}$$

where A is a constant. The angular frequency is connected with the wave number by the relation $\omega = \hbar k^2/2m$, which is equivalent to the classical relation

$$E = \frac{p_x^2}{2m} \tag{A.2}$$

connecting the momentum and energy of the particle. Differentiating $\Psi(x,t)$ with respect to time and twice with respect to x, we have

$$\frac{\partial}{\partial t}A\exp\{i[p_x x - Et]/\hbar\} = -\frac{iE}{\hbar}\mathbf{\Psi} \tag{A.3}$$

and

$$\frac{\partial^2}{\partial x^2} A \exp\{i[p_x x - Et]/\hbar\} = -\frac{p_x^2}{\hbar^2}\mathbf{\Psi} \tag{A.4}$$

respectively.

From the above equations we have

$$i\hbar\frac{\partial}{\partial t}\mathbf{\Psi}(x,t) = E\mathbf{\Psi}(x,t) = \frac{p_x^2}{2m}\mathbf{\Psi}(x,t) \tag{A.5}$$

and

$$\mathbf{\Psi}(x,t) = -\frac{\hbar^2}{p_x^2}\frac{\partial^2}{\partial x^2}\mathbf{\Psi}(x,t) \tag{A.6}$$

so that

$$i\hbar\frac{\partial}{\partial t}\mathbf{\Psi}(x,t) = -\frac{p_x^2}{2m}\frac{\hbar^2}{p_x^2}\frac{\partial^2}{\partial x^2}\mathbf{\Psi}(x,t) = -\frac{\hbar^2}{2m}\frac{\partial^2}{\partial x^2}\mathbf{\Psi}(x,t) \tag{A.7}$$

The above wave equation is known as the time-dependent Schrödinger equation for the motion of a free particle in one dimension. It is a linear and homogeneous equation for the wave function Ψ. This equation may be rewritten in the form

$$E_{op}\mathbf{\Psi}(x,t) = \frac{1}{2m}[(p_x)_{op}]^2\mathbf{\Psi}(x,t) \tag{A.8}$$

which is the quantum-mechanical 'translation' of the relation $E = p_x^2/2m$. The generalization of these considerations to free particle motion in three dimensions follows. A free particle of mass m having a well-defined momentum $\mathbf{p}$ and energy E is now described by a plane wave

$$\mathbf{\Psi}(\mathbf{r},t) = A\exp\{i[\mathbf{k}\cdot\mathbf{r} - \omega t]\} = A\exp\{i[\mathbf{p}\cdot\mathbf{r} - Et]/\hbar\} \tag{A.9}$$

so that

$$i\hbar\frac{\partial}{\partial t}\mathbf{\Psi}(x,t) = -\frac{\hbar^2}{2m}\mathbf{\nabla}^2\mathbf{\Psi}(\mathbf{r},t) \tag{A.10}$$

which is the *three-dimensional time-dependent Schrödinger equation for a free particle.*

Finally, using the fact that in wave mechanics the total energy E and the momentum p are represented by the differential operators, the above equation may also be written in the form

$$E_{op}\mathbf{\Psi}(\mathbf{r},t) = \frac{1}{2m}(\mathbf{p}_{op})^2\mathbf{\Psi}(\mathbf{r},t) \tag{A.11}$$

but we have that

$$T = \frac{1}{2m}(\mathbf{p}_{op})^2 = -\frac{\hbar^2}{2m}\boldsymbol{\nabla}^2 \tag{A.12}$$

which is called the kinetic energy operator of the particle. Generalizing the free-particle Schrödinger equation to the case of a particle moving in a field of force, we assume that the force $\mathbf{F}(\mathbf{r},t)$acting on the particle is derivable from a potential

$$\mathbf{F}(\mathbf{r},t) = -\boldsymbol{\nabla}V(\mathbf{r},t) \tag{A.13}$$

so that for the classical particle, the total energy is given by the sum of its kinetic energy $\mathbf{p}^2/2m$ and its potential $V(\mathbf{r},t)$

$$E = \frac{\mathbf{p}^2}{2m} + V(\mathbf{r},t) \tag{A.14}$$

V does not depend on $\mathbf{p}$ or E so that

$$E_{op}\mathbf{\Psi}(\mathbf{r},t) = \left[\frac{1}{2m}(\mathbf{p}_{op})^2 + \mathbf{V}(\mathbf{r},t)\right]\mathbf{\Psi}(\mathbf{r},t) \tag{A.15}$$

so that the generalization of the free-particle Schrödinger equation reads

$$i\hbar\frac{\partial}{\partial t}\mathbf{\Psi}(r,t) = \left[-\frac{\hbar^2}{2m}\boldsymbol{\nabla}^2 + V(r,t)\right]\Psi(r,t) \tag{A.16}$$

Note: The Schrödinger equation, like Newton's laws, cannot be proved to be true. Its best possible justification comes from an exhaustive comparison of the prediction based on this equation with experiment. It is the successful application of the Schrödinger equation to many problems which demonstrated its correctness in non-relativistic quantum

mechanics.

The operator inside the square brackets is called the Hamiltonian of the particle and is denoted by $\hat{H}$.

$$\hat{H} = -\frac{\hbar^2}{2m}\boldsymbol{\nabla}^2 + \mathbf{V} = \frac{1}{2m}(\mathbf{p}_{op})^2 + \mathbf{V} = T + V \tag{A.17}$$

and the time-dependent Schrodinger equation may be rewritten in the form

$$i\hbar\frac{\partial}{\partial t}\boldsymbol{\Psi}(\mathbf{r}, t) = \hat{H}\boldsymbol{\Psi}(\mathbf{r}, t) \tag{A.18}$$

Appendix B

Materials Modelling

The 'models' that most chemists first encountered are molecular models such as the 'stick' model devised by Dreiding or the 'space filling' model of Corey, Pauling and Koltum (commonly referred to as CPK models). This models are interactive, enabling the user to pose 'what if...' or 'is it possible to...' questions. Molecular modelling is concerned in both simple and abstract models, many of which have a distinguished history (e.g. quantum mechanics).

B.1 Meaning of Terms

'**Theoretical physics or chemistry**' is often considered synonymous with quantum mechanics, whereas computational physics or chemistry encompasses not only quantum mechanics but also molecular mechanics, minimization, simulations, conformal analysis and other computer-based method of understanding and predicting the behavior of molecular and solid system. Molecular modelers use all of these methods.

Coordinate system: Internal coordinates can usefully describe the relationship between the atoms in a single molecule, but Cartesian coordinates may be more appropriate when describing a collection of discrete molecules.

Potential energy surface: In molecular modelling the Born-Oppenheimer approxi-

mation is invariably assumed to operate. This enables the electronic and nuclear motions to be separated; the much smaller mass of the electrons means that they can rapidly adjust to any change in the nuclear positions. Consequently, the energy of a molecule in its ground electronic state can be considered a function of the nuclear coordinates only. If some or all of the nuclei move then the energy will usually change. Changes in the energy of a system can be considered as movements on a multi-dimensional 'surface' called the *energy surface*. The interest is in stationary points on the energy surface, where the first derivative of energy (force) is zero with respect to the internal or Cartesian coordinates. At a stationary point the forces on all the atoms are zero. Minimum points are one type of stationary point; these correspond to stable structures.

Molecular graphics: Vector devices were the mainstay of molecular modelling for almost two decades, but have now been superseded by raster devices. These divide the screen into a large number of small 'dots', called pixels. Each pixel can be set to any of a large number of colours, and so by setting each pixel to the appropriate colour it is possible to generate the desired image. Molecules are most commonly represented on a computer graphics screen using 'stick' or 'space-filling' representation, which are analogous to the Dreiding and CPK mechanical models. Sophisticated variation on these two basic types have been developed, such as the ability to colour molecules by atomic number and the inclusion of shading and lighting effects which give 'solid' models a more realistic appearance.

Surfaces: Many of the problems that are studied using molecular modelling involve the non-covalent interaction between two or more molecules. The study of such interactions is often facilitated by examining the van der Waals, molecular or accessible surface of the molecule. The *van der Waals surface* is simply constructed from the overlapping van der Waals spheres of the atoms (≈CPK model). Widely used algorithms for calculating the molecular and accessible surfaces were developed by Connolly 1983, and others [e.g. Richmond 1984] have described formulae for the calculation of exact or approximate values of the surface area.

Computer hardware and software: Developments in computers have increased the ratio of performance-to-price by an order of magnitude every five years or so.

Units of length and energy: The angstrom (1 Å = 10^{-10} m) is a non-SI unit, but is a very convenient unit to use, as most bond lengths are of the order 1-2 Å. One other very common non-SI unit found in the molecular modelling literature is the kilocalorie (1 kcal = 4.1840 kJ).

Mathematical concepts: A full appreciation of all the techniques of molecular modelling requires a proper understanding of mathematical concepts such as vectors, matrices, differential equations, complex numbers, series expansions, multiple integrals (Hartree-Fock theory) and Lagrangian multipliers and some very elementary statistical concepts (arithmetic mean, variance, standard deviation, and normal or Gaussian distribution).

Born-Oppenheimer Approximation: In dealing with systems of large numbers of electrons and ions, we wish to make the number of degrees of freedom of the system which have to be dealt with at any one time as small as possible. The forces on both the electrons and ions are of the same order of magnitude, so that their momenta are also comparable. However since the ions are so much more massive than the electrons, the kinetic energy of the ions is much smaller than that of the electrons. This idea forms the basis of the Born-Oppenheimer approximation [198] in which we assume that the electrons respond instantaneously to the motion of the ions. For any ionic configuration, we assume that the electrons are in the instantaneous ground-state and calculate the total energy of the system. Varying the ionic positions defines a multi-dimensional ground-state potential energy surface, and the motion of the ions can then be treated as classical particles moving in this potential.

Monkorst and Pack Scheme: The Monkhorst-Pack grid is created by dividing the reciprocal lattice basis vectors in equal segments and building a regular mesh in the reciprocal space. Inversion symmetry is always present in reciprocal space due to the presence of time-reversal symmetry, so that only half of the grid so created need be used

as a k-point set. The coordinates of the mesh points in each direction are obtained as follows:

$$X_i = W_i + \frac{K}{(2N)},$$

where W_i is the corresponding component of the shift vector. and K = 1,3, ..., N-1, for even N, and K = 0,2,..., N-1, for odd N.

The scheme is slightly modified for hexagonal lattices - the coordinates along the c-axis are obtained as above while the a and b are sampled differently.

$$X_i = W_i + \frac{(K-1)}{N}$$

where N is the corresponding Monkhorst-Pack parameter and K = 1,2, ... N. It is recommended that even values of Monkhorst-Pack parameters should be used, as the resulting grids provide comparable occupy to the mesh created by using (N+1) odd values (this does not apply to Monkhorst-Pack parameters for hexagonal lattice except for the c-grid sampling).

The Monkhorst-Pack parameters should be selected so as to provide as uniform a mesh in the BZ as possible. This implies that more points will be needed along a longer reciprocal space vector.

Appendix C

Generation of Pseudopotentials

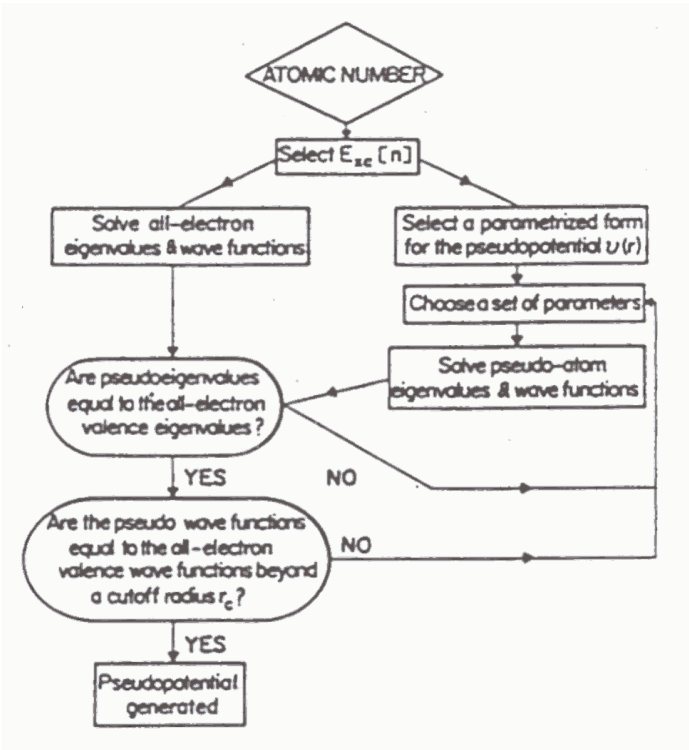

Figure C-1: Flow chart describing the construction of an ionic pseodopotential for an atom.

The typical method for generating an ionic pseudopotential for a atom of species

α, v_α is illustrated in Figure C-1 and proceeds as follows: All-electron calculations are performed for an isolated atom in its ground state and some excited states, using a given form for the exchange-correlation density functional. This provides valence electron eigenvalues and valence electron wave functions for the atom. A parameterized form for the ionic pseudopotential is chosen. The parameters are then adjusted, so that a pseudoatom calculation using the same form for exchange-correlation as in the all-electron atom gives both pseodowave functions that match the valence wave functions outside some cutoff radius r_c and pseudoeigenvalues that are equal to the valence eigenvalues. The ionic pseudopotential obtained in this fashion is then used, without further modification, for any environment of the atom. The electronic density in any new environment of potential obtained in this way and the same form of exchange-correlation functional as employed in the construction of the ionic pseudopotential. A generalization of this pseudopotential construction procedure for solutions of the atom that are not normalizable has been introduced by Hamann [248].

Finally it should be noted that ionic pseudopotentials are constructed with r_c ranging typically from one to two times the value of the core radius. It should also be noted that, in general, the smaller the value of r_c, the more "transferable" the potential. (The entire procedure for solving the problem of a solid, given an ionic pseudopotential, is outlined in the review by Payne et. al. [202])

Appendix D

BFGS Minimization Method

The BFGS (Broyden-Flecther-Goldfarb-Shanno) algorithm is a method for finding the minimum of a function of several variables. It seeks to take account of the different second derivatives of the function with respect to these variables, but using information only about the function and its first derivatives at each point.

Expanding the function $f(x)$ about the current position x_0 to second order in the displacement gives:

$$f = f(x_0) + \nabla f \cdot (x - x_0)^T \cdot \mathbf{A} \cdot (x - x_0) \tag{D.1}$$

where $\mathbf{A}$ is the second order derivative matrix. The optimal choice of x to minimize the energy would therefore be

$$(x - x_0) = \mathbf{A}^{-1} \cdot \nabla f \tag{D.2}$$

The problem is then to obtain a reasonable estimate of $\mathbf{A}^{-1}$. We start off with some approximation to the Hessian (see sub-section 2.3.8), which is then iteratively improved after each step. In fact, when far from the minimum our use of an approximate Hessian may be a better choice than the true Hessian, as we force the former to always be positive definite, ensuring the step direction chosen should always cause the energy to

decrease. However, this does not guarantee that the full step length suggested in Eq. D.2 will decrease the energy, just that the energy initially decreases along this direction. Therefore if the energy does increase we can adopt a backtracking strategy to choose a smaller step.

If the $i+1^{-th}$ step involves moving from x_i to x_{i+1}, and the gradients at each point are ∇f_i and ∇f_{i+1} respectively, then the next approximation for the Hessian $\mathbf{A}_{i+1}$ is obtained by updating the previous approximation $\mathbf{A}_i$, according to the formula below:

$$\mathbf{A}_{i+1} = \mathbf{A}_i + \left(1 + \frac{(\nabla f_{i+1} - \nabla f_i) \cdot \mathbf{A}_i \cdot (\nabla f_{i+1} - \nabla f_i)}{(x_{i+1} - x_i) \cdot (\nabla f_{i+1} - \nabla f_i)}\right) \frac{(x_{i+1} - x_i) \otimes (x_{i+1} - x_i)}{(x_{i+1} - x_i) \cdot (\nabla f_{i+1} - \nabla f_i)}$$

$$- \frac{\mathbf{A}_i \cdot (\nabla f_{i+1} - \nabla f_i) \otimes (x_{i+1} - x_i)}{(x_{i+1} - x_i) \cdot (\nabla f_{i+1} - \nabla f_i)} - \frac{(x_{i+1} - x_i) \otimes \mathbf{A} \cdot (\nabla f_{i+1} - \nabla f_i)}{(x_{i+1} - x_i) \cdot (\nabla f_{i+1} - \nabla f_i)} \tag{D.3}$$

The rigorous derivation of this formula shows that for an exactly quadratic N-dimensional energy surface, it will converge to the exact Hessian in N steps or less.

Appendix E

Steepest Descent Minimization Method

Steepest descent (SD) is one of the oldest and simplest methods. It is actually more important as a theoretical, rather than practical, reference by which to test other methods. However, 'steepest descent' steps are often incorporated into other methods (e.g., Conjugate Gradient, Newton) when round off destroys some desirable theoretical properties, progress is slow, or regions of indefinite curvature are encountered.

In the linear system $\mathbf{A}x = \mathbf{b}$ suppose the coefficient matrix $\mathbf{A}$ is symmetric and positive definite. Solving $\mathbf{A}x = \mathbf{b}$ is equivalent to minimizing the quadratic function

$$Q(x) = \frac{1}{2}x^T Ax - x^T b \tag{E.1}$$

The exclusive reliance on gradients by the steepest descents method, is both its weakness and its strength. Convergence is slow near the minimum because the gradient approaches zero, but the method is extremely robust, even for systems that are far from harmonic. It is the method most likely to generate the true low-energy structure, regardless of what the function is or where the process begins. Therefore, the steepest descents method is often used when the gradients are large and the configurations are far from

the minimum. This is commonly the case for initial relaxation of poorly refined crystallographic data or for graphically built models. In fact, as explained in the following sections, more advanced algorithms are often designed to begin with steepest descents as the first step.

Appendix F

Conjugate Gradients Minimization Method

The basic idea of the conjugate gradients method is similar to that of the BFGS scheme - using information from previous minimization steps to improve the choice of the next step. The conjugate gradient method is based on the idea that the convergence to the solution could be accelerated if we minimize Q over the hyperplane that contains all previous search directions, instead of minimizing Q over just the line that points down gradient.

The Conjugate Gradient (CG) algorithm is an iterative method in order to solve a system

$$\mathbf{A}x = \mathbf{b} \tag{F.1}$$

of N linear equations in N unknowns where the matrix $\mathbf{A} \in \mathbb{C}^{N \times N}$ is assumed to be Hermitian and positive definite. CG is an iterative method: given an initial guess $x^{(0)}$ at the solution, the method generates a sequence of increasingly improved approximate solutions $x^{(1)}$, $x^{(2)}$, ... The iteration terminates when the error is deemed "small enough," or when the user decides that the iteration has run for too long. A common measure of error is the residual:

$$r^{(i)} = \mathbf{b} - \mathbf{A}x^{(i)} \tag{F.2}$$

The conjugate gradient iteration keeps track (approximately) of the residual $r^{(i)}$ from step to step, so a convergence criterion based on the residual will be inexpensive. For a symmetric positive-definite system, solving $\mathbf{A}x = \mathbf{b}$ is equivalent to minimizing

$$Q(x) = \frac{1}{2}x^T\mathbf{A}x - x^T\mathbf{b} \tag{F.3}$$

The method of conjugate gradients works by moving "downhill" toward this minimum. To get the approximate solution $x^{(i)}$, the algorithm picks a search direction vector $p^{(i)}$ (also called the gradient) and then computes

$$x^{(i)} = x^{(i-1)} + \alpha_i p^{(i)} \tag{F.4}$$

where i is chosen to minimize $(x^{(i)})$. The gradients $p^{(i)}$ are chosen to be **A**-*conjugate* or **A**-*orthogonal*; that is

$$p^{(i)^T}\mathbf{A}p^{(j)} = 0 \ for \ i \neq j \tag{F.5}$$

These are the conjugate gradients that give the method its name.

Appendix G

Bulk Modulus and Elastic constant Calculations

The one dimensional analog of the Murnaghan equation [287] provides an approximation for describing the nonlinear relation between normalized lattice parameters and pressure P,

$$r/r_0 = \left[\left(\frac{B'}{B}\right)P + 1\right]^{-\frac{1}{B'}} \tag{G.1}$$

Here, r is the lattice constant along one of the crystal axes, $B^{-1} = -\left(\frac{\partial \ln r}{\partial P}\right)_{P=0}$ is the linear compressibility, and B' is the pressure derivative of B (i.e. $\frac{\partial B}{\partial P}$).

$$B' = \frac{\partial B}{\partial P}$$

$$\kappa = B^{-1} = -\left(\frac{\partial \ln r}{\partial P}\right)_{P=0}$$

$$c/c_0 = \left[\left(\frac{B'}{B}\right)P + 1\right]^{-\frac{1}{B'}} \tag{G.2}$$

$$a/a_0 = \left[\left(\frac{B'}{B}\right)P + 1\right]^{-\frac{1}{B'}} \tag{G.3}$$

and

$$V/V_0 = \left[\left(\frac{B'}{B}\right)P + 1\right]^{-\frac{1}{B'}} \tag{G.4}$$

G.1 Elastic Constant of Hexagonal Materials.

For the lattice constants at zero pressure a_0 and c_0, the ambient pressure volume is

$$V_0 = \frac{\sqrt{3}}{2}a_0^2 c_0 \tag{G.5}$$

For cubic materials, there are only three independent elastic constants while for a hexagonal lattice, there are five independent elastic constants (C_{11}, C_{12}, C_{13}, C_{33}, and C_{55}). A theoretical treatment of the elasticity of hexagonal systems is thus considerably more involved than for cubic systems. Transversely isotropic media also exhibit hexagonal symmetry that reduces to five the number of independent elastic constants.

The formulas for the volume elastic modulus (bulk modulus) B and the linear moduli B_a and B_c in terms of the elastic stiffness are

$$B = X(C_{11} + C_{12} + 2C_{33} - 4C_{13})^{-1}, \tag{G.6}$$

$$B_a = X[2(C_{33} - C_{13})]^{-1}, \tag{G.7}$$

$$B_c = X(C_{11} + C_{12} + 2C_{13})^{-1}, \tag{G.8}$$

where

$$X = C_{33}(C_{11} + C_{12}) - 2(C_{13})^2$$

and

$$B_c = \frac{1}{\kappa_c} \tag{G.9}$$

or

$$C_{33} = \frac{1}{\kappa_c} \tag{G.10}$$

The elastic stiffness constant matrix in the crystallographic axis (X,Y,Z) reference frame for a $\overline{3}$ crystal is

$$\begin{bmatrix} C_{11} & C_{12} & C_{13} & C_{14} & -C_{25} & 0 \\ C_{12} & C_{11} & C_{13} & -C_{14} & C_{25} & 0 \\ C_{13} & C_{13} & C_{33} & 0 & 0 & 0 \\ C_{14} & -C_{14} & 0 & C_{44} & 0 & -C_{25} \\ -C_{25} & C_{25} & 0 & 0 & C_{44} & C_{14} \\ 0 & 0 & 0 & C_{25} & C_{14} & C_{66} \end{bmatrix},$$

where

$$C_{66} = (C_{11} - C_{12}) \tag{G.11}$$

Hexagonal crystals have six different elastic coefficients where the elastic constant tensor $[C_{ij}]$ contains only five independent constants instead of 21 in the general case:

$$[C_{ij}] = \begin{bmatrix} C_{11} & C_{12} & C_{13} & 0 & 0 & 0 \\ C_{12} & C_{11} & C_{13} & 0 & 0 & 0 \\ C_{13} & C_{13} & C_{33} & 0 & 0 & 0 \\ 0 & 0 & 0 & C_{44} & 0 & 0 \\ 0 & 0 & 0 & 0 & C_{44} & 0 \\ 0 & 0 & 0 & 0 & 0 & C_{66} \end{bmatrix} \tag{G.12}$$

with $C_{66} = \frac{1}{2}(C_{11} - C_{12})$, associated with the order parameter. The elastic constant tensor is related to stress σ and strain ϵ by the following equation:

$$\sigma_i = \sum_{j=1}^{6} C_{ij}\epsilon_j \tag{G.13}$$

where i and j represent the six unequal combinations of three axes (x, y, and z).

A hexagonal or transversely isotropic medium is characterized by five nonzero elastic constants

$$C_{11}; C_{33}; C_{12}; C_{13} = C_{23}; C_{44} = C_{55}$$

The formulas for the bulk modulus along the a-axis and c-axis, i.e., linear moduli B_a and B_c in terms of the elastic stiffness constant C_{ij} are:

$$B_c = c_o \frac{dP}{dc} = \frac{B_a}{\beta} \tag{G.14}$$

$$B_a = a_o \frac{dP}{da} = \frac{\delta}{(1 + \alpha + \beta)} \tag{G.15}$$

where

$$\delta = C_{11} + 2C_{12}\alpha + 2C_{13}\beta + C_{33}\beta^2 + 2C_{13}\alpha\beta$$

For hexagonal systems

$$\alpha = 1 \text{ and } \beta = \frac{C_{11} + C_{12} - 2C_{13}}{C_{33} - C_{13}}$$

Appendix H

Publications and Papers Presented at International Conferences

H.1 Publications

- K. R. Kganyago and P.E. Ngoepe, "Effects of Local and Gradient-Corrected Density Approximation on the Prediction of the Interlayer Lattice Distance c, in Graphite and LiC_6"., Molecular Simulations. **22**, 39 (1999).
- KR Kganyago, PE Ngoepe and CRA Catlow, "Ab initio calculation of the voltage profile for LiC_6" , Solid State Ionics **159**, 21– 23 (2003).
- KR Kganyago, PE Ngoepe and CRA Catlow, "Voltage profile, structural prediction and electronic calculations for $Mg_xMo_6S_8$.", Physical Review B **67**, 104103 (2003).
- KR Kganyago and PE Ngoepe, "Structural and electronic properties of lithium intercalated graphite, LiC_6" Physical Review B **68**, 205111 (2003).
- KR Kganyago and PE Ngoepe, "Theoretical study of the pressure effect on the optical properties of lithium intercalated graphite", submitted to IOP

- KR Kganyago, PE Ngoepe and CRA Catlow, "First Principle study of the voltage profile $LiTiS_2$ and $LiMo_6S_8$", submitted to Elsevier - Solid State Ionics

- KR Kganyago, PE Ngoepe and CRA Catlow, "First Principle study of the voltage profile, electronic and optical properties of $LiTiS_2$.", in process

- KR Kganyago, PE Ngoepe and CRA Catlow, "Electronic and optical properties for the Chevrel phase $Mg_xMo_6S_8$ compounds.", in process

- KR Kganyago, PE Ngoepe and CRA Catlow, "First principles pressure studies of the Chevrel phase compound $Mg_xMo_6S_8$." in process

H.2 Papers Presented

H.2.1 International Conferences

- "Electronic and Structural Properties of Lithium Intercalated Graphite: A Density Functional Approach."

Kganyago K.R. and Ngoepe P.E., December 1997, Polar Solids Meeting, Liverpool, UK

- "Study of Electronic, Structural and Transport Properties of Lithium Intercalated Graphite (LiC_6)."

Kganyago K.R. and Ngoepe P. E., Institute of Physics, Condensed Matter and Materials Physics Conference, December 1997, University of Exeter, Exeter, UK.

- "Computer Simulation Studies of Lithium Intercalated Graphite"

Kganyago K. R., Ngoepe P. E., H. M. Sithole and A. M. Letsoalo, 9th International Battery Association: Battery Materials Symposium, March 1995, Cape Town, South Africa

- "Transport Studies in Lithium Intercalated Graphite: A Harris Functional Approach."

Kganyago K. R. and Ngoepe P. E., Spring Symposium, April 1998, San Franscisco, USA.

- "Study of Transport, Electronic and Structural Properties of First Stage Lithium Intercalated Graphite: Density Functional Approach."

  Kganyago K. R. and Ngoepe P. E., The 9th International Meeting on Lithium Batteries,July 1998, Edinburg, UK.

- "Theoretical Studies of Structural Stability of LiC_6",

  Kganyago K. R. and Ngoepe P. E., 14th International Battery Association – Battery Materials Symposium, March 2001, Kwa Maritane, South Africa.

- "Ab initio studies of structural and optical properties of layered hexagonal graphite and transitional metal dichalcogenides: effects of lithium intercalation".

  Kganyago K. R. and Ngoepe P. E., Materials Research Society Symposium, April 2001, San Francisco, USA.

H.2.2 Local Conferences

Also presented 28 papers at the following local conferences: Annual South African Institute of Physics (10), IUCr Structural Chemistry Indaba I and II (2), Annual FRD/Royal Society - Materials Modelling Meeting (12), Bi-Annual University of the North Interscience (4) and The 10th Chris Engelbrecht Summer School in Density Functional Theoretical Physics (1).